VORTEX FORMATION AND DRAG ON LOW ASPECT RATIO, NORMAL FLAT PLATES

Thesis by

Matthew James Ringuette

In Partial Fulfillment of the Requirements

for the Degree of

Doctor of Philosophy

California Institute of Technology

Pasadena, California

2004

(Defended May 21, 2004)

Acknowledgements

First, I would like to thank Michele Milano, whose friendship, guidance, and advice on time management helped to make this work possible. Many other group members, past and present, also helped along the way. In particular, I would like to thank Dana Dabiri, Paul Krueger, and David Jeon for their assistance with DPIV, lasers, and getting the Towing Tank running again. I would also like to acknowledge Phillip Zukin, John Dabiri, Tait Pottebaum, Flavio Noca, and Derek Lisoski, for their help with various aspects of the project. Most importantly, I would like to thank my advisor, Professor Mory Gharib. He gave me the freedom and trust to pursue my interests, encouraged creativity, provided ideas and direction when they were needed, stressed clarity and understanding, and taught me how do science that is both fascinating and relevant.

I also want to acknowledge Professor Anthony Leonard, who acted as my second advisor. His door was always open when I had a problem or idea that I wanted to go over. A discussion with Professor Leonard always resulted in understanding rooted in fundamentals, and new directions to consider.

Additionally, I would like to thank my committee, Professors Mory Gharib, Anthony Leonard, Michael Dickinson, and Joel Burdick, for their evaluation of this work and their suggestions, which led to a more solid final product. I also want to thank Professor Hans Hornung, who served on my candidacy committee.

My wonderful family and friends, who have supported and encouraged me throughout this endeavor, also deserve mention. Particularly my wife Jen, my mother, who kept me in touch with my family and reality, and my father, for his council, spiritual guidance, and friendship. I was also fortunate to have a great friend, Joel Tse, journey west to California with me, and, thanks to the divine hand and irony of Providence, head back east at the same time I did, each to pursue his own adventures.

Finally, I would like to thank the Atari VCS (2600) and its players. Specifically, Pitfall Harry, Roderick Hero, Frostbite Bailey, Ms. Pac-Man, and those pesky Space Invaders.

To my wife, Jen, whose love, patience, and support over these five years on opposite coasts made this endeavor possible.

Abstract

Experiments were done in order to investigate the role of vortex formation in the drag force-generation of low aspect ratio, normal flat plates, with a free end condition, starting from rest. This very simplified case is a first, fundamental step toward understanding the more complicated flow of hovering flight, which relies primarily on drag for propulsion. The relative importance of the plate's free end, or tip, with varying aspect ratio (*AR*) was also studied. Identifying the relationship among *AR*, vortex formation, and drag force can provide insight into the wing *AR*'s and kinematics found nature, with the eventual goal of designing man-made flapping wing micro air vehicles (MAVs).

The experiments were carried out using flat plate models in a towing tank at a moderate Reynolds number of 3000. An attached force balance measured the time-varying drag, and multiple, perpendicular sections of the flow velocity were measured quantitatively using digital particle image velocimetry (DPIV). Finally, since the flow is highly 3-D, flow visualization was done to characterize its structure and to augment the 2-D DPIV data. Two *AR*'s, 6 and 2, were considered, the latter in order to have a highly tip-dominated case.

The drag force for both *AR*'s was measured with the bottom end (or tip) free, and also with the tip of the $AR = 6$ plate "grazing" a bottom wall, to demonstrate the effects of *AR* and suppressing the flow around the free end, respectively. As the plate accelerates from rest, it generates vortices at its leading edges and tip edge. The velocity field of the leading edge vortices (LEVs) was measured using DPIV in chordwise planes at 50, 75, and 90% span, while the tip vortex (TV) was captured with DPIV in spanwise planes, parallel to the direction of travel, at mid-chord and at one leading edge (the flow is symmetrical about a spanwise plane at mid-chord). It has been hypothesized that the LEV and the TV are

responsible for the force generation in hovering flight. Vorticity fields and circulation were calculated from the DPIV data to identify any relationship between these vortices and features found in the drag force.

The effect of the plate's tip or free end is to induce a highly 3-D, low-pressure flow that keeps the LEVs near the tip attached to the plate. Chordwise DPIV data show that the accumulation of circulation in these LEVs is restricted, as compared to the LEVs away from the tip, creating a spanwise pressure gradient within the LEVs. This pressure gradient is responsible for spanwise flow within the cores of the LEVs, directed away from the tip, which gives them a helical or tornado-like structure.

For $AR = 6$, the "grazing," or nominally 2-D, lower end condition results in a minimum in the drag force at about 5 chord lengths of travel. A previous study attributed this minimum to the formation of a low-drag, recirculating LEV bubble along the span. The free end case generates instead in a drag maximum, about 46% higher, at the same distance. Chordwise and spanwise DPIV show that this maximum corresponds to the saturation of circulation within the strong LEVs at 50% span, and to the accumulation of attached vorticity near the tip, generated by the free end itself. This attached vorticity is a region of low pressure, and thus high drag. In addition, the induced flow from the tip prohibits the formation of the essentially 2-D LEV recirculating bubble, which also results in increased drag. The drag coefficient for $AR = 2$ was found to be higher than that of $AR = 6$, most likely because the attached vorticity generated from the tip acts over a relatively larger portion of its span. Therefore, the relationship between the drag force and plate aspect ratio was found to be a result of the vortex dynamics.

The flow for $AR = 2$ is very similar spatially to that of $AR = 6$, in terms of absolute distance from the plate tip. However, the $AR = 2$ flow evolves faster in time, implying that the effect of the tip increases with decreasing aspect ratio.

Coupled with data from previous work for $AR = 10$ and 17 plates, the findings of the present study show that a significant drag benefit is only achieved for the free end condition when the AR is reduced to about 6 or less. This is consistent with the range of AR's found in hovering animals. Additionally, the drag maximum for $AR = 6$, found at 5 chord lengths of travel, lies within the wing-stroke amplitude range found in insects. Finally, the results of the present work point to the induced flow from the tip as being responsible for the restricted circulation and attachment of the LEVs near the tip. This is in contrast to a previous study of hawkmoth hovering, which suggests that this effect is due to the spanwise flow within the LEVs.

Table of Contents

List of figures

List of symbols

Roman symbols

A	area over which circulation is computed
AR	aspect ratio
b	plate span
c	plate chord length
C_D	drag coefficient
D	drag
h	plate thickness
Re	Reynolds number
t	time
S	plate area
T	formation time
T^*	non-dimensional time, $T^* = tU/c$
U	plate velocity
U_{final}	final, constant plate velocity
$\overline{U}$	mean of plate velocity, U

Greek symbols

α	angle of attack (degrees)
Γ	circulation
ν	kinematic viscosity
ρ	density (typically of water)
ω	vorticity component normal to the plane under consideration

Abbreviations

DPIV	digital particle image velocimetry
LEV	leading edge vortex
TV	tip vortex

1 Introduction and background

1.1 Introduction

In recent years there has been a push to understand biological flight. Observation of a honeybee in a flower garden or a fly in the house reveals the reasons why. Flying animals are capable of extraordinary acrobatic maneuvers and operating in confined spaces. They also offer lessons in control system and actuator design. Biological inspiration coupled with a clear understanding of the underlying physics could lead to man-made devices with similar or superior capabilities. Micro air vehicles (MAVs), as such creations are called, would have military and civilian applications, such as reconnaissance and search and rescue.

Flight in nature is typically achieved through the use of flapping wings (the exception being whirlybird seedpods), in contrast to the fixed- and rotary-wing aircraft employed by humans. This thesis focuses on drag-based propulsion, which is exemplified by hovering flight. Hovering is the condition of staying aloft while having no mean translational motion. It is the most extreme and demanding aspect of flapping wing flight; only one of the bird species, the hummingbirds, is able to do it for long durations without taking advantage of air currents (Dhawan, 1988). During hovering, the wing typically oscillates along a horizontal path (Weis-Fogh, 1973; Ellington, 1984; Wang et al., 2004), with one back-and-forth motion being defined as a full wing stroke. Due to the high wing angles of attack (α), the wing acts as a bluff, rather than a lifting body. Thus, drag, which opposes the motion of the wing, is the primary fluid dynamical force generated during hovering. Hovering animals flap their wings in such a way that this drag has a net upward component, in order to overcome gravity, and no net sideways component.

A feature common to all creatures able to hover, namely, most flying insects and hummingbirds, is the low aspect ratio of their wings. Aspect ratio (*AR)* will be defined throughout this work as b^2/S, where *b* is the span of a *single wing*, instead of the conventional definition, which is the distance between both wing tips; *S* is the single-wing planform (top-view) area. Flying insects have *AR*'s between about 2.75 and almost 6, (Ellington, 1984; Dickinson, 1999), while hummingbirds have *AR*'s of around 4 (Dhawan, 1988); a soaring animal, such as the albatross, has an *AR* of about 9 (Dhawan, 1988). A finite *AR* wing, versus one of infinite span, experiences aerodynamic effects due to the tip, which increase relatively as the *AR* decreases. Therefore, for low *AR* wings, the influence of the tip is very significant.

The flow over a wing undergoing hovering kinematics is necessarily unsteady: during one half-stroke, the wing accelerates and rotates, all while traveling a distance of only about 3 to 5 chord lengths (Weis-Fogh, 1973; Wang et al., 2004). Separation occurs at the edges of the wing, due to the high angles of attack and the sufficiently high velocities. This results in the formation of wake vortices at the leading and trailing edges, as well as at the tip (Ellington et al., 1996; Wang, 2000; Birch & Dickinson, 2001). The leading edge vortex (LEV) has been shown to be partly responsible for the significant force generation exhibited during hovering (Ellington et al., 1996; Dickinson & Götz, 1992). For the 3-D flow over a hovering wing, studies have demonstrated that the LEV remains attached to the surface of the wing longer than if the flow were purely 2-D (Ellington et al., 1996; Birch & Dickinson, 2001). However, the mechanism responsible for this prolonged attachment is a matter of some controversy.

Upon performing flow visualization using a robotic model of a flapping hawkmoth, Ellington et al. (1996) observed significant spanwise flow (from wing root to tip) within the LEV core, which they attributed to a corresponding spanwise pressure gradient due to the higher velocities of the wing tip. They hypothesized that this spanwise flow drains some of the vorticity of the LEV outboard to the wing tip. This, they postulated, retards the vorticity accumulation in the LEV, as compared to the 2-D case (Dickinson & Götz, 1993), so that more time is required for the vortex to build up enough circulation to shed. Birch and Dickinson (2001), using digital particle velocimetry (DPIV) to measure the velocity field around a flapping robotic model of a fruitfly, found only a very small spanwise velocity in the LEV. Additionally, they observed a large tip vortex (TV) attached to the wing, which induced spanwise flow behind the LEV, near the wing's trailing edge, as well as a strong downward flow around the wing; the flow from the previous wing stroke also contributed to this downward flow. Birch and Dickinson proposed an alternative hypothesis that of Ellington et al., which is that this induced downward flow, or downwash, significantly lowers the effective angle of attack of the wing, compared to a purely 2-D case, thus retarding the growth of the LEV and increasing its time to shed. Although Ellington et al. also reported a large TV, after the middle of the downstroke, they only commented that the outboard portion of the LEV breaks down and "feeds" into it. Therefore, there is disagreement over the mechanism that keeps the LEV attached to a 3-D, hovering wing longer than its 2-D counterpart. Moreover, the importance of the TV, and its effect on the LEV, is in dispute.

In order to investigate the roles of the LEV and the TV in the force generation during something as complicated as hovering flight, the philosophy that it is better to start by understanding the simplest realization of the problem will be adopted. For this investigation,

the wing is modeled as a low *AR* flat plate of rectangular planform. The α is 90°, so that drag is the primary force that the plate experiences. Since each half-stroke has essentially mirror-image force generation, only one half-stroke will be modeled. Consequently, the problem reduces to an investigation of the vortex formation and force generation of a low *AR* flat plate accelerating from rest, oriented normal to its direction of travel. A brief history of previous work related to this problem must therefore include studies from the fields of biology and fluid mechanics. The literature pertaining directly to biological hovering will be discussed first, followed by a review of past studies on flat plate starting flow and *AR* effects.

1.2 Background

1.2.1 Hovering flight in nature

One of the first major investigations of hovering animals was done by Weis-Fogh in 1973. It contains a very thorough study of the many aspects of hovering flight, including aerodynamics, power, efficiency, wing kinematics, and some hypothesized unsteady lift-generation mechanisms such as the "clap" and "fling." His observations on hovering kinematics are especially applicable to the present work. Weis-Fogh found that most hovering animals exhibit similar kinematic behavior, which he thus called "normal hovering." He defined normal hovering kinematics as the animal flapping its wings "...through a large stroke angle and ... approximately in a horizontal plane." In addition, he investigated the ratio between the stroke arc length and the wing chord length (referenced at the radius of gyration of the second moment of the wing area, about the wing joint), which is the number of chord lengths traveled during a half-stroke, and observed that it is between 3 and 5 for most hovering animals (as mentioned above). However, throughout much of his analysis Weis-Fogh made the incorrect assumption that quasi-steady flow theory is sufficient

to explain the aerodynamic performance of most hovering animals, which severely limits the applicability of his results.

In 1984 Ellington published a 180-page, 6-part paper on the aerodynamics of insect hovering flight. It provides a detailed analysis of wing geometry, improved kinematics data, a discussion on aerodynamic mechanisms, and information on lift and power requirements. Ellington confirmed Weis-Fogh's observation that most hovering animals flap their wings in a horizontal stroke plane, but disagreed with Weis-Fogh's use of the quasi-steady flow assumption. More importantly, he examined the idea that vorticity generated by separation at the edges of the wing could be a lifting mechanism for hovering flight. Based on experiments by Maxworthy (1979), he speculated that the LEV may be the primary lift-generating vortex, and that the induced spanwise flow (from root to tip) due to the TV may keep the LEV from shedding throughout each half-stroke. Technological advances during the 1990's allowed for more advanced experiments to test these hypotheses.

In the study by Ellington et al. (1996), discussed in section 1.1, 3-D flow visualization was also performed on an actual hawkmoth flapping in a wind tunnel. These results, coupled with the flow visualization done on their robotic flapping model of the hawkmoth, provided new insight into hovering flight. As reported above, they observed a strong LEV during the downstroke, and spanwise flow within the LEV core from the wing root to the tip. They also found that the LEV had a helical structure similar to that of a delta wing, and they hypothesized that the spanwise flow was responsible for this. The fact that the LEV remains attached throughout the downstroke longer than if the flow were 2-D was attributed to its increase in circulation being slowed by the spanwise convection of its vorticity, via its helical structure, out of the LEV and toward the wing tip. This slower accumulation of vorticity, as

mentioned above, increases the time needed for the vortex to build up enough circulation to shed. During the latter half of the downstroke, the LEV was seen to merge with a large TV, but whether the TV itself was partly responsible for the spanwise flow in the LEV was not discussed.

A subsequent study by Liu, Ellington, and others (1998) compared direct numerical simulations of a hovering hawkmoth wing with the robotic flapper experiments of Ellington et al. (1996), and obtained a clearer picture of the interaction between the LEV and the TV. They found that early in the downstroke the LEV forms from the root to about 60 to 75% of the wing span, and has an essentially two-dimensional structure. By the end of the first half of the downstroke, they observed significant spanwise flow, directed toward the tip, within the LEV core, consistent with that reported by Ellington et al. (1996). They noted, as well, that the LEV had a helical structure, which they hypothesized was due to a spanwise pressure gradient created by the difference in velocity between the wing tip and root. For reasons given previously, they postulated that this helical structure prolongs the attachment of the LEV, which generates a large lift force. At the start of the second half of the downstroke, they observed a breakdown in the LEV at 75% span, which they reasoned was due to a reverse (decreasing toward the wing root) pressure gradient there and to wing deceleration. Additionally, they reported that the flow in the tip region separates and rolls up into a TV. Near the end of the downstroke, they found that a second LEV forms in this tip region and merges with the TV, but has an axial flow within its core toward the wing root, because of the reverse pressure gradient that was attributed to the TV. They concluded that high lift is thus generated in the latter half of the downstroke due to the initial LEV (which remains attached over 50 to 75% of the span throughout the entire half-stroke), and the addition of the

second LEV, both of which are finally shed at the end of the half-stroke. Again, whether or not the tip vortex itself is responsible for any force generation or the spanwise flow in the first LEV is not discussed.

As described in section 1.1, experiments done by Birch and Dickinson (2001) using a robotic model of a flapping fruitfly showed only a very small spanwise velocity component within the LEV core. They also observed a large TV, which, along with wake vorticity shed from the previous stroke, induced a strong downward flow about the wing. Further experiments were done to suppress any spanwise flow in the LEV (which had little effect), and to hinder the development of the TV by placing a wall at the wing tip, geometrically matched to the tip's trajectory. The latter experiment increased the strength of the LEV by 14%, and the overall force on the wing by 8%, although, interestingly, the LEV still did not shed; for the fruitfly, apparently, LEV strength, not shedding, is the force-limiter. These results led to the hypothesis that the prolonged attachment of the LEV is instead due to the aforementioned downwash from the TV and the previous stroke's wake. This downward flow, they postulated, lowers the effective angle of attack of the wing, thus decreasing the strength of the LEV and increasing its time to shed. Therefore, there is some controversy as to the role of the tip vortex in hovering flight. However, Birch and Dickinson noted that hawkmoths fly at Reynolds numbers of around 2000, while for fruitflies the Reynolds number is between 100 and 250. They suggested that the pressure gradient along a fruitfly wing may simply be too small to generate significant spanwise flow.

To the best of this author's knowledge, no study has yet explored the force generation due to the TV and its effect on the LEV, at Reynolds numbers on the order of 1000. However, direct numerical simulations of a flapping fruitfly wing (Reynolds number of order

100) done by Ramamurti and Sandburgh (2002) show that, for the case of symmetric (up- and downstroke) flapping kinematics, almost half of the total thrust is generated by the outboard 25% of the wing. Given this result and that the TV has been implicated in prolonging the attachment of the LEV, a further study of their interaction, and how it is affected by aspect ratio, is warranted.

1.2.2 Flat plate starting flow and aspect ratio effects

There is a great wealth of literature on bluff body flows. Much of it is concerned with circular cylinders, due to their many engineering applications. Of the studies on flat plates normal to the direction of travel, there are few that deal with the unsteady flow at the startup of motion; and there are virtually none that investigate low aspect ratio flat plates having a free end condition. Most studies present results on long time behavior, such as Strouhal shedding frequency, and mean and fluctuating force coefficients (see Lisoski (1993) for a thorough review). Some of the more well-known of these works are by Fage and Johansen (1927) and Roshko (1954; 1955).

Nominally 2-D flat plate starting flow was investigated experimentally by Sarpkaya and Kline (1982), Lian and Huang (1989), Dickinson & Götz (1992), and Dennis et al. (1993); experiments and computations were conducted by Chua et al. (1990) and Lisoski (1993); and Koumoutsakos and Shiels (1996) presented viscous computational simulations. Highlights from these investigations will now be summarized.

Sarpkaya and Kline (1982) measured the drag force on a flat plate at $\alpha = 90°$ in a water tunnel rigged to produce an essentially impulsively-started freestream. The measurements were taken at a Reynolds number (*Re*) of 21000, and plotted versus a non-dimensionalized time $T^* = Ut/c$, equivalent to the number of chord lengths traveled; where

U is the free stream velocity, t is time, and c is the plate chord length. They found a peak drag coefficient (C_D) of about 3 at $T^* = 1$, followed by a decrease to $C_D = 2.4$ until T^* of around 5, leveling off to an average C_D of 2.2 after $T^* = 6$ (measured out to $T^* = 13$). The large initial C_D was attributed to the symmetric growth of the starting vortices generated by the plate's 2 edges, and it was noted that shedding did not cause noticeable fluctuations in the C_D.

The experiments done by Chua et al. (1990) investigated the unsteady forces on a normal flat plate accelerating from rest in a towing tank to a constant velocity. The plate was accelerated until $T^* = 2$, then driven at a constant Re of 5000, with a total travel of 60 chord lengths. Initially, they measured a peak in the C_D of 4.5 at $T^* = 2$, which then dropped off to a minimum of 1.7 at $T^* = 8$, and finally rose to an average of 1.9 after $T^* = 12$. Although the C_D magnitudes are somewhat similar to Sarpkaya and Kline's, no drag minimum was observed in the previous study. This difference may be due to the difference in velocity profiles, or possibly Reynolds number, although Chua et al. obtained the same result for Re = 5000 and 10000. Using flow visualization, Chua et al. attributed this significant drag minimum, or "bucket," to the existence of a "symmetric vortex bubble region" behind the plate, which broke up at $T^* = 10$. Force measurements and visualization showed no vortex shedding between $T^* = 12$ and 30 to 40, after which shedding began and caused fluctuations in the C_D. The computations by Chua et al. did not agree well with their experiments for the starting flow case, probably due to unavoidable three-dimensionality in the experiments.

Dickinson and Götz (1993) measured the transient forces on impulsively started, nominally 2-D wings at high angles of attack. The experiments were done in a towing tank filled with a 54% sucrose solution, in order to achieve the low Reynolds numbers appropriate

for small insects such as fruitflies. A wall at each end of the wing ensured that the flow was primarily 2-D. They found that, for this essentially 2-D case, the LEV shed into the wake after about 2 chord lengths of travel. This distance, as discussed before, is shorter than the typical insect wing stroke amplitude of 3 to 5 chord lengths.

For their largest angle of attack, $\alpha = 90°$, with a total travel of 7 chord lengths at a *Re* of 192, their measured C_D agrees quite well with the results of Sarpkaya and Kline (1982), albeit with a higher initial peak C_D. The drag "bucket" measured by Chua et al. (1990) at $T^* = 8$ was not observed by Dickinson and Götz. This might be because their experiments did not go beyond 7 chord lengths of travel, or that their *Re* was so low that the recirculating wake bubble persisted throughout the entire run, and would have done so beyond 7*c*.

In 1996, Koumoutsakos and Shiels used vortex methods to compute the 2-D viscous flow around impulsively started and uniformly accelerated flat plates oriented normal to their direction of travel. The impulsively started case, computed at Reynolds numbers between 20 and 1000, agreed well with the flat plate flow visualization study of Dennis et al. (1993) for early times, when the experimental flows were still essentially 2-D. The longer-time C_D's (between 0.8 and 1.2 for $Re = 20$ to 40, $T^* > 10$) for both studies also agreed well; the computed C_D was infinity at time $t = 0$, and therefore not amenable to comparison. For the uniformly accelerated plate, Koumoutsakos and Shiels were the first to confirm computationally the existence of an instability along the shear layers emanating from the plate's edges, manifested as "centers of vorticity." This instability was observed experimentally by Lian and Huang (1989), who used the hydrogen bubble technique to visualize the starting vortices of a flat plate, and by Pullin and Perry (1980), who used dye flow visualization to study the starting vortex of "wedge-like" sharp edges of varying wedge

angles. Pullin and Perry speculated that the instability was triggered by vibrations, although very small, in their experimental apparatus, while Lian and Huang concluded that this instability is inherent to the flow. Koumoutsakos and Shiels also determined that the instability is in fact a feature of the flow. They showed that it is caused by the oscillatory behavior of the interaction of primary and secondary vorticity at the plate edges, which triggers Kelvin-Helmholtz-like instabilities in the shear layer.

Lisoski's Ph.D. thesis (1993) at the California Institute of Technology continued the work he contributed to Chua et al. (1990). He investigated experimentally and computationally the effect of "differing amounts of large-scale and small-scale three dimensionality" on the time-varying flow about a normal flat plate at Reynolds numbers between 1000 and 6000. Large-scale three-dimensional effects were studied using flat plate models with varying end conditions and aspect ratio, with the objective of determining how best to suppress these effects. The starting and intermediate-time flow, with the plate traveling a total of between 60 and 100 chord lengths, was studied in the same towing tank used in the present experiments. Longer-time flows were investigated in a water tunnel, which allowed runs equaling thousands of chord lengths. Force measurements and flow visualization were used to compare the experiments with one another, and with the results from a 2-D vortex element code.

For the towing tank experiments, Lisoski studied *AR*'s between 6 and 17, and end conditions at the bottom of the vertically mounted flat plate models as follows: no end plate, with an end plate whose angle of attack could be varied, and with the free end of the model 0.1 mm above (grazing) the tank floor; the end condition at the top of the model was a clean free surface. He found that, for the case of the free end moving just above the tank floor,

large-scale three-dimensionality was effectively suppressed: the results from $AR = 6$ to 17 were very similar. However, with an $AR = 10$ and the free end of the model significantly far away from the tank bottom, the drag "bucket" measured for his most nominally 2-D case ($AR = 17$, grazing), and reported in Chua et al. (1990), was not observed. In addition, Lisoski noted that this free end condition "... effectively suppressed organized vortex shedding [which occurs beyond $T^* = 30$ to 40] at both $AR = 10$ and $AR = 17$."

Lisoski's water tunnel experiments revealed that, for $AR = 6$ with an end plate mounted on the model, vortex shedding was intermittent, being absent for hundreds of chord lengths of travel at a time. This was evident in the time-varying drag and lift measurements, which showed little variation during periods of no shedding. Periodic vortex shedding was consistently observed, however, for AR's greater than 10, and no shedding was observed for $AR = 4$. Lisoski found that, when vortex shedding did occur for AR's ≤ 6, the flow lacked spanwise correlation. This decreased the drag by almost 40%, and suppressed the usual force oscillations at the Strouhal frequency. Finally, Lisoski concluded that the flow for $AR \leq 6$ plates, with their free end far away from the bottom wall, is significantly three-dimensional, but that higher AR plates with the same end condition probably have some portion along the span that exhibits primarily 2-D flow.

Two examples from the literature on circular cylinder flows are also relevent to the present work. The first is by Slaouti and Gerrard (1981), who used dye visualization to investigate how end conditions affect the wake of a circular cylinder being towed in a water tank at low Re's (100 to 142). They showed that a clean free surface (used by Lisoski) is the best upper-end condition for promoting a 2-D wake, since it deforms to match flow-induced pressures, and its slip condition allows vortex lines to intersect it normally. The case of a

cylinder with its end free and far away from the tank floor was studied, and they showed that vortex shedding near the end of the cylinder is suppressed; it only occurs 3 to 4 diameters from the end. Additionally, they observed that the oncoming flow near the free end is deflected upward, and that dye deposited on the end itself is "... drawn upwards into the wake, close behind the cylinder." This causes the wake vortices to bend toward the tip, which is seen in a side-view of the flow. After this "bowing" is observed, the vortex interactions near the tip become complicated. Slaouti and Gerrard wrote that "[a] contraction of the wake is thus gradually obtained as the lowest sections of the vortices disappear with downstream distance through cancellation of their vorticity due to mixing."

In 1992, Champion and Coutanceau presented a short paper at the IUTAM Symposium on Bluff-Body Wakes, Dynamics and Instabilities entitled "Development of the Near Wake Structure on a Cantilevered Circular Cylinder with a Free-End." They characterized this highly three-dimensional flow qualitatively using 3-D dye flow visualization, as well as time-exposed 2-D particle visualization for multiple chordwise cross-sections and a spanwise section bisecting the wake. A similar approach was used in conjunction with DPIV for the present study, so that flow cross sections could be captured quantitatively. Champion and Coutanceau tested cylinders with *AR*'s between 2 and 5 in a vertical water tank, at *Re* = 1000. One end of the cylinder was of course free, and a flat plate was mounted at the other end. Their multiple visualizations allowed for a temporal and spatial picture of the time-evolving near-wake. For the case of *AR* = 5, at $T^* = 2$ ($T^* = Ut/D$, where *D* is the cylinder diameter) there is a chordwise symmetric recirculating bubble (made up of the initial Bénard-von-Kármán wake vortices) whose length varies along the span. From the plate-end to *Z/D* = 3.5 (*Z* being referenced from the fixed end), these

vortices show a "quasi-2-D development." However, the flow near the free end remains very near to the cylinder and is highly 3-D, due to spanwise flow directed toward the fixed end. By $T^* = 3.5$, the vortex lines in the spanwise region $1 \leq Z/D \leq 3.5$ have bowed-out away from the cylinder, and are also asymmetric. However, the vortices near the free end remain closely attached to it, and no vortex shedding is seen. This same bending-in of the vortex lines toward the free end was observed by Slaouti and Gerrard (1981). Near the end plate, the vortices stay attached to the cylinder but become very 3-D and irregular, versus the clean free surface end condition used by Slaouti and Gerrard, which promotes 2-D flow.

The 3-D dye visualization revealed that the vortices generated near the free and fixed end have a helical structure. They propagate along the span in opposite directions, heading towards $Z/D = 2$, where they collide. This meeting of helical vortices propagating in opposite directions was also observed Liu et al. (1998). During the latter-half of the hawkmoth's downstroke, the helical LEV over the inboard 75% of the wing (which has a spanwise velocity component directed toward the tip) connects with the outboard helical LEV (that has a velocity directed away from the tip), and the spanwise flow at that location is reduced to zero.

Lastly, Champion and Coutanceau commented on the effects of decreasing the cylinder aspect ratio. They noted that the length of the recirculating bubble increases, as does its stretching speed. Also, the spanwise location where the helical vortices traveling in opposite directions collide was seen to be a linear function of AR.

1.3 Objectives and organization

The objective of the current work was to investigate the relationship between the vortex generation and drag force of a low-AR normal flat plate starting from rest, in order to

begin to understand the fundamental physics of hovering flight. In addition, the effect of varying the *AR*, which changes the relative influence of the plate's tip or free end, was explored to gain insight into *AR* selection in nature and for MAV design.

These goals were achieved through drag force measurements, quantitative measurements of multiple sections of the flow velocity, 2-D and 3-D flow visualization, and the formation time concept. The formation time is a non-dimensionalized timescale that can be used to relate the time it takes for a vortex to reach its final strength before pinch-off with the kinematics that generated it. Using this timescale, vortex saturation can be compared with other kinematics-dependent phenomena, such as peaks in the drag force. Measuring the drag on different *AR* plates, as well as varying their end conditions, establishes the relative importance of the tip effect for force generation. Using digital particle image velocimetry (DPIV), multiple chordwise and spanwise (2-D) sections of the flow velocity were captured quantitatively, in order to obtain vorticity and circulation data for the LEVs and the TV. This data allowed vortex formation, strength, and interaction to be related, through the formation time, to features in the measured force. Finally, flow visualization was used to choose the appropriate experimental parameters, obtain a picture of the full 3-D flow, and explain the DPIV results.

A more detailed discussion on the formation time concept and the experimental parameters chosen for this work is given in Chapter 2. Chapter 3 describes the experimental setup and techniques, and the results are reported in Chapter 4. Conclusions and recommendations for future work are presented in Chapter 5, and additional information on the experimental setup is provided in the Appendix.

2 Parameters

2.1 Introduction

The parameters and concepts relevant to this work are presented in this chapter. First, the experimental parameter selection is explained. Following this is a discussion on the vortex formation time theory, which was first used to characterize vortex ring formation, and has also been applied to circular cylinder starting flows. Formation time relates the growth and final strength of a vortex to the kinematics of the system that generated it, and is thus very useful for understanding vortex-based propulsion. Therefore, formation times for the plate's 2 LEVs and its TV are defined, and their physical meaning is discussed.

2.2 Experimental parameters

The choice of experimental parameters was discussed only briefly in Chapter 1, so elaboration is needed. It must be emphasized that this work represents a preliminary and fundamental step in understanding hovering flight, adopting the philosophy that it is best to first understand a case with fewer degrees of freedom. Hovering kinematics involve three degrees of freedom: wing revolution or sweeping about the wing joint in the horizontal and vertical directions, and pitching or rotation of the wing about its own spanwise axis. For the present investigation, pitching about a ball-and-socket-type joint are not considered. In addition, the wing sweeping is simplified to pure translation along a single direction. Finally, since the forces generated during hovering flight are essentially symmetric about the vertical axis, only one-half of the full back-and-forth wing stroke is considered. Thus, this work focuses on an appendage accelerating from rest in pure translation and in a single direction.

2.2.1 Model geometry

A flat plate of rectangular planform was chosen as the experimental model because it is one of the simplest representations of a thin flapping wing appendage. Additionally, having three distinct edges (the fourth is outside the working fluid) allows for predictable vortex generation: 2 vortices (the LEVs) will form at the long edges, while a tip vortex will roll up over the short edge; Chapter 4 will show that vortices also form at the plate's corners. Although insect and especially bird wings deform, the models tested did not include this variable. Dickinson et al. (1999) found that exchanging the rigid wings for flexible ones on their robotic fruitfly did not affect the forces appreciably, but this is probably due to their low operating Reynolds numbers. An angle of attack of 90 degrees was selected in order to ensure that the force generation would be primarily drag-based, which is consistent with hovering flight.

2.2.2 Aspect ratio

The range of aspect ratios tested was based on biological data and previous work in fluid mechanics. In Chapter 1, it was stated that insect single-wing *AR*'s range from 2.75 to 6, while hummingbird *AR*'s are around 4. Also, Lisoski (1993) found significant 3-D effects for flat plates when the *AR* was reduced to 6, while Champion and Coutanceau (1992) observed highly 3-D flow for cantilevered cylinders with *AR*'s between 2 and 5. This investigation, therefore, considered two *AR*'s: 6, as the prototypical case, and 2, in order to have a TV dominated flow.

2.2.3 Reynolds number

Similar considerations, along with flow visualization, led to the choice of Reynolds number. Insect flight *Re*'s are on the order of 10^2 to 10^4 (Dudley, 2000). The experiments by Lisoski (1993) ranged from *Re* = 1000 to 6000, while Champion and Coutanceau (1992)

performed their cylinder experiments at Re = 1000. In order to compare the present work with those studies just mentioned, and still be within the insect flight regime, a Re on the order of 1000 was chosen. Reynolds number for the current flat plate study is defined as

$$Re = \frac{cU_{final}}{\nu}$$

Where c is the plate chord length, ν is the kinematic viscosity of water, and U_{final} is the final, constant velocity of the plate after it accelerates from rest (see Chapter 3). Dye flow visualization in chordwise planes at 50, 75, and 90% span (measured from the plate root) was performed for AR = 6 at Re's of 1000, 2000, 3000, 5000, and 10000, to determine an appropriate Re more precisely. For Re = 1000, the symmetry of the recirculating bubble behind the plate was random: most runs exhibited wake symmetry, but some runs, after about 5 chord lengths of travel, did not, probably depending on the level of background noise in the water tank.

A more repeatable flow, obtained by increasing the Re, was desirable, but the size of the shear layer instability described in Koumoutsakos and Shiels (1996) was found to scale with Re. A compromise was reached at a Reynolds number of 3000, which provided consistent results along with the least amount of contamination from the instability. The investigation was performed at only one Re, since 2-D and 3-D flow visualization showed that the flow was similar for Re between 2000 and 5000; this was true even for the Re = 10,000 case, although the shear layer instability was very large. Finally, the signal-to-noise ratio for the drag force measurements was much better at Re = 3000 versus 1000.

2.3 Vortex formation time

The connection between how a vortex is generated and the resulting final vorticity field was not established in detail until Gharib, Rambod, and Shariff (1998) investigated

vortex ring formation over long timescales. A vortex ring, which is a vortex with it ends connected together, is a clean, well-studied flow, with a simple generation mechanism. Gharib et al. produced vortex rings in a water tank using a piston to push a column (or slug) of water of length *L* through a cylindrical nozzle of diameter *D* (equal to the piston diameter). The vorticity fed into a forming vortex ring is provided by the separated shear layer at the nozzle exit, which is driven by the moving piston. Stopping the piston after a certain distance prohibits the shear layer vorticity flux, so that the final circulation of the vortex ring is approximately equal to that generated at the nozzle exit; this is true for small $\frac{L}{D}$'s. The question that Gharib et al. asked is the following: for large $\frac{L}{D}$'s, given a fixed mean piston velocity, is there a limiting process that keeps the circulation of the vortex ring from growing indefinitely, despite the vorticity flux emanating from the shear layer? They found such a process by using digital particle image velocimetry (DPIV) to capture the formation, growth, and subsequent pinch-off of vortex rings generated by various piston kinematics.

In order to compare runs with different piston velocity programs and nozzle diameters, time was non-dimensionalized into what Gharib et al. (1998) referred to as "formation time" (*T*) using the running average of the piston speed *U* and the nozzle diameter as follows:

$$T = \frac{t\overline{U}}{D} = \frac{t}{D}\frac{1}{t}\int_0^t U(t')dt' = \frac{L}{D}$$

As the formula shows, formation time for this case is also equal to the stroke ratio, $\frac{L}{D}$, which is the number of diameters the piston traveled. For small $\left(\frac{L}{D}\right)_{\max}$, the vortex rings were

compact and clean, consistent with previous studies. However, for T greater than about 4, the circulation of the vortex rings did not increase indefinitely. Instead, it saturated, and the remaining circulation generated by the shear layer at the nozzle trailed the vortex rings in a jet-like structure. Regardless of the $\left(\frac{L}{D}\right)_{\max}$, Gharib et al. found that the maximum circulation of the vortex rings was acquired around $T = 4$, which they called the "formation number." Jeon (2000) studied the vortex formation of essentially 2-D cylinder starting flow, and also found vortex saturation at about $T = 4$ for many cases. This showed that the formation time concept can be applied to bluff bodies, and suggested that the magnitude of the formation number might be similar for different vortex generators.

The formation number is the non-dimensional time at which a vortex achieves its maximum circulation before pinch-off. Pinch-off occurs when a vortex is no longer being fed by the shear layer that generated it, and the two become distinct entities in terms of vorticity. This does not necessarily happen exactly at the formation number (it typically happens sometime afterward), but pinch-off cannot occur before the vortex acquirers its maximum circulation. The experiments by Gharib et al. (1998) showed that the pinch-off process for a vortex ring starts at around $T = 4$, but it is not clearly complete until T is about 7 or 8. This formation and pinch-off process will be described for low AR flat plates in this section and later chapters.

The significance of the formation number for vortex-based propulsion can be seen by considering animals that use vortex rings for locomotion, such as jellyfish and squid. Based on the formation number concept, an animal would obtain the maximum amount of thrust by ejecting a slug of fluid in such a way that $T = 4$; anything beyond 4 would result in a loss of efficiency.

The low *AR* plates considered in the present work were oriented vertically in a water tank, piercing the free surface so that three edges, the two leading or side edges and the tip edge at the bottom, were underwater (see Chapter 3). As discussed above, vortices are generated at the two leading edges and at the tip of the plate as it accelerates from rest. The two LEVs rotate primarily in the horizontal plane, while the TV rotates primarily in the vertical plane. Using DPIV to obtain velocity and vorticity fields in horizontal and vertical sections (akin to the flow visualization study done by Champion and Coutanceau (1992)), formation numbers can be defined for the vortices that are visible in each section. The variation of the LEVs along the span of the plate and in time was captured using DPIV data taken at horizontal (chordwise) sections at 50, 75, and 90% spanwise locations (measured from the top). Visualization in 2-D and 3-D for $AR = 6$ revealed a complicated flow above 40% span after the initially 2-D vortex generation phase, which was also observed by Champion and Coutanceau. Although their root end condition was an endplate, while the upper-end condition for the present study was a clean free surface, something about the low *AR*s considered seems to cause significant 3-D flow at *both* ends of the body. Since the present work is focused on phenomena near the plate tip, only the flow away from the upper end was considered. The TV was investigated by taking DPIV data in two vertical (spanwise) sections: one at mid-chord, parallel to the direction of travel and in the symmetry plane of the LEV wake, and one at one of the leading edges, also parallel to the plate velocity, and within the rotating flow of the LEV there.

Formation time for the present work is defined as follows:

$$T = \frac{t\overline{U}}{c} = \frac{t}{c}\frac{1}{t}\int_0^t U(t')dt'$$

where c, again, is the plate chord length, and $\overline{U}$ is the running mean of the plate velocity. Since the plate is a bluff body, it is appropriate to use its chord, or frontal projected length, as the normalizing length scale. The formation time T is approximately equal to the number of chord lengths the plate has traveled, and it is very useful for comparing runs with different kinematics and chord lengths. The formation number is the formation time at which a vortex generated by one of the plate edges acquires its maximum circulation. It is found using circulation data obtained from DPIV measurements, which will now be discussed.

The case of $AR = 6$, $Re = 3000$, and DPIV data taken in a horizontal (chordwise) plane at 50% span will be used as an example of computing the formation number. The DPIV measurements provide the time-varying velocity field in an area surrounding the plate. From the velocity data, quantities such as vorticity can be calculated. At this Reynolds number and spanwise location, the starting flow is symmetric about a line at mid-chord parallel to the direction of travel. Therefore, when flow quantities at one edge, such as the circulation, are desired, the quantities at each edge can be averaged. In order to obtain the formation number, the total circulation generated at the edge as well as that within the LEV are computed from the DPIV vorticity data using Stokes' theorem in 2-D:

$$\Gamma = \int_A \omega dA$$

where ω is the vorticity, and A is the area enclosing it. A curve of total and LEV circulation versus formation time can then be constructed.

Figure 2.1 gives both the total and LEV circulation at 50% span, with insets showing the vorticity field at significant formation times. The LEV circulation was computed automatically, as the average of that of both LEVs, using a Matlab program to track the vortex itself. This was done for all data sets, since computing the circulation of the vortex

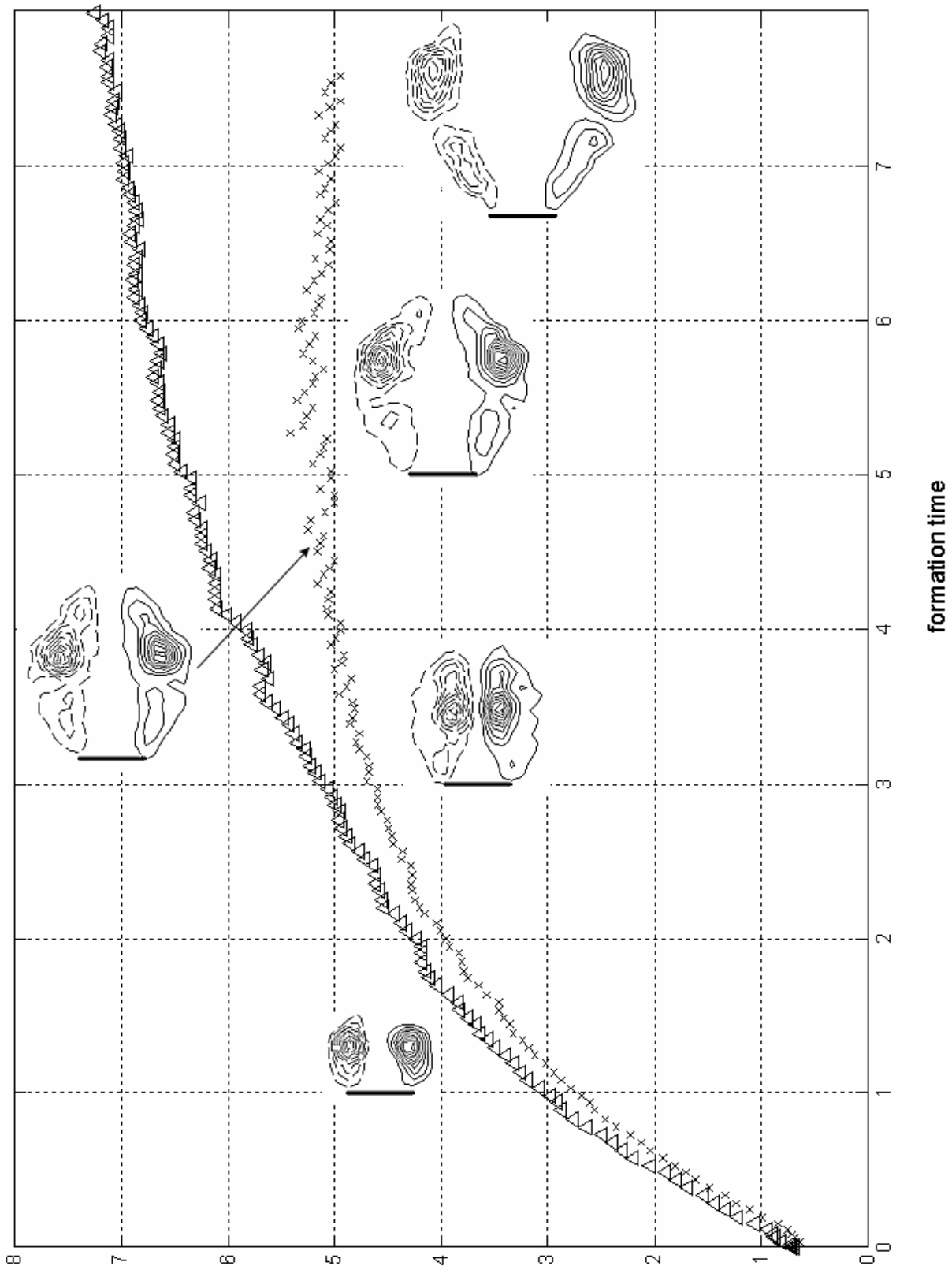

Figure 2.1 Circulation at *AR* = 6, 50% span, with vorticity field insets. Triangles: total circ.; x's: LEV circ.

manually, especially before pinch-off, is somewhat arbitrary. The total circulation was also computed using Matlab, and it is the average of the circulation generated at each edge. Initially, the total and LEV circulation are equal (see Figure 2.1). However, with time they begin to diverge, and at T equal to the formation number (in this case about 4.5), the LEVs saturate and can no longer accept vorticity from the separated shear layer that formed them. From this time on, the LEV circulation measurements are essentially constant, within the experimental error. The formation number is therefore the formation time at which the LEV circulation data become constant. After the formation number, the shear layer and the LEV then start to become separate entities (see the vorticity field inset at $T = 5$ in Figure 2.1). Finally, at pinch-off ($T = 6.67$ in Figure 2.1), the two are entirely distinct, which shows up on a vorticity contour plot as a disconnection of their contours, with a minimum of vorticity between the two. For the cases where no pinch-off exists (which occurs near the tip), formation numbers can still be computed if the circulation of the vortices saturates, despite their continued attachment to the plate.

Similar to the example of vortex ring propulsion given earlier, a hovering animal's kinematics may be based on the formation numbers of its vortices. However, flapping wings differ from the vortex ring case in that there are multiple vortices involved: the LEV and the TV. The goal of the present study is to clarify the effect of the tip on the leading edge vortex generation. Comparing the formation number of each vortex will show how the growth of the TV influences the strength and pinch-off of the LEVs. For example, Chapter 4 reports that the formation number for the TV is equal to that for the LEVs at 90% span. This implies that the tip vortex has a strong influence on the LEVs close to it. Knowing the interaction of the tip and leading edge vortices in terms of formation time may serve as a guide for

hovering kinematics. The influence of the tip can be exploited to generate maximum force, or to optimize power efficiency.

3 Experimental setup and methods

3.1 Introduction

This chapter presents the details of the experimental setup and methods. First, the towing tank facility, where all the experiments were done, will be described. Next, the specifications of the flat plate models and kinematics are given, followed by a brief discussion on the dye flow visualization. After that, the force balance and data acquisition system are described. Lastly, the details of the DPIV system and post-processing are given.

3.2 Towing tank

Towing tanks, as opposed to wind and water tunnels, are very useful for studying unsteady starting flows, due to their capability of accurately "towing" models at pre-programmed unsteady velocity profiles. The GALCIT towing tank was used for all the experiments done for this thesis, as its size and the velocity range of its drive system were appropriate.

3.2.1 Towing tank description

Originally designed for flow visualization (see Williamson, 1988), the tank has four uninterrupted glass side-walls, and a glass bottom covered only across its midpoint by a cross-bar support; the top is open to the air. The interior dimensions of the tank are 450 cm in length and 96 cm in width, with a depth of 78 cm. It is raised up above the ground on six legs, which can be adjusted to level it, providing space to perform visualization and acquire DPIV data from below. Figure 3.1 shows a side-view sketch of the towing tank, along with the laser and CCD camera configurations for DPIV and flow visualization.

Two parallel cylindrical rails are mounted on the top of the tank, one above each of the long sides. Riding on Teflon slider bearings above the rails is a carriage, below which

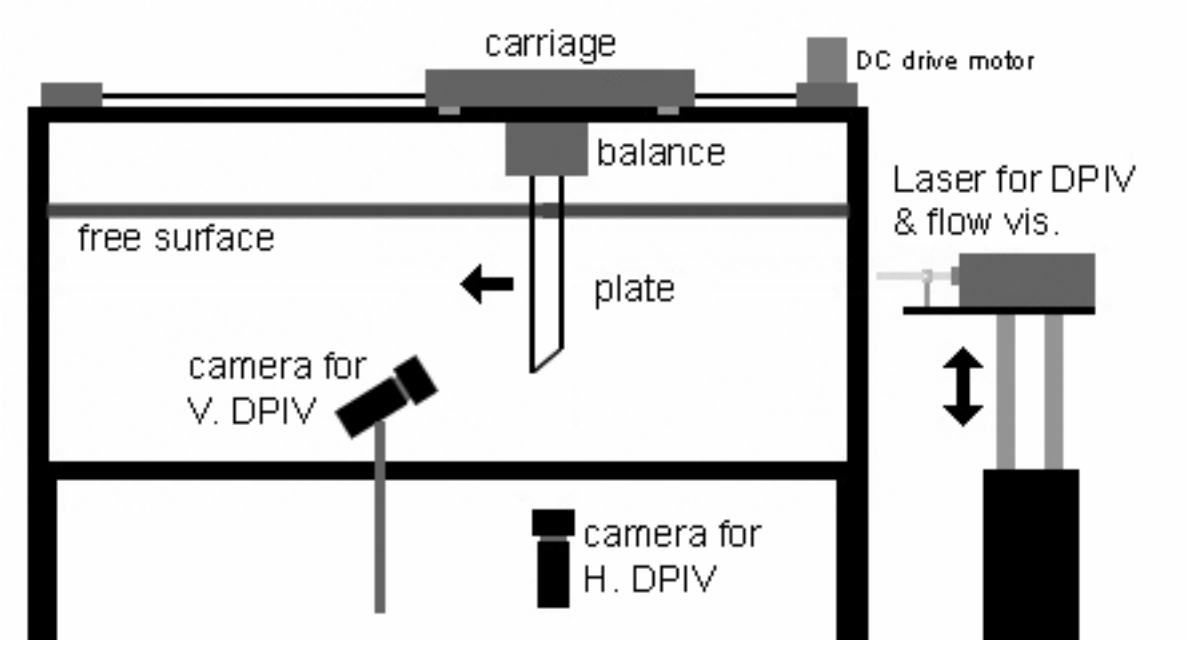

Figure 3.1 Towing tank and hardware for DPIV and flow visualization.

the force balance and flat plate models are attached. The carriage is moved using a 2-pulley and cable drive system located along one of the side rails. The pulley at one end of the tank is driven by a DC servomotor combined with a gearbox, while the pulley at the opposite end is free. A smaller version of this drive system is located on the carriage itself, but oriented perpendicularly to the larger one. The force balance and model combination are actually attached to the smaller carriage of this secondary system. Thus, models can be moved in two dimensions, but only the main drive system was needed for the present work.

The DC servomotor is a PMI model OP-01206-026 (type U12M4HT/GH/M23) with an attached gearbox having a 20:1 input-to-output ratio. The motor is driven by a PMI model 00-88029-006 multi-axis switching servo amplifier (type CX-75-10-30), which obtains tachometer feedback from the motor in order to close the velocity loop for motor control. The position loop consists of an encoder and a motion controller, described next.

A PMI optical encoder with a resolution of 1024 counts per revolution is attached to the drive shaft of the DC servomotor, in order to provide position feedback to the motion controller. The gearing of the servomotor is such that there are about 1427 counts per cm of carriage travel, providing more than enough position control accuracy for this study. Position information from the encoder is fed into a Delta-Tau Mini-PMAC (programmable multi-axis controller), which is mounted in a PC as a standard card, and thus allows the motor to be controlled by the PC. The position control loop is closed by the command signal that is sent from the Mini-PMAC to the amplifier, which in turn drives the motor in the desired manner.

Software provided by Delta-Tau allows the controller gains to be tuned, the encoder output to be calibrated, and pre-programmed motion profiles to be sent to the motor. The Mini-PMAC uses a proportional-integral-derivative (PID) control scheme to minimize the following error between the commanded an actual position of the motor. Velocity and acceleration feed-forward gains are adjusted by the user via the software, utilizing the position information from the encoder, to optimize motor performance. Once the controller is tuned, motion programs that prescribe velocity or position as a function of time can be written and used to command the motor. The software allows for an almost unlimited variety of motion trajectories, restricted only by the mechanical properties of the system, and thus affords more than adequate control of the towing tank carriage.

3.2.2 Towing tank procedures

The experimental procedures common to both the force and DPIV measurements will now be discussed, and those specific to each type of measurement will be described in later sections.

The working fluid in the towing tank was water, and the plate upper-end condition was a clean free surface, for the reasons given in Chapter 1. Before a series of data sets was taken the free surface was cleaned, and it stayed that way for many hours. Due to the air filtration system in the laboratory, and the height of the tank above the floor, dust contamination on the free surface was minimal. Slaouti and Gerrard (1981) noted that minor contamination of the free surface did not significantly affect vortex impingement there. To clean the free surface, a fan at one end of the tank was used to blow any debris toward the opposite end of the tank. A tube connected to a shop vac, and hovering just above the free surface, was then used to suction away the debris there. This left a clean surface that was evident by its appearance, as well as wave generation and prolonged wave action at the slightest disturbance. Some of the 10 micron particles used to seed the flow during DPIV measurements inevitably floated to the surface due to a slight density difference between them and the water, but they did not appreciably affect the behavior of the free surface. If, however, the amount of particles on the surface became large, the surface was cleaned again as a precaution.

The ambient fluid motion in the tank at the start of each data set was directly related to the amount of time the water was allowed to settle between sets. A short time after a run, leftover flow was still present in the tank. However, if the water was left undisturbed for too long, thermal convection cells developed due to the height-wise temperature gradient. To obtain adequate run conditions, the water was stirred randomly using the plate model in order to eliminate the convection cells before a series of runs; then the flow was left to settle for about an hour to an hour and a half. The wait-time between data sets was then determined by trial and error using the measurement technique at hand. For force measurements, the flow

was judged to be significantly settled when the force balance was no longer able to distinguish the ambient flow from its at-rest noise level. This typically took about half an hour. The DPIV measurements were a bit more sensitive, since the flow velocity itself is being measured, and wait-times between runs ranged from half an hour to an hour. For the DPIV experiments, the initial tank stirring coincided with seeding the water with the tracer particles. If any subsequent seeding in the middle of a series of data sets was needed, the stirring was repeated, and the flow was allowed to settle for an hour to an hour and a half.

When the GALCIT towing tank was chosen for the present work, its carriage was outfitted with wheels to roll it along the rails. Although the wheels provided very low friction for the servomotor to overcome, and they did not require additional measures such as greasing the rails, the vibrations they transmitted to the carriage due to imperfections in the rails and their own construction were unacceptable. Therefore, these wheels were removed and the run technique established by Lisoski (1993), which employed Teflon slider bearings along with greased rails, was used.

Before a series of data sets was taken, the carriage was elevated above the rails using its existing screw-jacks, and the four Teflon slider bearings (two on each side) were coated with a thick layer of Mystik JT-6 Multi-Purpose (anhydrous calcium-based) Grease. The carriage was then lowered back onto the rails, and the rails themselves were coated with a thin, uniform layer of the same grease. Initially, the carriage was jacked-up and the Teflon bearings were greased before each run. However, this created a grease buildup along the rails near the middle of each run, which led to spurious vibrations. The best results were obtained with the following procedure. The carriage was raised and the Teflon bearings greased only at the beginning of a series of experiments. It was then lowered, and a thin,

uniform layer of grease was applied to the rails. One run, which involved the carriage moving forward to its final destination, then backing-up and returning "home," was done to smooth-out the grease under the Teflon. Following this, only the rails were greased before each data set was taken. The forward-and-back travel of the carriage kept the Teflon bearings greased uniformly, which minimized the starting friction. This procedure produced lower levels of vibration than those experienced with the wheels, although the servomotor had to overcome much more friction. Finally, backlash was removed from the pulley-cable system before each run by backing-up the carriage beyond "home," then moving it forward again to the starting point.

3.3 Flat plate models and kinematics

3.3.1 Flat plate model materials and dimensions

The flat plate models used for force and DPIV measurements were made from different materials. For DPIV, a virtually transparent plate was desirable, while light weight and rigidity were necessary to obtain satisfactory force measurements.

For the DPIV measurements, the flow was illuminated with a laser sheet directed at the leeward face of the plate through one end of the tank. An opaque plate would have cast a shadow over part of the flow field, and its parallax as it moved through the fixed field of view of the camera would also mask part of the image. Although the laser sheet struck the rear face of the plate, and the current study was only concerned with the plate's wake, a moving shadow in the DPIV images would have created numerous problems during data processing. An opaque plate also has parallax, which becomes a problem when the plate is in the far end of the image at start up: the perspective seen when looking at the plate from below reveals that it blocks part of the wake. This effect is eliminated when the plate reaches

the midpoint of the image field, so using an opaque plate would only allow for half of the DPIV image field to be utilized. The simplest way to avoid these problems was to use a virtually transparent plate. Standard 1/8 in. thick window glass was found to have adequate transparency and rigidity, and was light enough to be supported by the force balance.

The flat plate model used for the force measurements was made from a unidirectional carbon fiber composite, which gave it exceptional stiffness and light weight. This model was one of the flat plates left over from Lisoski's Ph.D. work, and was used with permission. The GALCIT towing tank is known to experience carriage vibrations generated by its drive system and rails, and the heavier and less rigid glass plates described above transmitted these vibrations to the force balance at an unacceptable level. Therefore the carbon fiber plate was necessary, since the force balance is more sensitive to these vibrations than the DPIV measurements.

Lisoski beveled the edges of both carbon fiber plates at a 30-degree angle, on the leeward face, in order to have a model with sharp edges that more closely matched a theoretical flat plate. This beveling was not possible for the glass plates, due to chipping, nor was a transparent material found that could be beveled successfully, yet have an acceptable stiffness at a reasonably small thickness. The glass plates therefore had flat edges, which were left after they were cut to size. Edge geometry, however, had little or no effect on the flow, since the thickness-to-chord ratio of the plate models was small. The edge instabilities predicted by Koumoutsakos and Shiels (1996), for example, were observed for the carbon fiber and a glass plates alike.

Table 3.1 gives the specifications and use of the flat plate models for the present work. Aspect ratios were set by adjusting the water level in the towing tank. Therefore, only

one plate was used for the AR = 2 and 6 DPIV experiments, and similarly for the force measurements.

chord, *c*	**thickness, *h***	***h*/*c* ratio**	**max span**	***AR*'s used**	**material**	**used for**
2.5 in	1/8 in	5%	23 in	6, 2	window glass	DPIV
5 cm	3.4 mm	6.8%	50 cm	6, 2	unidirectional carbon fiber	force meas.
3.5 in	1/8 in	3.6%	24 in	6	window glass	flow vis.

Table 3.1 Flat plate model specifications

3.3.2 Run kinematics

As given in Chapter 2, the Reynolds number for the DPIV and force measurements was 3000, based on the plate chord length as follows:

$$Re = \frac{cU_{final}}{\nu}$$

where c is the plate chord length, U_{final} is the final velocity of the plate, and ν is the kinematic viscosity of water. The velocity profile chosen was a constant acceleration over a distance of 1/4c to a final, constant velocity. It is a gentler version of an impulsive start, in order to not overstress the mechanical drive system and cause excessive plate vibrations at the start up, yet generate strong starting vortices. The formation time concept, discussed in Chapter 2, allows the comparison of results from different plate chord lengths and velocities, in addition to data from other studies.

3.4 Dye flow visualization

Flow visualization was done with flourescene dye, which fluoresces when struck with the green laser used also for the DPIV experiments. Horizontal and vertical laser sheets were employed to perform sectional visualization of chordwise and spanwise planes, respectively. A laser cone provided illumination for the fully 3-D flow visualization. The Pulnix CCD

video camera used for DPIV (see section 3.6.2 below) was also incorporated for the dye flow visualization; camera orientations were similar to those required for DPIV.

For all but one set of the visualizations, dye blobs were used to tag the flow. The dye was cooled in a container submerged in the tank water, in order to have the same buoyancy as the water itself. Dye blobs were deposited, or "painted," on the leeward face of the glass plate model in the desired locations using a long, thin syringe. If cooled properly, the dye remained essentially where it was deposited until the run was started. For the global, 3-D flow visualization, described in section 4.5, two rakes were used to inject dye at the upstream face of the plate near the tip, so that the plate velocity would force the dye into the leading and tip edge shear layers. The rakes were long syringes attached to the upstream face of the plate, each parallel to the span and located equidistant between the mid-chord line and the closest leading edge. Small holes were drilled in the upstream side of each syringe (the end holes of the syringes were plugged), and these drilled holes were located starting from near the tip up to about one chord length away from the tip. This was done so that only the flow in the tip region would be tagged, and therefore the fluid near the tip could be followed if it convected away from the tip. The leeward face of the plate that contained the dye rakes was painted and roughened up, to eliminate reflections due to the laser passing through the plate and striking the rakes.

Flow visualization was done using glass plates of a longer chord length, 3.5 in, than that used for DPIV, and always with an $AR = 6$. The increased size of the plate provided a larger, more detailed view of what turned out to be a significantly complicated flow. Different Reynolds numbers were used based on which flow features were to be captured, but the characteristic plate velocity profile was always the same (based on the chord length).

Whenever dye flow visualization results are presented in this work, the details of the particular experimental conditions are also given, so there is no need to outline them here.

3.5 Force measurements

3.5.1 Force balance

Force measurements were done with a force balance designed and built specifically for the GALCIT towing tank by Lisoski (1993). The balance is attached to the underside of the carriage, and, with a special clamp, it suspends the flat plate models vertically in the water (a function it served for all of the experiments). It is capable of resolving time-varying forces on small models at low speeds, yet it can also hold large models and measure forces at high accelerations.

The force balance (see Figure 3.2) consists of a rigid, 5-sided box-like frame to which three Interface MB-5 5 lb. strain gage load cells were attached. A separate platform with threaded mounting holes for test models makes up the bottom side of the box. The mounting platform is supported from inside the box frame by three vertical flexural beams, which extend down from the top. These beams restrict the mounting platform to horizontal movement only, while three other flexural beams, oriented horizontally and mounted just above the platform, attach it to the three load cells. The ends of the flexural beams were designed with biased rigidity, so that the entire flexural framework transmits forces only in a horizontal plane (i.e., parallel to the mounting platform) to the load cells. When the force balance is mounted below the towing tank carriage, two of the load cells (labeled *N1* and *N2*) are oriented to measure drag, while the other (labeled *D*) measures lift. The drag force is

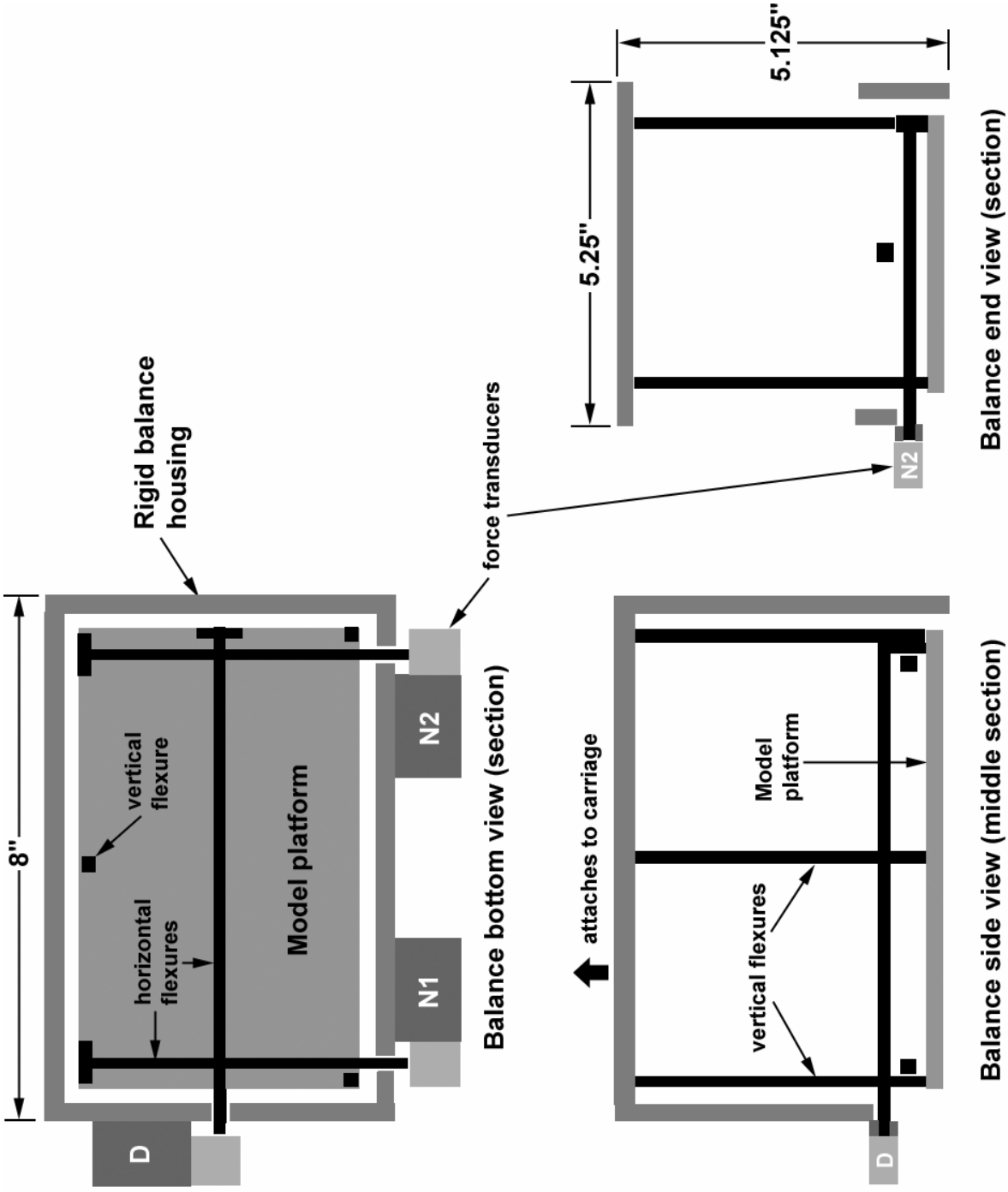

Figure 3.2 Schematic of force balance. See Lisoski (1993) for a more detailed schematic.

then the output of *N1* plus *N2*, the lift is simply the output of *D*, and the pitching moment is proportional to *N1* minus *N2*. For the present work, with an angle of attack of 90 degrees, the outputs of *N1* and *N2* were indistinguishable. Therefore, only the *N1* transducer was used, and the drag force was equal to twice the output of *N1*.

The force balance was calibrated by using a pulley and wire rig to attach a series of known weights to the transducer. Weights were hung on one end of the wire, the other end of which was then run through a pulley and fixed to the load cell. The pulley was needed in order to change the vertical weight into a horizontal force the balance could measure. Lisoski (1993) provides a very thorough treatment of the capabilities and calibration of this particular force balance. The resolution of the force balance, which mechanically amplifies the force on the plate before it reaches the load cells, is ±0.0005 N, equating to a resolution of ±0.02 in the drag coefficient for $AR = 6$, and ±0.06 for the $AR = 2$ C_D.

3.5.2 Flat plate model clamp

A rotating optical stage was mounted to the center of the measurement platform of the force balance, in order to change the angle of attack of the plate for other studies. Attached to this rotating stage was the model clamp, which was a simple sandwich-style clamp, made from aluminum. The aluminum bracket that fixed the clamp to the optical stage was designed so that the chordline of the plate intersected the center axis of the stage. Since the optical stage was centered on the balance's measurement platform, centering the plate itself on the stage ensured that no moment arm between the model and the platform (parallel to the plane of measurement) was created.

3.5.3 Amplifier and data acquisition

An Interface model SGA/A strain gage amplifier was used to power the load cell and amplify and filter its output signal. Designed specifically for Interface force transducers, the SGA/A has a large range of output voltage gains, an adjustable low pass filter, adjustable output ranges, and an adjustable offset of up to 79% full-scale in order to "zero" the transducer. For all force measurements, the load cell excitation was 10 V, the output was set to ± 5 V, the gain was set to 17.35, and the low pass filter was set to a cutoff frequency of 5 Hz. This particular gain gave a force transducer output calibration of 0.0023 V/g.

The amplifier output was sent via a breakout board to a PC-mounted data acquisition card, a National Instruments PCI-1200. The PCI-1200 converted the differential analog input into a 12-bit digital signal for the PC. A custom LabVIEW program was written to control the data capturing, including the sampling rate. To avoid picking up the ambient 60 Hz noise in the laboratory, while ensuring that the force balance signal (which included the noise from the drive system) was sampled adequately, a sampling rate of 20 Hz (4 times the 5 Hz cutoff frequency of the amplifier's low pass filter) was chosen.

3.5.4 Towing tank noise and signal conditioning

As mentioned above, vibrations from the drive system of the towing tank introduced noise in the force measurements, making it necessary to condition the amplifier output in hardware and in software. Tests were done to determine the characteristics of the noise from the pulley cable and the rails. Depending on the carriage location, the noise from the pulley cable had a frequency of between 6 and 10 Hz, while the noise from the rails and pulley system combined had frequencies between 4 and 10 Hz. Since the drive system noise varied with the carriage motion, a resonance filter could not be used to eliminate it. Therefore, low pass filters were used, the first being that of the amplifier, which was set to a cutoff

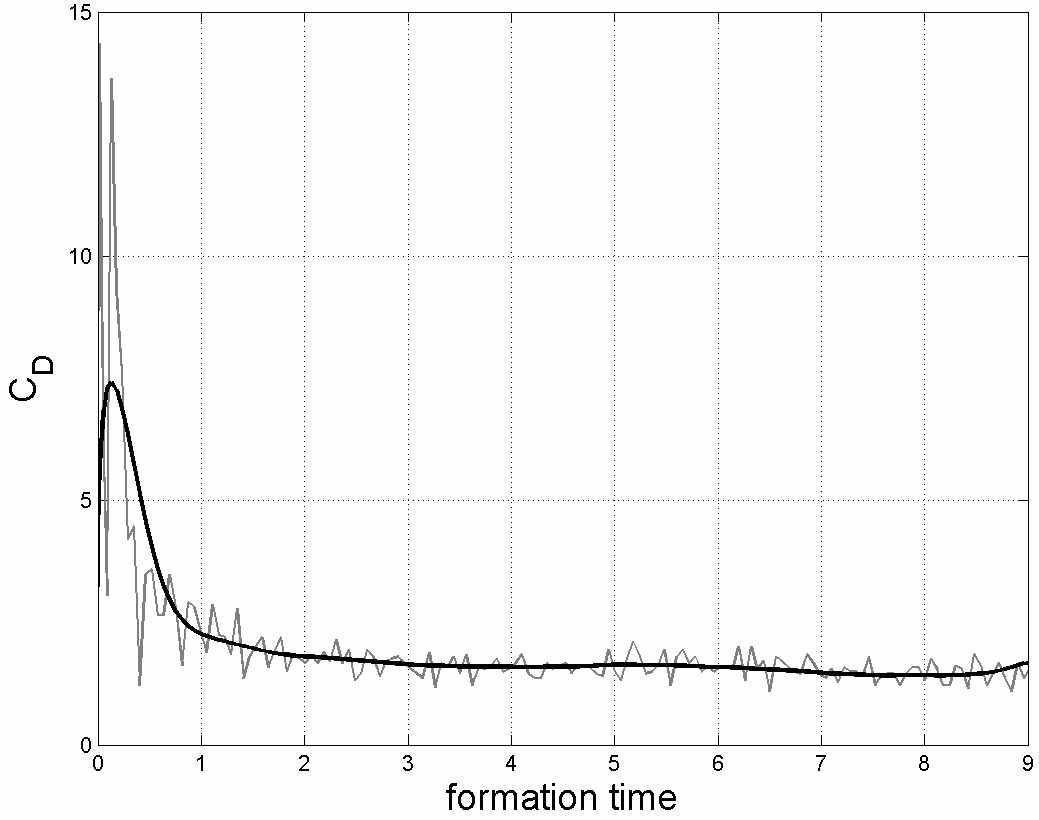

Figure 3.3 C_D from amplifier output vs. averaged & digitally filtered C_D. AR = 6, Re = 3000. Gray line: amplifier output from one run; black line: average of 10 digitally low-pass filtered runs.

frequency of 5 Hz to get rid of the larger magnitude cable noise. The subsequent amplifier output was filtered digitally in Matlab with a cutoff frequency of 2 Hz, which removed the drive system noise while preserving the lower frequency features resulting from the nearly constant kinematics described above. To avoid picking up the ambient 60 Hz noise in the laboratory, while ensuring that the force balance signal was sampled adequately, a sampling rate of 20 Hz was chosen.

Finally, using the experimental procedures described in section 3.2.2, the runs were found to be very repeatable. However, to reduce the impact of the small run-to-run variations, 10 runs for each aspect ratio were averaged to produce the final force trace.

An example of the amplifier output for a single $AR = 6$ run (already low-pass filtered with a 5 Hz cutoff frequency) is given by the gray line in Figure 3.3, while the average of all 10 runs, each filtered digitally in Matlab before the averaging, is given by the thicker black line in the same figure.

3.6 DPIV system

3.6.1 DPIV

To capture 2-D sections of the flow velocity quantitatively, and therefore extract quantities such as vorticity, and circulation, digital particle image velocimetry (DPIV) was used. This technique, developed by Willert and Gharib (1991), uses cross-correlation to obtain velocity fields from the displacement of particles between two images separated in time. First, the flow to be interrogated is seeded with particles. Next, a pulsed or chopped laser sheet is used to briefly illuminate an essentially 2-D section of the flow at a periodic rate, and a synchronized video camera then captures a time-sequence of the nearly instantaneous particle images. Each image in a pair is divided into a set of smaller interrogation windows, which are cross-correlated between the pair to obtain the particle displacement field. Finally, a scaling factor converts the displacement field into the desired velocity field. The computational techniques implemented for the DPIV of the present work are those described in Willert and Gharib (1991) and Westerwheel, Dabiri, and Gharib (1997).

3.6.2 DPIV hardware setup

The towing tank was seeded with neutrally-buoyant, silicon-coated, hollow glass spheres approximately 10 microns in diameter, which followed the flow very well and scattered the laser light sufficiently. Particle illumination for sections of the flow was

accomplished using a New Wave Gemini PIV pulsed Nd:YAG laser, which delivered 124 mJ in the 532 nm wavelength per 5 ns pulse. An extremely short duration, high-powered pulse is required so that the captured particle images are essentially instantaneous (or "frozen" in time), but with sufficient luminosity.

As stated in Chapter 2, DPIV data were taken in horizontal (chordwise) planes at three different locations along the plate, 50, 75, and 90% span, as well as in vertical (spanwise) planes perpendicular to the plate chordline, at mid-chord and at one of the leading edges. The laser beam was spread into an appropriately sized sheet using two identical cylindrical lenses, which could be rotated and leveled so as to produce horizontal or vertical laser sheets. As shown in Figure 3.1, the laser sheet was directed into the tank end closest to the plate. In order to change the height of the horizontal sheets to interrogate different spanwise locations, the head of the Gemini laser, along with the optics, was placed on a height-adjustable pneumatic die table, which could also be rotated to square-up the vertical sheets.

A Pulnix TM-9701 black and white digital CCD video camera, with a resolution of 768 by 480, was used to capture the particle images for DPIV. To image chordwise flow sections, the camera was placed below the tank, looking upward (see Figure 3.1). The camera was mounted on a tripod and pointed at the side of the tank in order to capture the spanwise flow sections. A custom-built timing box synchronized the 30 Hz frame rate of the camera with the laser pulses.

The 30 Hz frame rate of the camera was too slow to capture snapshots of the flow for this work, which required time steps on the order of 5 milliseconds. In order to achieve such small time steps, the laser pulse to illuminate the first image in a pair was delivered near the

very end of the exposure time for its corresponding video frame, while the laser pulse for the second image in the pair was fired near the very beginning of the exposure time for its, the next, video frame. Thus, the actual time between the pulsed illuminations was much shorter than the full exposure time of one frame (1/30 sec). However, the resulting DPIV velocity fields, one field corresponding to each image pair, were then each separated in time by (1/15 sec). Therefore, the temporal resolution of the overall flow evolution was sacrificed for better temporal resolution of the "instantaneous" flow at each time step; for the moderate Reynolds number of the current investigation, this trade-off was entirely acceptable. Westerwheel, Dabiri, and Gharib (1997) offer a much more thorough treatment of the subject of time resolution.

3.6.3 DPIV processing

The DPIV processing was done using a 32 by 32 pixel interrogation window, with a 16 by 16 pixel overlap. This gave 48 by 30 (or 1440) vectors for each velocity field, and resulted in a typical resolution, depending upon the imaged section of the flow, of about 7 mm in the horizontal and vertical directions, which was then improved upon using a window shifting technique with the same interrogation window size and overlap (see Westerwheel, Dabiri, & Gharib, 1997). The interrogation window and overlap sizes were chosen so that the number of errant vectors, or outliers, in each velocity field was minimized. The small number of outliers, if any, that appeared in the velocity fields, especially near the plate itself, were removed and replaced by a vector interpolated from its surrounding neighbors via the DPIV software (see Willert & Gharib, 1991).

Although the resolution after using the window shifting algorithm was better than 7 mm, it was still not adequate enough to resolve the small-scale instability in the leading edge

shear layers, visible in the chordwise dye flow visualization. The under-resolved instability thus appeared as noise. Since the period of the shear layer instability was much smaller than the timescale of the leading edge and tip vortex formation, and this investigation was concerned only with the more gross features of the flow (namely, the larger-scale vortex formation), it was decided to use a low-pass filter to remove the instability. The vorticity field, $\omega(\underline{x},t)$, calculated from the DPIV velocity data was therefore smoothed in time with the following low-pass filter:

$$\omega_f(\underline{x},t_{k+1}) = 0.8\omega_f(\underline{x},t_k) + 0.2\omega(\underline{x},t_{k+1})$$

This filter did not appreciably affect the overall behavior of the circulation with time, as Figure 3.4, which shows circulation calculated from filtered and unfiltered vorticity field data, illustrates.

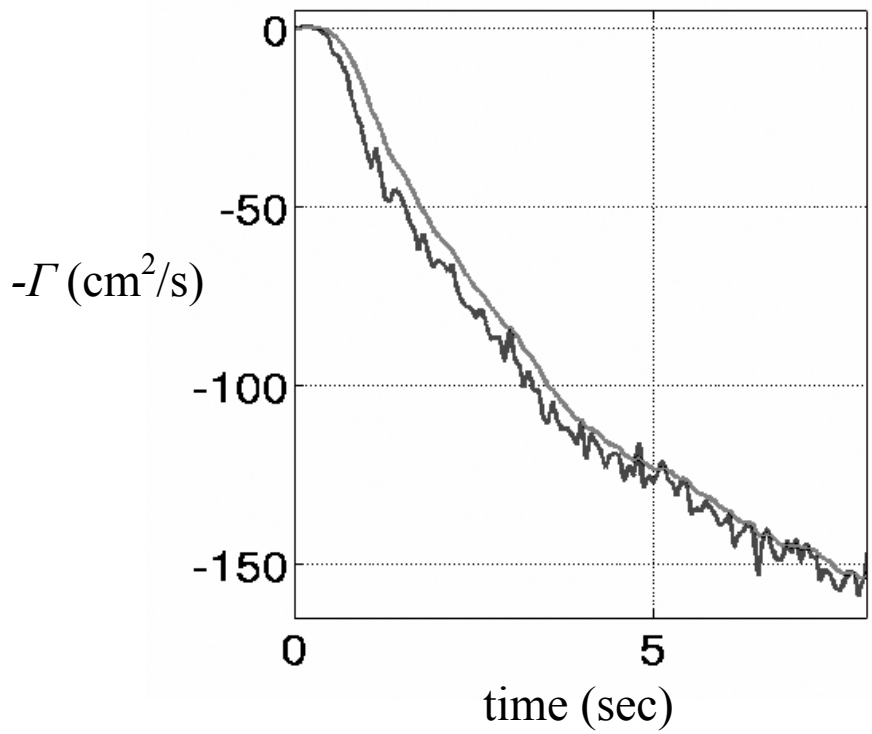

Figure 3.4 Circulation calculated from filtered and unfiltered vorticity data. *AR* = 6, 50% span. Darker, jagged line: circulation from unfiltered vorticity; lighter line: circulation filtered using the low-pass filter given in the text.

4 Results

4.1 Introduction

The results from the force measurements, DPIV experiments (including circulation and vorticity), and dye flow visualization will be presented in this chapter, in that order. More features of the flow will be brought out with each new section, and a model to explain the results at the startup will be presented at the end.

4.2 Force measurements

4.2.1 Aspect ratio 6

The drag coefficient, C_D, versus formation time for aspect ratio 6 is plotted in Figure 4.2.1a, and with a zoomed-in C_D-scale in Figure 4.2.1b. For all force measurements, the drag coefficient is computed using the measured drag, D, the final, constant velocity, U_{final}, the plate area, S, and the density of water, ρ, as follows

$$C_D = \frac{2D}{\rho U_{final}^2 S}$$

As described in Chapter 3, the forces plotted are the average of 10 measurements, unless otherwise noted, each of which is low-pass filtered.

Figure 4.2.1a shows an initial peak C_D of about 7.4, corresponding to the constant acceleration portion of the velocity profile. During acceleration only, added mass and the inertia of the plate model contribute to the total drag force. Throughout the entire run, the drag force has a component due to the pressure field created by the LEVs and the TV, in addition to a small contribution from viscosity. The C_D then drops below 2 at a formation time of 1.5, and remains between 1.4 and 1.65 for $T > 3$. After the startup peak, the most noticeable feature of the data is a broad "hump" with its maximum at about $T = 5$ (see Figure 4.2.1b). The sections following this discussion on the force data will present

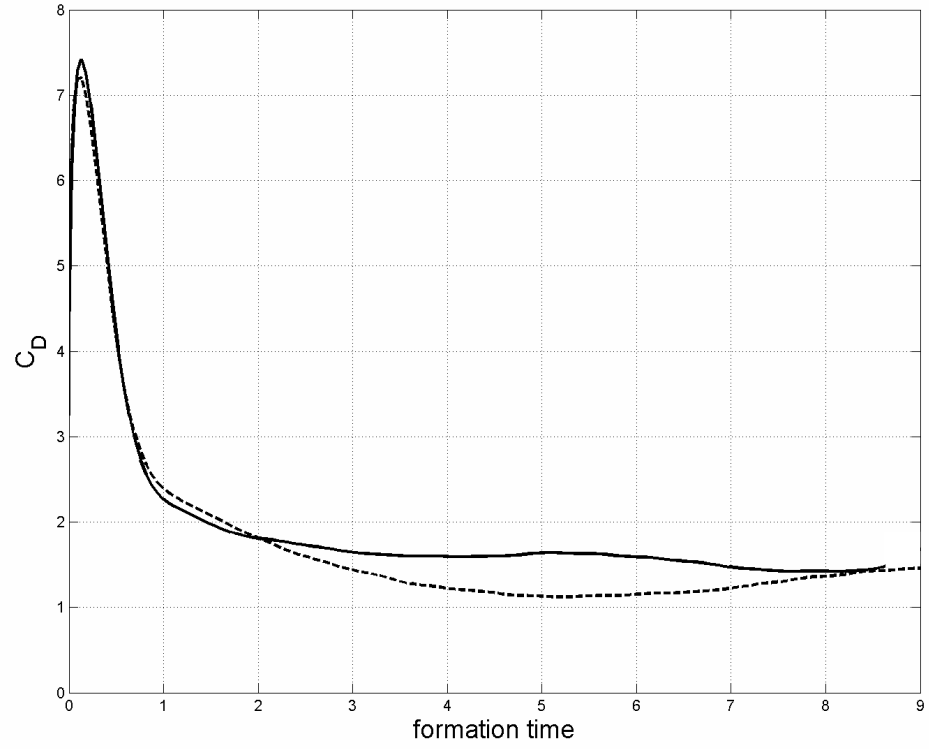

(a)

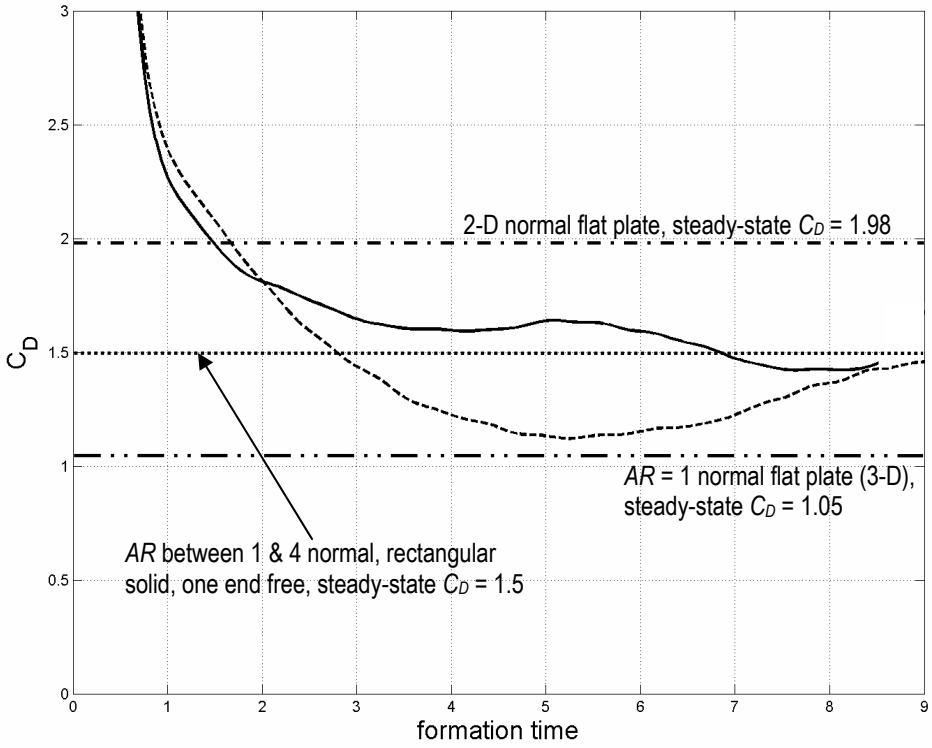

(b)

Figure 4.2.1 Measured C_D vs. formation time, AR = 6. Solid line: free end; dashed line: tip grazing bottom wall. (b) zoomed-in C_D-scale, with 2-D normal flat plate & 3-D AR = 1 normal flat plate steady-state C_D's.

circulation measurements and chordwise (horizontal) vorticity fields from DPIV that show flow phenomena occurring around $T = 5$. Additionally, spanwise (vertical) vorticity fields as well as dye flow visualization will shed light on the role of the tip vorticity and the overall flow in the force generation.

In order to gain insight into the influence of the plate tip on the drag force, in addition to the information obtained from DPIV and flow visualization experiments, the drag measurements were retaken with the setup modified to suppress the flow around the tip, i.e., the tip vorticity. Specifically, a raised platform with a flat, smooth upper surface was placed below the plate, creating a new bottom wall with only a paper-thin gap between it and the plate tip. This "grazing" end condition (along with a clean free surface) was recommended and used by Lisoski (1993) and Slaouti and Gerrard (1981) for achieving highly 2-D flow; Lisoski did experiments with these end conditions with *AR*'s ranging from 6 to 17, and found little variation in C_D with *AR*. The dashed line in Figure 4.2.1 is the average of two such runs (which were very repeatable) from the present work, with $AR = 6$, and the major difference between this and the original force trace is that there is a minimum instead of a maximum around $T = 5$. This result has important implications for flyers in nature that use low *AR* wings to hover, an assertion that will be supported with the following discussion.

It is well known that, under steady-state conditions, the drag on three-dimensional bodies at Reynolds numbers (*Re*'s) > 100 is lower than that of their two-dimensional counterparts. For example, the drag coefficient of a sphere at $Re = 10^3$ is 0.41, while the C_D of a 2-D (i.e., infinite *AR*) circular cylinder at the same *Re* is 1.0 (Blevins, 1984). For a normal flat plate of infinite *AR*, C_D is 1.98 (McCormick, 1995), while an $AR = 1$ plate (having all four edges free), oriented with its broad side to the flow, has a C_D of 1.05

(Blevins, 1984). In fact, for a variety of shapes over a wide range of Reynolds numbers, the ratio of the 2-D steady-state C_D to its 3-D (body of revolution) counterpart is about 1.8 (McCormick, 1995). This is due to the difference in the flow separation over a 2-D versus a 3-D body. For a 2-D normal flat plate, separation occurs only over the 2 leading edges. Considering a 3-D example, such as an $AR = 1$ plate fully submerged (with its edges free) in a fluid and oriented normal to the flow, separation occurs at all 4 edges. At sufficient *Re*, a 2-D flat plate has an LEV that rolls up from each of its 2 edges to form a certain-sized wake, whereas a 3-D plate has 2 pairs of LEVs rolling up from its perpendicular pairs of edges, creating a more contracted wake that results in lower drag. However, if the *AR* of a 2-D (in terms of end conditions) normal flat plate or circular cylinder is about 5 or less, the 2-D C_D becomes approximately equal to the 3-D C_D with the same *AR* (McCormick, 1995).

Although the current work considers only starting flow, the data on steady-state drag coefficients can provide some insight into the present $AR = 6$ results. Based on the steady-state findings, the drag of the grazing (2-D) case should be similar to that of the free-end case, at $AR = 6$, if the upper-end (i.e., that closest to the free surface) condition of this free-bottom-end case was also a free end, far away from the free surface. However, the flow considered in the present work is that of a flat plate with 2 different end conditions, one nominally 2-D (the free surface) and one 3-D (the free end), which more closely approximates a biological wing (more on this below). This mixture of end conditions results in a drag force that is lower (after the initial acceleration) than the purely 2-D (i.e., infinite-*AR*) normal flat plate steady-state case, but higher than the nominally 2-D, $AR = 6$ unsteady grazing case, as well as the steady-state, $AR = 1$ (3-D) normal flat plate case (Figure 4.2.1b reports all of these C_D's). Mixed end conditions in steady-state also produce C_D's that are

higher than the fully 3-D case, but lower than the 2-D case, consistent with the unsteady results of the present work. For example, a rectangular solid of square cross section attached to a wall at one end and having the other end free (such that it looks like a miniature building), has a C_D of about 1.5 if the AR (or length to side ratio) is between 1 and 4, and it is oriented normal to the flow (this is true if most of the solid is well out of the boundary layer at the end wall, see Blevins, 1984). The C_D of the same solid if the AR were infinite is 2.2, while the C_D is 1.05 for an AR = 1 normal cube (i.e., the fully 3-D case) with all of its sides free (Blevins, 1984). As will be shown presently, the mixed end condition phenomenon, which for the present work produces higher drag than the grazing flat plate and the AR = 1 normal plate cases, is AR-dependent. Unsteady flow results from the thesis of Derek Lisoski (1993) will be used next to show the effects of AR and end conditions on the drag force. In addition, the results from the current work will be compared with those of previous studies, cited in Chapter 1.

In Chapter 1, it was noted that Chua et al. (1990) and Lisoski (1993) observed a drag "bucket," or low drag region, centered around $T^* = 8$. The drag minimum of the present study occurs earlier than that reported by Chua et al. and Lisoski, presumably because the beginning plate acceleration, over a distance of only 1/4 chord, is more aggressive than their acceleration distances of $2c$ and $1.31c$, respectively. Sarpkaya and Kline (1982) and Dickinson and Götz (1993) did not, however, record drag buckets, and this will be discussed below. Lisoski reported drag buckets for all of his experiments (from AR = 6 to 17) whose plate end conditions promoted nominally two-dimensional flow, and attributed the phenomenon to a symmetric recirculating bubble behind the plate, which becomes nonsymmetric (breaks down) before $T^* = 20$. He hypothesized that a closed, recirculating

wake bubble, made up of the pair of LEVs, induces flow near the wake centerline that is toward the rear face of the plate. This creates higher pressure on the rear face than would exist without the bubble. As the LEVs grow stronger, the induced velocity and base pressure increase, causing the drag minimum observed before the bubble breaks open.

For the case of an $AR = 17$ plate with a free lower end, Lisoski also reported a drag bucket, albeit with a slightly higher minimum. However, for the case of an $AR = 10$ plate with a free end, he found no drag bucket. This illustrates that the effect of the tip (free end) for a plate with a 2-D upper end condition does not become important until the AR is reduced to at least about 10. The findings of the present study suggest that a significantly beneficial gain in drag force, in this case about 46% at the C_D maximum at $T = 5$, is not achieved unless the AR is reduced further to 6.

Given the above results and discussion, it seems that a wing designed for hovering flight, which must generate primarily drag force, should have one free end and an AR of around 6 or less. Indeed, as stated in Chapter 1, hovering animals have AR's between 2.75 and almost 6. Additionally, physiology dictates that the wings of flying animals can have only one free end, the other being attached to the body.

Although the alternative, a single wing with both ends completely free, is not possible biologically, (single) wing shapes that approximate something close to 2 free ends can be imagined. For example, this could be achieved by cutting out an area of the wing between the leading and trailing edge spars, somewhere along the span, so that the remaining wing area between the cutout and the actual wing tip acts like an outboard body with 4 free edges. However, such a configuration, with two 3-D, or free, end conditions, would most likely be unfavorable. While the results from the present work show that, for unsteady starting flow,

"mixed" end conditions generate significantly higher drag than the nominally 2-D case, the steady-state data suggest that there are limitations to the benefits of 3-D flow. Steady-state experiments (discussed above) show that the C_D of a body with fully 3-D end conditions is *lower* than, or at most comparable to at low *AR*, its 2-D counterpart; a body with mixed end conditions has a C_D somewhere in between the two extremes. This information suggests that mixed end conditions may be more advantageous than purely 2-D or 3-D ones. Indeed, the DPIV and flow visualization results of the current study, provided in the next sections, will show the benefits of a single tip vortex. It acts to suppress the pinch-off of the LEVs near the tip, which creates a highly 3-D, low-pressure flow there that generates high drag. However, it also allows the LEVs away from the tip to grow stronger than those near the free end, generating high drag that peaks before they pinch-off. Without the TV, the LEVs along the span would grow and form a coherent, low-drag recirculating bubble, which results in the drag minimum measured for the grazing case (see Figure 4.2.1). A plate with 2 TV's, one at each end, would most likely limit the growth of the LEVs farthest away from the tips more than a single TV does. This would reduce their force contribution, resulting in less drag than the single TV case.

The outboard ends of bird and insect wings are free, while, inboard, the ends attach to the animal's body. The latter end condition cannot have a significant tip vortex for two reasons. First, because, the inboard end of the wing is attached to the body through a joint, it moves very little during hovering flight, compared with the outboard wing tip. Second, although some insect wings may narrow at the wing-body joint, so that they are geometrically like a wing tip, the connection to the body interferes with flow from the

underside of the wing curling up over the wing's end to the top surface, i.e., tip vortex roll up.

The current drag force data for $AR = 6$ will now be compared with the other studies cited in Chapter 1. Sarpkaya and Kline (1982) performed their measurements on an $AR = 8$ plate nearly impulsively started with a final Re of 21000, and having the wind tunnel walls as end conditions. Theirs was the only investigation to report a drag maximum, albeit slight, at around the same time, $T^* = 4.5$, as that measured in the present work. However, since their plate model did not have one end free, it is unclear why they did not observe a drag bucket, nor what the cause of their drag maximum was. The essentially impulsive start in addition to the high Reynolds number may not have allowed for a long-lived symmetrical recirculation bubble, which would explain why no drag bucket was observed. The slight drag maximum may have been due to the saturation and subsequent pinch-off of the LEVs. Finally, for the very low Reynolds number (192) case studied by Dickinson and Götz (1993), with grazing conditions at both plate ends, a recirculating wake bubble was probably present throughout the entire 7 chord lengths of total travel. This would result in low drag (compared to a free end case) throughout the entire run, after the initial acceleration peak, similar to the grazing case of the present work if it was taken out to just $T = 7$. This low drag could only be labeled a "bucket" if the experiments were run for longer time to obtain the drag after $T = 7$ for comparison.

4.2.2 Aspect ratio 2

The drag coefficient for $AR = 2$ is plotted along with that of $AR = 6$ in Figure 4.2.2a, and with a smaller C_D-scale in Figure 4.2.2b. The initial peak in the C_D corresponds to the constant acceleration over ¼c, during which added mass and the inertia of the model

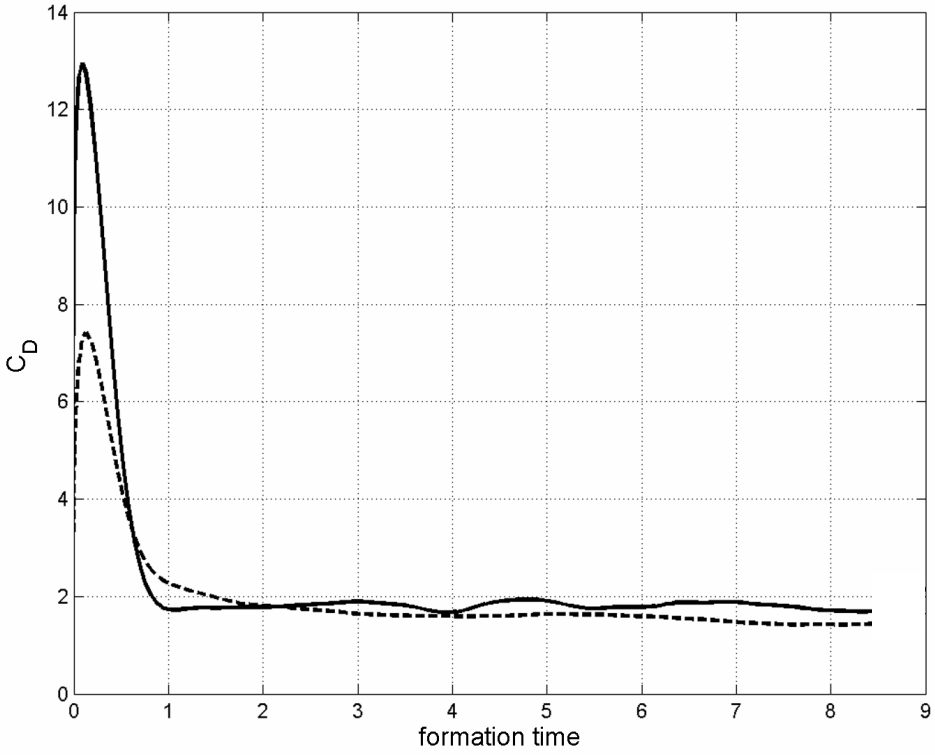

(a)

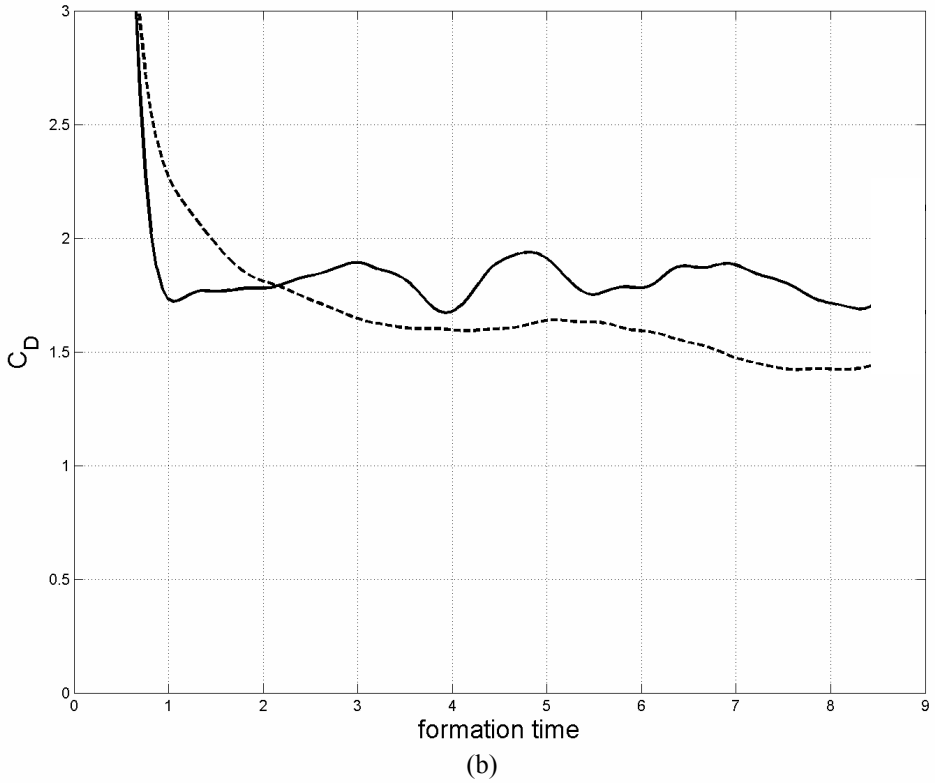

(b)

Figure 4.2.2 Measured C_D vs. formation time, AR = 2 and 6. Solid line: AR = 2; dashed line: AR = 6. (b) zoomed-in C_D-scale.

contribute significantly to the overall drag. For $AR = 2$, the peak C_D is about 1.8 times that of $AR = 6$. In order to explain this difference, the drag coefficient due to added mass and inertia for both AR's was estimated. The added mass of thin plates of finite aspect ratio was obtained from calculations given in Sarpkaya and Isaacson (1981), and it is $0.7568\pi\rho bc^2/4$ for an $AR = 2$ plate, and $0.909\pi\rho bc^2/4$ for an $AR = 6$ plate. Since the same plate model was used for both AR's (the AR was varied by changing the water level in the tank), the inertial force measured by the balance during the acceleration is the same for both cases. The added mass for $AR = 2$ is 0.1486 kg, while it is 0.535 kg for $AR = 6$; the mass of the plate model is 0.1239 kg. Since the added mass and inertial force are both proportional to the acceleration of the plate (equal to 0.144 m/s^2), they are both constant during the acceleration. The drag due to the inertia of the model is 0.0178 N, the force due to added mass for $AR = 2$ is 0.0214 N, and for $AR = 6$ the added mass force is 0.077 N. Computing the drag coefficient (defined as above) due only to added mass and inertia, for $AR = 2$, $C_D = 4.36$, while for $AR = 6$, $C_D = 3.51$; the ratio of the two C_D's (that of $AR = 2$ to $AR = 6$) is 1.24, compared to the measured ratio of 1.8. Considering added mass only, the C_D for $AR = 2$ is 2.38, and for $AR = 6$, $C_D = 2.85$, with their ratio being 0.84.

These calculations show that the significant difference in C_D between $AR = 2$ and 6 is most likely not due to added mass (given the C_D ratio of 0.84). Instead, the force from the inertia of the plate, as measured by the balance, accounts for much of the difference. Since the inertia of the plate is the same for both cases, its contribution to the $AR = 2$ C_D is higher because the drag coefficient formula includes the plate area. The fact that the computed drag coefficients are smaller than those measured by the balance, as is the ratio between them, could be due to a number of factors. First, the towing tank drive system may introduce some

mechanical whiplash at the startup. Second, the plate model bends, although slightly, as it is accelerated from rest. Both of these non-ideal effects would be felt by the force balance. In addition, since the water level for the $AR = 2$ plate is different from that of $AR = 6$, the damping that the water provides is less, but the relative moment from the resultant drag on the plate is higher. These effects may contribute to the peak C_D for $AR = 2$ being larger. Finally, viscous effects and pressure drag, although both are small at the startup, were neglected in the above computations.

After $T = 1.5$, the magnitude of the C_D for both cases resides between 1.5 and 2. However, instead of a single "hump" at $T = 5$ like the $AR = 6$ case, the $AR = 2$ data exhibit a "wiggling" behavior starting at $T = 3$ and ending at $T = 7$ (see Figure 4.2.2b). Spanwise (vertical) vorticity fields from DPIV data, as well as images from flow visualization, indicate that vorticity from the plate's corners convects into the mid-chord plane and then upward to impinge the free surface during this time. This creates secondary vorticity and free surface deformation, which affects the drag force measurements. Spanwise vorticity in the leading edge plane, due to the LEVs, exhibits similar behavior. Additionally, vorticity fields and circulation measurements from horizontal DPIV show interesting flow phenomena, such as "inward" LEV pinch-off and wake contraction, at these formation times. The "wiggles" in the drag force, which are not always in phase from run to run, are therefore a result of complex flow interactions that will be made clearer when the DPIV and flow visualization results are given in later sections. Also, an explanation for the fact that the $AR = 2$ C_D is higher than that of $AR = 6$ after $T = 2$ will be proposed.

4.2.3 Drag force components

There are many factors responsible for the total drag on the flat plate as measured by the force balance. Specifically, these components are added mass (during acceleration), viscous effects, the inertia of the model itself, and the induced pressure field around the plate due to the vortices it generates. To investigate the role of each component more easily, a gentler velocity profile with an acceleration portion over a distance of 10 times that of the original, i.e., 2.5*c*, followed by a constant velocity at $Re = 3000$, was chosen. This milder profile ensured that any mechanical vibration at the startup was minimized, yet also that the acceleration portion did not extend into the region of vortex saturation, 3 to 5*c*, so that added mass and vortex effects did not entirely overlap.

Figure 4.2.3 shows the resulting C_D versus real time for an $AR = 6$ plate with a free end, represented by the solid line (average of 4 runs), and the same plate with the grazing end condition, shown as a dashed line (average of 2 runs). The velocity profile, with its magnitude scaled to fit on the plot, is also provided to aid the discussion.

When a body is accelerated through a fluid, energy must also be expended to accelerate the fluid that it is displacing around it. This increases the force required to accelerate the body beyond that needed if the body was in a vacuum. To experience this same force needed to accelerate the body through a fluid if it is then placed in a vacuum, mass must be added to the body, and this extra mass is called "added mass" (Daniel, 1984). The force on a body due to added mass is directly proportional to the body's acceleration. It also depends on the body's shape relative to its direction of travel: an ellipsoid accelerating in a direction parallel to its long axis has a higher added mass than the same ellipsoid moving parallel to its short axis (Daniel, 1984). Figure 4.2.3 shows that the slope of the velocity profile reaches its maximum at about 1 second, remains constant until about 3 seconds, then

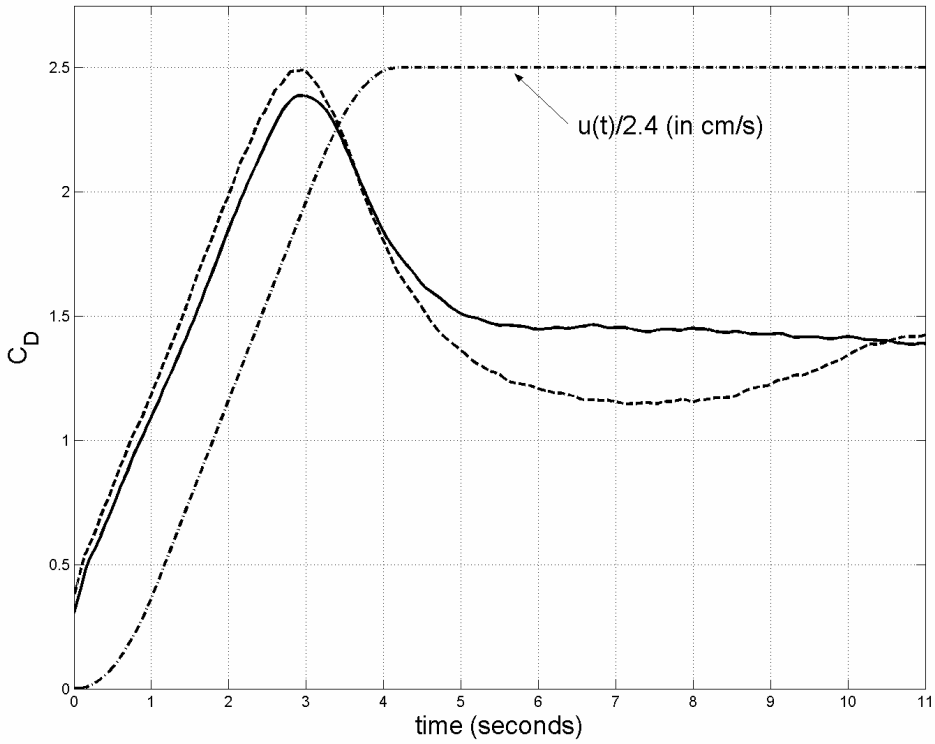

Figure 4.2.3 Measured C_D vs. real time, AR = 6, acceleration over 2.5c.
Solid line: free end; dashed line: tip grazing bottom wall; dash-dot line: velocity profile.

decreases until the velocity is constant at about 4.2 seconds. The force on the plate due to added mass should therefore increase at the startup due to the increase in acceleration, remain constant between t = 1 and 3 seconds, then drop to zero from 3 to 4.2 seconds. Indeed, for both end conditions there is a sharp rise before t = 1 second (though it is somewhat lost in the filtering), and a drop in the drag force around t = 3 seconds. Although the force due to added mass is significant, it is not the focus of the present work because such forces average to zero during the back-and-forth wing motions used for hovering (Wang et al., 2004).

The force measured by the balance during the non-zero acceleration portion of the velocity profile also includes a contribution from the inertial force of the plate model itself. The inertial force is directly proportional to the plate's acceleration, so, like the force due to added mass, it increases until t = 1 second, then remains constant, and finally decreases to

zero starting at $t = 3$ seconds. Therefore, the drop in drag after $t = 3$ seconds is partially the result of both the force due to added mass and the inertia of the plate falling-off as the acceleration diminishes.

Viscous drag, although small for a thin body oriented normal to the flow, adds to the overall force, as well. It is proportional to the plate velocity, and therefore increases until $t =$ 4.2 seconds, then levels off to a constant value.

Finally, the remaining drag force is due to the pressure on the plate induced by the vortices it generates. Initially, as the LEVs and TV form and grow, they are small and close to the plate edges that formed them, and their high velocities make them regions of low pressure. This causes an increase in the plate's drag. For the grazing case, the LEVs become larger after a certain time (a behavior that is partially masked by the other forces discussed above) and probably form a recirculating bubble behind the plate. The induced upstream flow from the recirculation would increase the base pressure, thus decreasing the drag. Such an effect is observed in the grazing case after $t = 4$ seconds, and it reaches its maximum shortly after $t = 7$ seconds, which presumably corresponds to the saturation time of the LEVs. For the free end case, the situation is more complicated. The interaction between the TV and the LEVs certainly raises the drag force significantly above that measured for the grazing case after $t = 5$ seconds. However, the exact mechanism through which this is accomplished can only be revealed by techniques such as DPIV and flow visualization, the results of which will be shown in the following sections.

4.3 Chordwise flow sections: DPIV, circulation, and formation number

4.3.1 Aspect ratio 6

Chordwise sections of the flow velocity for aspect ratios 6 and 2 were captured at 50, 75, and 90% spanwise locations, measured from the free surface, using DPIV. The total circulation (the average of that generated by each edge) and leading edge vortex circulation (the average of that of each LEV) were calculated using Stokes' theorem in 2-D,

$$\Gamma = \int_A \omega dA ,$$

and vorticity field data from the DPIV (see Chapters 2 and 3 for details on the theory and the experimental setup, respectively). Figure 4.3.1 shows the total and leading edge vortex circulation versus formation time for all three spanwise locations for $AR = 6$; the individual cases will be described separately, along with their corresponding vorticity fields and flow visualization, following this discussion.

The circulation data in Figure 4.3.1 were obtained from DPIV data normalized using the plate chord length and the final velocity, so that each case could be compared easily. At the start of the plate motion, when the flow is primarily 2-D, the circulation for each spanwise location is about the same, and increases at nearly the same rate. However, after a formation time of about 0.5, the total circulation for 75 and 90% span start to diverge from and become lower than that at 50% span. Then at $T = 2$, the total circulation for 90% span flattens out, while at 50 and 75% span, it continues to increase. At $T = 5$, the total circulation at 75% span starts to decrease, then flattens out and comes nearer to the circulation at 90% span after $T = 6.3$. Shortly after the total circulation at 75% span begins to decrease, there is a small, temporary drop in the circulation at 90% span having its minimum at $T = 5.5$. Significant losses in this total, sectional circulation generated by each edge are possible

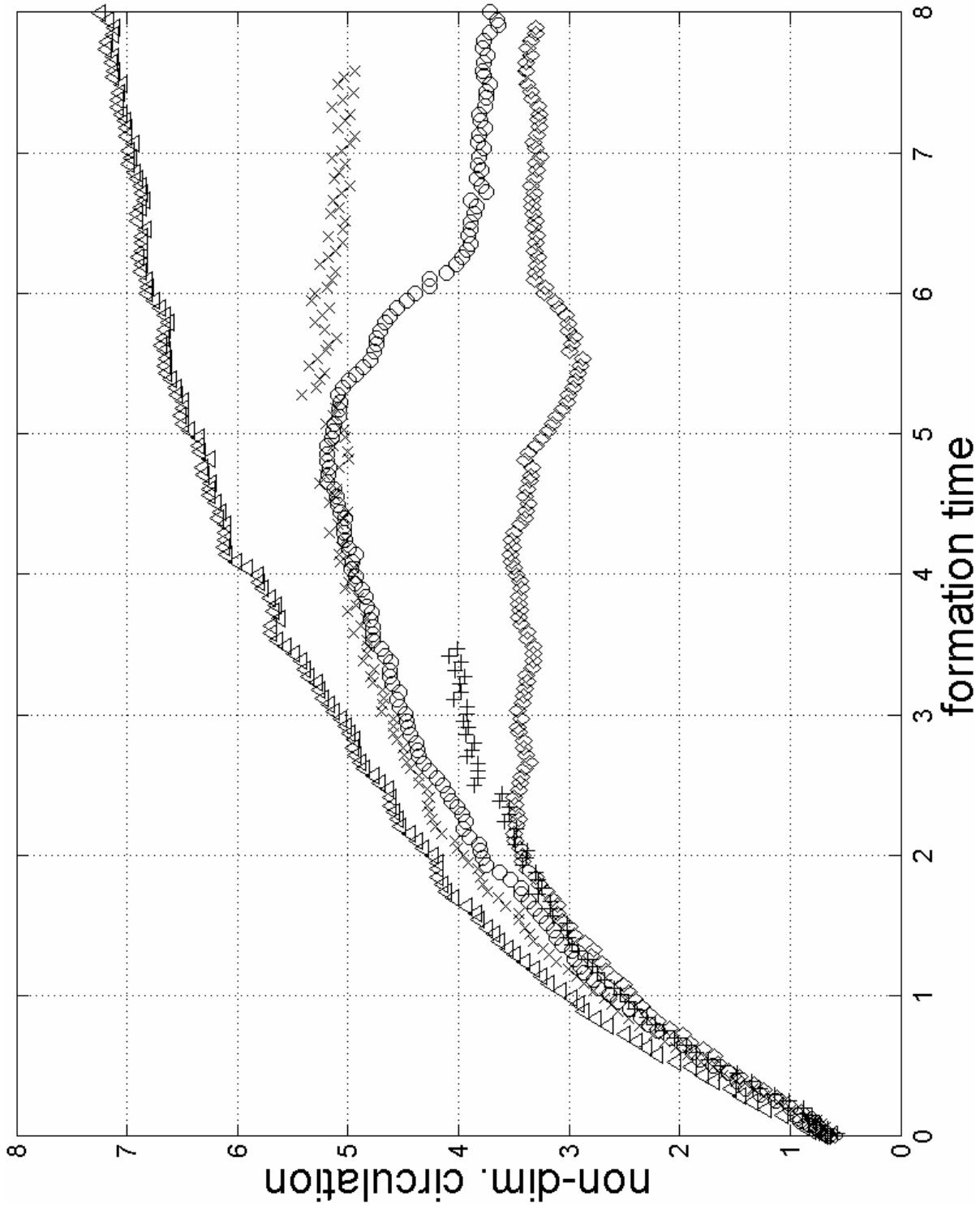

Figure 4.3.1 Circulation vs. formation time, $AR = 6$.
Triangles: total circ., 50% span; x's: LEV circulation, 50% span; circles: total circ., 75% span; crosses: LEV circulation, 75% span; diamonds: total circ., 90% span.

because the flow is highly 3-D. In order to begin to understand the overall trend of higher circulation with increasing distance from the tip, as well as the more salient features of the data, such as the leveling-off of the circulation at 90% span, and the drops in circulation at 75 and 90% span around $T = 5$, the evolution of the vorticity fields with formation time at each spanwise station will be shown. First, however, the circulation of the leading edge vortices for each case will be discussed.

For $AR = 6$, only the 50% spanwise location exhibited leading edge vortex formation and clear pinch-off. The LEV formation number is defined as the formation time at which the LEVs reach their maximum circulation, or saturate (see Chapter 2), before pinch-off. Referring to the circulation data in Figure 4.3.1, the formation number for the $AR = 6$, 50% span case is therefore about 4.5. The formation and growth of the LEVs at 75% span are similar initially to the 50% span case, but they occur more quickly. By $T = 3$, the LEVs have achieved their maximum circulation. However, as will be evident when the vorticity fields are shown, the LEVs do not experience a complete pinch-off. Instead, by $T = 4$, they merge back with the shear layers from the plate's edges that originally formed them, and a much more complicated wake follows after $T = 5$. Finally, for 90% span there are no LEV circulation data separate from the total circulation because the two are coincident. The vorticity fields there show that the LEVs remain attached to the plate throughout the entire run. Therefore, the formation number for this case is the formation time at which the total circulation saturates or levels off. This occurs at $T = 2.2$, leading to the result that the formation number decreases as the distance from the plate tip decreases.

The circulation at 50% span, along with insets showing vorticity field snapshots at key formation times, is given in Figure 4.3.2. A larger set of vorticity field snapshots,

highlighting significant points during the evolution of the flow with formation time, is provided in Figure 4.3.5. At $T = 1$, the wake of the plate consists of a symmetrical pair of compact LEVs that are growing with formation time. The circulation increases as the LEVs become larger and elongate in the direction of the flow, which occurs until shortly after $T = 4$. At $T = 4.5$, the formation number, the LEVs have begun to pinch-off, or become separate vorticity entities, from the plate leading edge shear layers that formed them. This process evolves through $T = 5$, and, although the total circulation continues to increase, the LEV circulation remains at the formation number value, since the LEVs are no longer being fed by the plate's shear layers. Finally, at $T = 6.67$, the pinch-off process is complete, since there is a near-zero region of vorticity between the shear layers and the LEVs. However, the LEVs do not subsequently shed. Instead, they merge again with their forming shear layers, as seen at $T = 7.02$ and 8.01 in Figure 4.3.6. This is due to the highly 3-D flow induced by the plate tip, which will be explored in further detail in subsequent sections using the vertical DPIV data and dye flow visualization. Figure 4.3.6 shows that by $T = 9.3$, new LEVs have formed and induced an opposite sign vortex dipole slightly aft of themselves and closer to the wake centerline. In addition, the original LEVs have moved farther from the wake centerline, and are no longer symmetrical.

A plot of the circulation at 75% span, with insets of vorticity field snapshots, is given in Figure 4.3.3. Figure 4.3.6 provides a greater number of snapshots to show the evolution of the flow in more detail. At early formation times, the flow develops much like that at 50% span: 2 symmetrical LEVs form and grow, and therefore the circulation increases. However, the pinch-off process starts at $T = 2$, rather than $T = 4.5$. By about $T = 3$, the formation number for this case, the LEVs have achieved their maximum circulation, and have almost

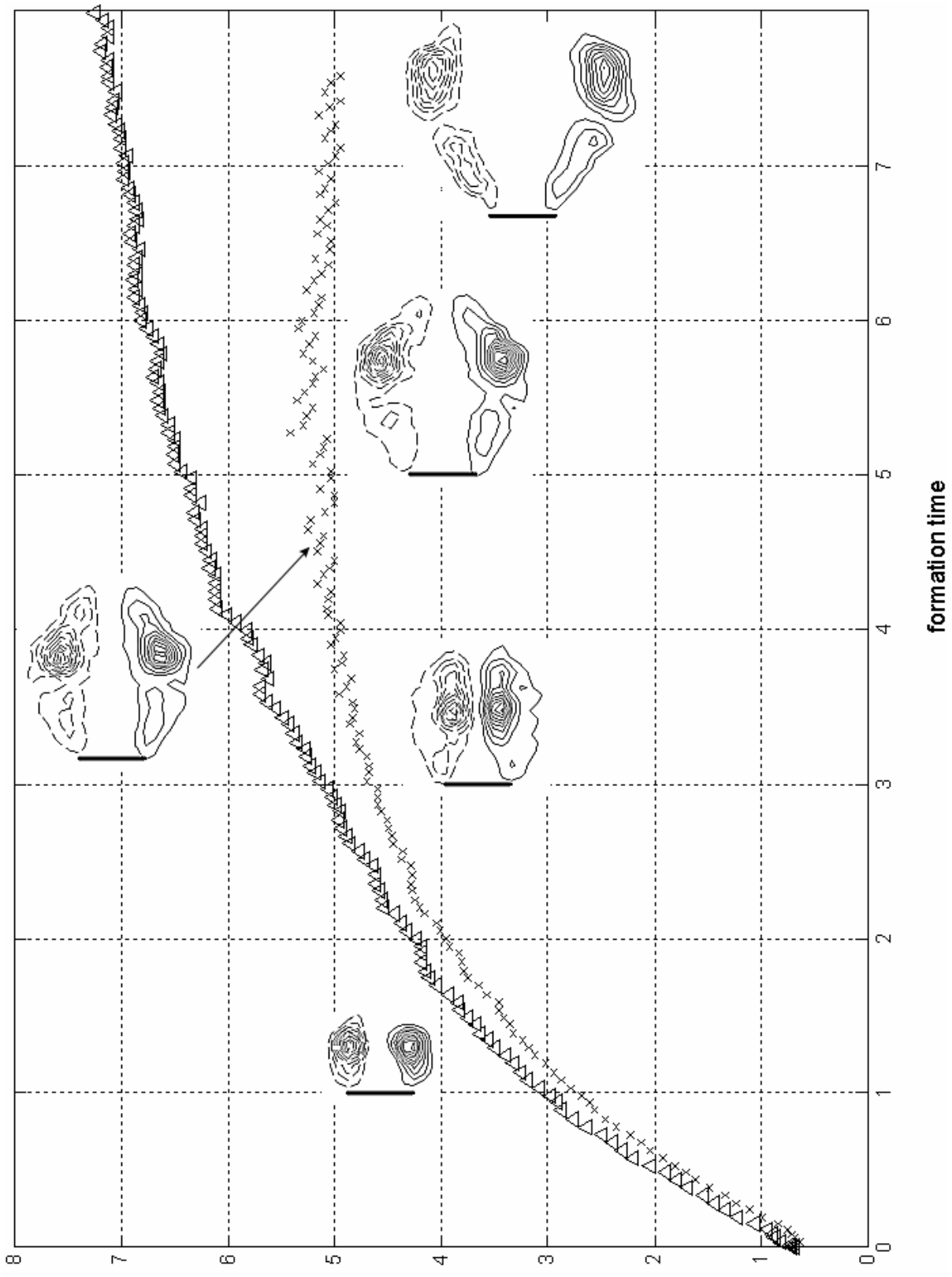

Figure 4.3.2 Circulation at *AR* = 6, 50% span, with vorticity field insets. Triangles: total circ.; x's: LEV circ.

pinched-off. Before the pinch-off is completed, though, the LEVs merge again with the leading edge shear layers that formed them, then subsequently grow and elongate. This continues, with the total circulation increasing correspondingly, until the circulation reaches a maximum at about $T = 4.8$. After this formation time, the total circulation drops and the structure of the wake changes substantially. The LEVs again start to pinch-off from the plate's leading edge shear layers, but instead of moving outwardly, they are drawn in toward the wake centerline and the leeward side of the plate itself. A momentary, "inward" pinch-off occurs at $T = 5.73$. However, by $T = 7$, the LEVs have merged with the shear layers again, leaving a complicated, elongated wake. During this last wake transition, at about $T = 6.5$, the total circulation stops decreasing and levels off at about 73% of the maximum value. For $AR = 6$, the 75% span case is the most complicated. The behavior of the wake, which differs substantially from that of 50% and 90% span, is due to interaction between the tip and leading edge vortices. Spanwise (vertical) DPIV and flow visualization given in the next section will show the (sectional) out-of-plane flow responsible for these wake features.

A glance at Figure 4.3.4, which shows the total circulation at 90% span along with insets of vorticity field snapshots, reveals that the chordwise section of the flow at this spanwise location is much simpler than the others. The LEVs remain attached to the plate throughout the entire run, and no pinch-off process is observed. Flow visualization shows that, near the plate tip, the interaction between the tip and leading edge vortices creates 2 tornado-like LEV structures that emanate from the corners on the leeward side of the plate. The 90% spanwise location is near the base of these LEV "tornadoes," which is evident by the fairly compact vortices displayed in the chordwise cross section of the flow there.

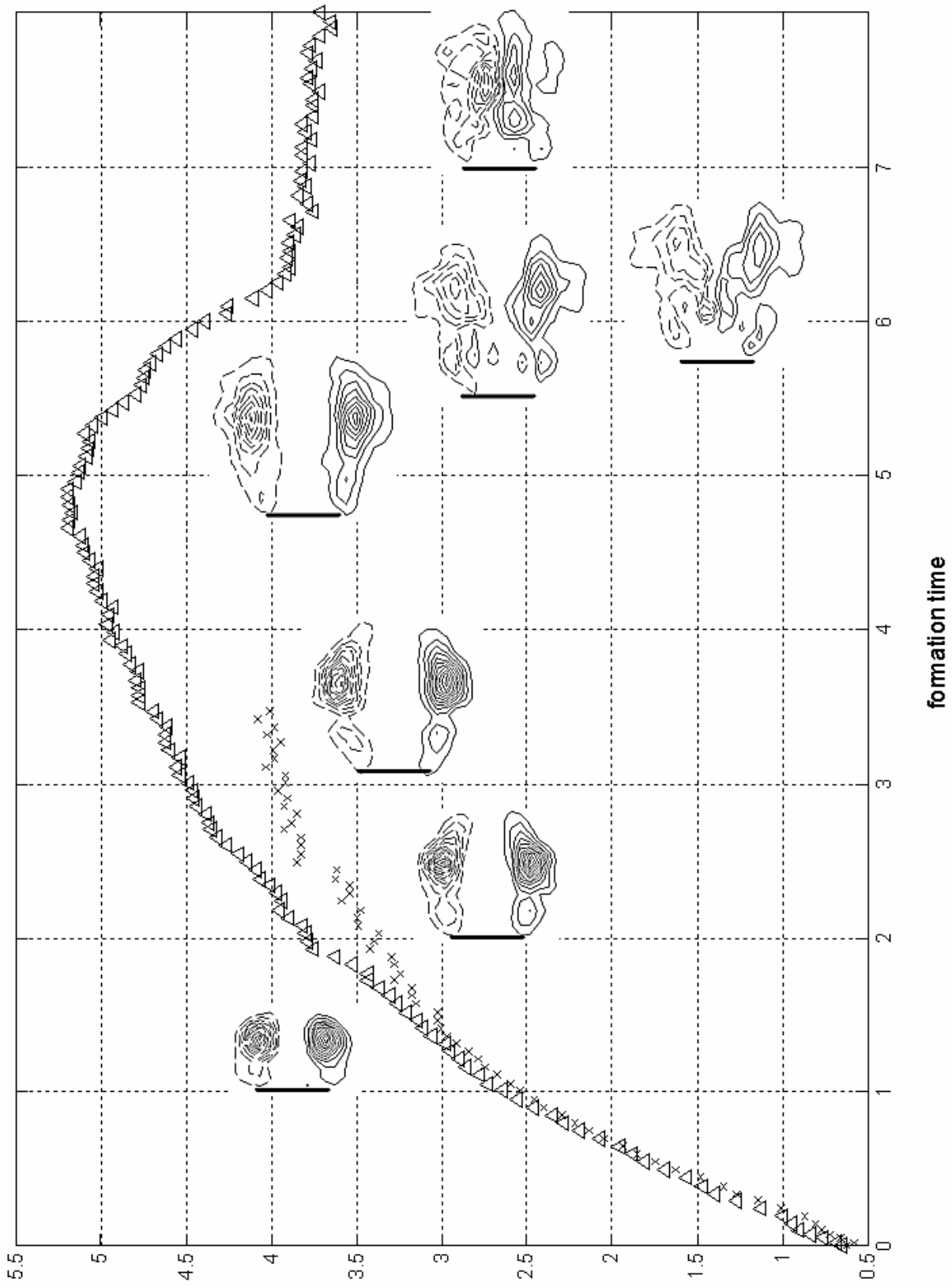

Figure 4.3.3 Circulation at *AR* = 6, 75% span, with vorticity field insets. Triangles: total circ.; x's: LEV circ.

Again, at early formation times the flow is similar to that at 50 and 75% span: a symmetrical pair of LEVs forms and grows, and the total circulation increases. At $T = 2.2$, the formation number, the circulation flattens out or saturates, and the LEVs are still fairly compact. After this formation time, the circulation fluctuates between 3.3 and 3.5, until about $T = 4.8$, during which time the wake structure changes (see Figure 4.3.7 for a larger number of vorticity snapshots). As seen at $T = 3$, the sides of both LEVs closest to the wake centerline are drawn together toward the middle of the leeward face of the plate, where previously there was little vorticity. By $T = 4.29$, a symmetrical recirculating bubble narrower and fuller than the original wake has formed. Following this, the circulation drops to a local minimum at $T = 5.5$, corresponding to the LEVs becoming more compact and pull away from the plate near the wake centerline. The LEVs remain in this configuration and grow in strength until most of the lost circulation is recovered by $T = 6.2$, after which they elongate slightly.

Looking at the circulation data and vorticity fields for 50, 75, and 90% span, all three cases exhibit significant changes around $T = 4.5$ to 6. Specifically, the circulation data in Figure 4.3.1 show that, at $T = 4.5$, the LEVs at 50% span saturate, after $T = 4.8$ the total circulation at 75% span drops and does not level off until $T = 6.5$, and starting at $T = 4.9$ the circulation of the flow at 90% span drops and reaches a local minimum at $T = 5.5$. At $T = 4.5$ the LEVs at 50% span start to pinch-off, after $T = 4.8$ the LEVs at 75% span begin the complicated "inward" pinch off, and by $T = 5.5$ the LEVs at 90% span have transitioned from a narrow but full recirculating bubble to more compact structures. Finally, it is worth repeating the above result that the formation number decreases with decreasing distance from the tip.

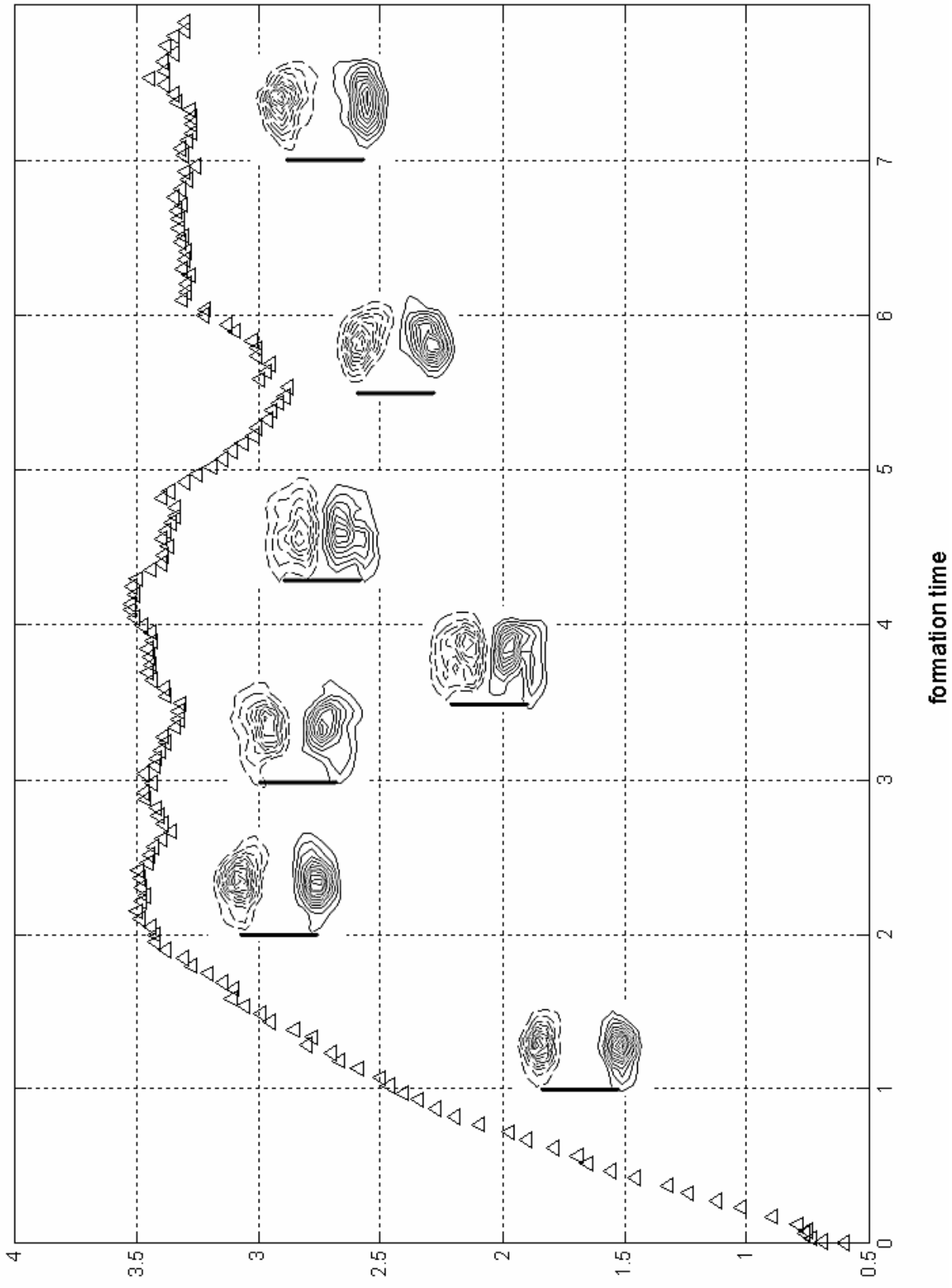

Figure 4.3.4 Circulation at $AR = 6$, 90% span, with vorticity field insets.

Recalling the drag force "hump" or maximum at $T = 5$, it seems likely to be due to the features seen in the circulation data around that time. The saturation of the 50% span LEVs and the maximum of the total circulation at 75% span occur at that time. Additionally, the circulation at 75% span falls off after $T = 5$, and there is a temporary drop in circulation at 90% span at $T = 5.5$, implying a decrease in C_D after $T = 5$. However, an explanation of the measured drag force is lacking without DPIV data in perpendicular (spanwise) planes, and 2-D and 3-D flow visualization to complete the picture. After the aspect ratio 2 case is discussed, this data will be presented in the next sections.

4.3.2 Aspect ratio 2

The total circulation at 50, 75, and 90% span for $AR = 2$ is shown in Figure 4.3.8. There are no separate curves for the LEV circulation because the LEVs do not undergo a pinch-off process similar to that at $AR = 6$, 50% span. Up until $T = 6$, the total circulation at 50% span resembles that of $AR = 6$ at 75% span over the range of $T = 0$ to 8: it increases until it reaches a maximum, then decreases and levels off. However, the maximum occurs at $T = 3.75$, rather than $T = 4.8$, and the circulation increases again after leveling off. Similarities in the flow for both cases, as will be seen below, are responsible for this qualitative agreement. There is also a likeness between the total circulation for $AR = 2$, 75% span and that of $AR = 6$, 90% span. Both increase until $T = 2$, then approximately level off, and both have local minima around $T = 5.5$. These similarities are reflected in the vorticity fields of both flows, but they end after $T = 6$, when the wake of the $AR = 2$ plate becomes very different, and the circulation increases again. Interestingly, the two pairs of cases that resemble each other are close in absolute spanwise locations when measured from the plate tip (recall that both AR plates have the same chord length). The $AR = 6$ 75% spanwise location is 3.75 in. from the

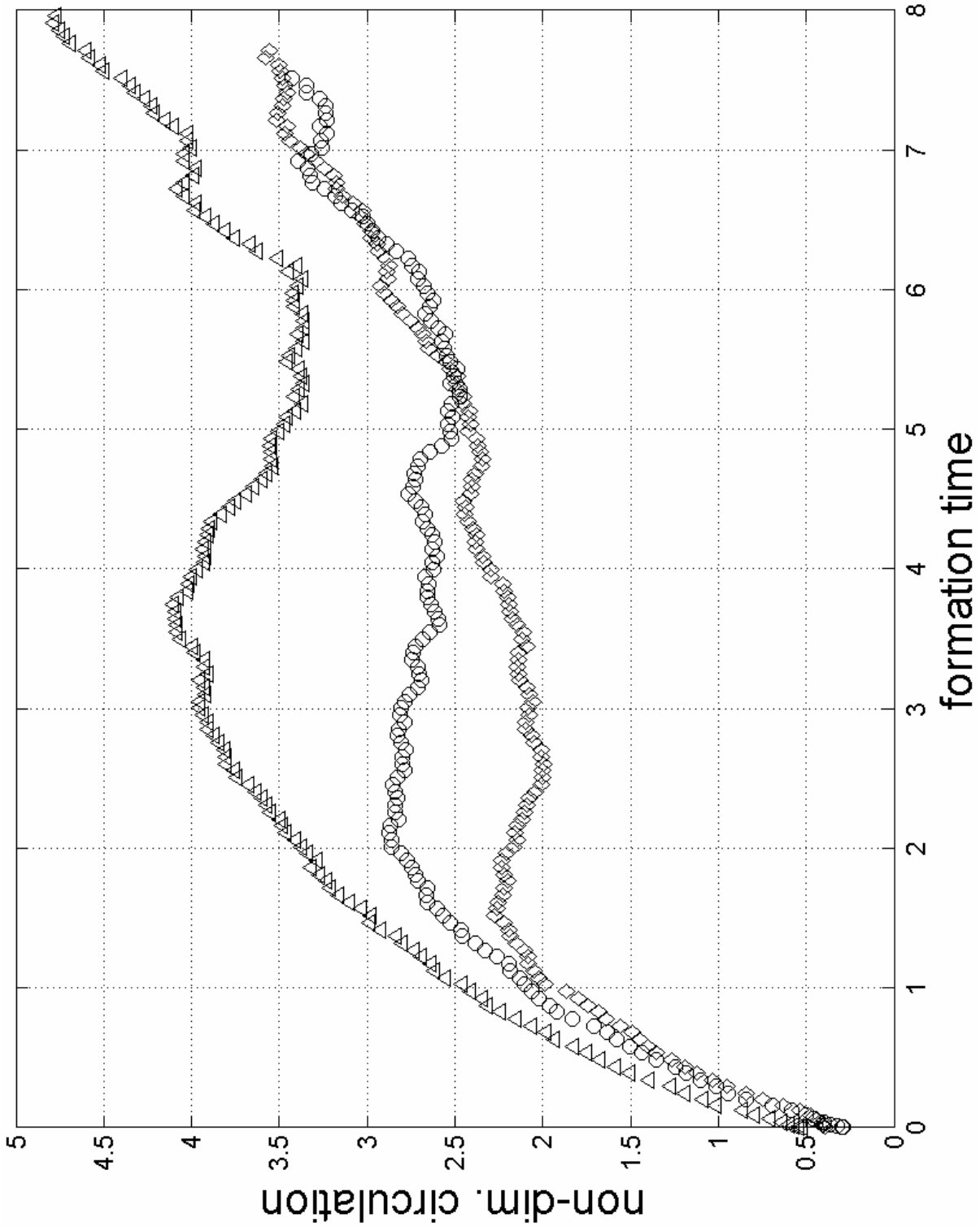

Figure 4.3.8 Circulation vs. formation time, $AR = 2$.
Triangles: total circ., 50% span; circles: total circ., 75% span;
diamonds: total circ., 90% span.

plate tip, while the $AR = 2$ 50% span location is 33% lower at 2.5 in. Ninety percent span for $AR = 6$ is 1.5 in. from the plate tip, while 75% span for $AR = 2$ is at 1.25 in. The circulation for $AR = 2$, 90% span, however, does not have a close parallel to any of the $AR = 6$ cases. It rises until $T = 1.5$, then decreases to a slight local minimum at $T = 2.5$, and finally continues to gradually increase afterward until the end of the run. As with the discussion on $AR = 6$ above, the vorticity fields for each spanwise location will be provided next to help explain the behavior of the circulation plots, as well as elucidate their similarities and differences with the $AR = 6$ case. Finally, it should be noted that the circulation at each spanwise location for $AR = 2$ is less than that at the corresponding location for $AR = 6$. This is expected, since, given that both plates have the same chord length and move at the same velocity, the one with the greater span generates stronger vortices at its leading edges.

Figure 4.3.9 shows the total circulation at 50% span for $AR = 2$, along with insets of significant vorticity field snapshots; a larger set of snapshots is given in Figure 4.3.12. Until $T = 2$, the flow for this case is very similar to that of $AR = 6$, 75% span. The vorticity field at the circulation maximum at $T = 3.75$ is also very close to that at the $AR = 6$ maximum at $T = 4.8$: the LEVs for both cases are elongated, and are starting to be drawn into the wake centerline. However, no near-pinch-off around $T = 3$, as with the $AR = 6$, 75% case, occurs. This is probably due to the fact that the $AR = 2$ case is more tip-dominated, and thus less apt to exhibit primarily 2-D features (i.e., LEV pinch-off) than its $AR = 6$ counterpart. As with the $AR = 6$, 75% case, the LEVs are pulled toward the wake centerline and the base of the plate after the circulation maximum. At about $T = 4.4$, the original LEVs pinch off in the inner part of the wake, and new LEVs have formed. The circulation then flattens out to a value 17% lower than the original maximum, and, as the new LEVs grow, the pinched-off

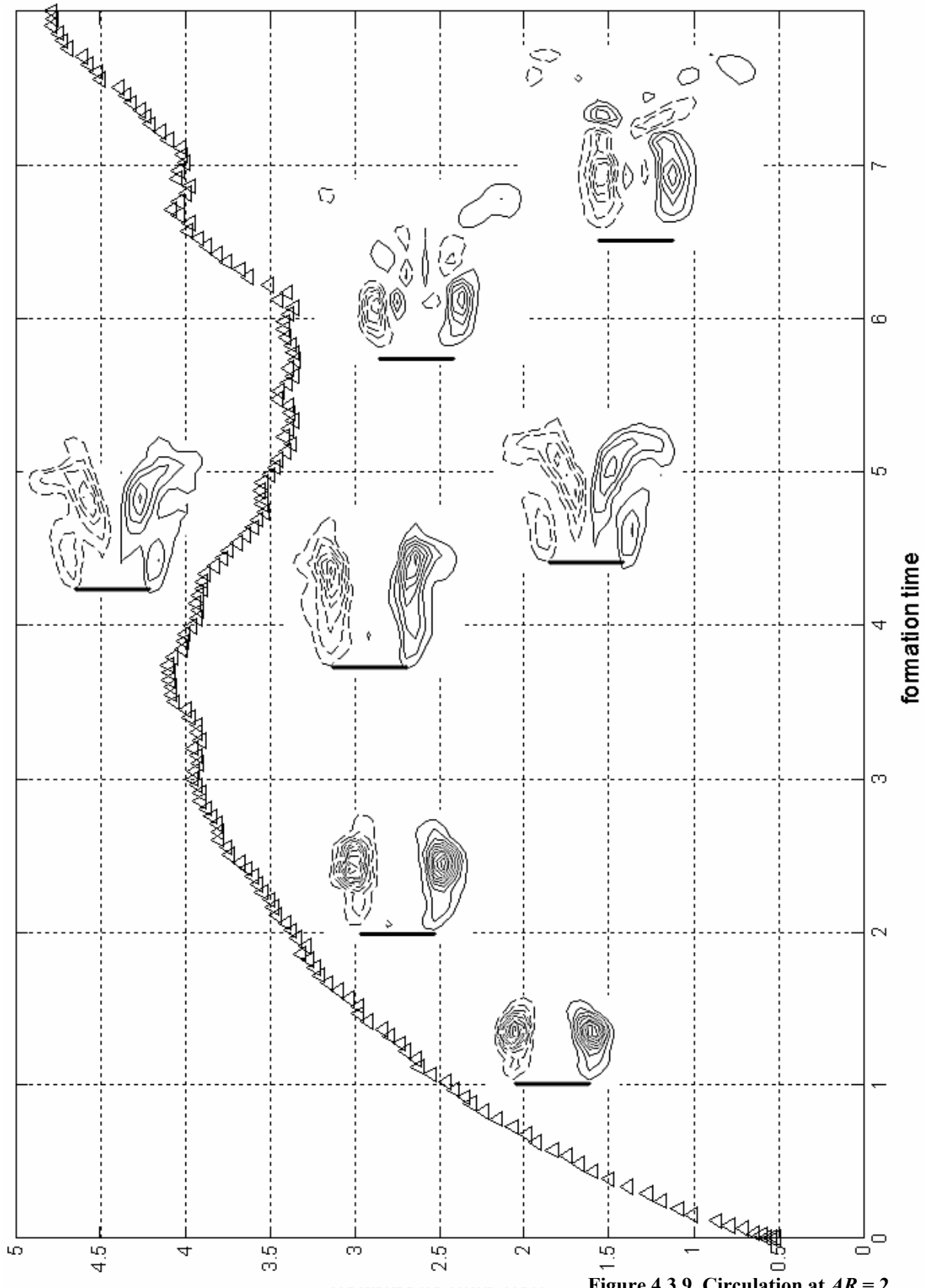

Figure 4.3.9 Circulation at $AR = 2$, 50% span, with vorticity field insets.

original LEVs in the inner wake disappear. Finally, the new LEVs then become larger and dominate, raising the circulation until it goes beyond the original maximum after $T = 7$. In the $AR = 6$ case, the original LEVs do not disappear after they pinch off, nor do new LEVs form. Instead, the wake eventually collapses into a complicated, elongated bubble, and the circulation levels off after having decreased from the maximum. The "disappearance" of the original LEVs after they inwardly pinch off is due to 3-D flow not captured in this sectional DPIV. Spanwise DPIV and flow visualization, discussed later, will shed more light on this phenomenon.

The total circulation as well as vorticity field snapshots for $AR = 2$, 75% span are given in Figure 4.3.10 (Figure 4.3.13 contains a larger collection of snapshots). Just like the $AR = 6$, 90% span case, two symmetrical LEVs form at the startup, and the circulation grows and saturates at $T = 2$. The circulation then decreases very gradually, and, by $T = 3.2$, the LEVs are drawn in toward the wake centerline so that the overall wake is more compact and full, becoming a recirculating bubble after $T = 4$. A similar phenomenon occurs around the same formation time for $AR = 6$, 90% span. Around $T = 5.3$ there is a small, local minimum in the circulation. This corresponds to a deformation in the 2 LEVs, which appear as if their leeward portions are being pinched together. At the same minimum for $AR = 6$, 90% span, the LEVs actually become more compact and stand off farther from the plate, essentially remaining that way until the end of their run. The $AR = 2$ wake, however becomes more complicated, and the circulation rises again after the minimum. By $T = 6.7$, the LEVs have become disorganized into mitten-like structures with the "thumbs" pointing rearward. The flow phenomena after $T = 5$ are probably related to that observed at the same formation time

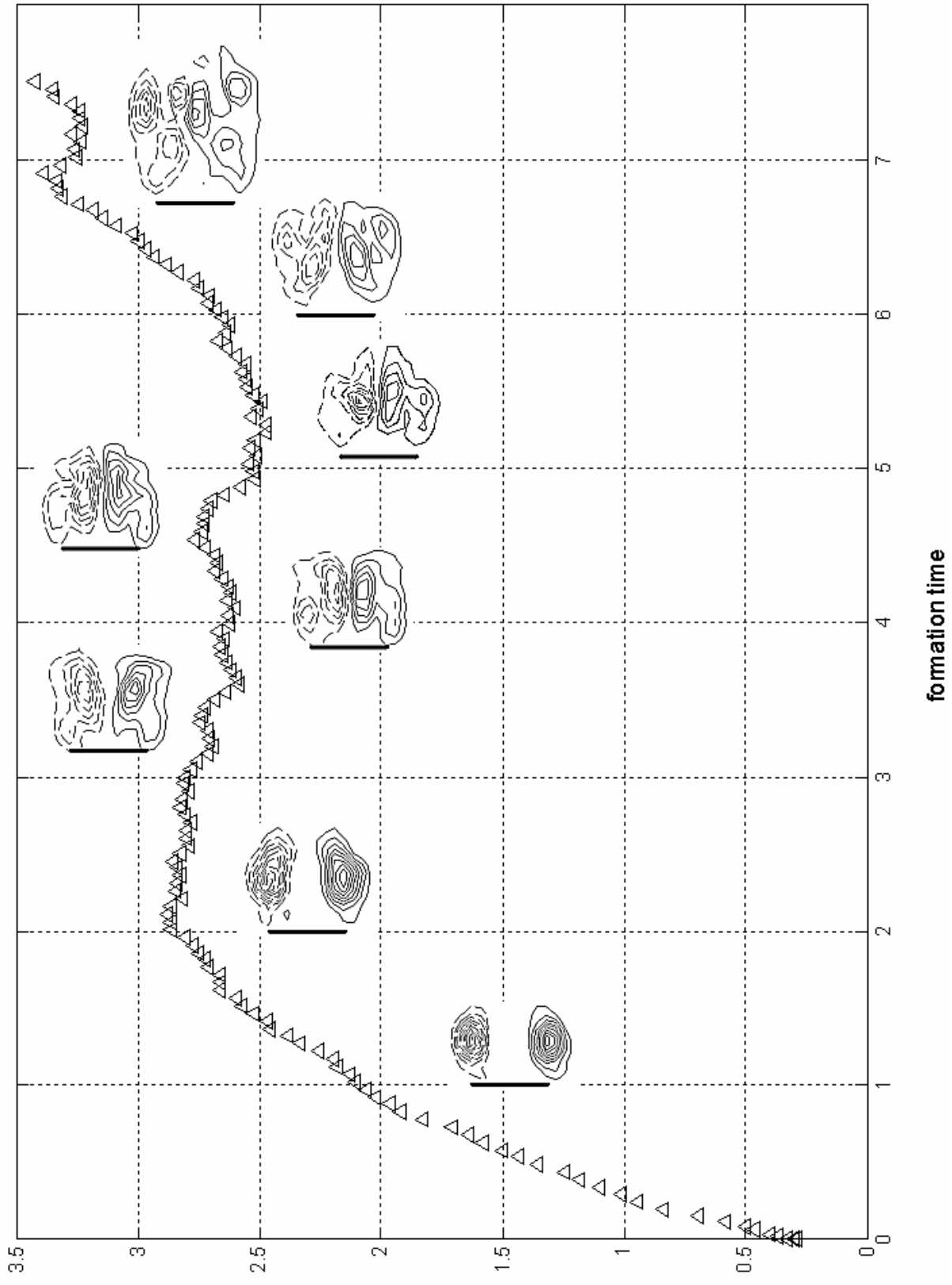

Figure 4.3.10 Circulation at $AR = 2$, 75% span, with vorticity field insets.

at 50% span. The vertical DPIV and dye flow visualization discussed below will help connect the two data sets.

Finally, the total circulation at 90% span is given in Figure 4.3.11, along with the usual vorticity field snapshots; the extended set of snapshots is provided in Figure 4.3.14. As with $AR = 6$, this spanwise location has the simplest flow. In the beginning, two LEVs form and grow, and the circulation increases monotonically, much like the 75% span case. However, the rise in circulation ceases earlier at $T = 1.5$, as opposed to $T = 2$. After this circulation maximum, there is a slight local minimum around $T = 2.7$, corresponding to the LEVs becoming smaller. The circulation then rises gradually throughout the rest of the run, except for another small minimum at $T = 4.8$. At about $T = 4$, the LEVs have become larger and less compact, creating a wider and longer wake bubble. They momentarily stand off a bit farther from the plate at the $T = 4.8$ minimum, then they start to elongate at $T = 5.4$. Also, the positive LEV becomes larger at $T = 5.4$, introducing a slight asymmetry in the wake. The circulation increases as the LEVs elongate, which continues through the remainder of the run. Interestingly, the flow after $T = 6$ resembles that at 50% span, while the 75% span case is markedly different. Again, the vertical DPIV and flow visualization presented in the next sections will be used to help explain these results.

Defining the formation number of the initial LEVs as the formation time when their circulation saturates or reaches a maximum, for 50% span this occurs at $T = 3.75$, and for 75 and 90% span the formation numbers are 2 and 1.5, respectively. Therefore, as with $AR = 6$, the formation number for $AR = 2$ decreases as the distance from the tip decreases The formation numbers for $AR = 2$ are also less than their $AR = 6$ counterparts, implying that the flow at $AR = 2$ develops more quickly (discussed more in section 4.4). Additionally, like the

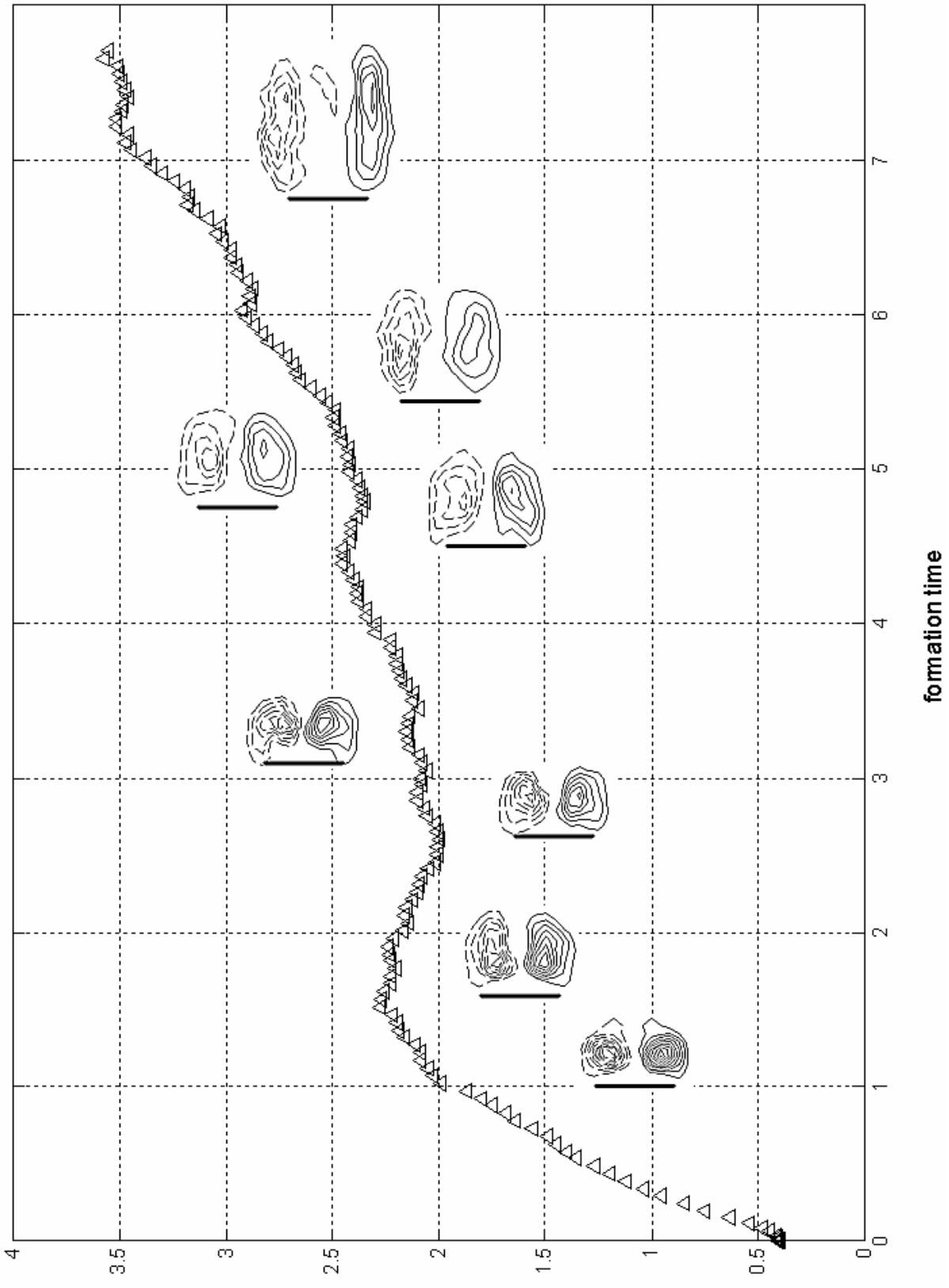

Figure 4.3.11 Circulation at $AR = 2$, 90% span, with vorticity field insets.

AR = 6 case, the total circulation becomes lower closer to the tip, although it is nearly the same for 75 and 90% span after T = 5.

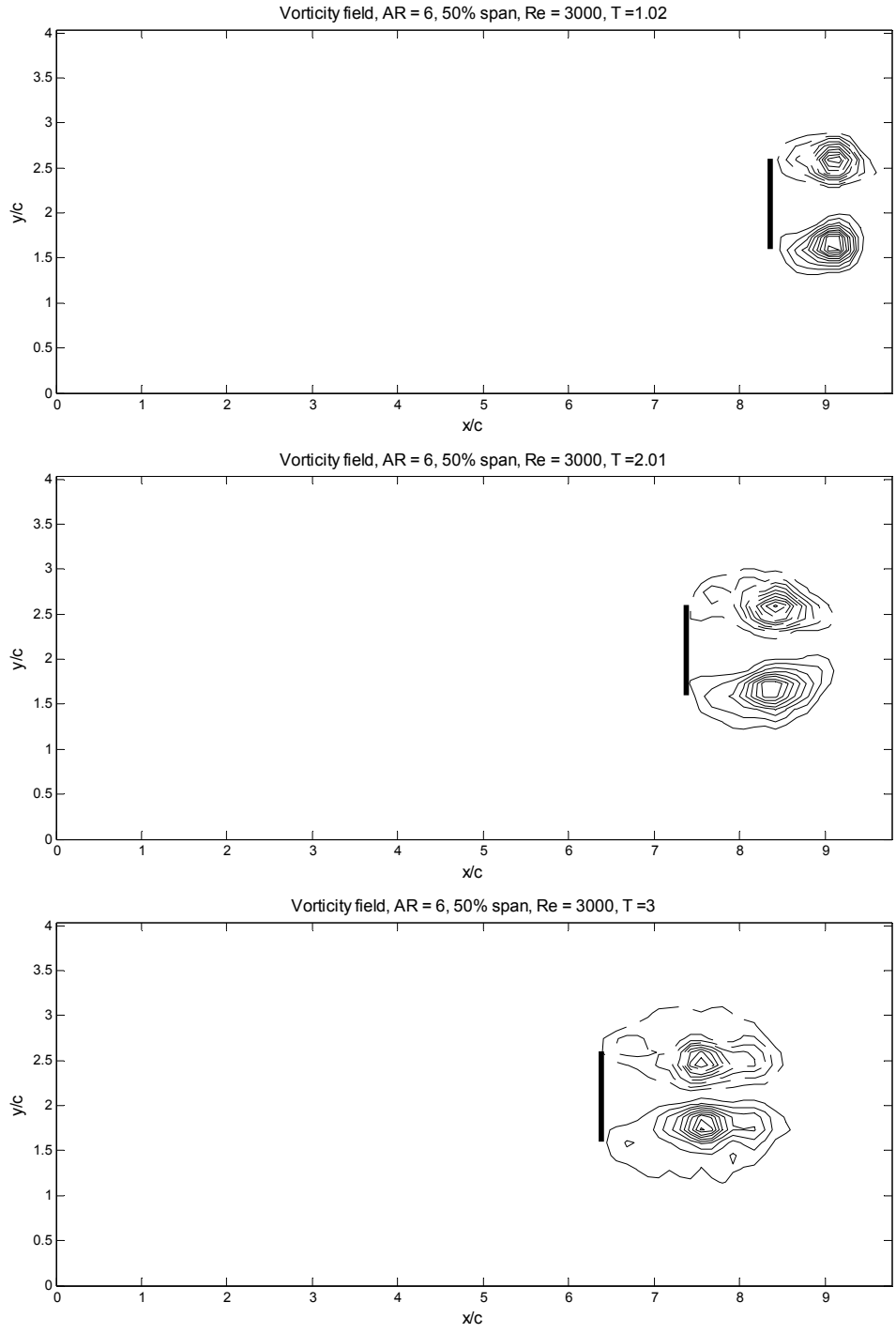

Figure 4.3.5(i) Evolution of the vorticity field for *AR* = 6, 50% span.

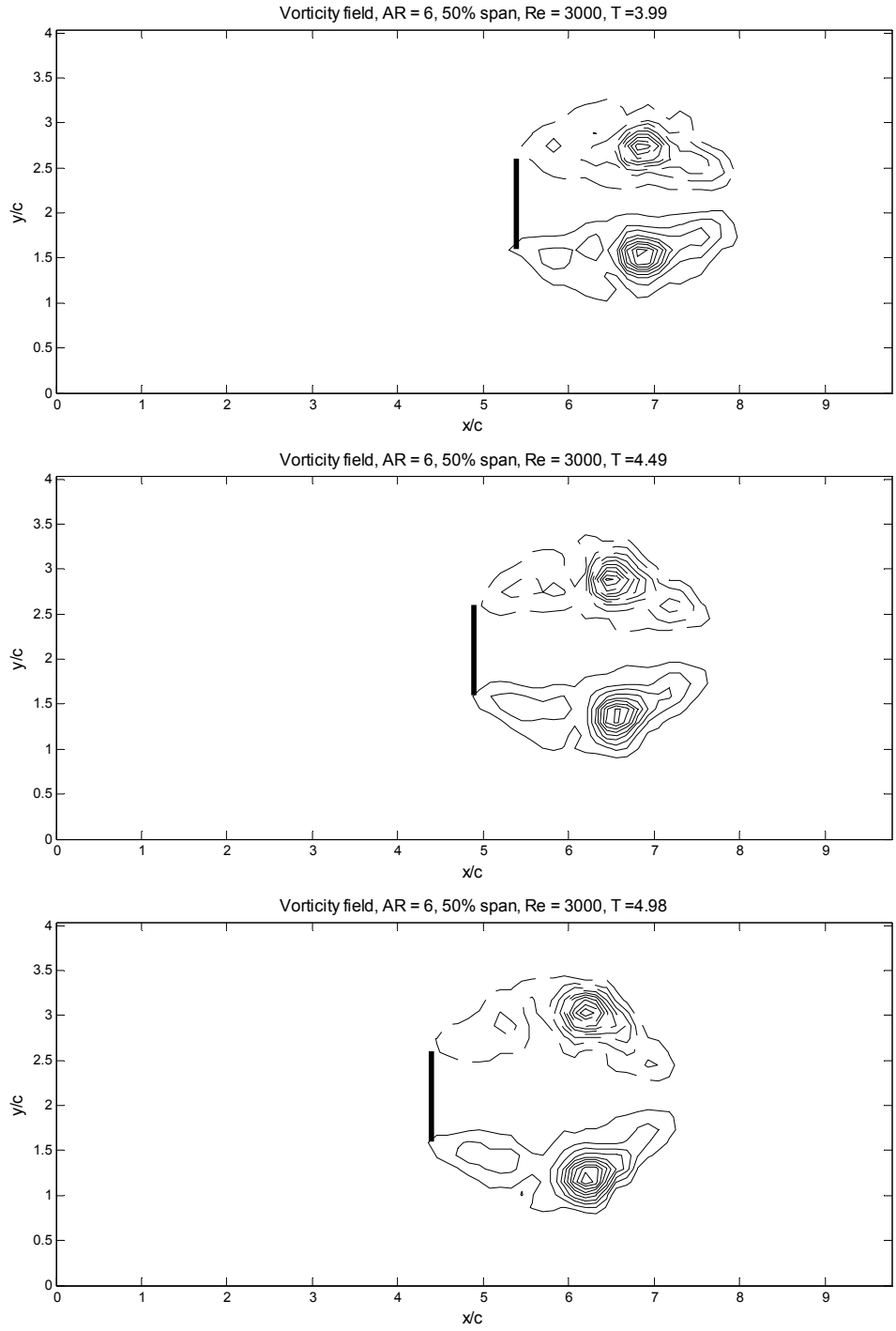

Figure 4.3.5(ii) Evolution of the vorticity field for *AR* = 6, 50% span.

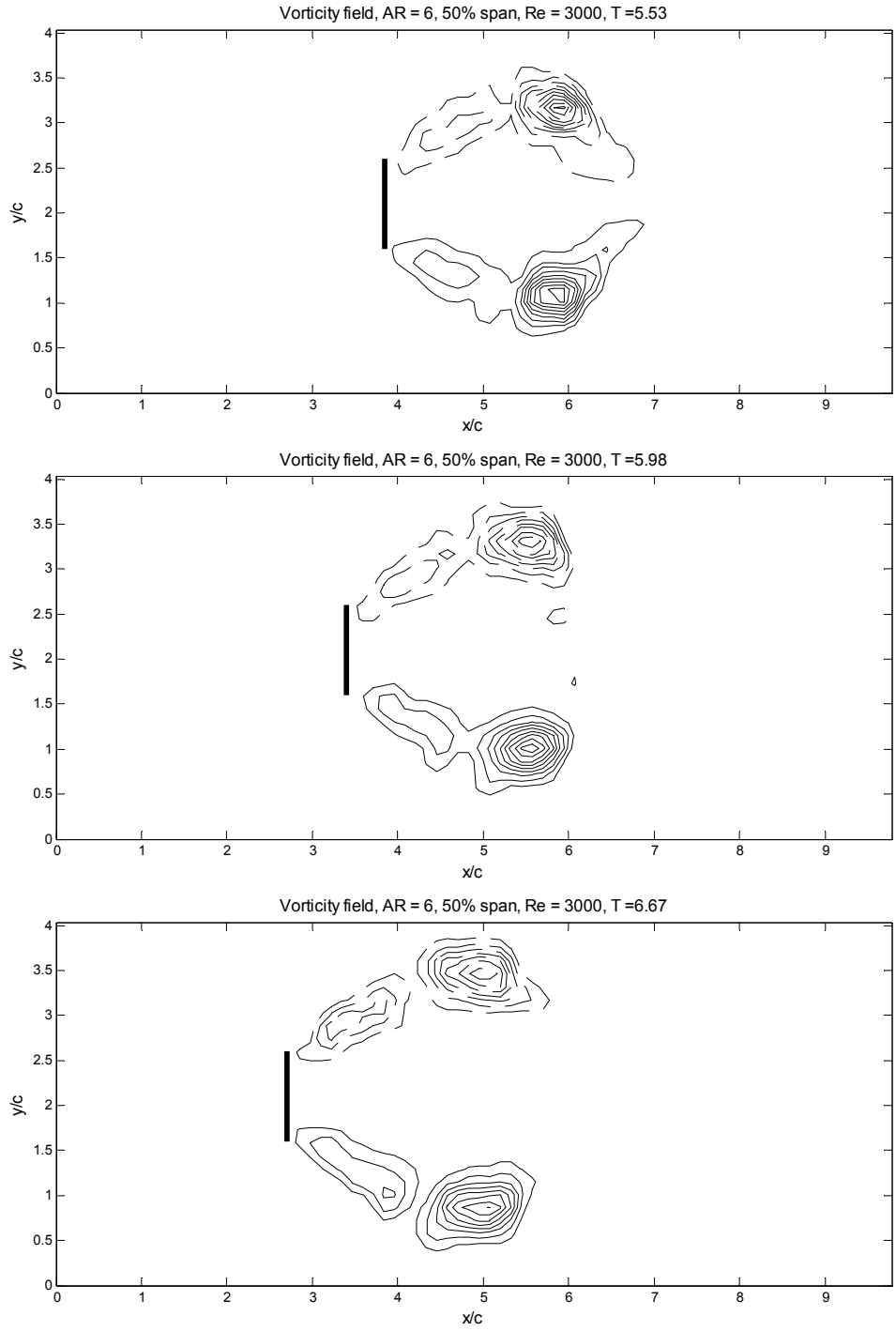

Figure 4.3.5(iii) Evolution of the vorticity field for *AR* = 6, 50% span.

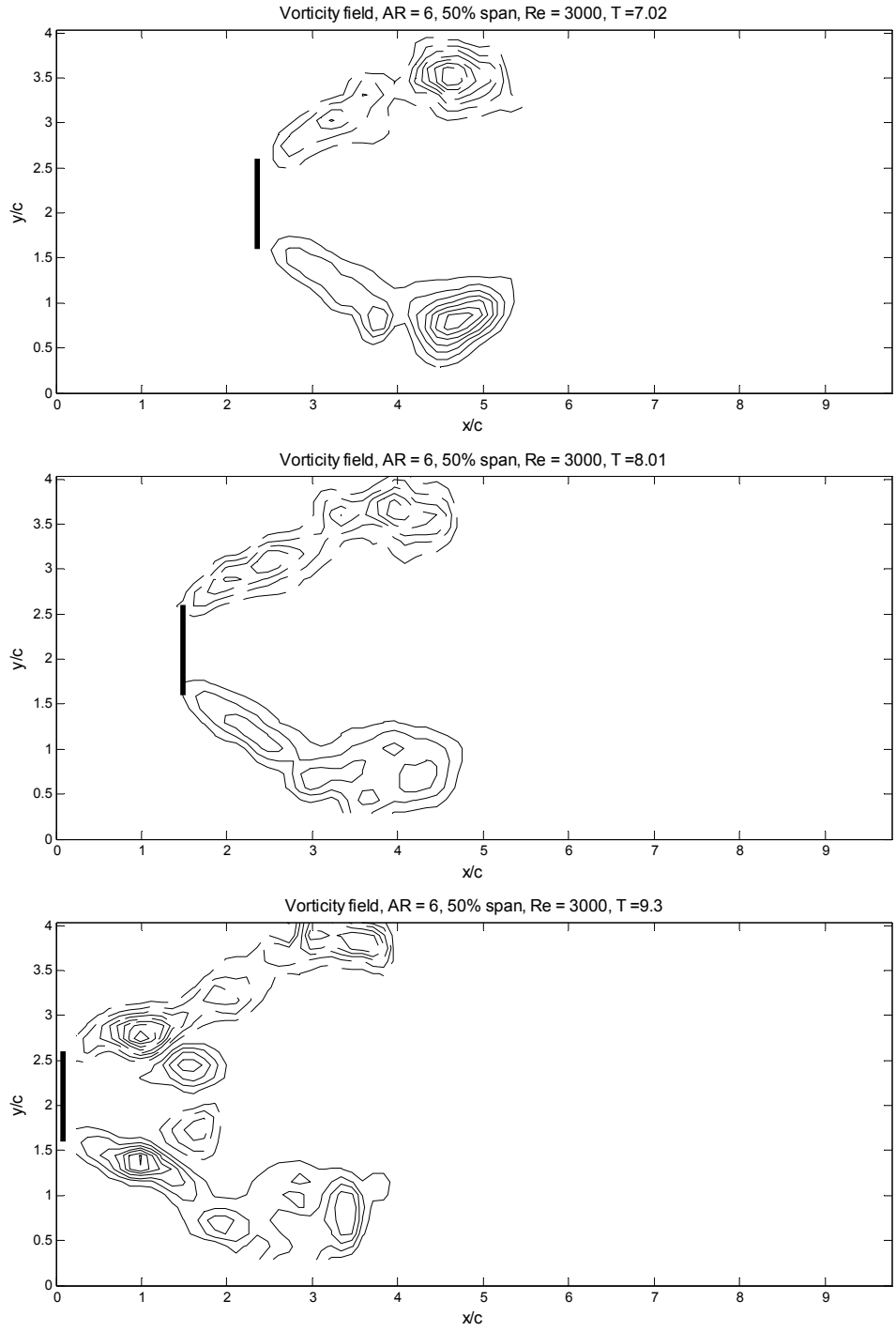

Figure 4.3.5(iv) Evolution of the vorticity field for *AR* = 6, 50% span.

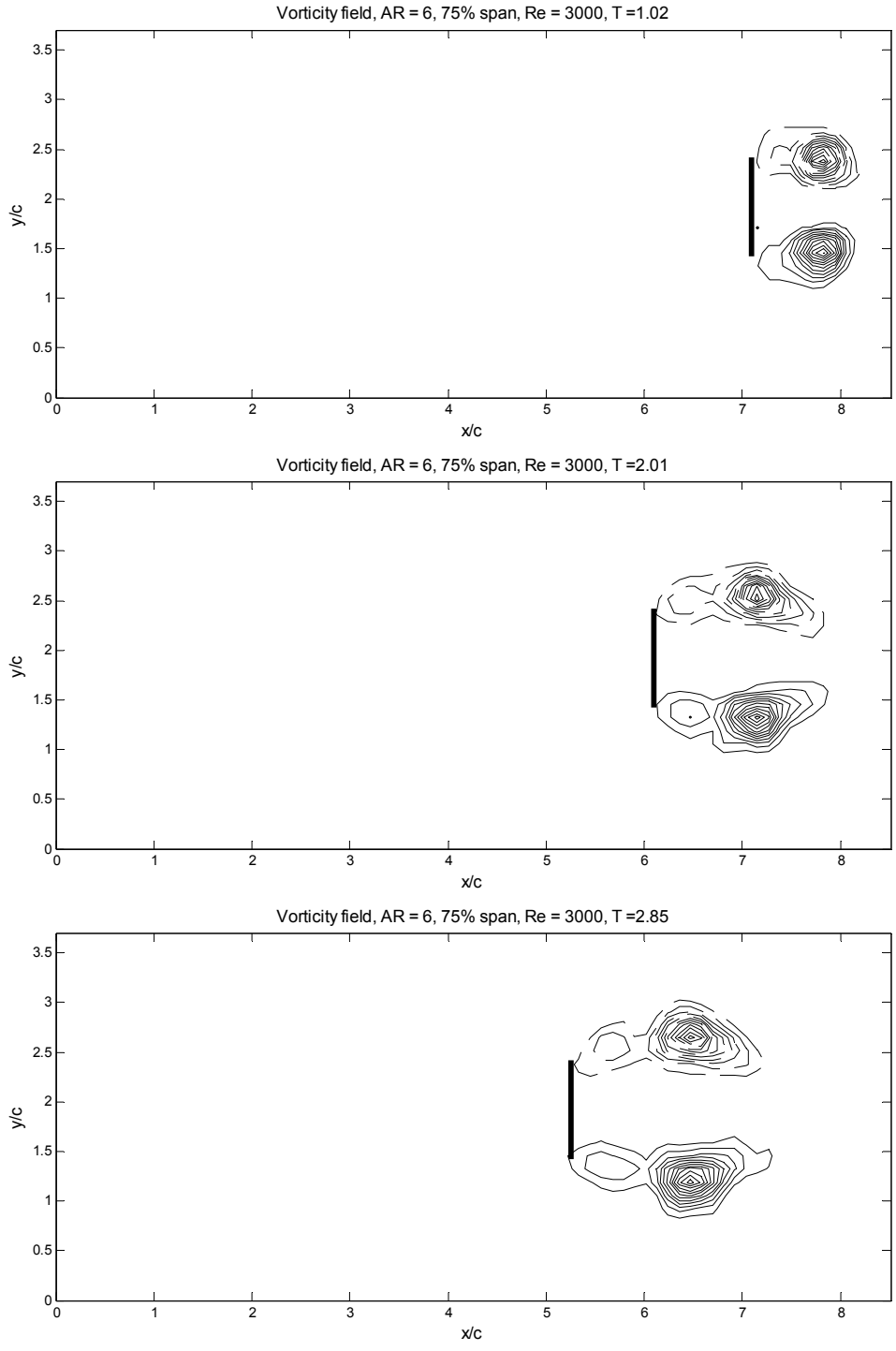

Figure 4.3.6(i) Evolution of the vorticity field for *AR* = 6, 75% span.

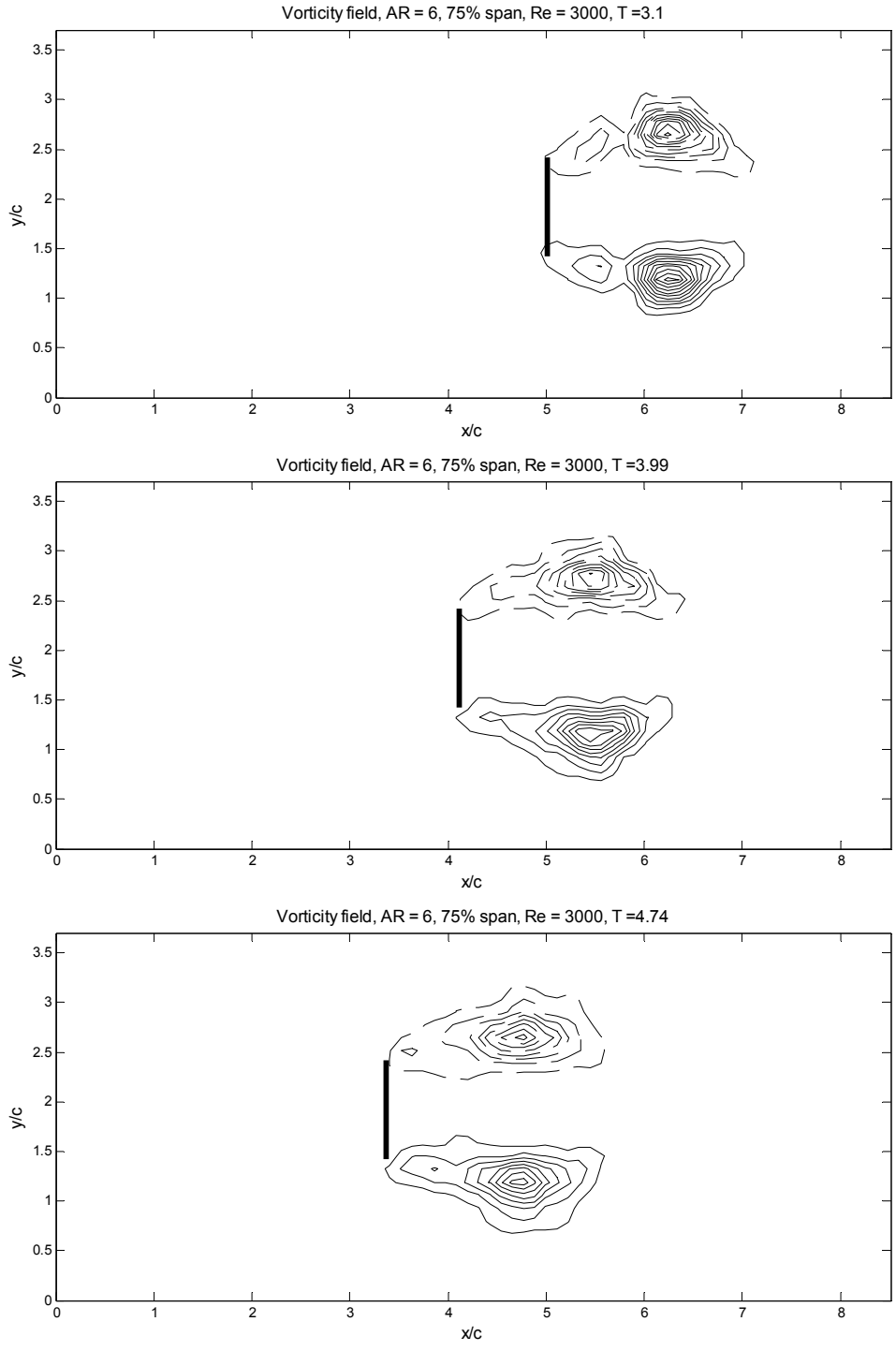

Figure 4.3.6(ii) Evolution of the vorticity field for *AR* = 6, 75% span.

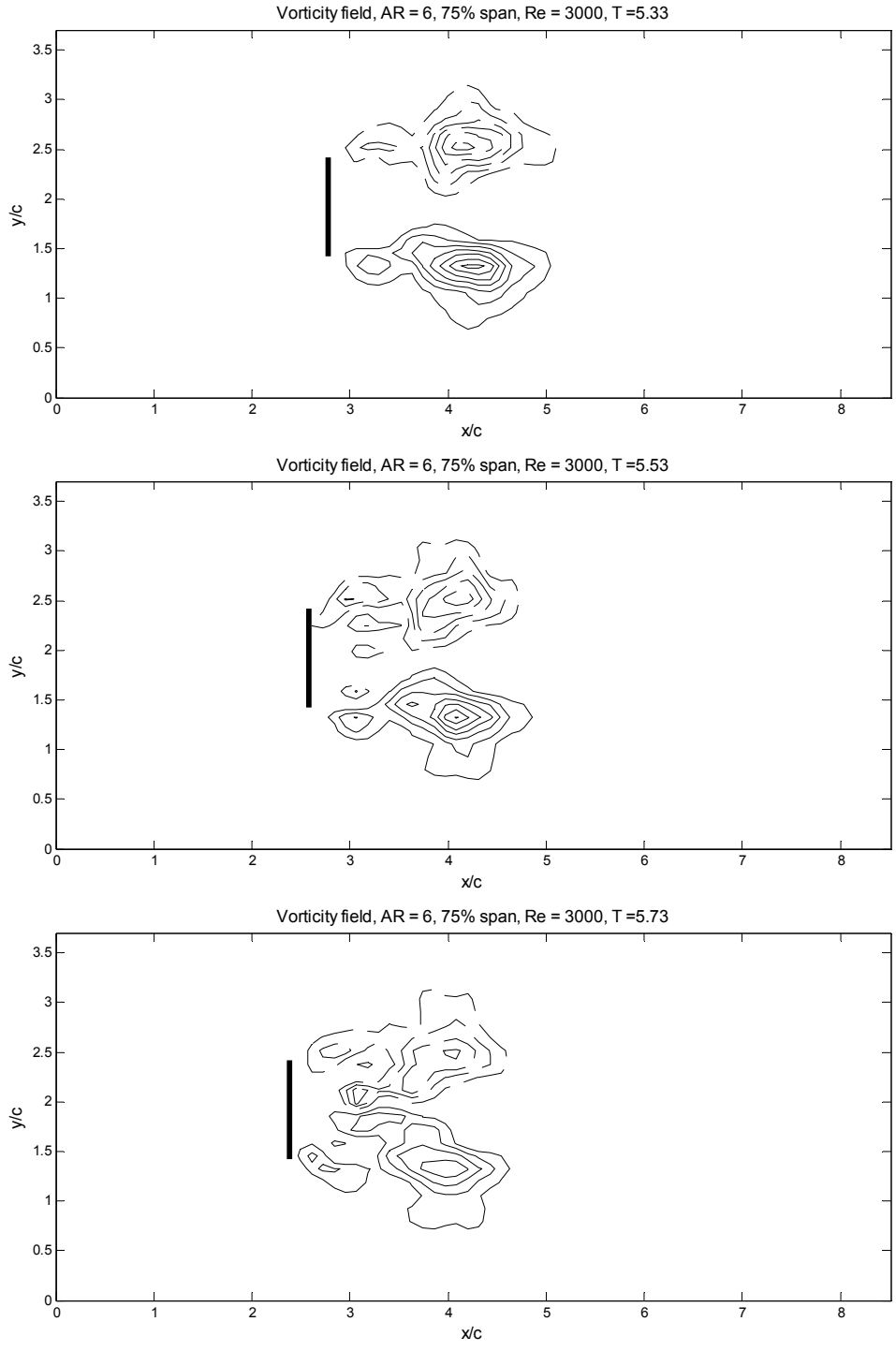

Figure 4.3.6(iii) Evolution of the vorticity field for *AR* = 6, 75% span.

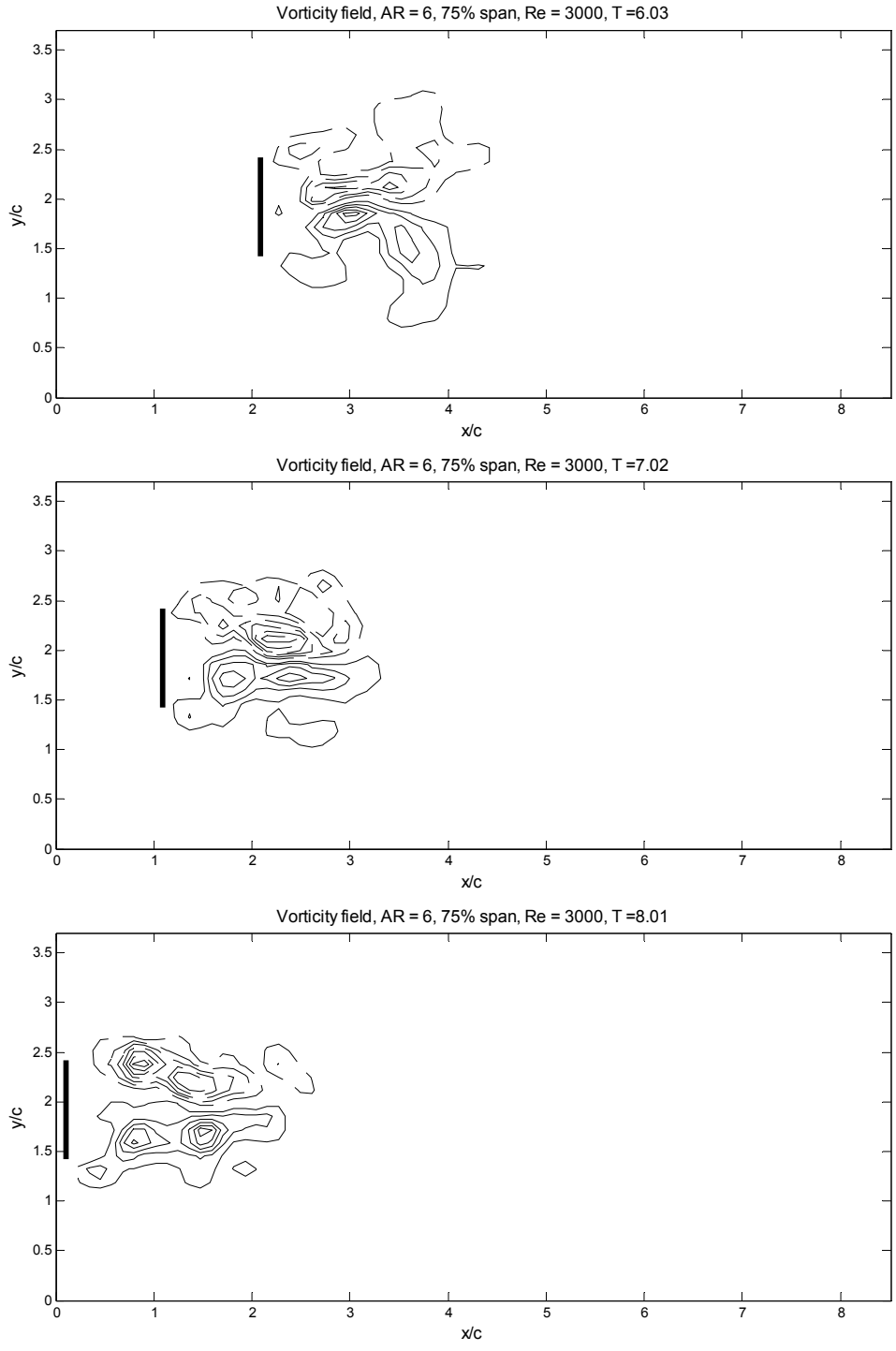

Figure 4.3.6(iv) Evolution of the vorticity field for *AR* = 6, 75% span.

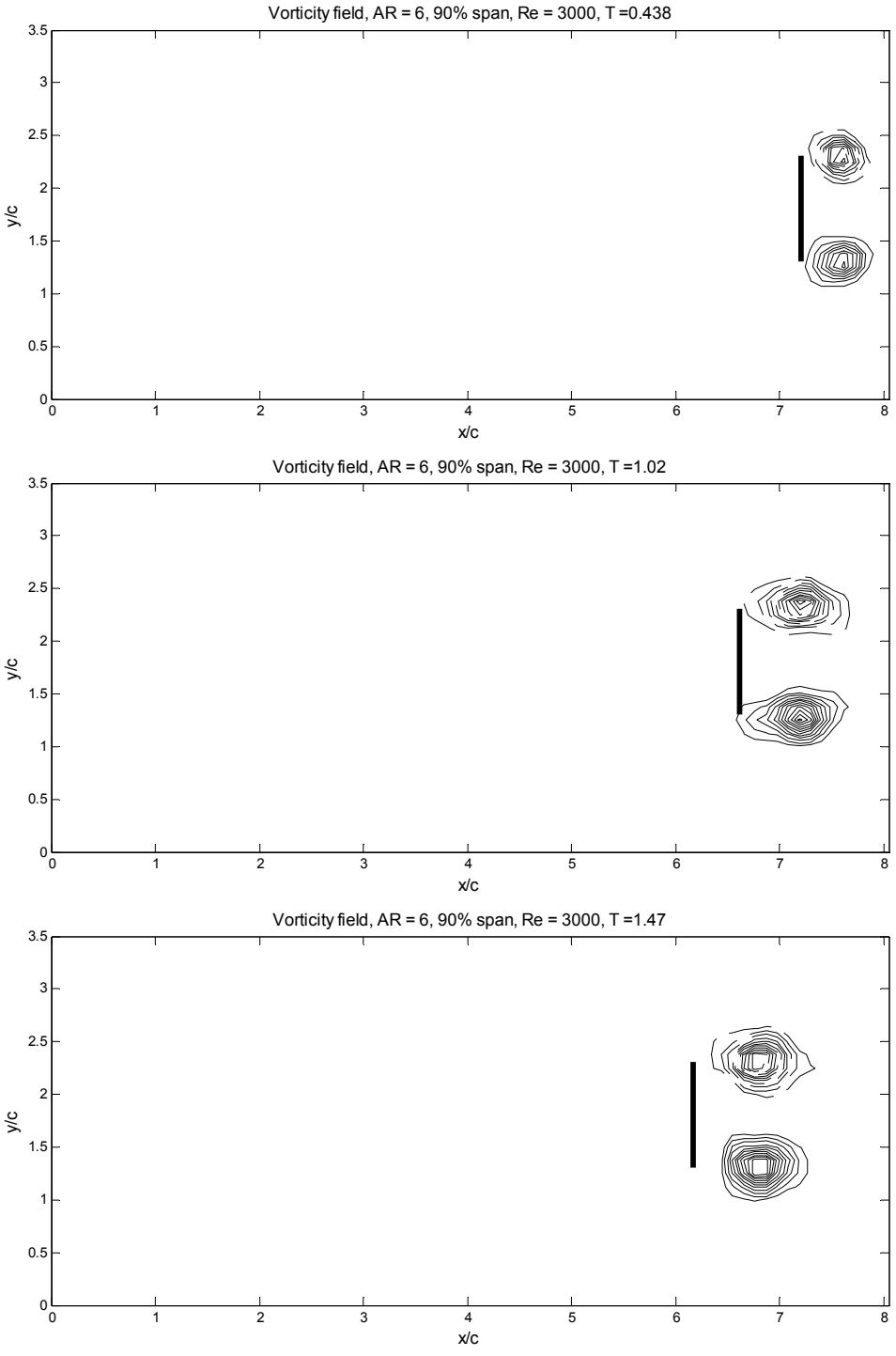

Figure 4.3.7(i) Evolution of the vorticity field for AR = 6, 90% span.

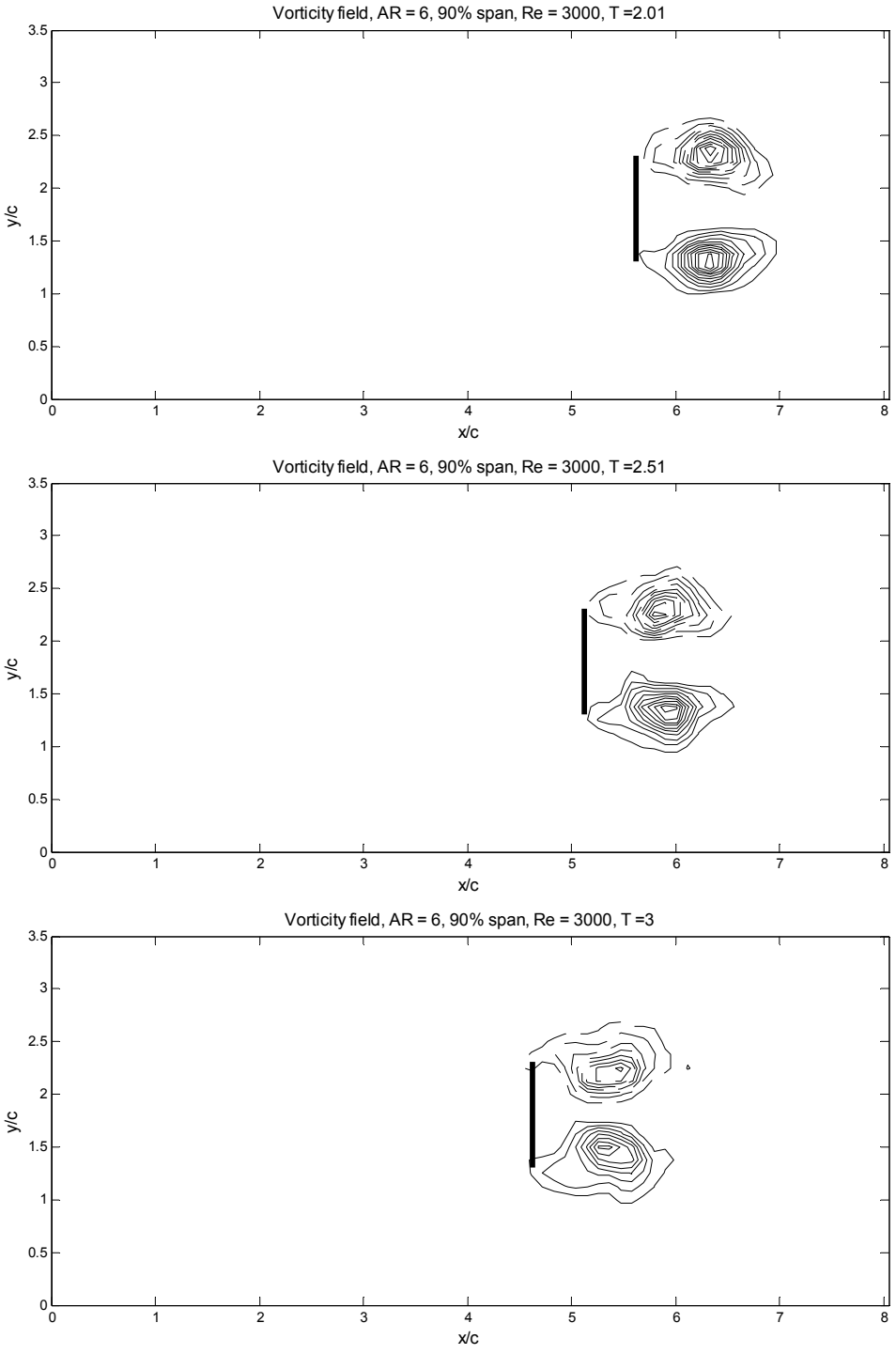

Figure 4.3.7(ii) Evolution of the vorticity field for *AR* = 6, 90% span.

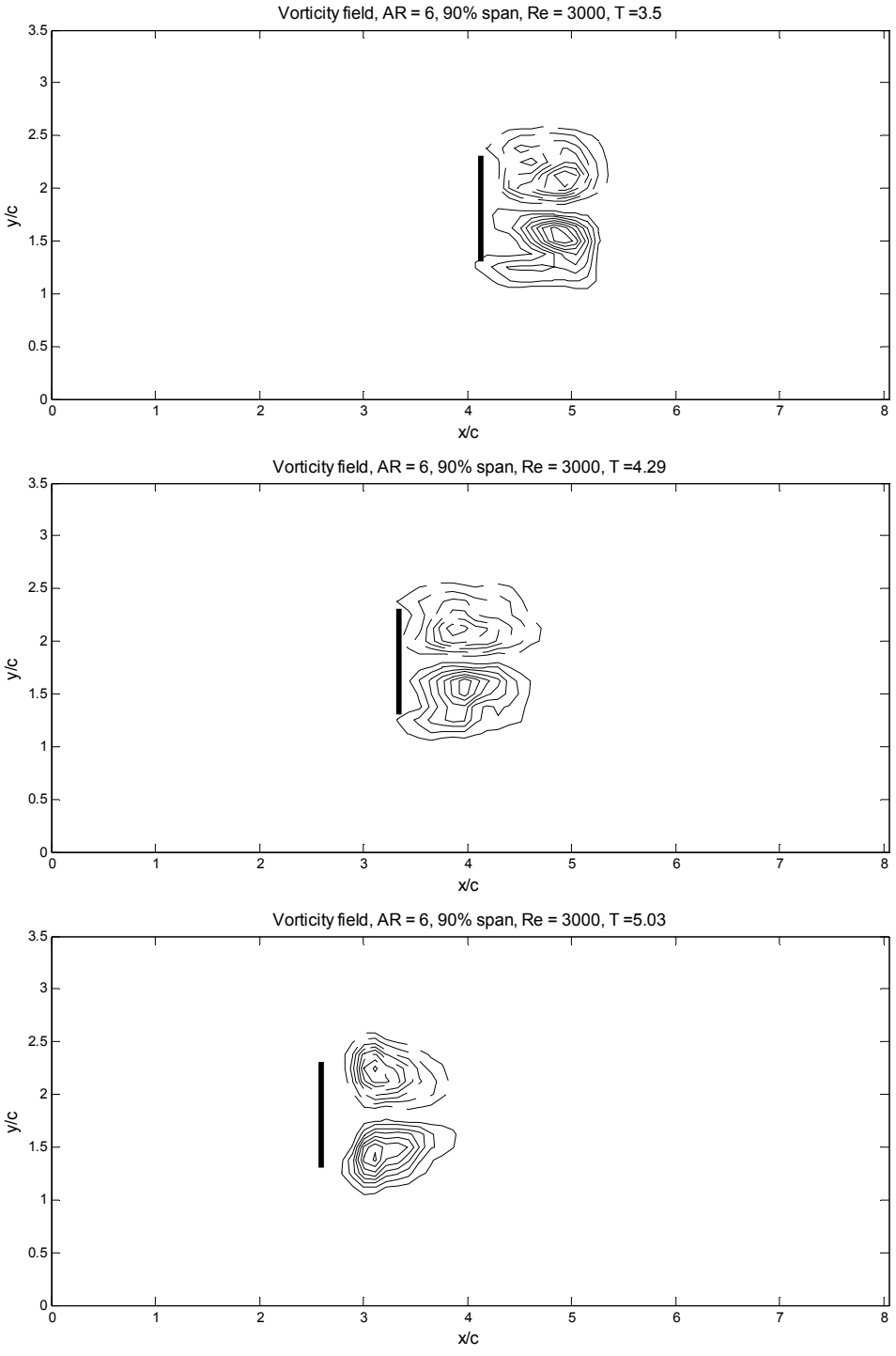

Figure 4.3.7(iii) Evolution of the vorticity field for *AR* = 6, 90% span.

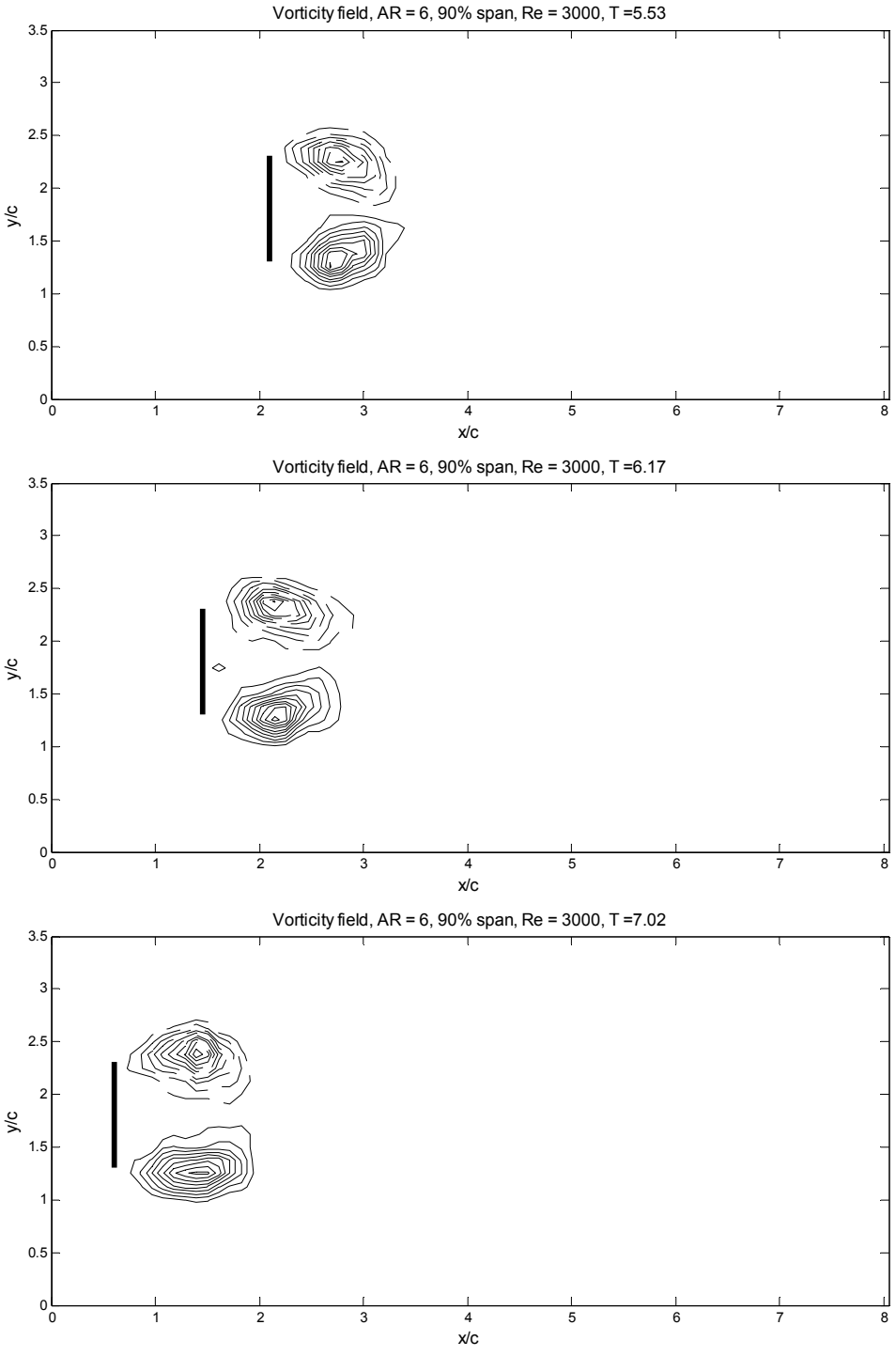

Figure 4.3.7(iv) Evolution of the vorticity field for *AR* = 6, 90% span.

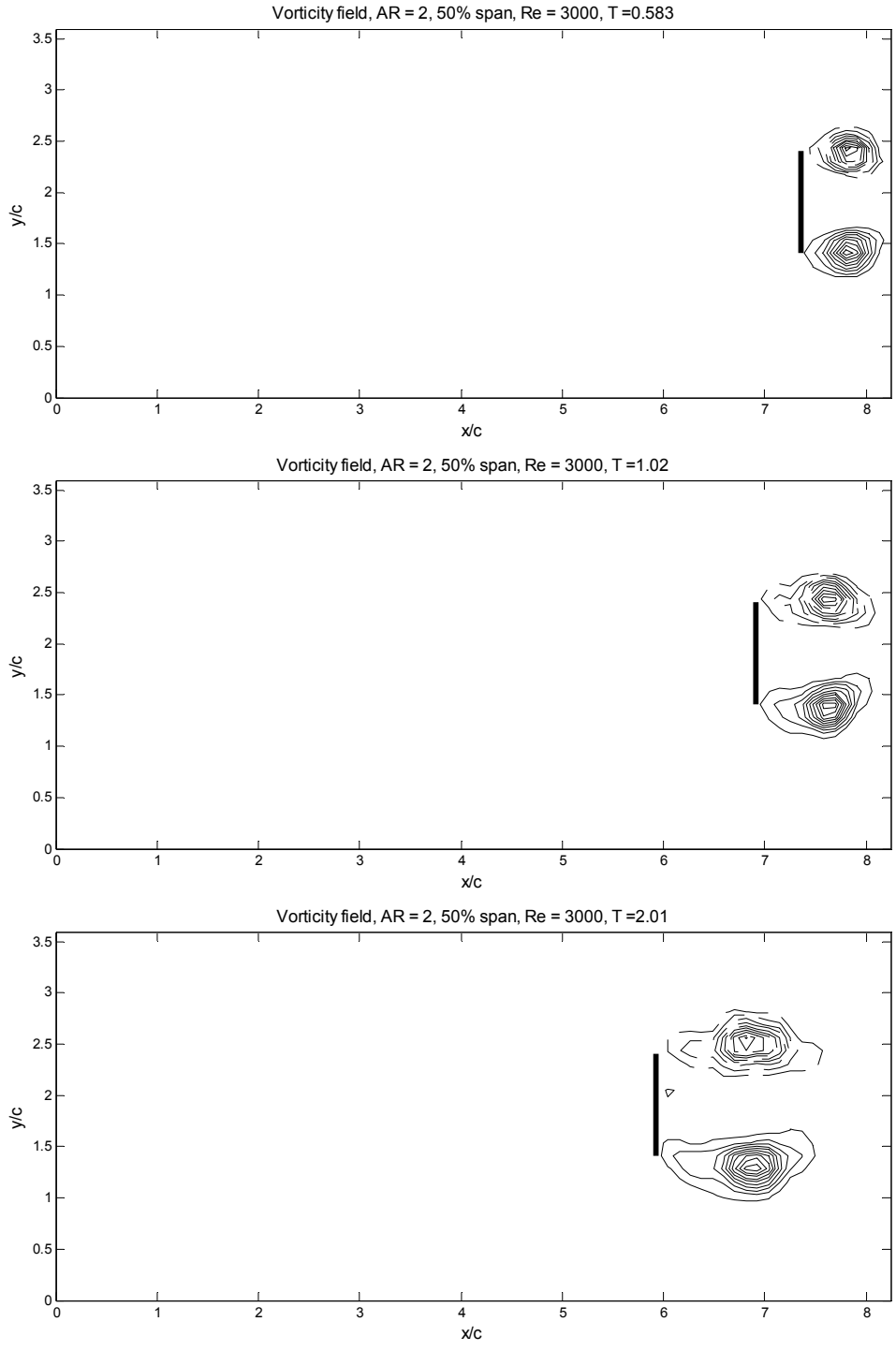

Figure 4.3.12(i) Evolution of the vorticity field for *AR* = 2, 50% span.

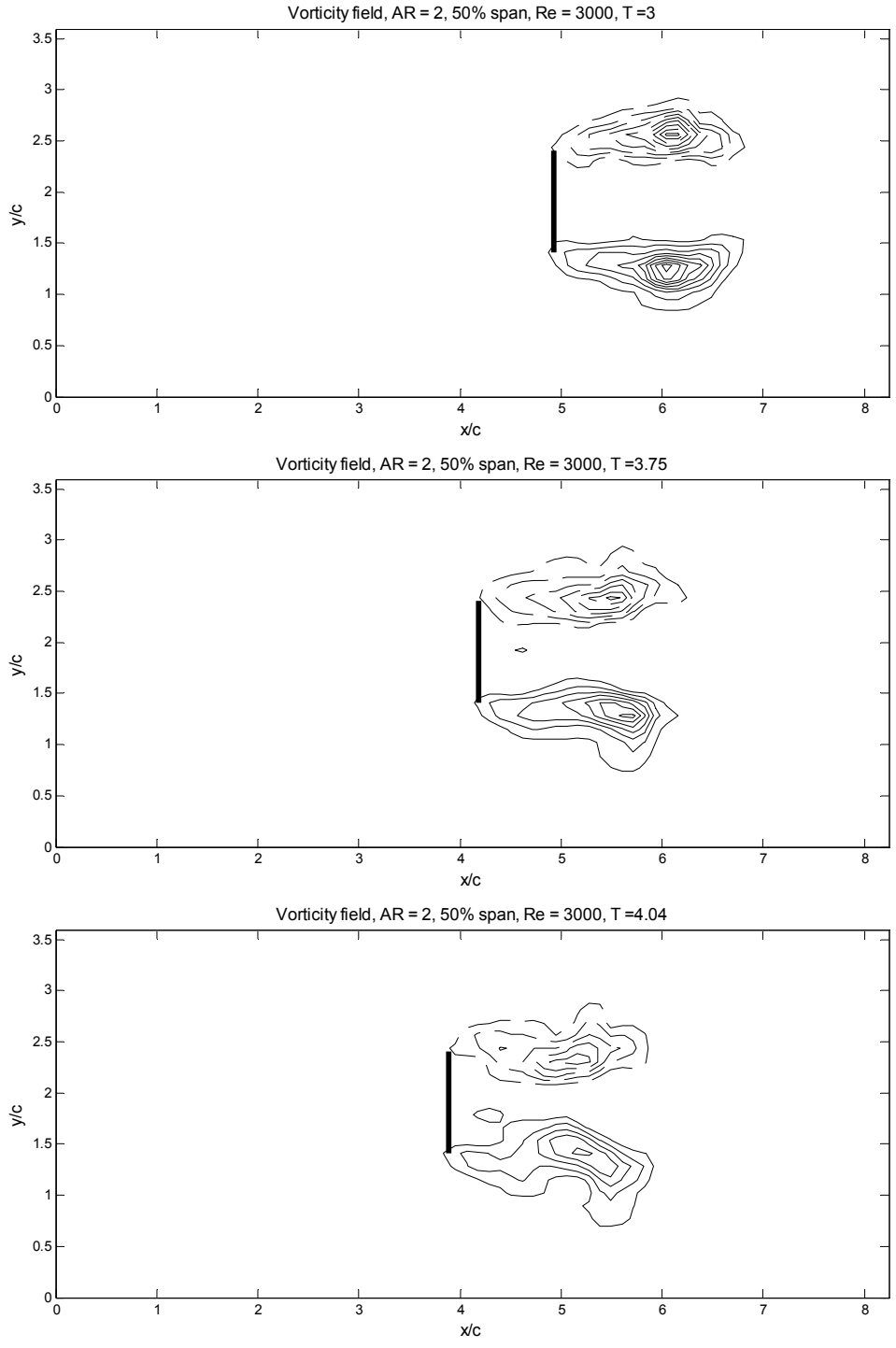

Figure 4.3.12(ii) Evolution of the vorticity field for *AR* = 2, 50% span.

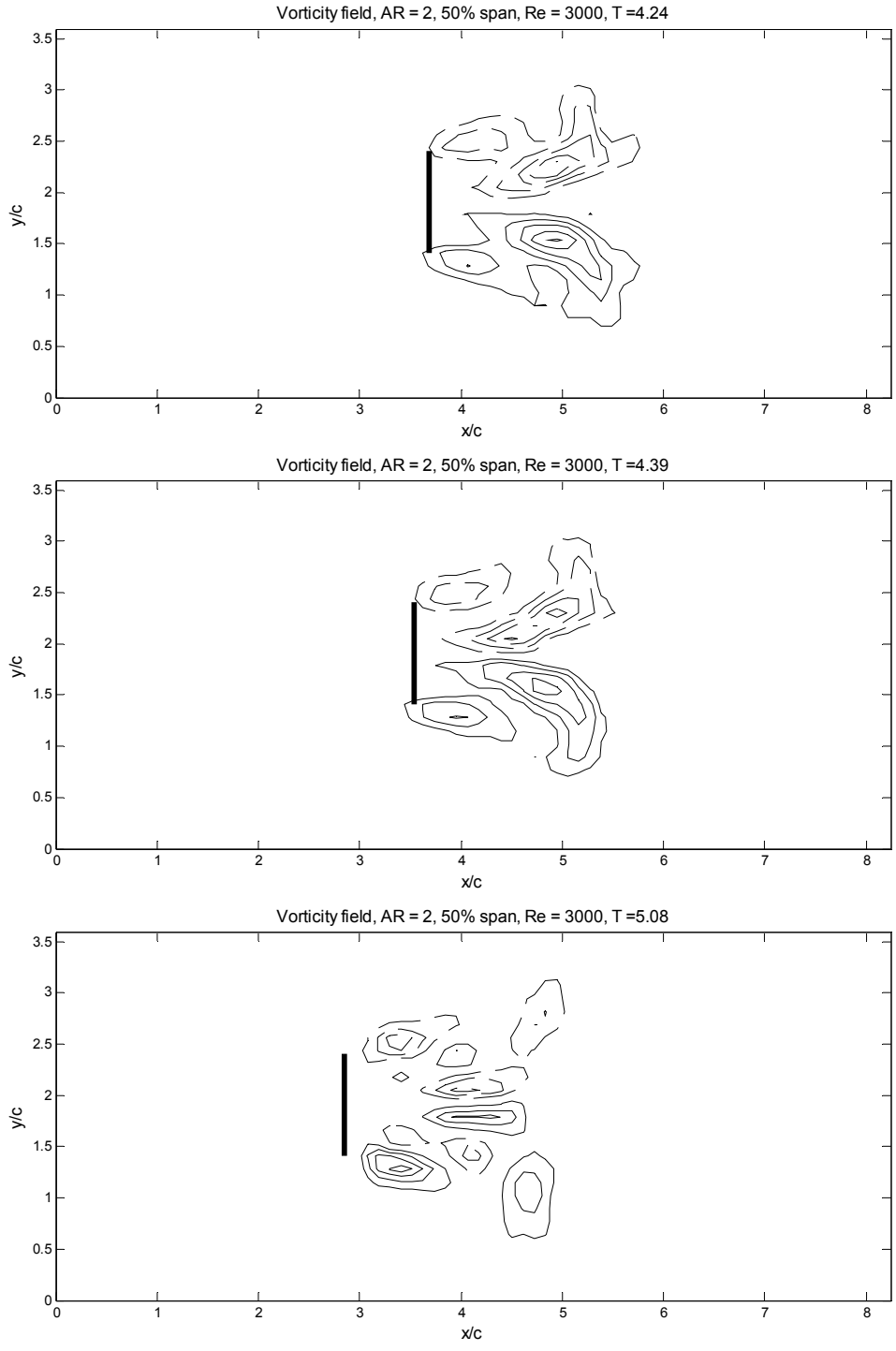

Figure 4.3.12(iii) Evolution of the vorticity field for *AR* = 2, 50% span.

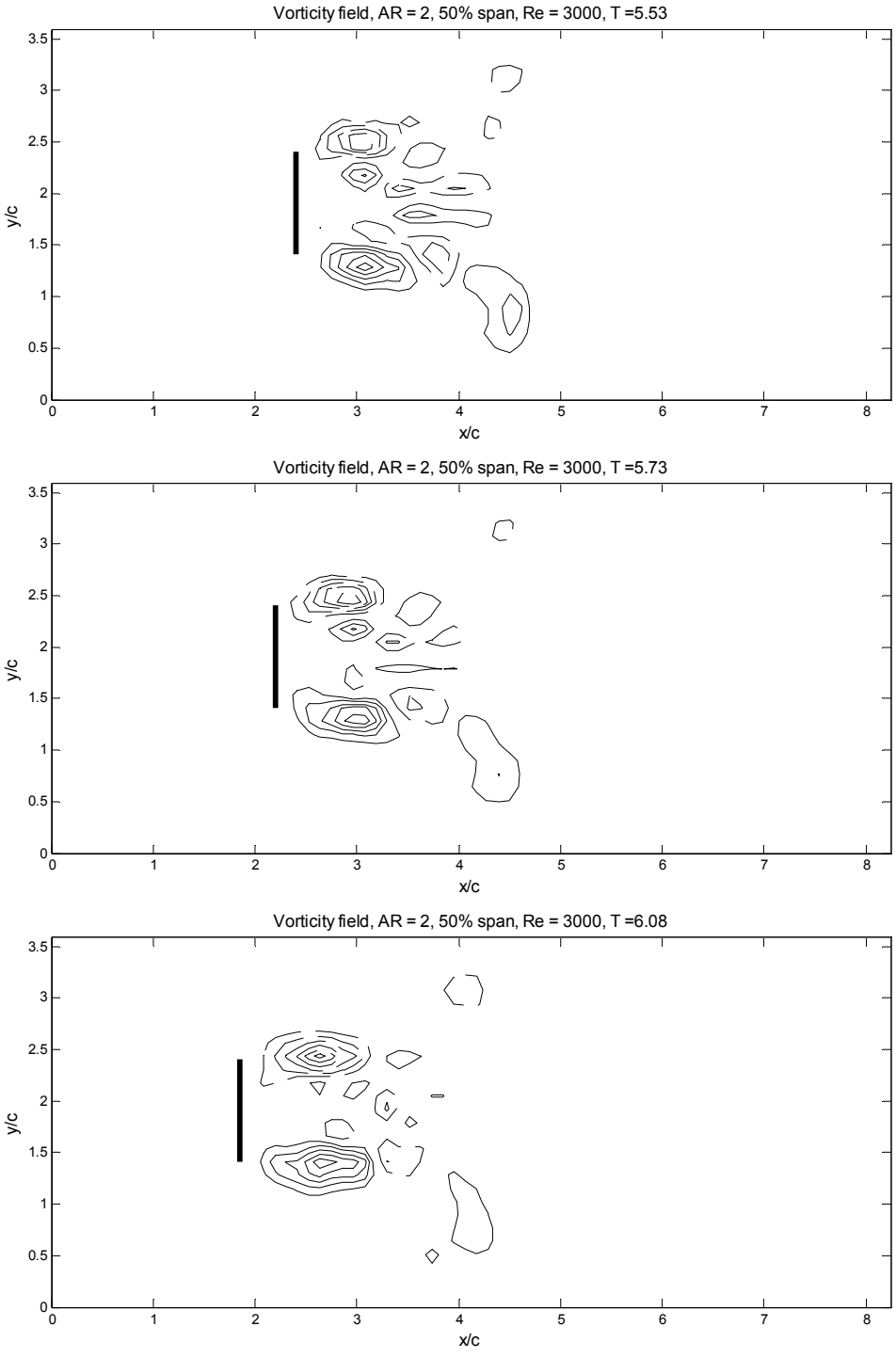

Figure 4.3.12(iv) Evolution of the vorticity field for *AR* = 2, 50% span.

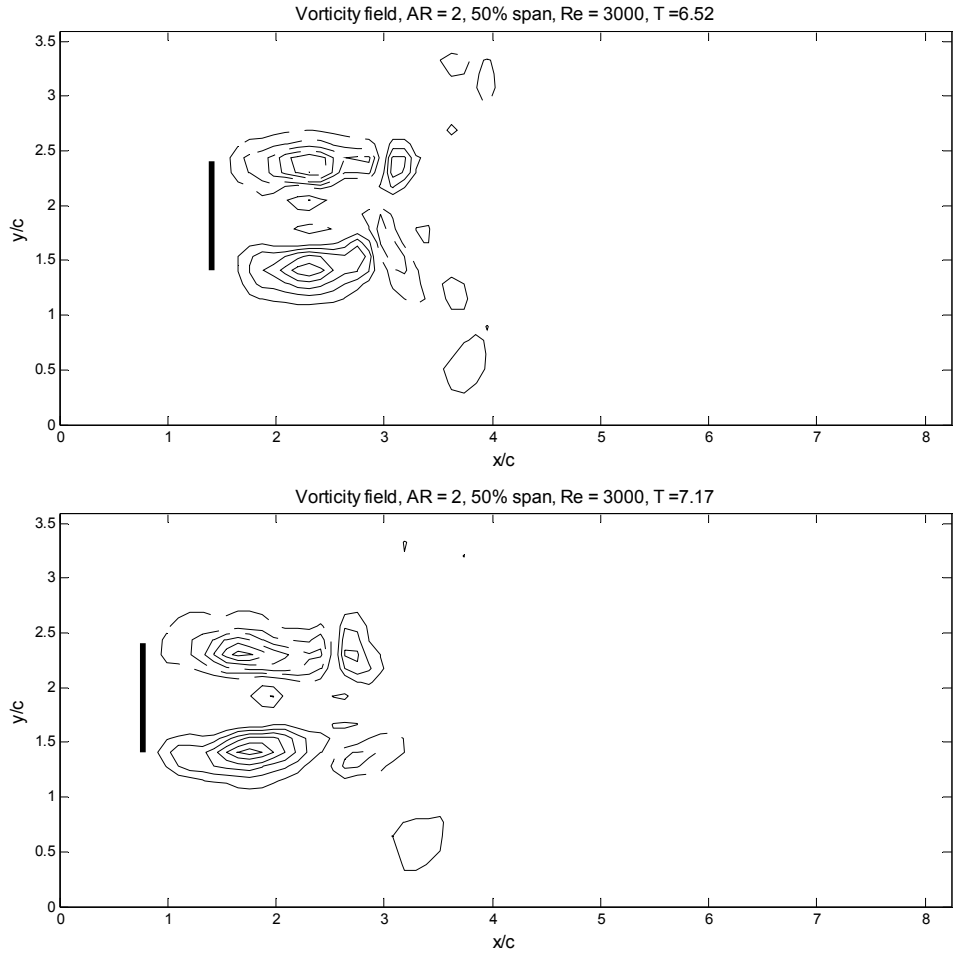

Figure 4.3.12(v) Evolution of the vorticity field for *AR* = 2, 50% span.

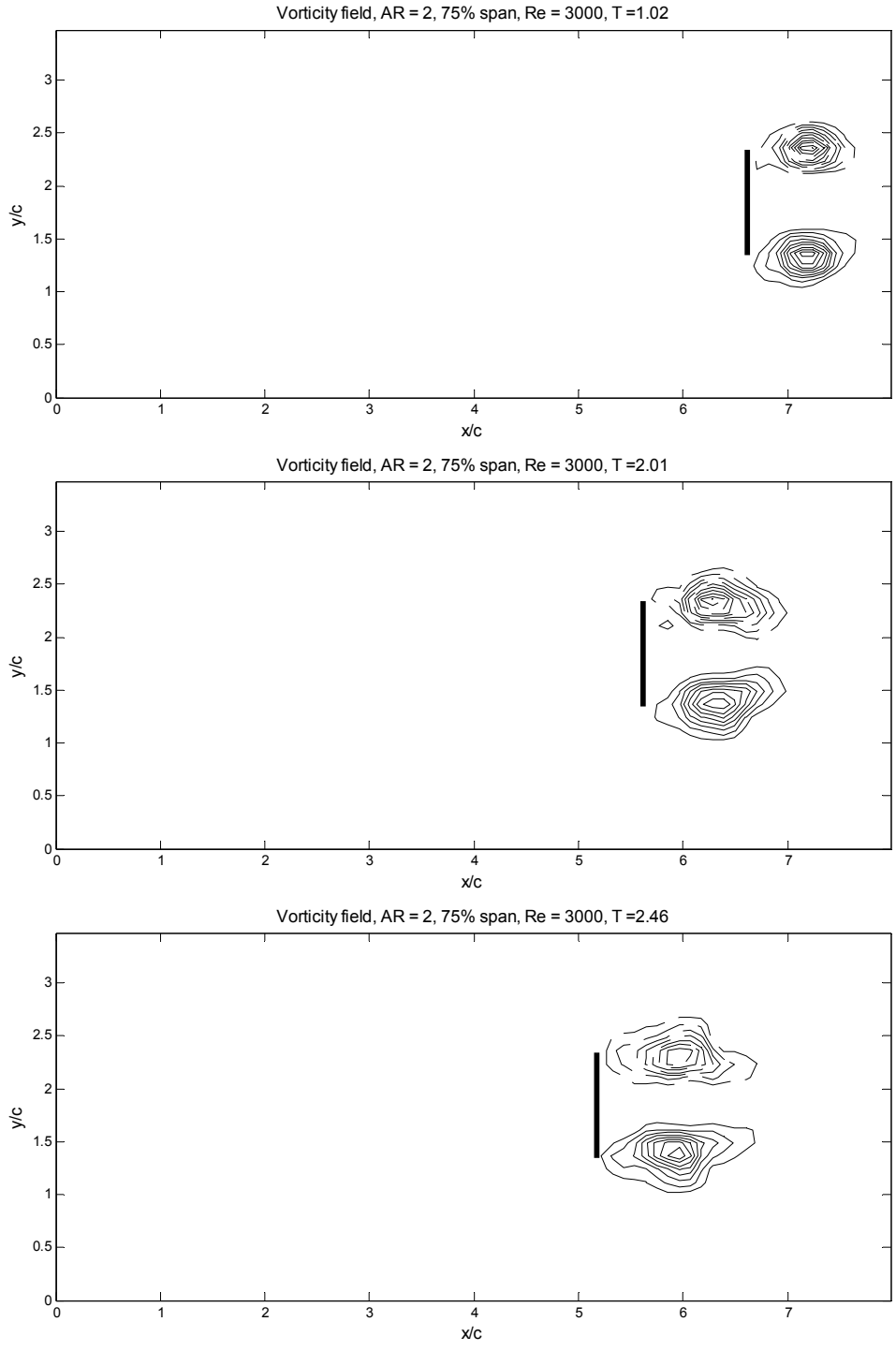

Figure 4.3.13(i) Evolution of the vorticity field for *AR* = 2, 75% span.

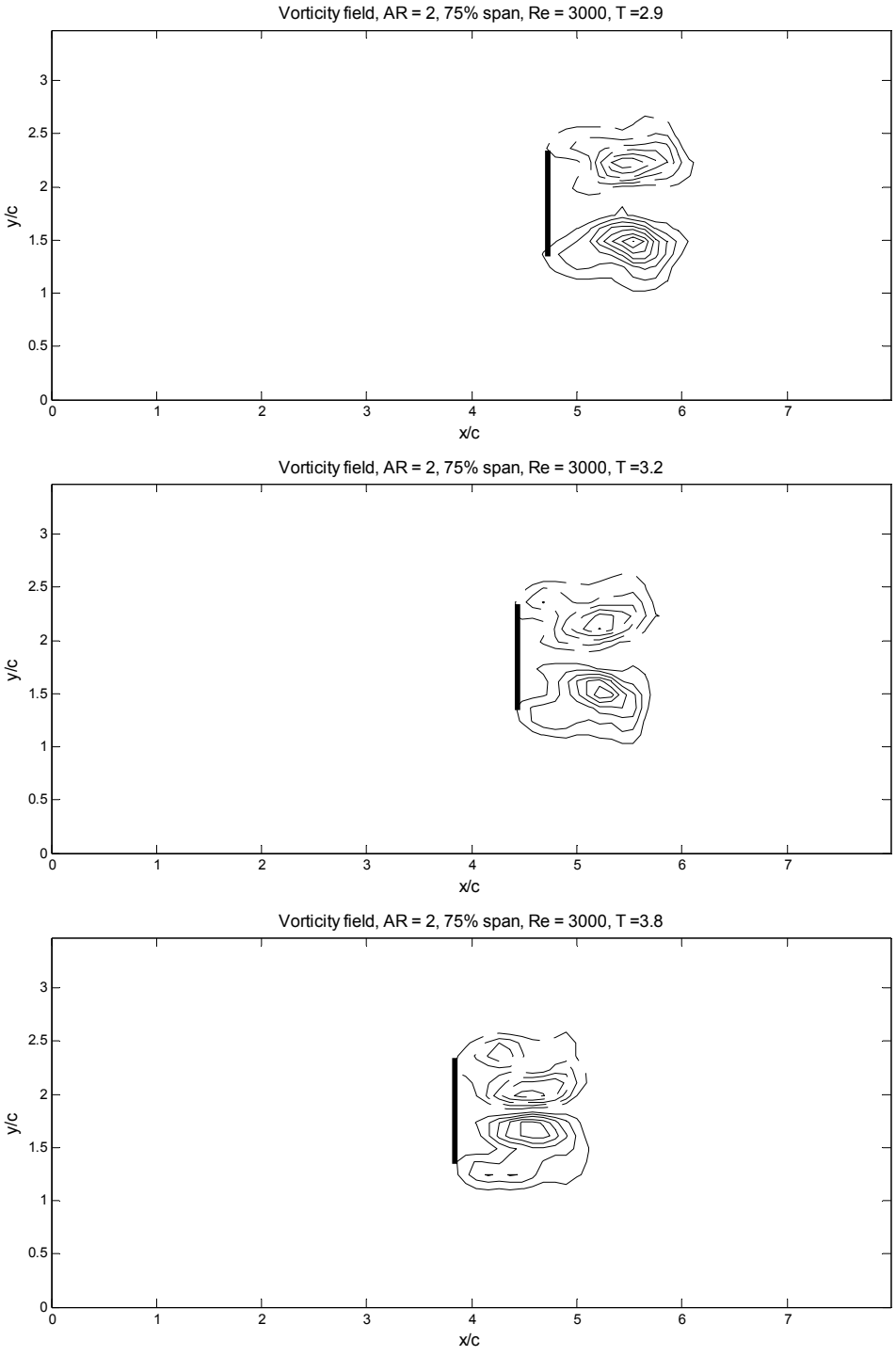

Figure 4.3.13(ii) Evolution of the vorticity field for *AR* = 2, 75% span.

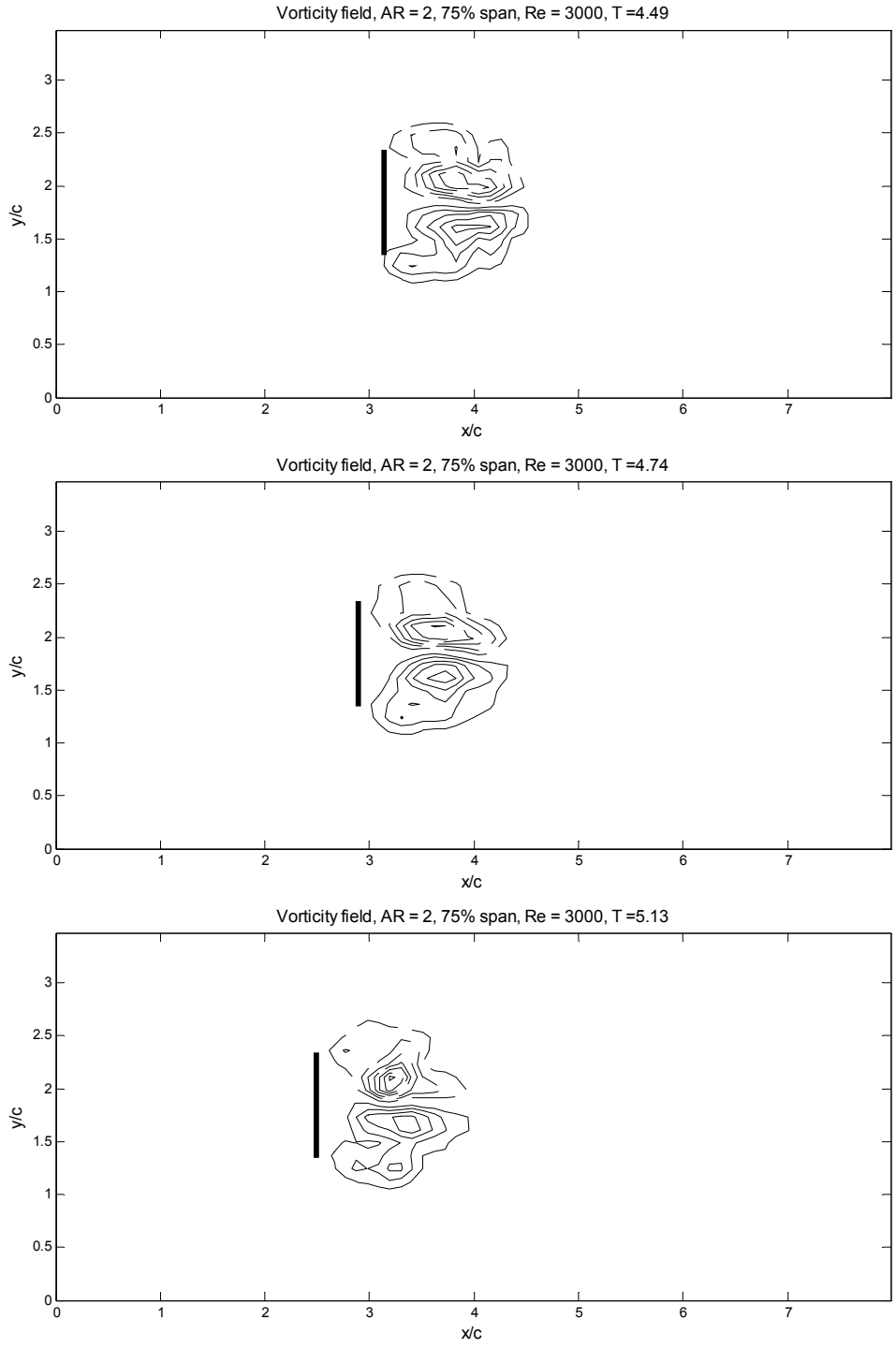

Figure 4.3.13(iii) Evolution of the vorticity field for *AR* = 2, 75% span.

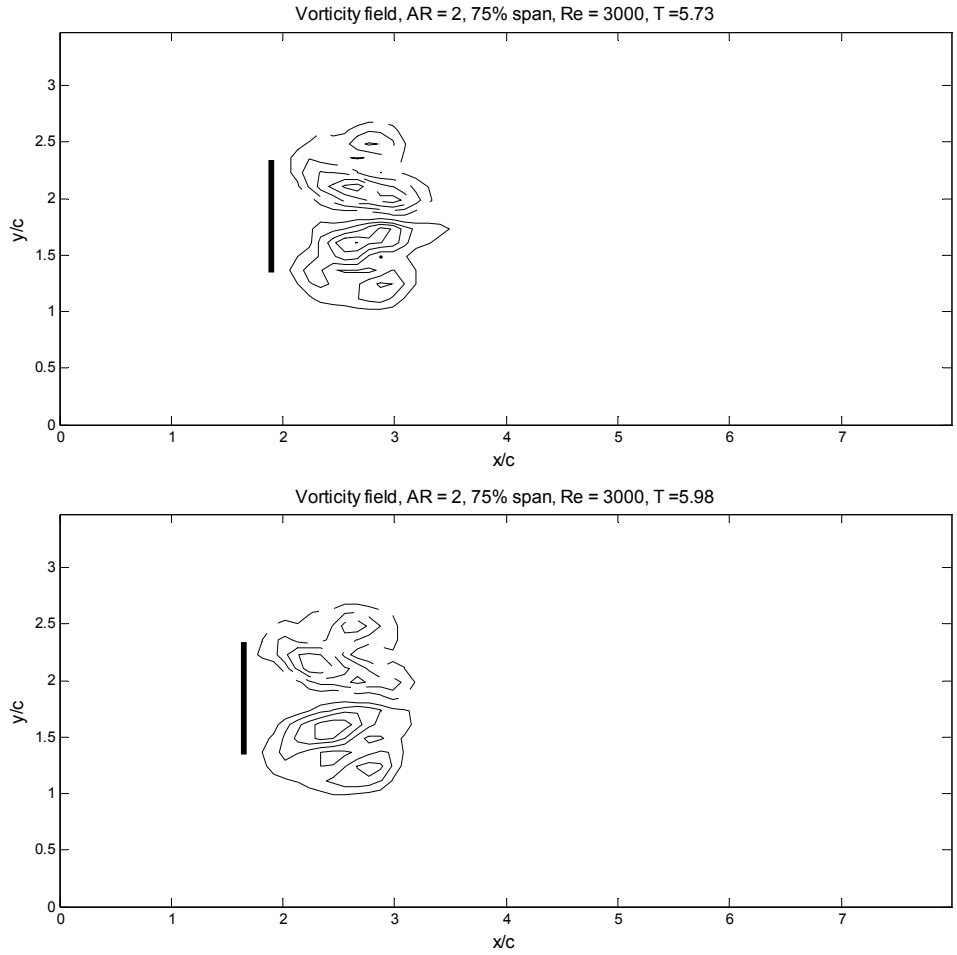

Figure 4.3.13(iv) Evolution of the vorticity field for *AR* = 2, 75% span.

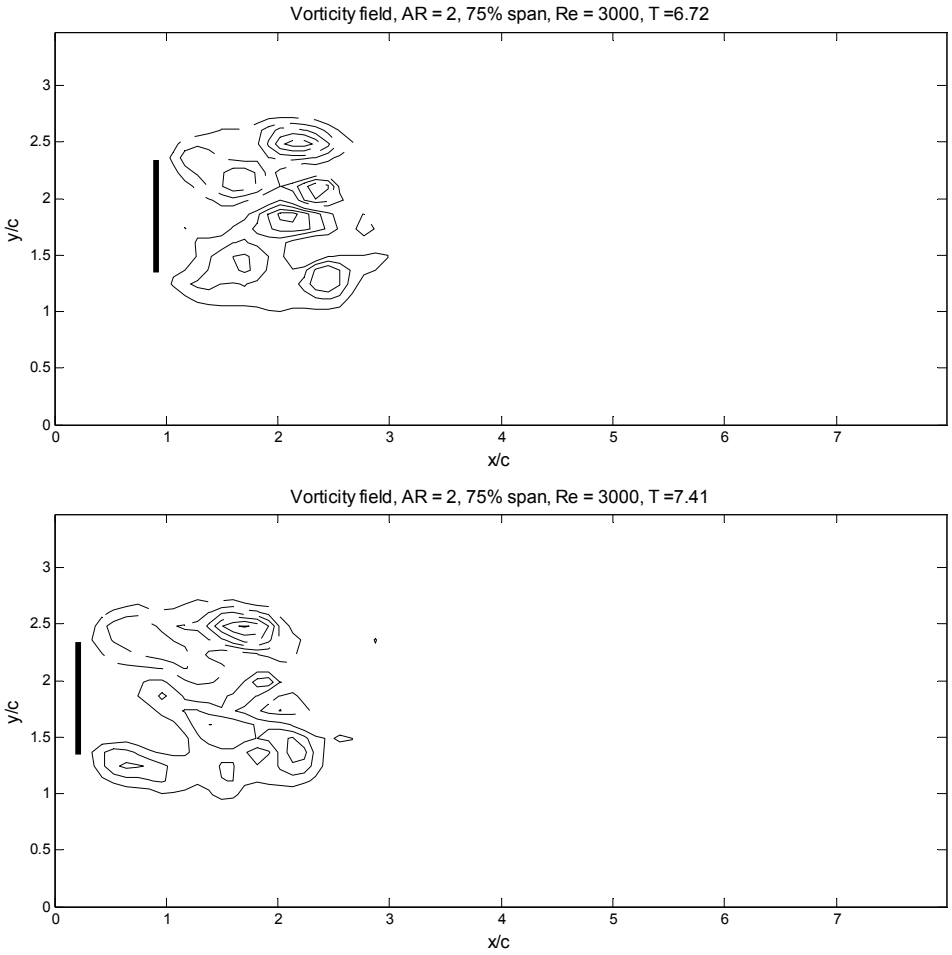

Figure 4.3.13(v) Evolution of the vorticity field for *AR* = 2, 75% span.

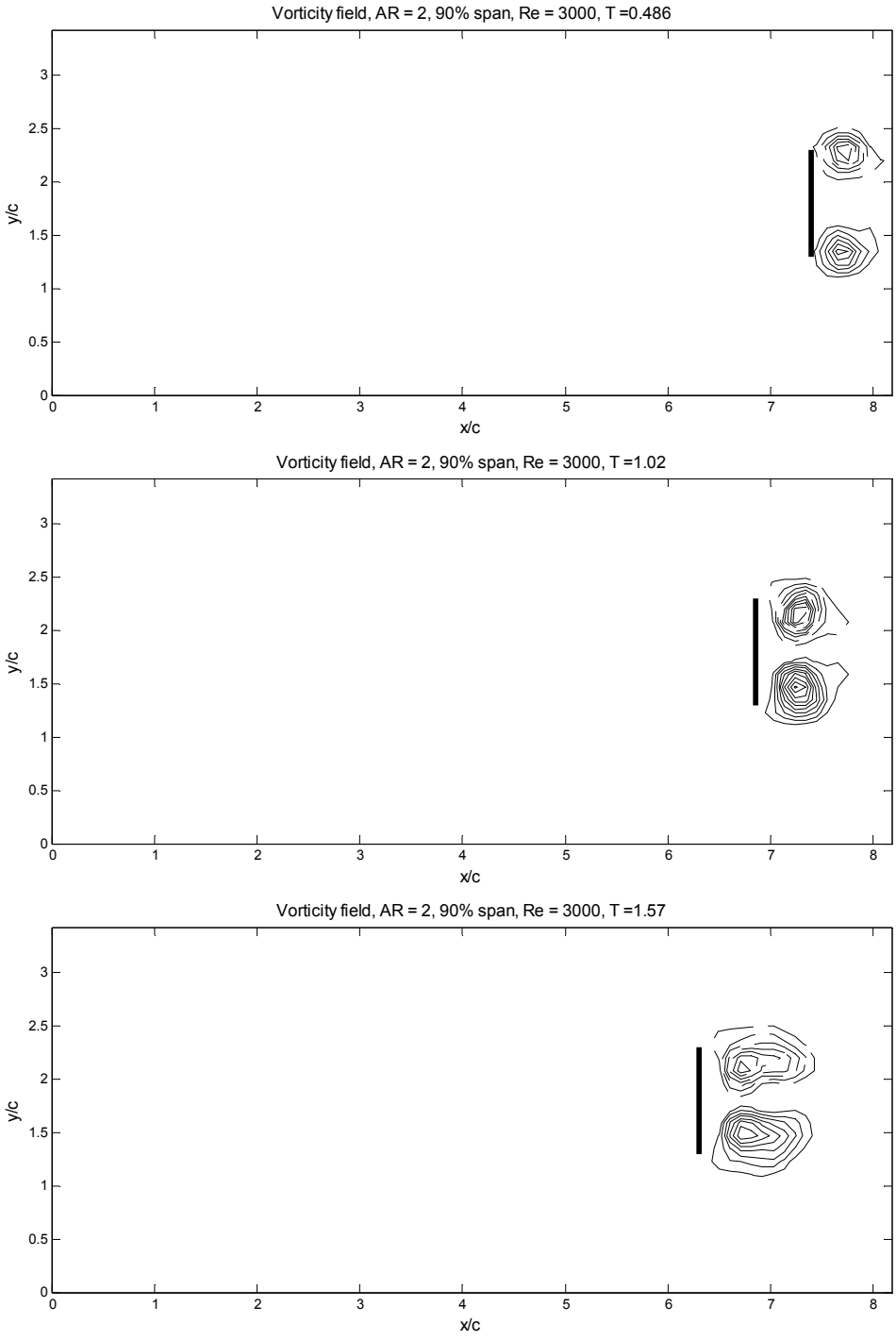

Figure 4.3.14(i) Evolution of the vorticity field for *AR* = 2, 90% span.

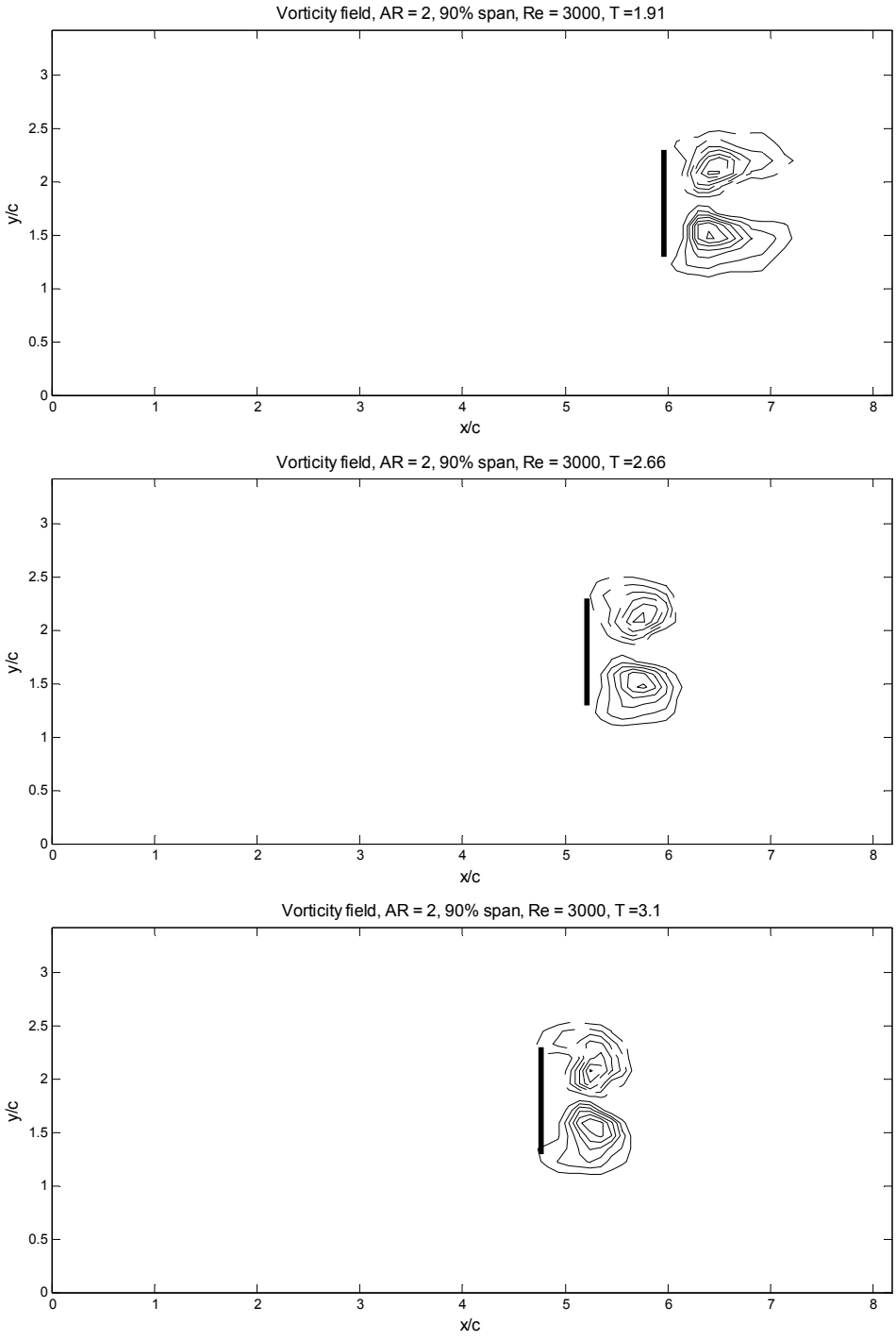

Figure 4.3.14(ii) Evolution of the vorticity field for *AR* = 2, 90% span.

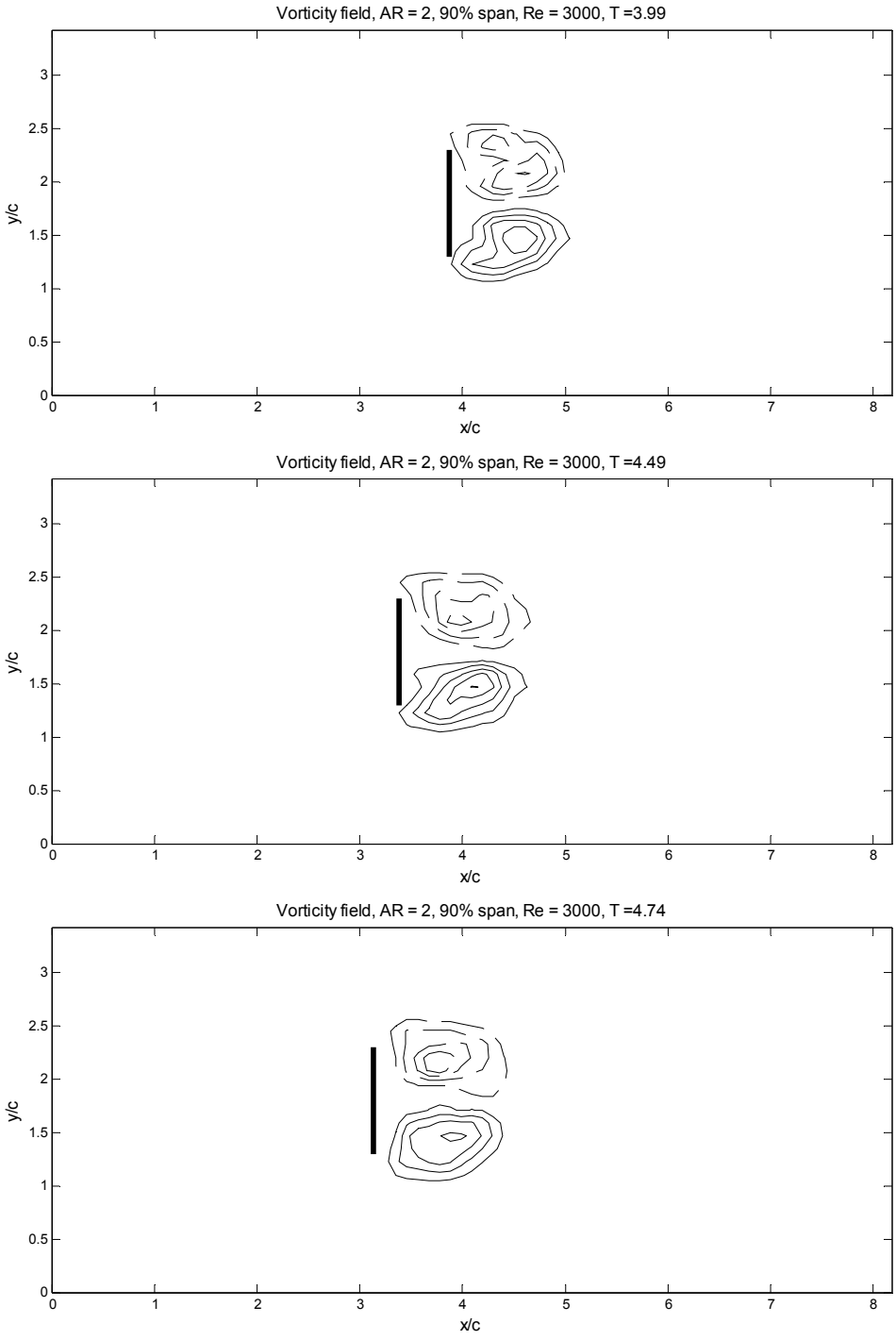

Figure 4.3.14(iii) Evolution of the vorticity field for *AR* = 2, 90% span.

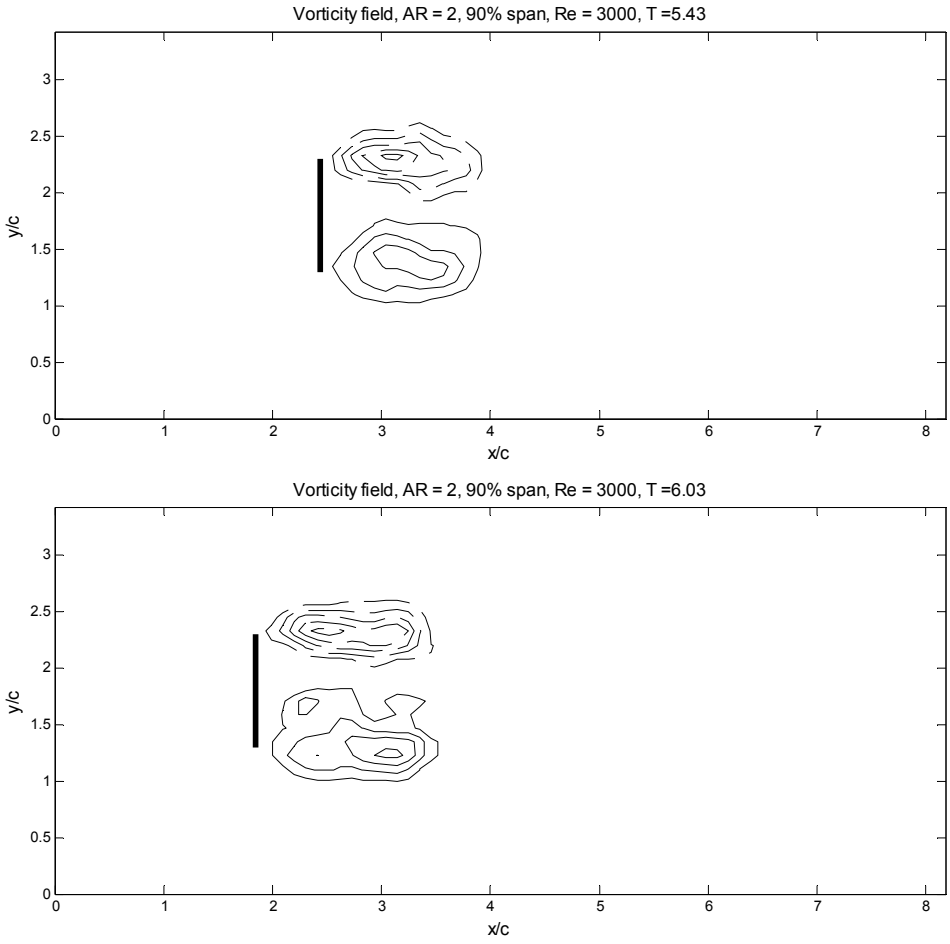

Figure 4.3.14(iv) Evolution of the vorticity field for *AR* = 2, 90% span.

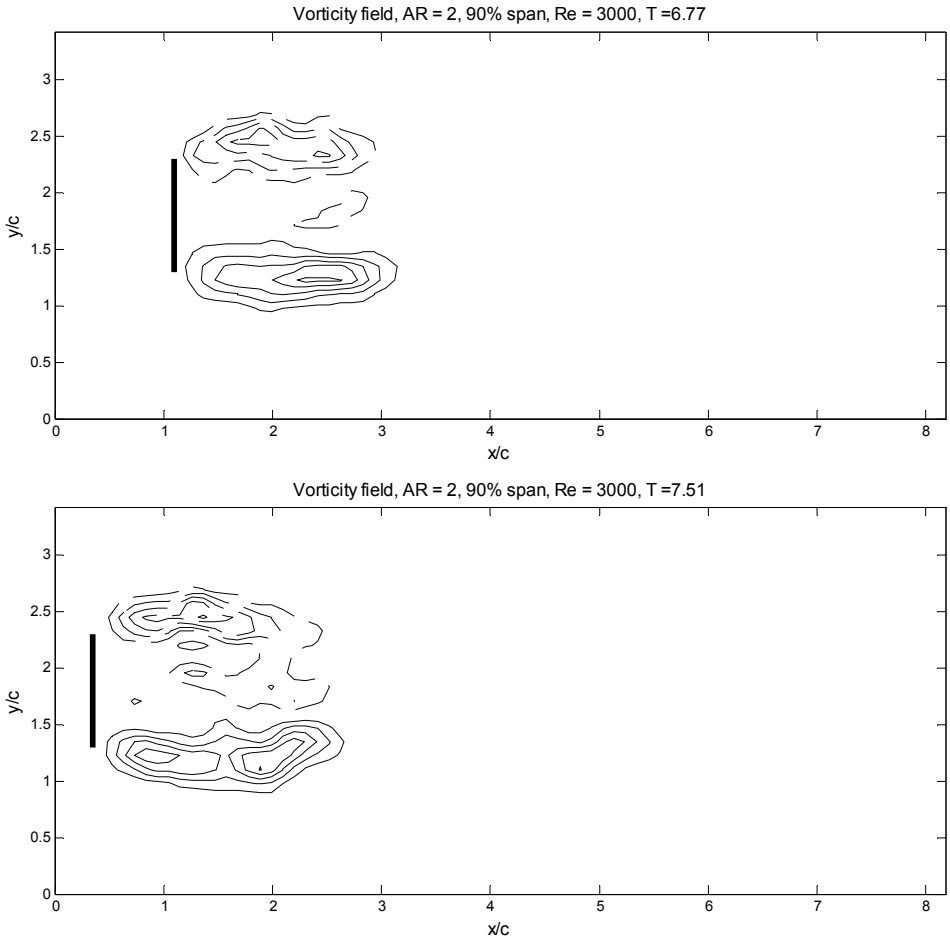

Figure 4.3.14(v) Evolution of the vorticity field for AR = 2, 90% span.

4.4 Spanwise and chordwise flow sections, and measured drag revisited

4.4.1 Introduction

The vorticity fields obtained from spanwise (vertical) sections of the flow at mid-chord (center wake) and at one of the leading edges, in planes parallel to the direction of travel, will now be presented. These results will be shown alongside the chordwise (horizontal) DPIV data and the force measurements reported above, so that the overall picture of the flow will become clearer. In section 4.5, images from dye flow visualization will be used to formulate a vortex model that explains the flow near the tip at the startup, and the global flow, as it relates to the DPIV sections, will be described using 3-D flow visualization.

In the figures below, all five sectional vorticity fields are given at once when the flow is shown at each formation time. The vorticity fields for the five cases, 50, 75, and 90% span in the chordwise direction, and at mid-chord and at one leading edge in the spanwise direction, are arranged in a "tiled" format. The three chordwise cases are displayed in descending order on the left-hand side, while the mid-chord case is in the middle, with the leading edge case to its right (see Figures 4.4.7a-i). All the vorticity fields in each set of tiles, for a specific aspect ratio, are at the same scale, so that the sizes and locations of wake vortices can be compared within and across sets of tiles; the location of each chordwise data set on the spanwise datasets is also labeled.

4.4.2 Aspect ratio 6

Since the force balance measures the resultant force on the plate due to the LEVs *and* the tip vortex (in addition to added mass at the startup, etc.), the force phenomena discussed in section 4.2 will be revisited and compared with the tiled vorticity fields. The measured C_D

for $AR = 6$ is given here again in Figures 4.4.2 and 4.4.3, along with insets showing the tiled vorticity fields at significant formation times. A larger set of tiled vorticity fields is provided in Figures 4.4.7a-i, in order to present the evolution of the flow in more detail. In addition, the circulation of the tip vortex itself in the mid-chord plane is plotted in Figure 4.4.1. The circulation data were obtained by distinguishing the TV from the added vorticity that appears above it after $T = 2$, which is actually convected into the mid-chord plane from the plate's corners (see below). This figure will be referred to when features of the circulation data correspond to flow phenomena.

Figures 4.4.7a-b show that nothing surprising occurs in the plate's vorticity field at early formation times. The flow at the startup should be primarily 2-D, and vortices should form at each of the plate's edges due to separation caused by the high initial acceleration. Indeed, at $T = 0.486$ (Figure 4.4.7a), compact vortices have developed at each edge, and the LEVs from 50 to 90% span are predominantly 2-D, since their sizes and core locations are similar. However, by this time the TV, which spans the entire bottom edge, is larger at mid-chord than at the leading edges. The 3-D development of the vortices in the plate's corners, discussed in detail in section 4.5, will show why the TV appears smaller in the vertical plane at the edge.

By $T = 2$, which is the formation number for 90% span, the measured drag on the plate has settled down from the initial peak to below 2 (see Figure 4.4.2), and significant changes in the flow have occurred. The TV at mid-span appears to have grown upward through 90% span (more on this later), and there are three distinct vortices in the leading edge plane, most notably a vortex of opposite sign, with respect to the TV, just above 75% span. The existence of these vortices in the leading edge plane, which are weaker than the

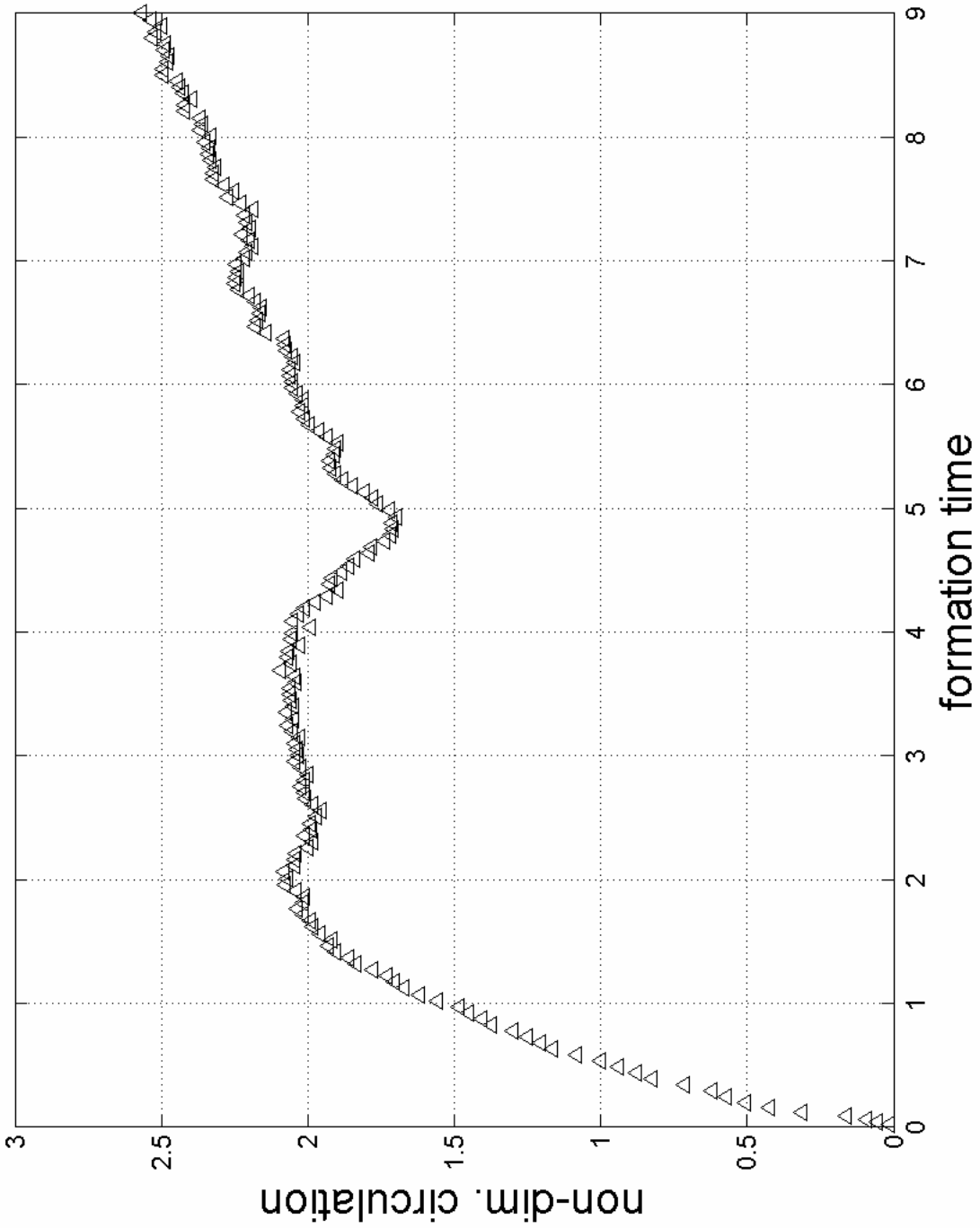

Figure 4.4.1 Circulation of the *AR* = 6 tip vortex seen in the mid-chord plane.

chordwise LEVs, suggest that the LEVs below 50% span have developed a more 3-D overall structure by this formation time. This is supported by the fact that only the vortices at 75% span have begun a pinch-off process. Finally, it should be noted that $T = 2$ is the formation number for the TV (see Figure 4.4.1) as well as for the LEVs at 90% span. Although no specific force phenomena occur at this time, it is significant because it is the time needed for the TV to develop its full circulation or strength and begin to affect the rest of the flow significantly. The LEVs at 90% span probably saturate at $T = 2$, rather than 3.1 or 4.5 like 75 and 50% span, respectively, because they are strongly influenced by the TV; the fact that they remain closely attached to the plate throughout the entire run supports this. This strong interaction between the TV and the LEVs is consistent with the work of Birch and Dickinson (2001), who demonstrated that the TV limits the growth of the LEV, thus keeping it attached to the wing longer than the 2-D case. However, as will be shown below, the LEVs for the present study have a strongly 3-D helical structure and thus a spanwise flow component, which was observed by Ellington et al. (1996); section 4.5 will elaborate upon and attempt to reconcile the current work with these previous studies.

At $T = 3.1$, the C_D has dropped to 1.65, from 1.8 at $T = 2$ (see Figure 4.4.2). The LEVs at 75% span have reached the end of their near-pinch-off (recall from section 4.3 that the pinch-off is never completed, as shown in the inset at $T = 4.49$ in Figure 4.4.2), and the LEVs at 50% span are more elongated and also closer to the wake centerline than at $T = 2$. Also, the LEVs at 90% span have been drawn toward the center wake and begun to form a recirculating bubble there. Given these observations, a possible explanation for the decrease in drag from $T = 2$ to 3.1 is that the plate's base pressure has increased due to recirculation bubbles starting to form at 50 and 90% span. However, the drop in drag is not dramatic

because the low pressure due to the vorticity in the mid-chord plane (which includes the TV) and the near pinch-off occurring at 75% span offsets it.

The change in the 90% span wake at $T = 3.1$ coincides with vorticity in the mid-chord plane "growing" upward. As the flow visualization images of section 4.5 will show, this new vorticity actually comes from the separation at the plate's corners and the leading edges near the tip. This vorticity is convected into the mid-chord plane by the LEVs, which have a helical (tornado) structure near the tip by this time. The increasing three-dimensionality of the LEVs with time, and over a greater distance away from the tip, is indicated by the fact that the three regions of vorticity in the leading edge plane at $T = 2$ have grown stronger at $T = 3.1$, with the negative vorticity having been convected upward so that its upper bound crosses 50% span. This helical, 3-D structure of the LEVs is consistent with the flow visualization results of Ellington et al. (1996). As mentioned above, section 4.5 will provide a more detailed comparison of the current results with those of Ellington et al. and Birch and Dickinson (2001).

The drag force remains basically unchanged from $T = 3.1$ to $T = 4.49$, after which it increases until the "hump" or maximum at $T = 5$. At $T = 4.49$, the recirculation bubble at 90% span has fully formed, and the LEVs at 75% span have rejoined the shear layers that generated them, creating more elongated vortices (see Figure 4.4.2). The vorticity at mid-chord has continued increase in magnitude and height above the tip, and 3 centers of vorticity within it have appeared; the bottom-most and strongest is the TV. Also, the three-dimensionality of the LEVs has increased, since the two largest vortical structures in the leading edge plane, visible at $T = 3.1$, have grown stronger, with the negative vorticity convecting above 50% span. As before, there continues to be a small vortex right at the tip in

the leading edge plane, which is a region of interaction between the LEVs and the TV. At 50% span, the LEVs have reached their maximum strength, and the pinch-off process has just begun. Despite these changes, the C_D at $T = 4.49$ is about the same as it was at $T = 3.1$ because of competing effects. The low-drag recirculating bubble at 90% span opposes the higher drag due to the saturated LEVs at 50% span and the low-pressure region of vorticity at mid-chord.

At the drag maximum at $T = 5$, the flow in the mid-chord plane has become more interesting (see Figure 4.4.3). Although the vorticity in the leading edge plane has not changed significantly, which may imply that the overall 3-D structure of the LEVs has stabilized, the vorticity at mid-chord has formed a "neck" at 90% span, above the primary TV. Looking ahead to the tiled vorticity insets at $T = 5.73$ and 6.67, it is clear that this is the start of an "upward" pinch-off process, where the vorticity at mid-chord above the TV pinches-off from the TV itself. The pinch-off in this plane occurs right at 75% span, and coincides with very interesting phenomena there, which will be discussed below.

This "upward" pinch-off is also reflected in the circulation of the TV in the mid-chord plane (see Figure 4.4.1). There is a local minimum in the TV circulation around $T = 5$, followed by a steady increase, past the original saturation value at $T = 2$, through $T = 9$. These deviations from the initial saturation value imply that significantly 3-D flow is being reflected in the 2-D DPIV measurement, which is also evident in the complex flow at 75% span (see below). It is the most likely explanation for such loss and gain in the circulation of this vortex for three reasons. First, given the moderate formation time of 5, losses to viscous diffusion are probably not yet significant. Second, since the velocity is constant after $T = 0.25$, there can be no gains in vorticity due to plate acceleration. Finally, because the TV is

perpetually attached to the plate (it does not pinch-off into the wake), its strength could not increase, if the flow were 2-D, after its formation number (at $T = 2$). In section 4.4.3, it will be shown that the $AR = 2$ TV exhibits similar circulation behavior.

The tiled vorticity plots reveal many reasons for a drag maximum centered around $T = 5$. First and foremost is the existence and influence of persistently attached vorticity in the mid-chord plane (including the strong TV), which, when suppressed as in the free end "grazing" case mentioned in section 4.2, causes a drag minimum instead. The attached vorticity in the mid-chord plane is a region of low pressure, and is therefore responsible for an increase in C_D. Second, the drag "hump" coincides with the formation number of the LEVs at 50% span.

If the flow at 50% span is considered to be primarily 2-D (which is the case until after the LEVs pinch-off), the following formula for the force due to a set of 2-D point vortices can be used to show how the LEVs for this case contribute to the force on the plate (the quantity in square brackets is the impulse) (Batchelor, 1967):

$$F \propto \frac{d}{dt}\left[-\left(\sum_i Y_i \Gamma_i \right)\hat{i} + \left(\sum_i X_i \Gamma_i \right)\hat{j} \right]$$

As just mentioned, this formula treats each LEV (subscript i) as a point vortex, i.e., with all of its circulation Γ_i concentrated at a point (X_i,Y_i), which is spatially the centroid of its vorticity. The positive x-direction, $\hat{i}$, will be defined to be pointing right (i.e., opposite to the direction of the plate motion) with the origin located at mid-chord, and the positive y-direction, $\hat{j}$, will be defined as pointing upward in the same plane. Since the flow is essentially symmetrical about the x-axis, the circulation of the negative LEV, Γ_1, is nearly equal in magnitude (but of course of opposite sign) to that of the positive LEV, Γ_2, and their

x-direction vorticity centroid locations, X_i, are about equal. Therefore, they exert little lift force (i.e., force in the y-direction) on the plate. The dominant force on the plate due to the LEVs (looking at the signs of each of their circulations coupled with their y-centroid locations) is thus drag, and the formula shows that, as the LEVs move away from the wake centerline, the drag force they generate on the plate increases. Referring to the vorticity field insets of Figure 4.4.3, the LEVs reach their maximum distance from the wake centerline right around the drag maximum. However, after the LEVs pinch-off (see the T = 6.67 inset) they merge again with the shear layers that generated them, but they become weaker and disorganized due to 3-D effects (see Figure 4.4.7i); thus, their contribution to the drag after the pinch-off decreases.

The vorticity field at 90% span at T = 4.98 shows LEVs that "stand-off" farther from the rear face of the plate than their counterparts at T = 4.49. This means that the induced upstream velocity on the rear face of the plate, that existed when the recirculating LEVs were attached there, is now drawn outward, which reduces the pressure there and creates higher drag.

At T = 5.73, the flow at 50% span has evolved as expected, the LEVs at 90% span have elongated and "pealed away" from the wake centerline near the rear face of the plate, and the vorticity in the leading edge plane remains basically unchanged (see Figure 4.4.3). However, as mentioned above, the "upward" pinch-off of vorticity in the mid-chord plane has progressed and is almost completed, and the wake at 75% span has changed substantially. The fact that the locations of the pinched-off vorticity at mid-chord and the vortex projected in the leading edge plane are essentially the same, as are their signs of rotation, may imply a connection between the two. Since this flow is highly 3-D, such a connection cannot be

proved or disproved based solely on these cross sections, and must await the dye visualization and vortex model discussed in section 4.5. Regardless, it is clear that the mid-chord plane pinch-off is related to the "inward" pinch-off seen at 75% span, which will be discussed next.

The induced flow from the "arm" of the mid-chord plane vorticity that extends up to 75% span tends to pull the portion of the LEVs near mid-chord toward the plate and the wake centerline, while the pinched-off vorticity just above 75% span tends to also pull the LEVs toward the wake centerline, but away from the plate. These partially opposing actions cause the LEVs at 75% span to be drawn toward the wake centerline, but also to become trapped there, allowed neither to reach the rear face of the plate nor to escape downstream from the near wake. The vorticity at $T = 6.67$ and at a later time shown in Figure 4.4.7i illustrates this last condition: the wake has become more complicated and concentrated along the centerline, but no attached recirculating bubble exists, nor is there any evidence of a possible pinch-off process. Also at $T = 6.67$, the spanwise vorticity at mid-chord has completely pinched-off, and secondary vorticity of opposite sign has been generated between it and the "arm" connected to the TV. These three regions of alternate sign vorticity create the complicated wake at $T = 6.67$, and persist afterward so that the wake at 75% span retains the same character beyond $T = 7$ (see Figure 4.4.7i).

Liu, Ellington, and others (1998) also observed interesting phenomena around 75% span. During the first half of the downstroke, they found that the LEV forms from the wing root to about 60 to 75% span. At the beginning of the second half of the downstroke, they reported that this LEV has a significant spanwise flow toward the tip, but that it breaks down at 75% span, which they attributed to a reverse (decreasing toward the wing root) pressure

gradient there, and to wing deceleration. They also remarked that the flow in the tip region separates and rolls up at that time into a TV. Finally, toward the end of the downstroke, they observed that a new LEV forms over the tip region and joins with the TV. They found that this second LEV has a spanwise flow toward the wing root, because of a reverse pressure gradient due to the TV. At 75% span, they noted that the opposite spanwise flows of the first and second LEVs collide, bringing the spanwise flow there to zero. Section 4.5 will show that the spanwise flow of the LEVs, up to at least 50% span, is away from the tip. However, the pressure gradient at the plate surface near the free end, due to the TV, opposes this. It causes the flow near the tip and at the plate surface to travel downward before it curls aft and then upward into the LEV "tornadoes." This behavior might account for the complicated flow seen at 75% span. The flow of the current study appears to disagree with the results of Liu et al. on some points (for example, the spanwise flow, toward the root or free surface, for the $AR = 6$ plate extends beyond 75% span), although this may be due in large part to the difference in wing and plate kinematics of both studies. Again, when the flow visualization results are presented in section 4.5, these issues will be revisited in detail.

The decline in C_D after $T = 5$ to a minimum of about 1.4 at $T = 7.5$ may be due to a number of events. Most likely, as discussed above, the pinch-off and subsequent reattachment and weakening (due to 3-D effects) of the LEVs at 50% span should cause a decrease in the drag force. Also, the narrower and more disorganized wake at 75% span (see the $T = 6.67$ inset in Figure 4.4.3) creates less drag than its counterpart at $T = 4.98$, which consists of coherent LEVs attached to the plate's leading edges and located farther away from the wake centerline. The flows at 90% span and in the leading edge plane do not change substantially after $T = 5.73$, and so are probably not responsible for any significant

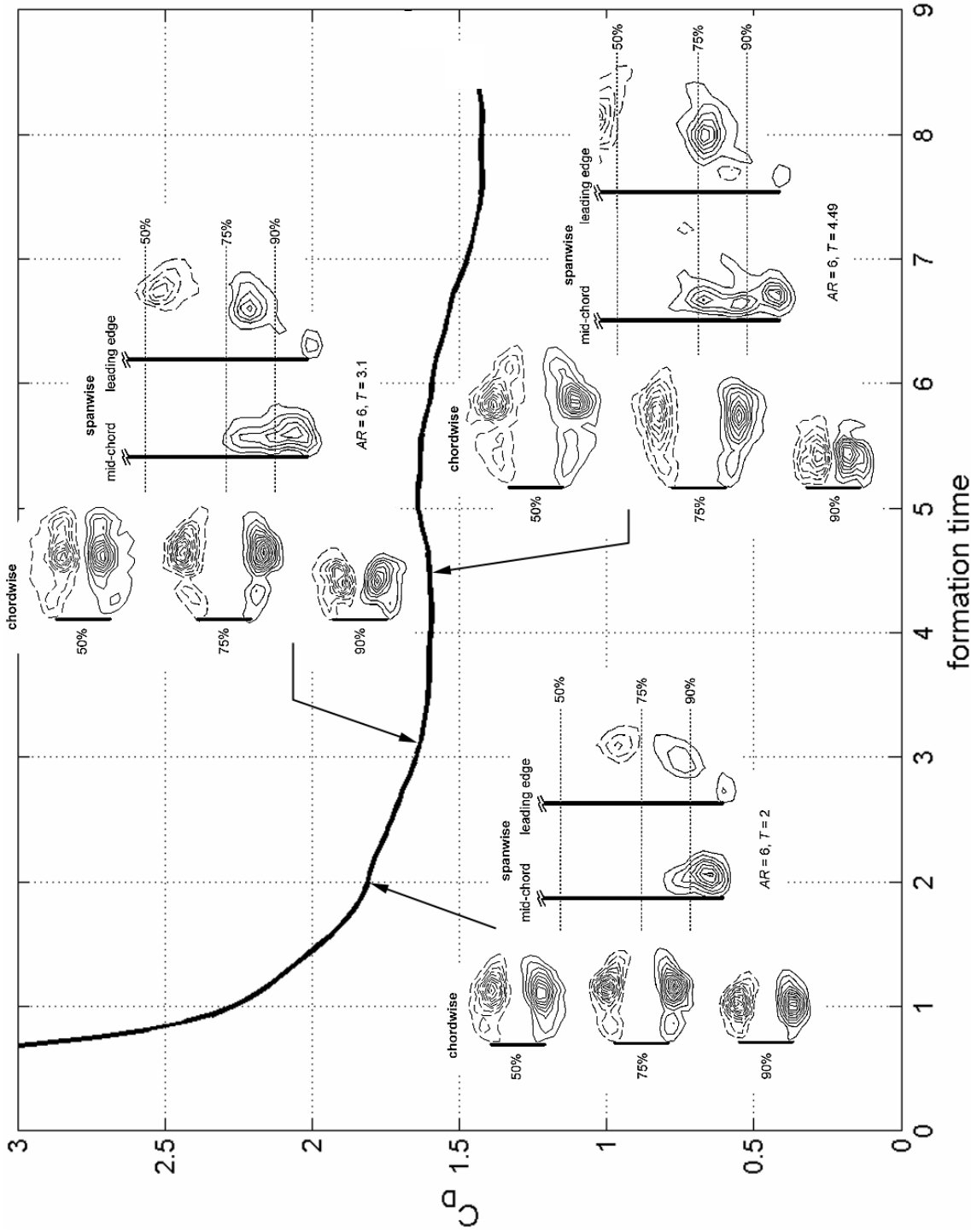

Figure 4.4.2 Measured C_D vs. T for AR = 6 (part 1), including tiled vorticity insets to show the flow at significant formation times.

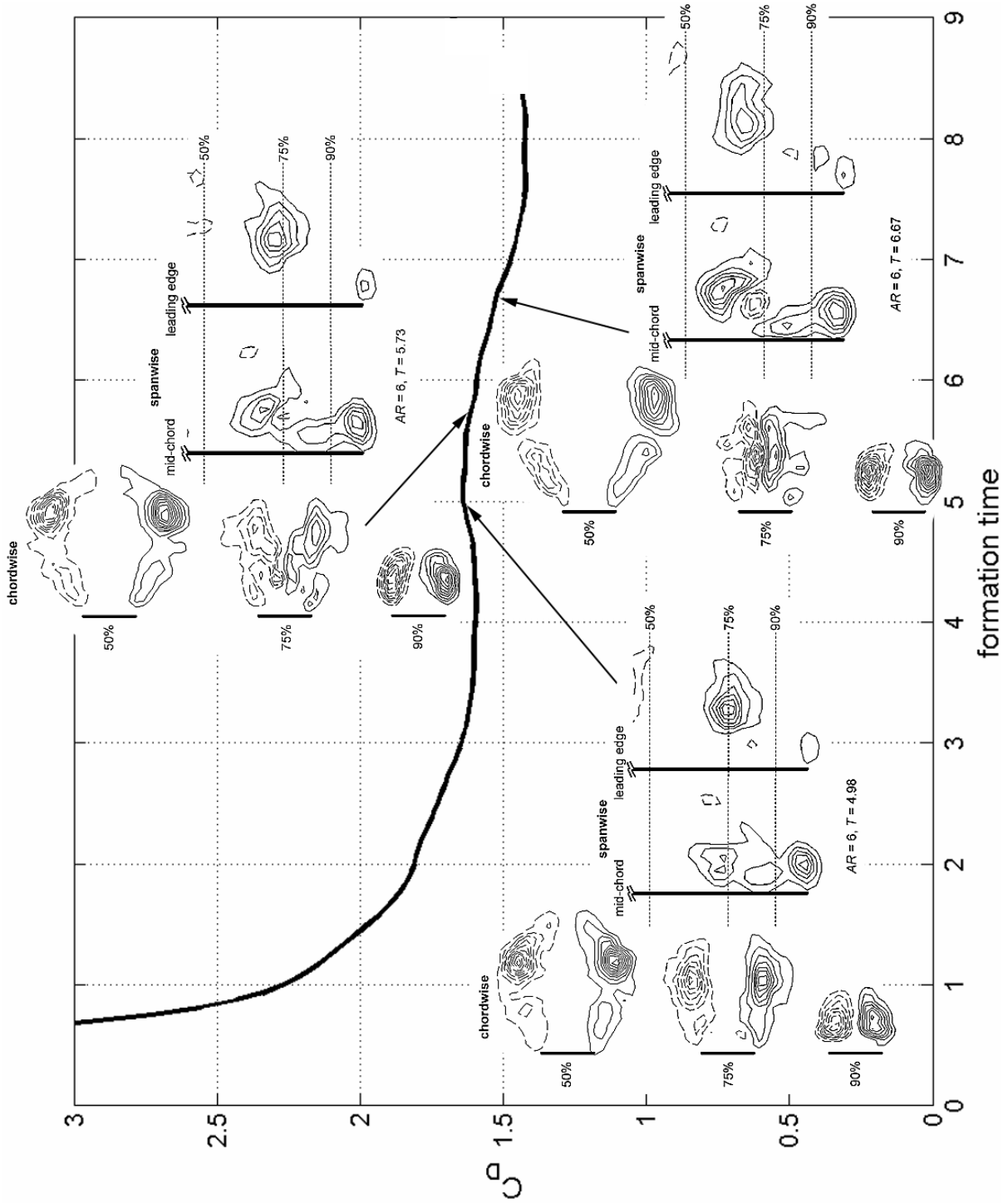

Figure 4.4.3 Measured C_D vs. T for AR = 6 (part 2), including tiled vorticity insets to show the flow at significant formation times.

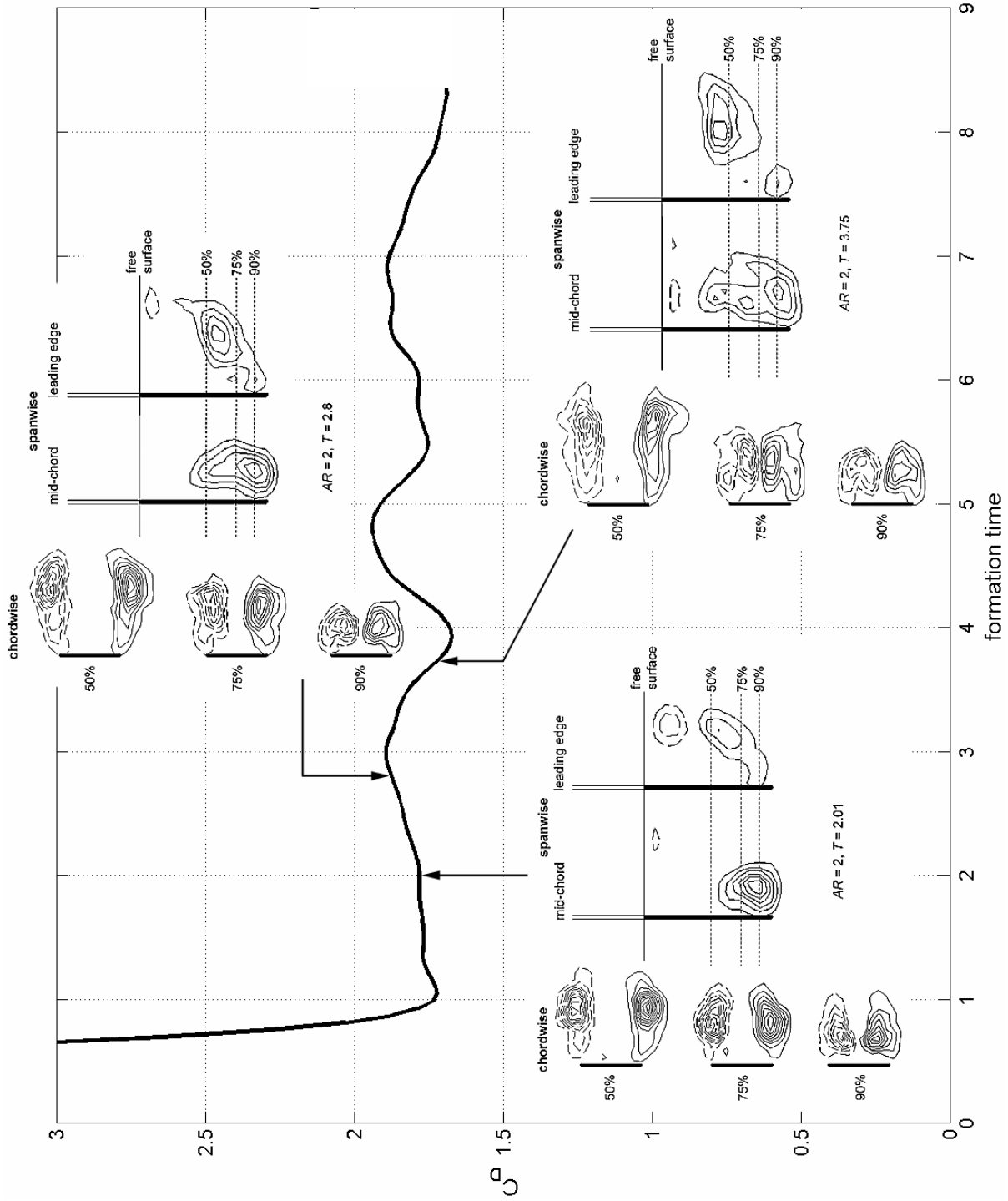

Figure 4.4.4 Measured C_D vs. T for AR = 2 (part 1), including tiled vorticity insets to show the flow at significant formation times.

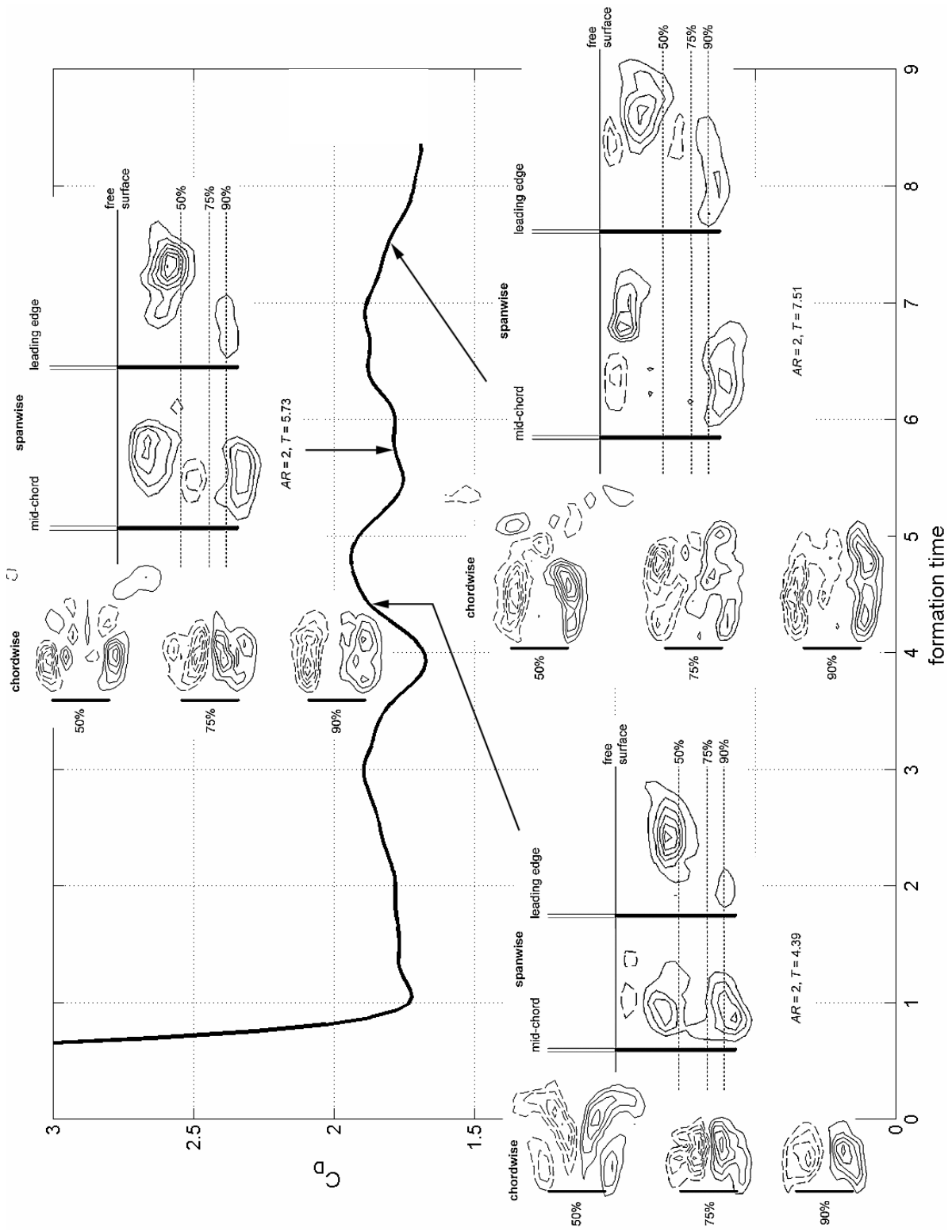

Figure 4.4.5 Measured C_D vs. T for AR = 2 (part 2), including tiled vorticity insets to show the flow at significant formation times.

changes in drag.

4.4.3 Aspect ratio 2

A plot showing the measured C_D for AR = 2 with tiled vorticity insets is given in Figures 4.4.4 and 4.4.5; a larger set of tiled vorticity plots is provided as Figures 4.4.8a-i. Also, Figure 4.4.6 shows the circulation of the TV in the mid-chord plane for AR = 2, compared with that of AR = 6, described above. Figures 4.4.8a-b show that the flow at early formation times for AR = 2 is very similar to that of AR = 6. This is expected, since both flows are highly 2-D at the startup, and the induced flow from the tip for AR = 2 does not reach the free surface immediately.

By T = 1.5, Figure 4.4.6 shows that the circulation of the TV for AR = 2 has reached a maximum. As with AR = 6, the formation numbers of the TV and LEVs at 90% span coincide, indicating the strong influence of the TV at that location. Although the TVs for both AR = 2 and 6 saturate at essentially the same dimensional circulation value (the normalization constant for both cases is the same), the AR = 2 TV reaches that value more quickly. This supports the assertion, made below, that the AR = 2 flow develops faster than its AR = 6 counterpart, because of the relatively stronger influence of its tip or free end. In addition, after their circulation minimums between T = 4 and 5, the circulation for the AR = 2 TV is higher and grows faster than that of AR = 6. For AR = 6, this growth in circulation beyond that at the formation number was attributed to significantly 3-D or out-of-plane flow being reflected in the 2-D DPIV measurements. If this is the case, the circulation data for AR = 2 imply that, after T = 5, the TV becomes more 3-D more quickly than that of AR = 6. Again, this is most likely due to the relatively stronger effect of the tip for AR = 2

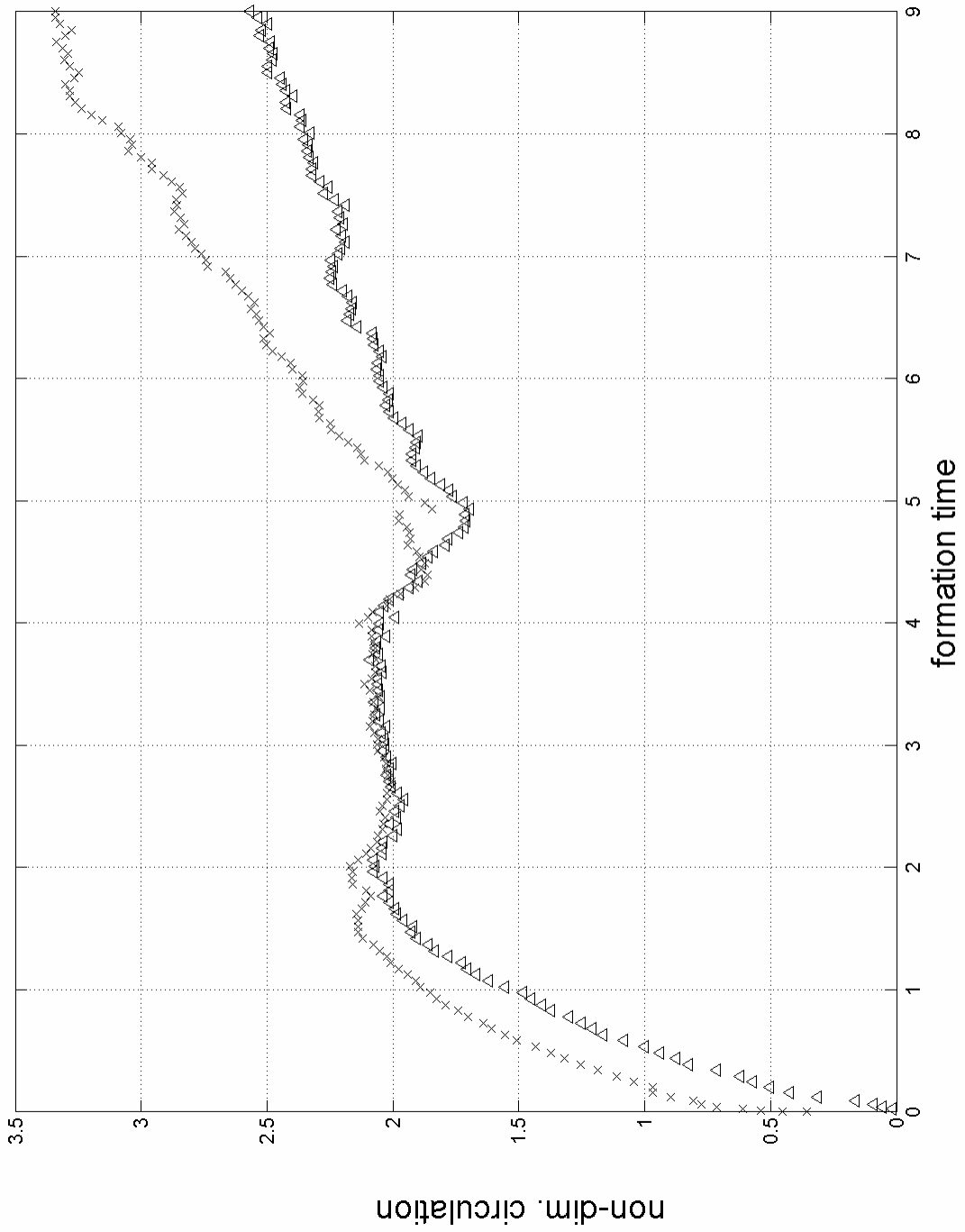

Figure 4.4.6 Circulation of the *AR* = 2 & 6 tip vortices seen in the mid-chord plane. Triangles: *AR* = 6; x's: *AR* = 2.

At $T = 2$, both flows are still very much the same, as are both drag coefficients (see Figure 4.4.4). As noted in section 4.3.3, the flows are similar in terms of absolute distance from the tip rather than relative. The flow at $AR = 2$, 50% span resembles that at $AR = 6$, 75% span, and the vortices at $AR = 2$, 75% span are very similar to those at $AR = 6$, 90% span. This agreement extends also to the flow at mid-chord and in the leading edge plane. As with $AR = 6$, the existence of significant vorticity in the leading edge plane (see the $T = 2.01$ vorticity inset, Figure 4.4.4) implies that the LEVs of $AR = 2$ have acquired a more 3-D structure by $T = 2$. Additionally, at this formation time, the spanwise vorticity generated by the 3-D LEVs has reached the free surface, and the behavior of the C_D afterward differs from that of $AR = 6$.

Indeed, at $T = 2.8$ the C_D is higher than that of $AR = 6$ (see Figure 4.4.4), and this remains true throughout the rest of the run. The flow at this formation time still shares similarities with that of $AR = 6$, but some of these agreements are found at later times. At 50% span, the vorticity field looks remarkably like that of $AR = 6$, 75% span at $T = 4.49$. While at 75% span, the LEVs have started to move closer to the wake centerline and the rear face of the plate, as in the 90% span case for $AR = 6$ at a similar time to 2.8, $T = 3.1$. As for 90% span, the LEVs have become more compact, forming a tighter wake behind the plate; they remain in this general state until about $T = 4.5$. The flow in the mid-chord plane, like the 75% span case, does resemble its $AR = 6$ counterpart: the vorticity from the plate's corners has extended up through 50% span. In the leading edge planes of both aspect ratios, the positive vortex above the tip has grown stronger and larger by this formation time. However, the negative vortex, observed at $T = 2$, has for $AR = 2$, $T = 2.8$ been nearly destroyed by its interaction with the free surface.

Section 4.2 attributed the "wiggles" in the AR = 2 force data, which occur from about T = 3 to T = 7.5, to such interactions between vorticity generated by the 3-D induced flow from the tip and the free surface. Supporting this is the fact that no such features appear in the C_D of AR = 6. The tiled vorticity field insets in Figures 4.4.4 and 4.4.5 (and Figures 4.4.8a-i) show that vorticity from the tip-induced 3-D flow impinges the free surface in the leading edge plane at T = 2, 2.8, 6.77, and 7.51, and in the mid-chord plane at T = 3.75, 4.39, 5.73, 6.77, and 7.51. These interactions produce small waves on the free surface, which affect the force measurements.

The changes in the drag force due to the tip-generated vorticity impinging on the free surface also serve to mask any formation number effects. For the AR = 6 case, the formation number at 50% span can be directly linked to the maximum at T = 5. However, for AR = 2, the formation numbers at 50, 75, and 90% span, which are 3.75, 2, and 1.5, respectively, occur just at the start of the free surface phenomena. It is possible that the initial peak at T = 3 is due to the combined effect of all 3 formation numbers, but it is not certain.

By T = 3.75, the flow at 50% span for AR = 2 resembles that of AR = 6, 75% span at T = 5.33 (see section 4.3.2). The flow at 75% span is close to that of AR = 6, 90% span at T = 3.5, and the vorticity in the spanwise sections appears to be at an intermediate stage between that of AR = 6, T = 4.49 and 4.98. At T = 4.39 (see Figure 4.4.5), an "inward" pinch-off of the LEVs is observed at 50% span for AR = 2, while an “upward” pinch-off of the vorticity from the tip is seen in the mid-chord plane. As with AR = 6, this “upward” pinch-off process corresponds to a drop in the AR = 2 mid-chord circulation (see Figure 4.4.6). Both of these events, the “inward” and “upward” pinch-off, occur in similar manners and in similar spatial locations for AR = 6, but at a later formation time, T = 5.73. Given these results, it can be

concluded that above the absolute location of 75% span (as measured for $AR = 2$), the flow induced by the tip progresses more quickly for $AR = 2$ than for $AR = 6$. In other words, the tip effect for $AR = 2$ is relatively stronger than that for $AR = 6$, showing that the influence of the tip increases with decreasing AR, as expected.

It follows, then, that the most plausible explanation for the drag coefficient of $AR = 2$ being higher than that of $AR = 6$, after $T = 2$, is the relatively stronger influence of its tip vortex and other mid-chord vorticity. This attached vorticity dominates a much greater portion of the span for $AR = 2$ than for $AR = 6$. Since this vorticity is a region of low pressure, it creates drag on the plate, which is relatively higher for $AR = 2$.

The flow at $T = 5.73$ for $AR = 2$ is very complicated in the chordwise planes (see Figure 4.4.5), and differs significantly from anything observed for $AR = 6$. At 50% span, the LEVs that pinched-off "inwardly" at $T = 4.39$ are almost completely destroyed, most likely due to out-of-plane flow, evident in the mid-chord plane. The recirculating bubble at 75% span has deformed, and the LEVs at 90% span are exhibiting asymmetry. In the spanwise planes, the flow still resembles that of $AR = 6$, albeit at $T = 6.67$. At mid-chord, the "upward" pinch-off of the vorticity away from the tip has been completed, and secondary, negative vorticity has been induced between it and the tip vortex. Also, the large positive vorticity in the leading edge plane is still present, and roughly in-line with the pinched-off vorticity in the mid-chord plane. However, the tip vortex itself has become more elongated and weaker than its $AR = 6$ counterpart.

The overall wake of the plate becomes more elongated and disorganized as T reaches 7.51 (see Figure 4.4.5). At 75 and 90% span, the LEVs have deteriorated into longer structures with multiple centers of vorticity. At 50% span the primary LEVs have instead

reestablished themselves, possibly due to the lack of spanwise flow at that location. The spanwise sections reveal that the tip vortex has continued to elongate, in the direction of the freestream, since $T = 5.73$, but it remains attached to the plate. As mentioned above, spanwise vorticity in both the mid-chord and leading edge planes impinges upon the free surface at this time. In both planes, the positive vorticity has induced new negative vorticity near the surface. The decrease in drag at this point, leading to a minimum at about $T = 8.4$, is due to the relative disorganization of the wake, and the vorticity in the mid-chord plane, that is no longer attached to as great a portion of the plate's span.

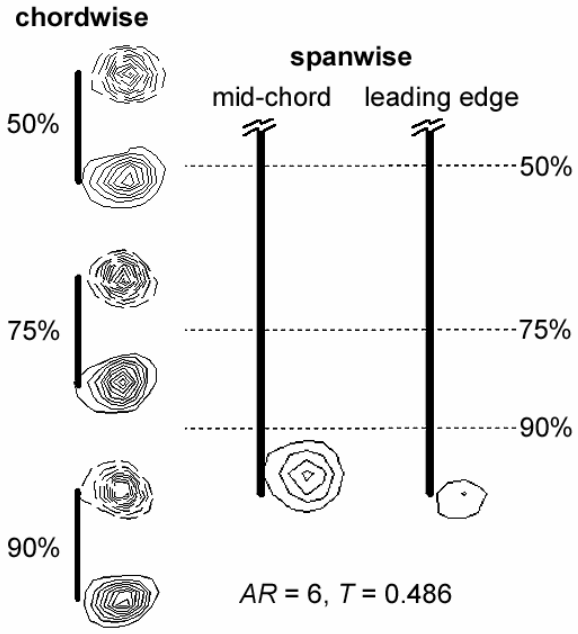

Figure 4.4.7a Tiled vorticity fields for *AR* = 6, *T* = 0.486.
Chordwise: 50, 75, & 90% span; spanwise: mid-chord & leading edge planes.

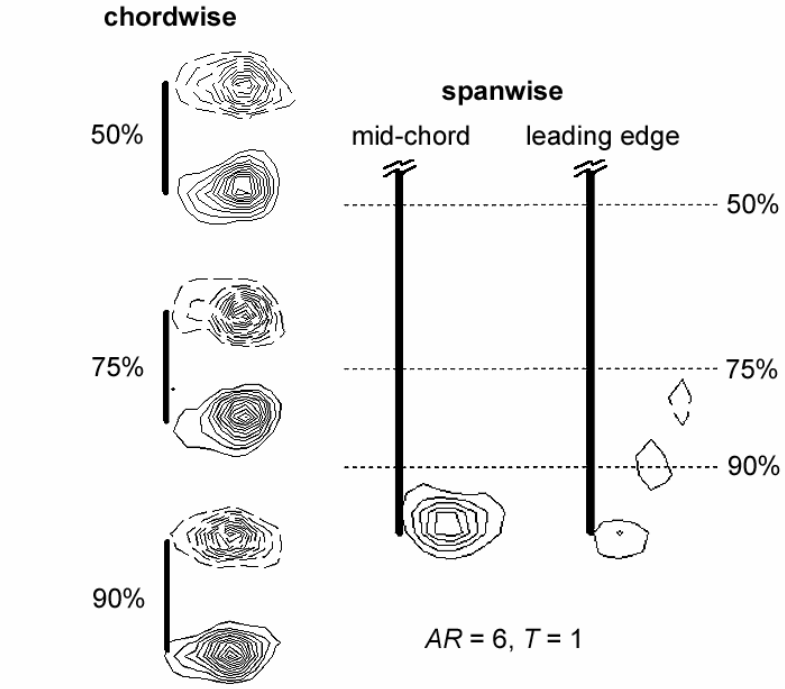

Figure 4.4.7b Tiled vorticity fields for *AR* = 6, *T* = 1.
Chordwise: 50, 75, & 90% span; spanwise: mid-chord & leading edge planes.

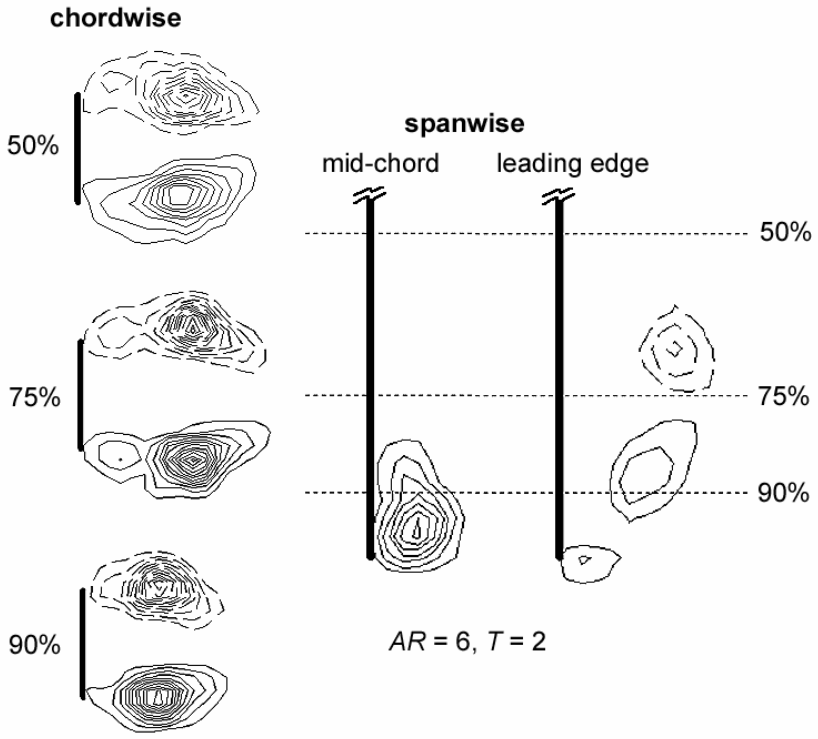

Figure 4.4.7c Tiled vorticity fields for *AR* = 6, *T* = 2.
Chordwise: 50, 75, & 90% span; spanwise: mid-chord & leading edge planes.

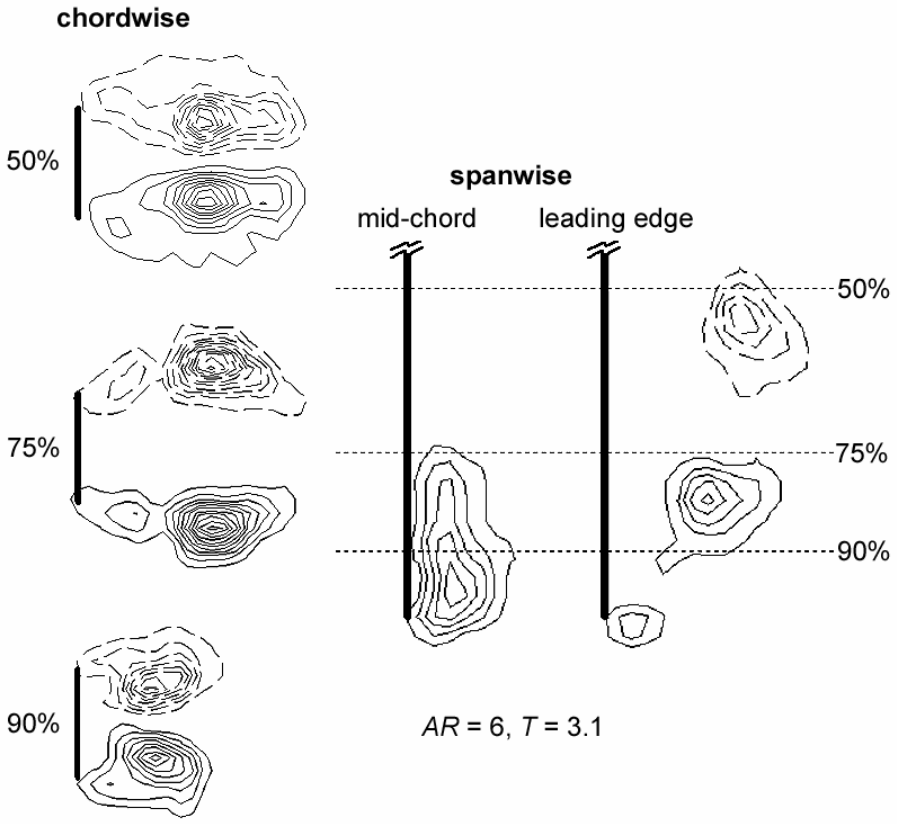

Figure 4.4.7d Tiled vorticity fields for *AR* = 6, *T* = 3.1.
Chordwise: 50, 75, & 90% span; spanwise: mid-chord & leading edge planes.

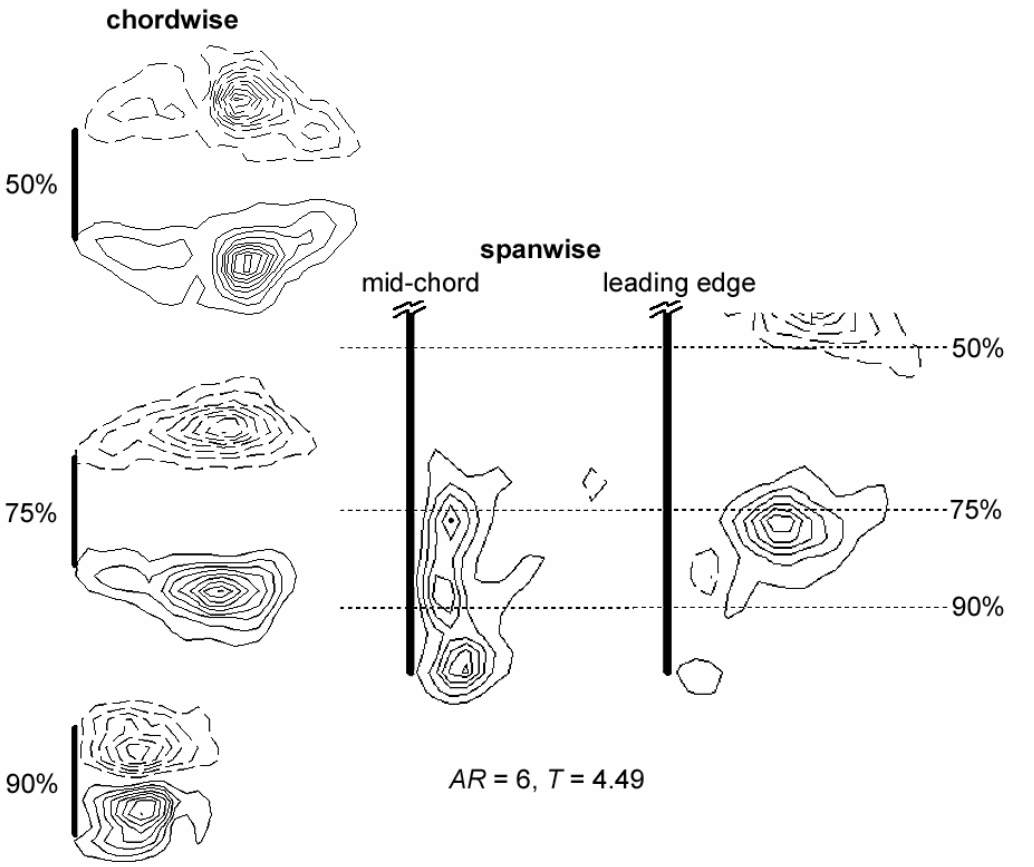

Figure 4.4.7e Tiled vorticity fields for *AR* = 6, *T* = 4.49.
Chordwise: 50, 75, & 90% span; spanwise: mid-chord & leading edge planes.

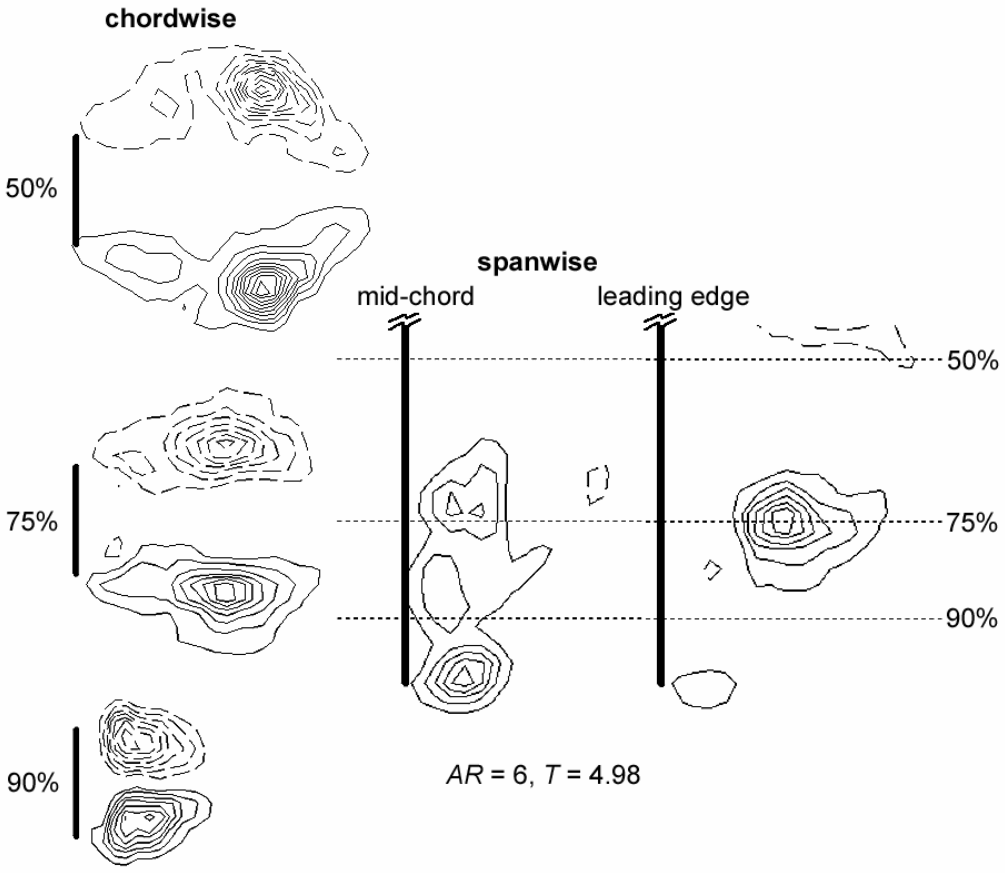

Figure 4.4.7f Tiled vorticity fields for *AR* = 6, *T* = 4.98.
Chordwise: 50, 75, & 90% span; spanwise: mid-chord & leading edge planes.

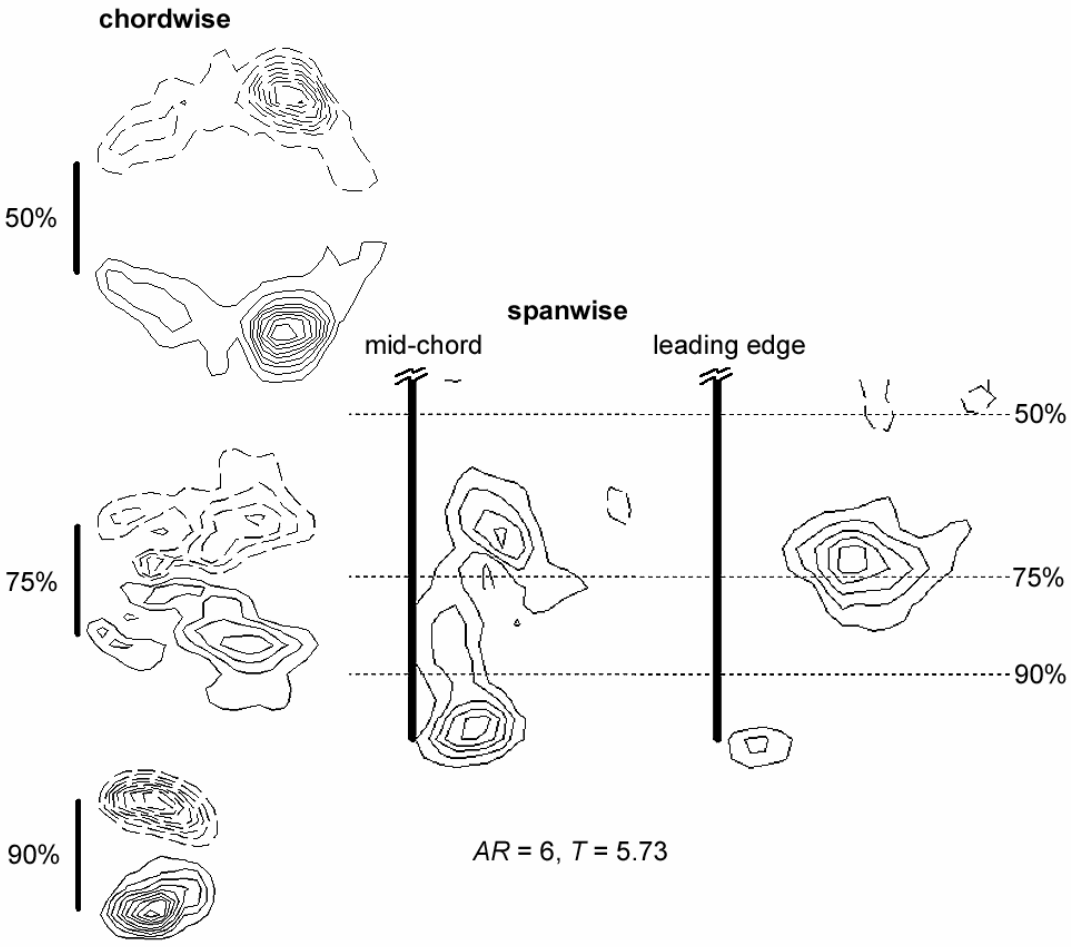

Figure 4.4.7g Tiled vorticity fields for *AR* = 6, *T* = 5.73.
Chordwise: 50, 75, & 90% span; spanwise: mid-chord & leading edge planes.

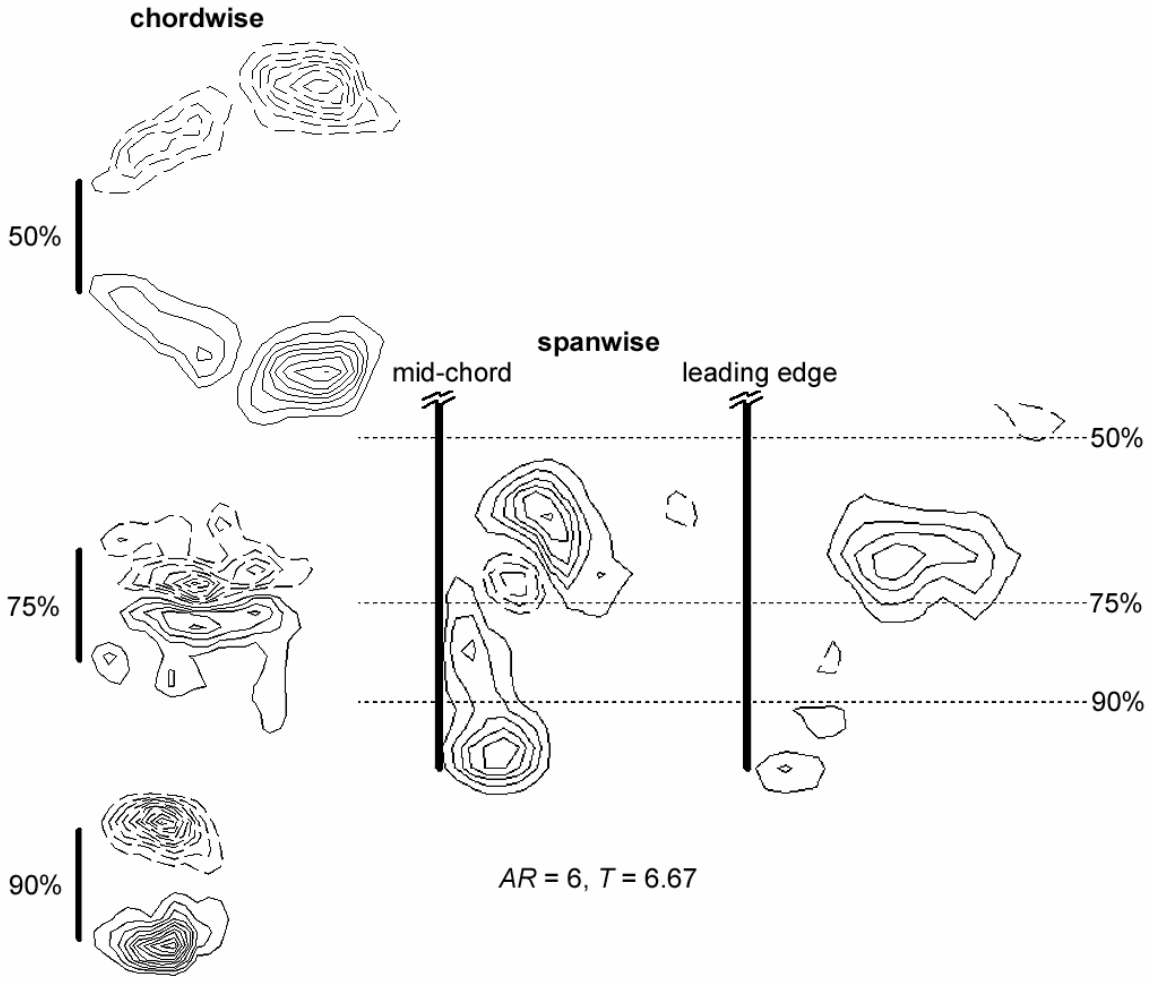

Figure 4.4.7h Tiled vorticity fields for *AR* = 6, *T* = 6.67.
Chordwise: 50, 75, & 90% span; spanwise: mid-chord & leading edge planes.

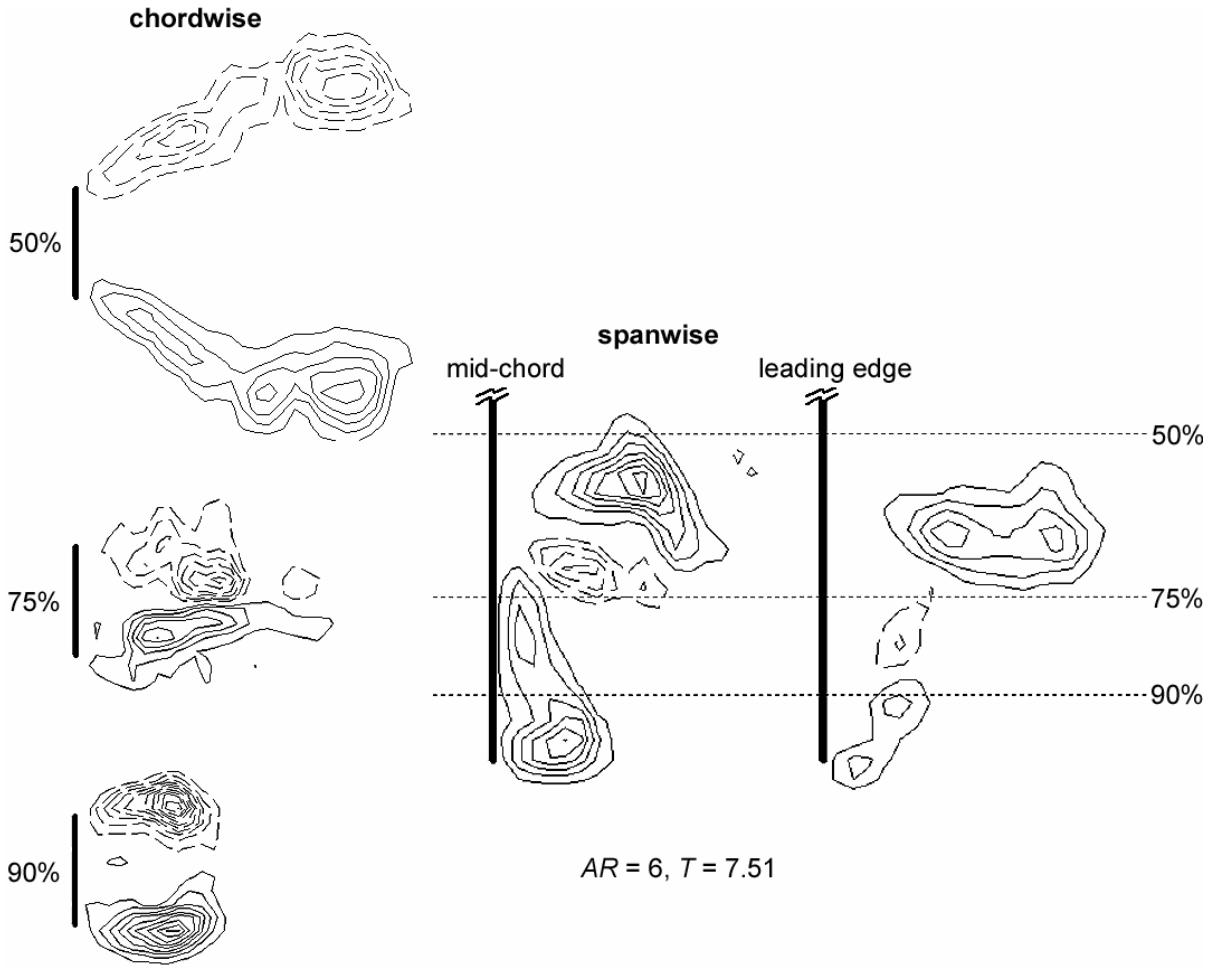

Figure 4.4.7i Tiled vorticity fields for *AR* = 6, *T* = 7.51.
Chordwise: 50, 75, & 90% span; spanwise: mid-chord & leading edge planes.

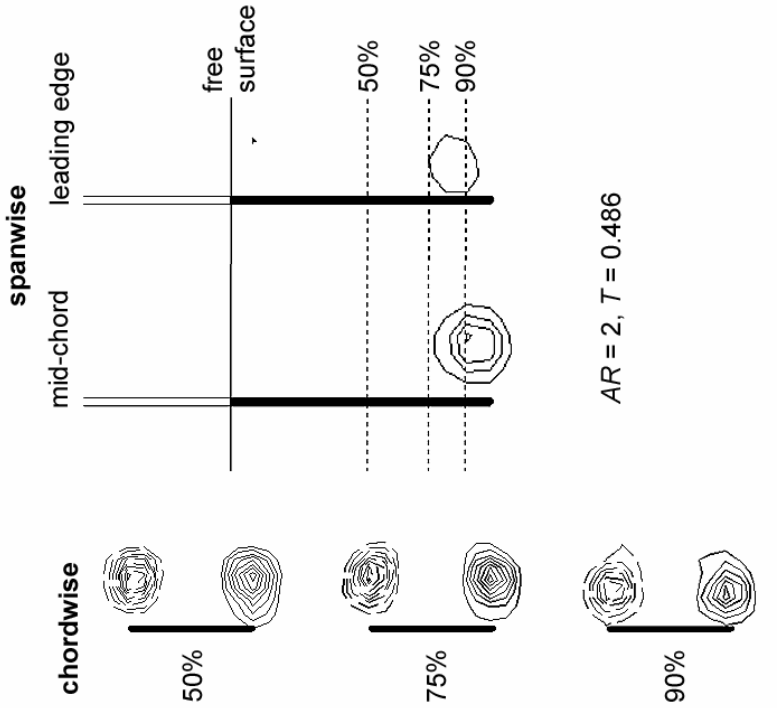

Figure 4.4.8a Tiled vorticity fields for *AR* = 2, *T* = 0.486.
Chordwise: 50, 75, & 90% span; spanwise: mid-chord & leading edge planes.

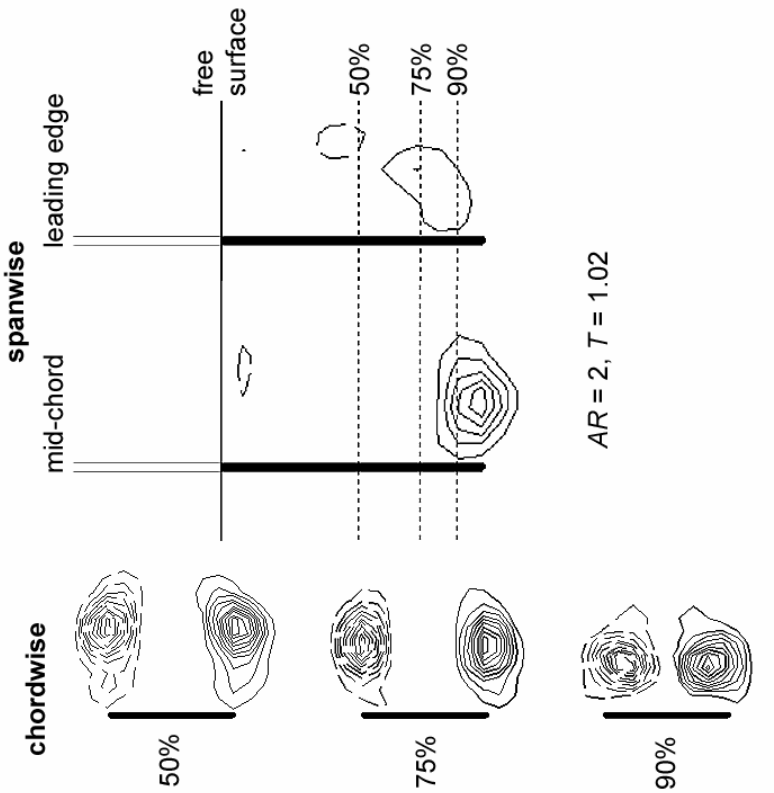

Figure 4.4.8b Tiled vorticity fields for *AR* = 2, *T* = 1.02.
Chordwise: 50, 75, & 90% span; spanwise: mid-chord & leading edge planes.

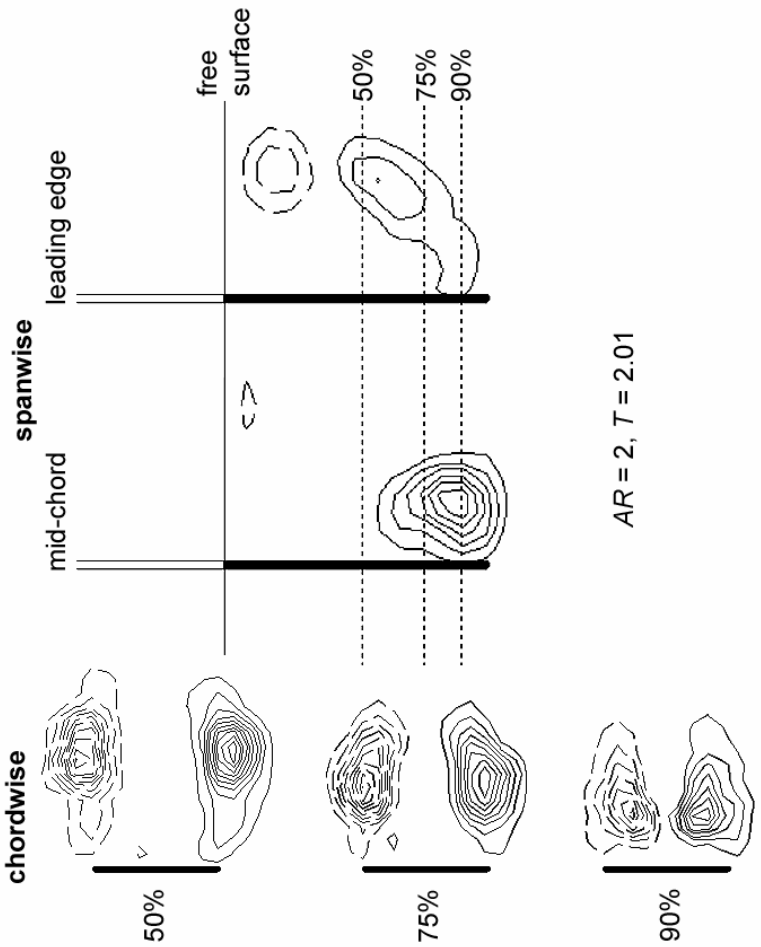

Figure 4.4.8c Tiled vorticity fields for *AR* = 2, *T* = 2.01.
Chordwise: 50, 75, & 90% span; spanwise: mid-chord & leading edge planes.

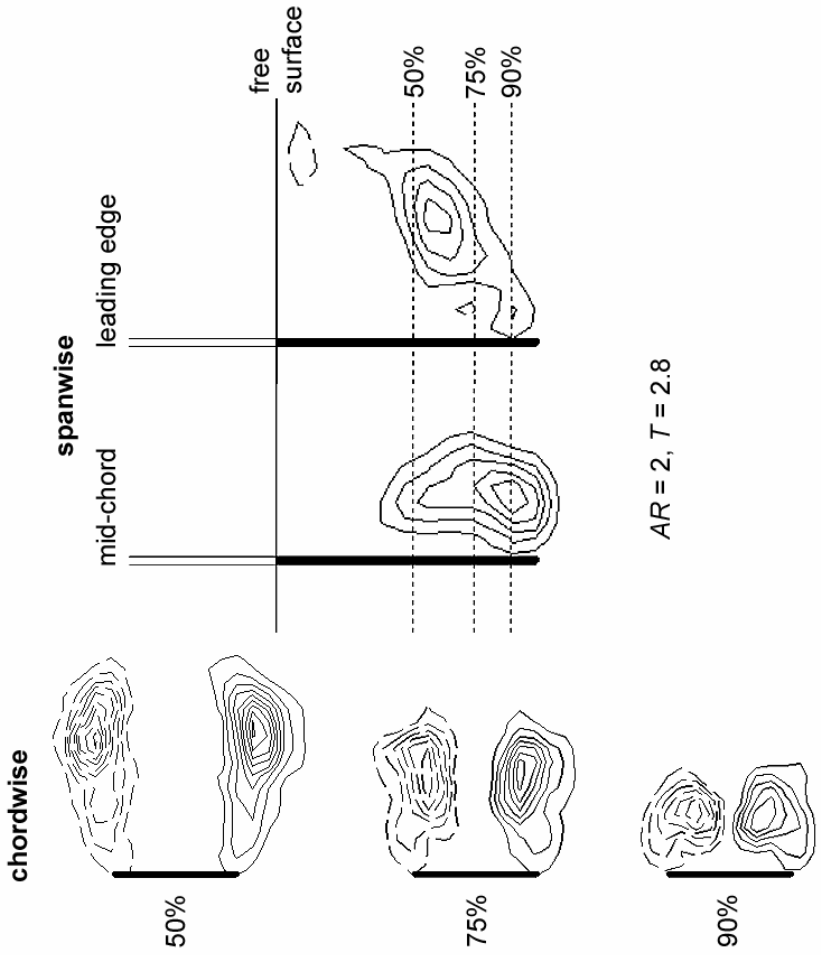

Figure 4.4.8d Tiled vorticity fields for *AR* = 2, *T* = 2.8.
Chordwise: 50, 75, & 90% span; spanwise: mid-chord & leading edge planes.

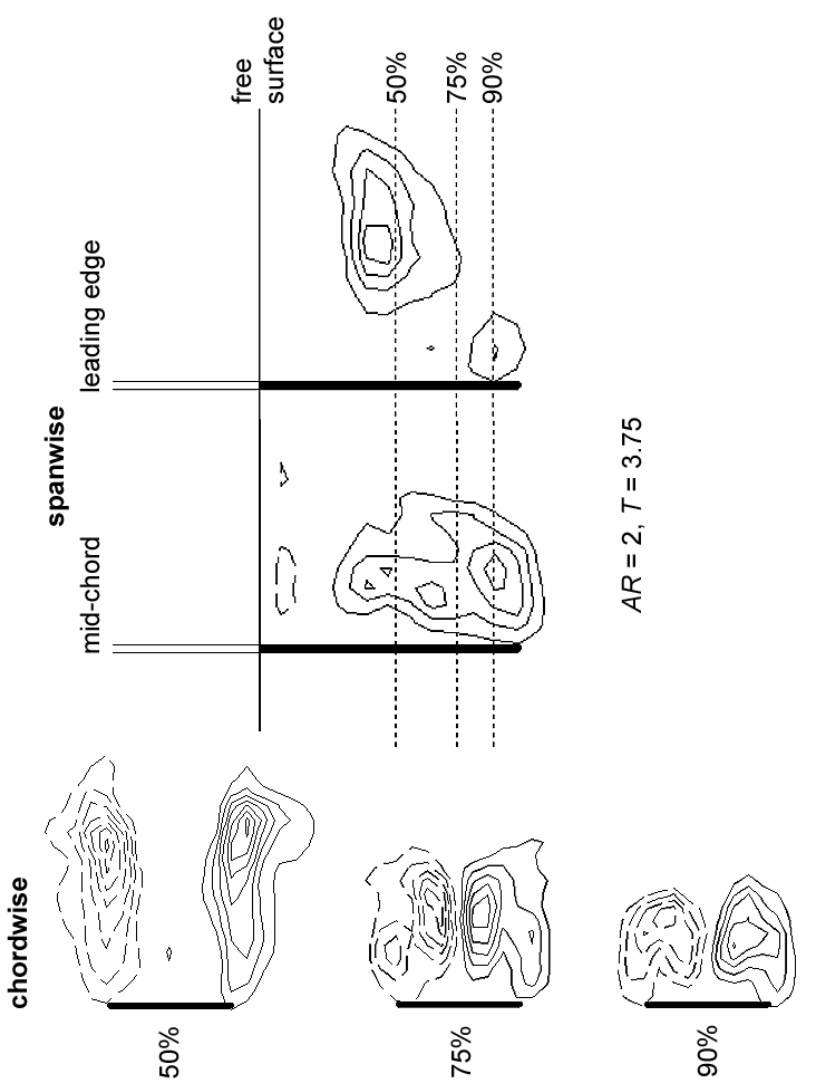

Figure 4.4.8e Tiled vorticity fields for *AR* = 2, *T* = 3.75.
Chordwise: 50, 75, & 90% span; spanwise: mid-chord & leading edge planes.

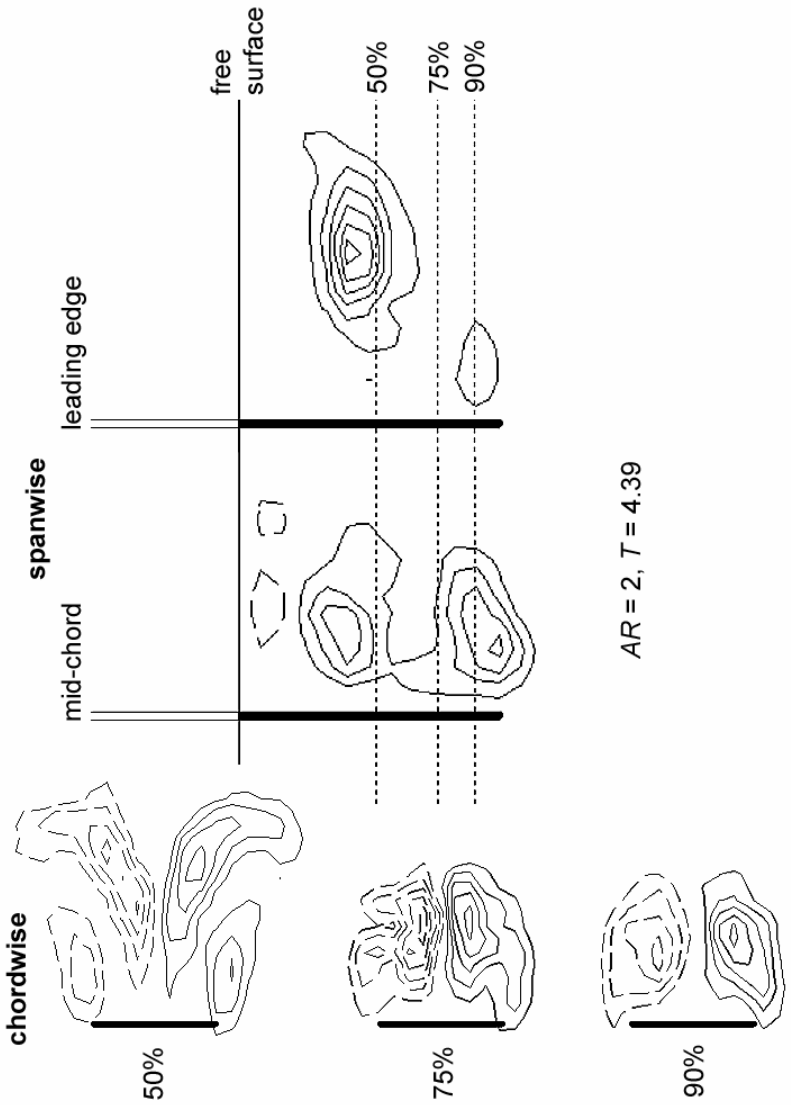

Figure 4.4.8f Tiled vorticity fields for *AR* = 2, *T* = 4.39.
Chordwise: 50, 75, & 90% span; spanwise: mid-chord & leading edge planes.

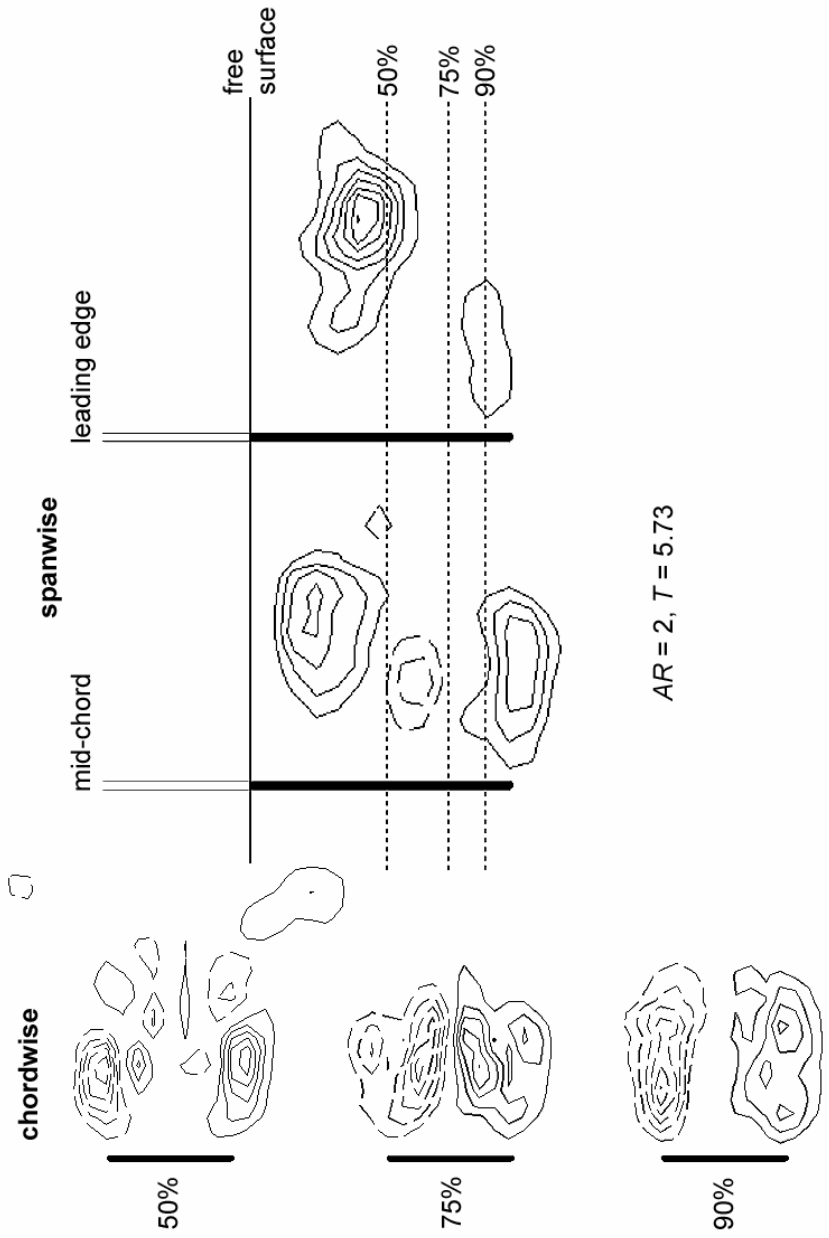

Figure 4.4.8g Tiled vorticity fields for AR = 2, T = 5.73.
Chordwise: 50, 75, & 90% span; spanwise: mid-chord & leading edge planes.

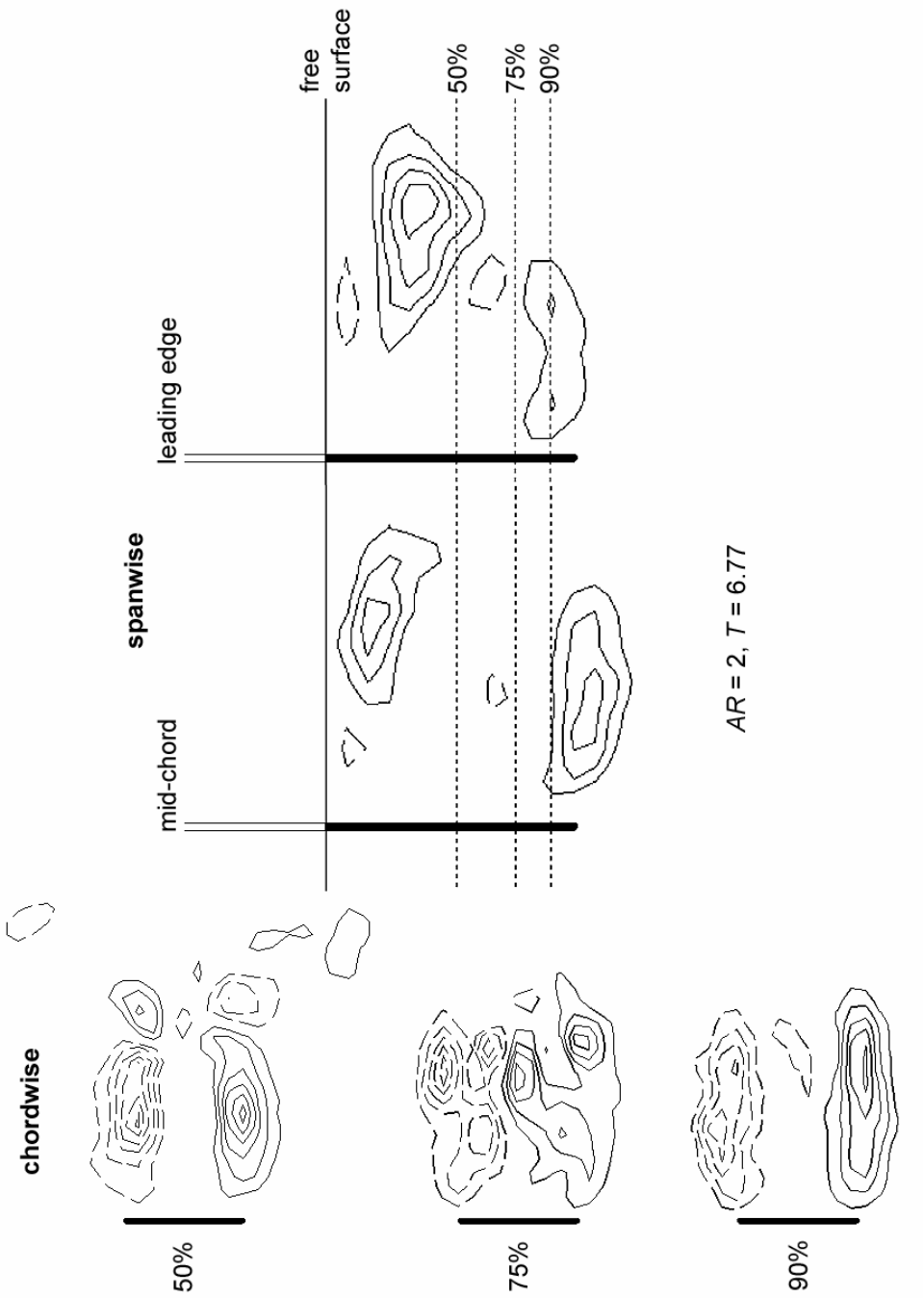

Figure 4.4.8h Tiled vorticity fields for *AR* = 2, *T* = 6.77.
Chordwise: 50, 75, & 90% span; spanwise: mid-chord & leading edge planes.

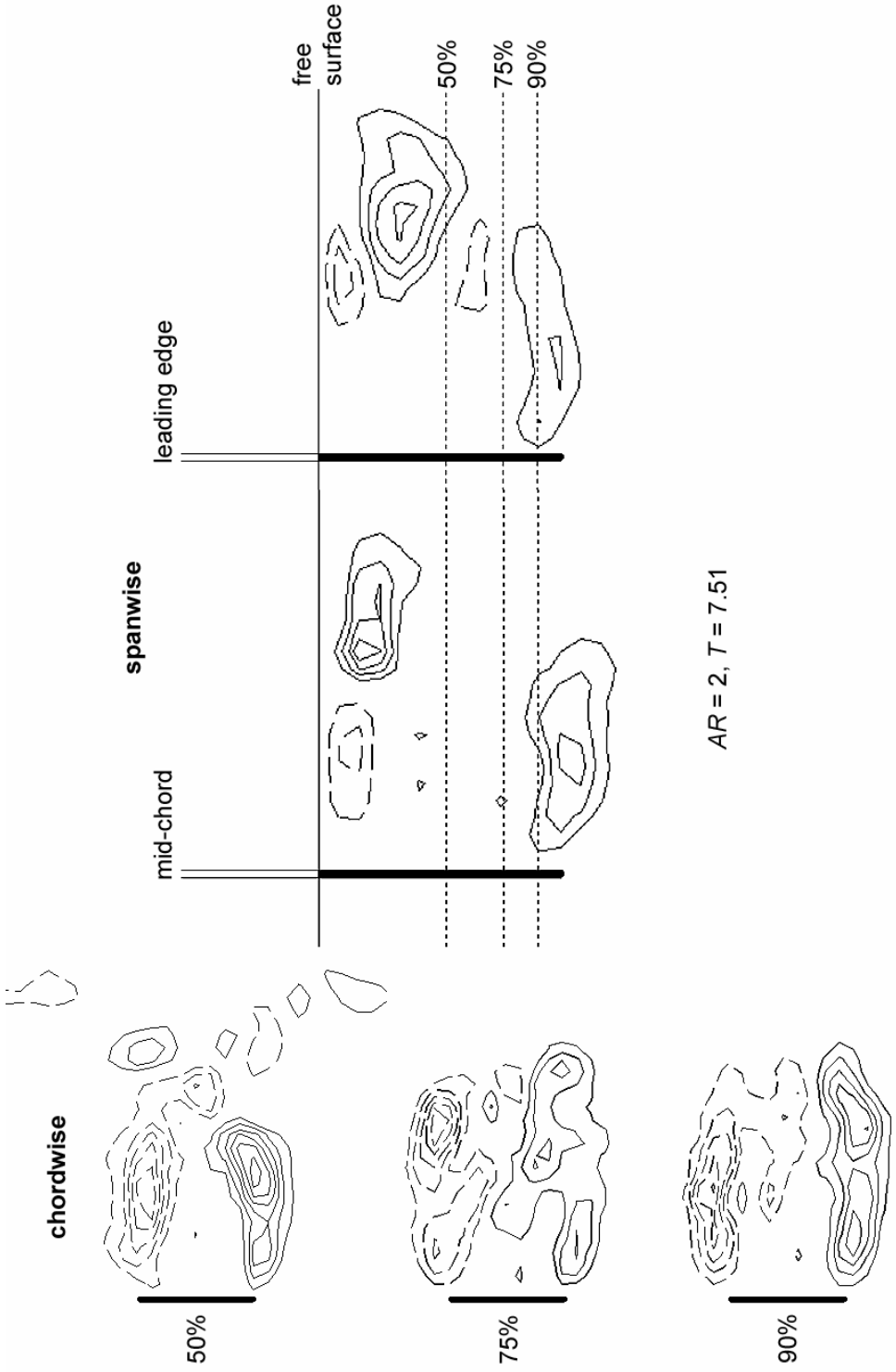

Figure 4.4.8i Tiled vorticity fields for *AR* = 2, *T* = 7.51.
Chordwise: 50, 75, & 90% span; spanwise: mid-chord & leading edge planes.

4.5 Dye visualization and flow features explained

4.5.1 Introduction

In this section a model for the flow near the tip at the startup, using vortex line behavior based on flow visualization, will be presented. Following that, the global flow will be described based on 3-D flow visualization and the DPIV results. Next, the flow near the tip will be reconciled with the global flow using evidence from flow visualization. Afterward, some of the features in the spanwise DPIV sections, such as the vorticity in the leading edge plane and the rapid growth of vorticity at mid-span, will be explained via flow visualization. Finally, a comparison will be made with previous work.

4.5.2 Vortex line model of the startup

The evolution of the vorticity generated by the plate near the tip at the startup will now be modeled using a sequence of vortex line snapshots, based on induced velocity arguments and evidence from flow visualization. Figures 4.5.1a-f show a close-up view of the bottom right corner of the leeward face of the plate. The thin lines in the Figures are vortex lines, and the arrows show their sense of rotation. During the initial acceleration from rest, the flow separates at the leading edge and the tip edge, and rolls up to form vortices behind each edge (see Figure 4.5.1a). The flow is primarily 2-D at this stage, since the vortices have not yet had enough time to interact and viscous effects are small; this makes the vortex lines essentially straight. Additionally, the vortices at each edge connect in the corner, because the flow that separates there shares their rotational sense, which is directed away from the plate's edges.

As the leading edge and tip vortices grow stronger, they interact in the corner region, inducing a velocity on the corner vortex that acts to rotate it up and away from the surface of

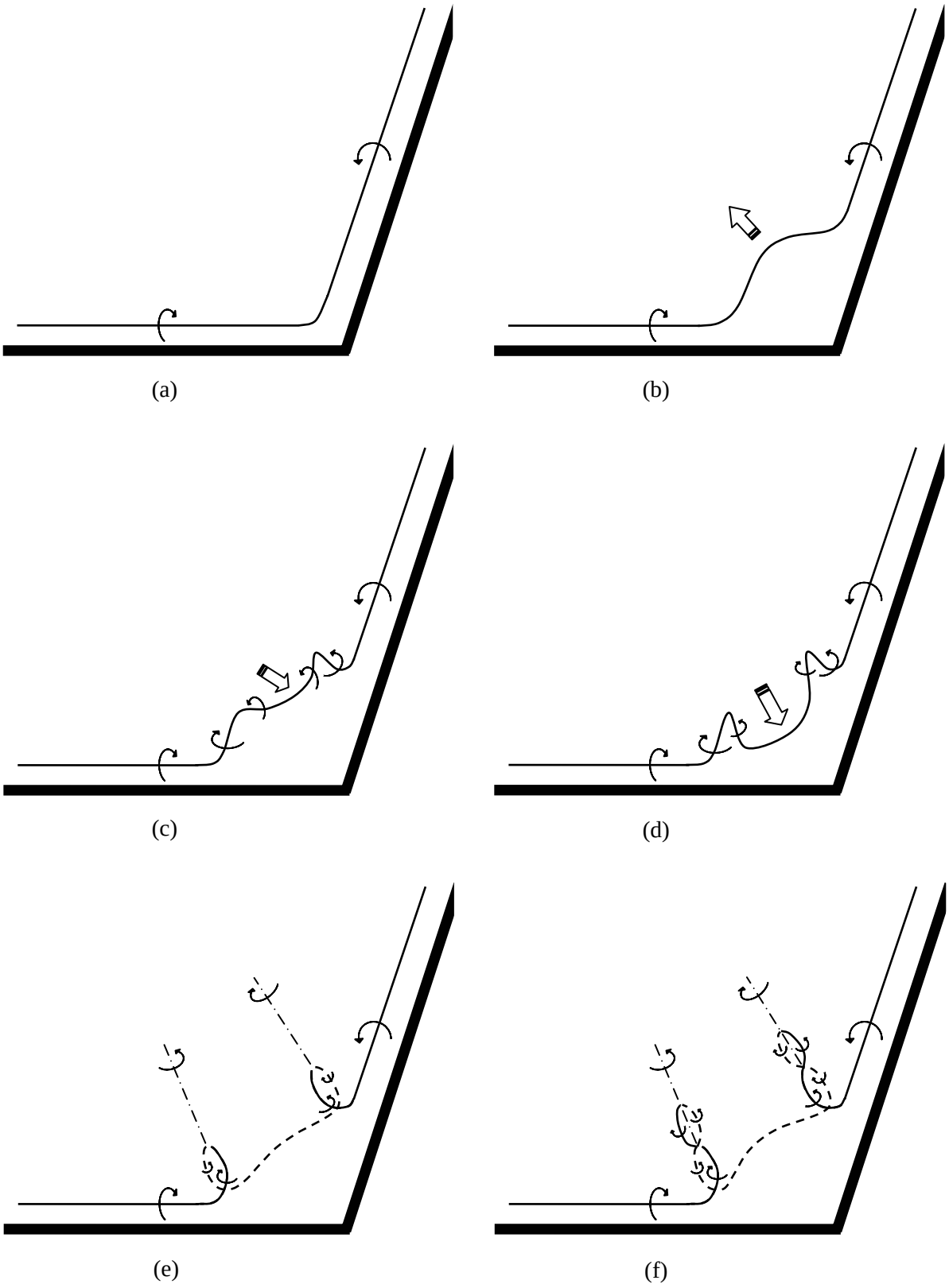

Figure 4.5.1 Vortex line model of the flow near the tip at the startup. Right-hand corner of leeward plate face shown; flow is symmetrical about mid-chord line.

the plate and away from the corner itself (see Figure 4.5.1b). Once the corner vortex is lifted upward, its "upright" sides, which have opposing senses of rotation, induce velocities such that they fold slightly toward each other. This causes the vortex line connecting them to bow, in a plane roughly parallel to the plate face, back toward the corner (see Figure 4.5.1c). In this orientation, the induced velocities from the ends of the bowed line segment, as seen in Figure 4.5.1c, act to push it downward toward the plate face (see Figure 4.5.1d). This causes each end of the bowed segment to kink and pinch together to form an inverted V, with adjacent legs of the V having opposite rotational directions.

From the flow visualization, which will be described next, it is clear that the strength of the two inner inverted V legs, i.e., those attached to the bowed connecting vortex line, coupled with the induced velocity from the 2 primary edge vortex lines, which acts away from the corner and also down toward the plate face, is enough to twist the two inner V legs back behind and around the outside of the outer V legs. This also stretches the connecting vortex line and pulls it away from the corner, giving rise to the configuration shown in Figure 4.5.1e. The centerlines emanating from the twisted V's show the rotational sense of the twisting. Finally, the twisting of each set of vortex lines perpetuates into a helical pattern, and both helices are drawn away from the plate's edges and toward the interior of the wake by the induced velocity from the tip and leading edge vortices (see Figure 4.5.1f).

The dye blob method used to visualize the flow at the startup was not able to capture the initial 2-D phase shown in Figure 4.5.1a, nor was it able to capture the lifting up of the corner vortex illustrated in Figure 4.5.1b. Both are very short-lived, and are lost in the initial dye blob that is "painted" on the plate. However, the chordwise and spanwise vorticity fields obtained from the DPIV measurements, and reported in the tiled Figures in section 4.4, show

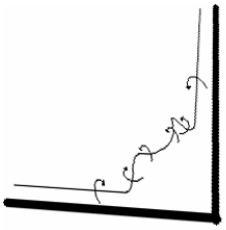

Fig. 4.5.1c **(c)**

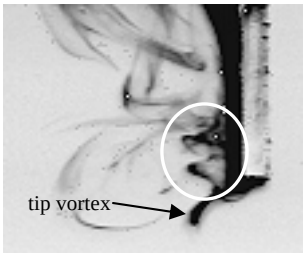

right-side view

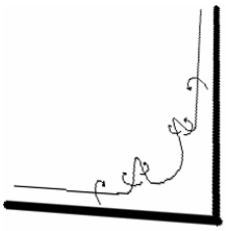

Fig. 4.5.1d **(d)**

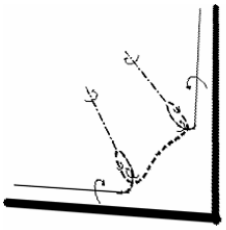

Fig. 4.5.1e **(e)**

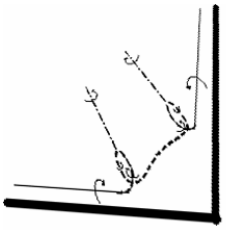

Fig. 4.5.1e **(e+)**

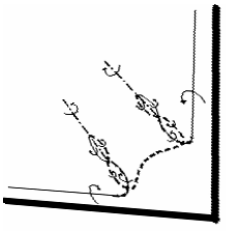

Fig. 4.5.1f **(f)**

Figure 4.5.2 Comparison of dye blob visualization with vortex line model.

the edge vortices in question, and that the flow is very 2-D at the startup for both aspect ratios 6 and 2. Additionally, the dye blob visualization shows evidence of the flow in Figure 4.5.1c, of which Figures 4.5.1a and b are legitimate precursors. Given this, coupled with the induced velocity arguments, it is very likely that the actual flow starts out the same way as the model.

Figure 4.5.2 gives a side-by-side comparison between the remaining steps of the vortex line model and the 3-D dye blob visualization. In the left-hand column, Figures 4.5.1c-f are reproduced and skewed to the appropriate orientation to match the visualization images. The right-hand column consists of the corresponding dye blob snapshots; the letter labels of both figures have also been matched. Figure 4.5.2 (c) shows that the dye has been lifted off the corner and is concentrated in the "upright," inwardly folded sides of the corner vortex. In Figure (d), where the model predicts that the vortex line connecting the sides of the corner vortex should be bent down toward the plate, this can be seen in the upper-right side of the corner vortex. The dye that is initially lifted up in that side curls back toward the plate as it approaches the middle of the corner vortex. This downward motion of the connecting vortex line creates kinks, resembling inverted V's, in each of its ends. These 2 kinks or V's, with their apices pointing left, can be seen in the blob visualization snapshot at the far left in Figure 5.4.2 (d), which shows a view of the right side of the plate. The model predicts that the inner legs of both V's will then twist behind (i.e., away from the corner) and around the outside of the outer legs. The result of this motion can be seen in the blob visualization snapshots of Figures 5.4.2e and e+ (a short time later); the video that the snapshots were taken from confirms this twisting mechanism. Finally, the helical pattern that results from the interaction of the twisting vortex lines, which is then drawn into the wake,

can be seen in the upper pair of twisting vortices in the snapshot in Figure 4.5.2f; there is too much dye in the lower helix to resolve its details. Thus, the flow visualization supports each of the main steps of the proposed vortex line model.

4.5.3 Global flow

The larger-scale 3-D flow around the aspect ratio 6 plate was visualized using fluorescent dye injected from two rakes attached to the upstream face of the plate; the dye injection holes were in the tip region. As expected, the results agreed with the sectional DPIV measurements. However, since 2-D DPIV does not capture flow perpendicular to the measurement plane, this visualization was necessary to establish the 3-D structure of the flow.

Figures 4.5.3a through d show snapshots from the movie of this dye flow visualization, which was taken at a Reynolds number of 2000 so that the details would be cleaner. Given the perspective of the movies, it should be noted that the top of the plate in each image at about 50% span. Since the dye was injected from the upstream face of the plate, it fed into the wake via the shear layers at the edges. This created an absence of dye near the leeward surface of the plate in the vicinity of the tip, because the shear layers enclose the wake there. However, the dye did highlight the evolution of the LEVs, which was the purpose of the experiment, and it also captured the tip vortex at the startup. Although the flow features local to the tip were described above, two additional snapshots from a larger-scale blob visualization are given in this section to show the flow in the corners when it is more fully developed at later times. Finally, it should be remarked that the flow visualizations show the instability in the edge shear layers discussed in earlier chapters. This

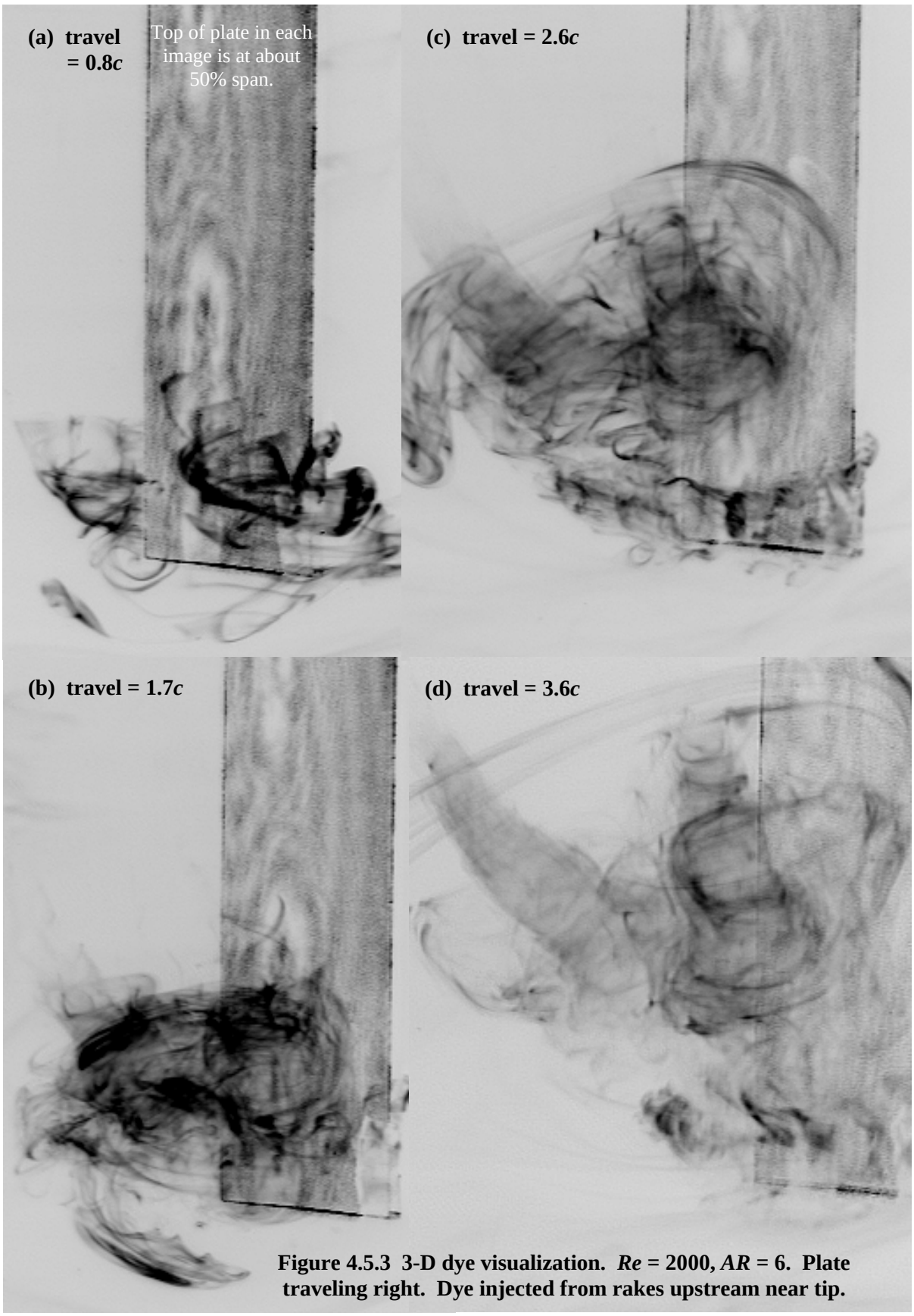

Figure 4.5.3 3-D dye visualization. *Re* = 2000, *AR* = 6. Plate traveling right. Dye injected from rakes upstream near tip.

is particularly evident in Figure 4.5.3c, where the leading edge instabilities are manifested as vertically-oriented ripples in the shear layers inclosing the wake near the tip.

An image taken after about 0.8 chord lengths of travel is shown in Figure 4.5.3a. The tip vortex can be seen in the left-hand corner, and the dye in the leading edge shear layers has rolled up into the LEVs, which already have a significant upward spanwise velocity. The 3-D development of the LEVs is now evident. The low pressure created at the tip by the induced flow from the tip vortex causes the LEVs there to stay closely attached to the plate, and to remain weaker than their counterparts away from the tip (recall the LEV circulation measurements of section 4.3). Since the LEVs away from the tip are stronger, they have comparatively lower pressure than those closer to the tip. This pressure gradient within the LEVs causes a spanwise flow (again, within them) that is directed away from the tip. When coupled with their rotation, this gives them a helical structure. As the plate continues forward to a distance of about 1.7 chord lengths, the upward convection of the LEVs continues (see Figure 4.5.3b). At this point, the LEVs near the plate tip have remained close to each other and the plate, but, at higher spanwise locations, their cores have grown farther from the wake centerline and the plate face; this is in total agreement with the DPIV data. Additionally, the helical structure of the LEVs is illustrated by 2 dye filaments at the top of the right-most LEV. By 2.6 chords of travel, shown in Figure 4.5.3c, the dye within the LEVs has been convected farther from the plate tip, and it reveals that, at these spanwise locations, the LEVs continue to grow away from the plate, while the LEVs near the tip remain tightly attached. The curved “front” of dye traveling up the face of the plate, which is connected to more dye seen to the lee of the left-most LEV, is actually dye drawn into the wake centerline that is pulled toward the face of the plate. Finally, Figure 4.5.3d reveals the

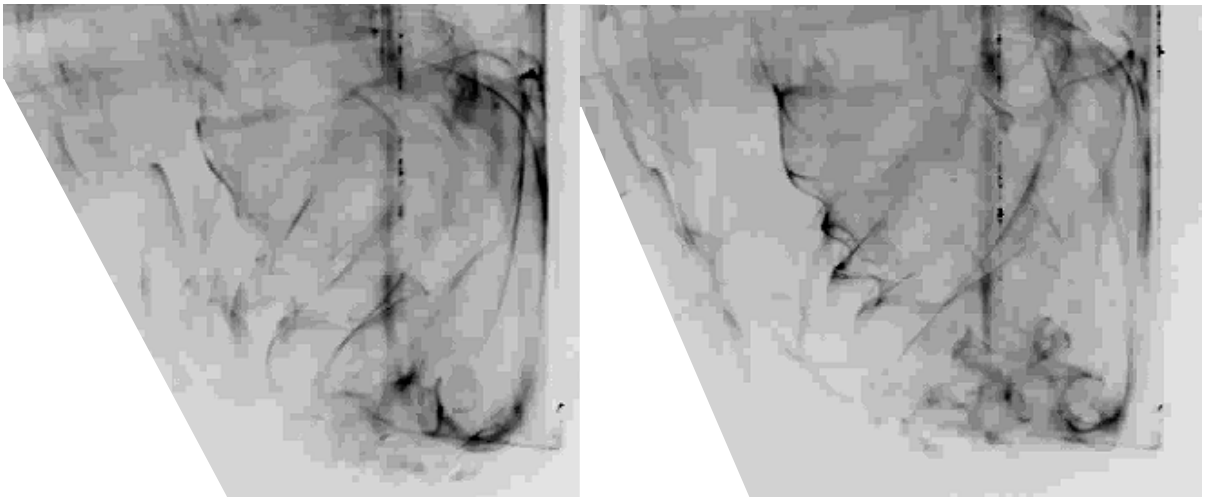

(a) ~ 4*c* of travel (b) ~ 4.5*c* of travel

Figure 4.5.4 3-D dye blob visualization, isometric view of leeward face of plate. *Re* = 2000, *AR* = 6. Plate moving right. Dye blob "painted" on leeward face.

situation after the plate has moved about 3.6 chord lengths. The flow at this point has evolved much as before: the LEVs are still attached near the plate tip, while at higher spanwise locations they bow out and proceed toward pinching-off. This snapshot also shows that the tip effect causes the LEVs to stretch, which is evident by their change in radius as the dye is convected upward.

Figure 4.5.4a shows the same flow at about 4 chord lengths of travel, visualized by depositing a large blob of dye on the rear face of the plate. Although the cores of the LEVs are not captured in this visualization, it does show their external, bowed structure, along with folds indicative of the shear layer instability. More importantly, it shows how the vortex lines in each of the plate's corners have evolved from the two counter-rotating helices described in the previous section. They have merged together and are rotating in the direction of the (upper) helix that emanated from the leading edge vortex (which is stronger than the tip vortex); the snapshot is part of a movie, which shows the sense of rotation clearly. Also, it reveals that these merged vortex lines, which grow out of the plate's corner region, are first drawn down toward the tip before they subsequently bend back upward and

are fed into the leading edge vortex closest to them. This indicates that, near the tip, there is a pressure gradient along the face of the plate that draws the flow toward the tip. This pressure gradient is most likely due to induced velocity from the tip vortex where it is adjacent to the plate. However, within the LEVs, the pressure gradient draws the flow away from the tip. The second snapshot (Figure 4.5.4b), taken a short time later after about 4.5 cords of travel, demonstrates again the helical structure of the LEVs, which have induced the same behavior in the corner vortices.

An explanation is now possible for the presence of vortical structures in the vorticity fields obtained from the DPIV in the leading edge plane. From the 3-D visualization in Figure 4.5.3, it is apparent that the tip effect bends the LEVs so that their vorticity vectors have components perpendicular to the leading edge plane. Given the rotational sense of the LEVs, if they are bent outwardly, or away from the wake centerline, when they intersect the leading edge plane, the vorticity in that plane will appear to have the same sign as the tip vortex (in this case positive). If the LEVs are bent inwardly where they impinge the leading edge plain, the resulting vorticity in that plane will be negative.

Three of the tiled vorticity field diagrams from section 4.4, for $AR = 6$, are reproduced in Figure 4.5.5 to illustrate this point. In the chordwise vorticity sections, the leading edge plane is marked by a dash-dot line, and the corresponding vorticity in that plane is, as before, given in the right-most tile of each diagram. The core of each LEV in the chordwise sections is marked with a large dot, so that the position of the core with respect to the leading edge plane is highlighted.

The vorticity at $T = 2$ is shown in Figure 4.5.5a. At 50% span, the LEV cores are very close to the leading edge plane; the core of the positive LEV is just inside (i.e., closer to

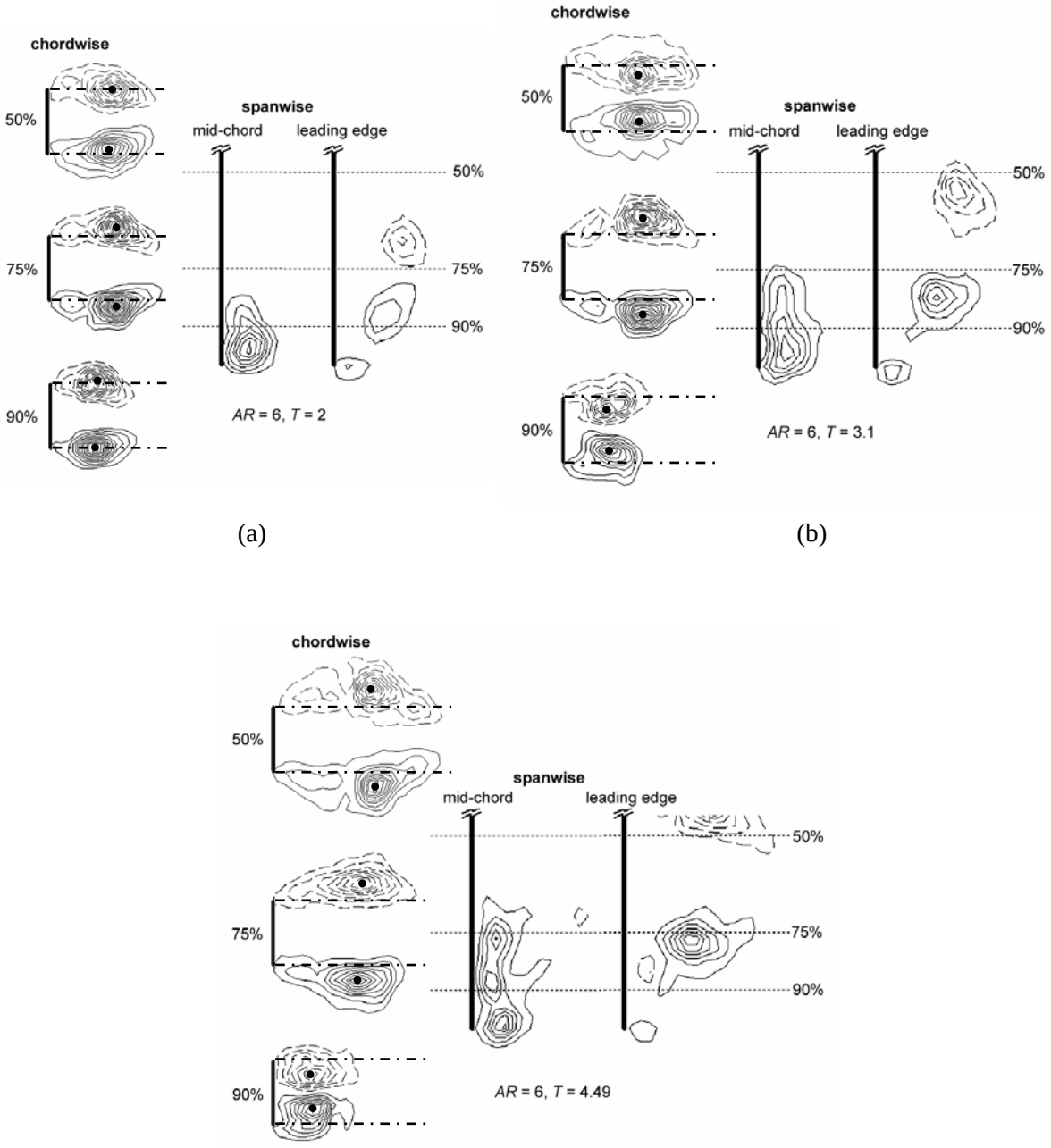

Figure 4.5.5 Tiled vorticity plots, for *AR* = 6, from section 4.4 illustrating the connection between vorticity in the leading edge plane and LEV core locations in the chordwise planes. In the chordwise tiles, the positions of the leading edge planes are marked with a dash-dot line, while the LEV core locations are marked with black dots. The flow is essentially symmetrical, so DPIV data was taken in only one leading edge plane.

the wake centerline) of it. The LEV cores at 75% span are a bit outside (relative to the wake centerline) of the leading edge planes. Therefore, between 75 and 50% span, the LEVs bend slightly inward, toward the center wake. According to the prediction above, this should result in the appearance of a negative vortex in the leading edge plane between 75 and 50% span, which Figure 4.5.5a shows. The LEV cores at 90% span are very close to the leading edge, implying that between 90 and 75% span, the LEVs are bent outwardly. This should produce a positive vortex in the leading edge plane between 90 and 75% span, which can be seen in the Figure. At $T = 3.1$, the chordwise shift in LEV core locations from 90 to 75% span is more extreme (see Figure 4.5.5b), and the LEVs themselves have acquired more circulation. This causes the positive vortex visible in the leading edge plane, between those spanwise locations, to grow stronger (see Figure 4.5.5b). Also, the LEV cores at 75% span are more leeward than those at 90% span. This implies that the rearward location of the core of the positive vortex in the leading edge plane should be somewhere in between, which it is. The LEVs at 50% span have moved closer to the wake centerline and increased in circulation, which results in the negative vortex between 75 and 50% span growing stronger than its $T = 2$ counterpart. Finally, Figure 4.5.5c shows the vorticity at $T = 4.49$. The cores of the LEVs at 75 and 50% span are nearly the same chordwise distance from the leading edge planes, and so there is little vorticity in the leading edge plane between these spanwise locations. Between 90 and 75% span, the LEV core locations have not changed significantly since $T = 3.1$. However, the circulation of the LEVs at 75% span is greater, so the positive vortex in the leading edge plane is stronger.

The tiled vorticity diagrams in Figure 4.5.5 show that the positive and negative vortices in the leading edge plane grow stronger and propagate away from the plate tip with

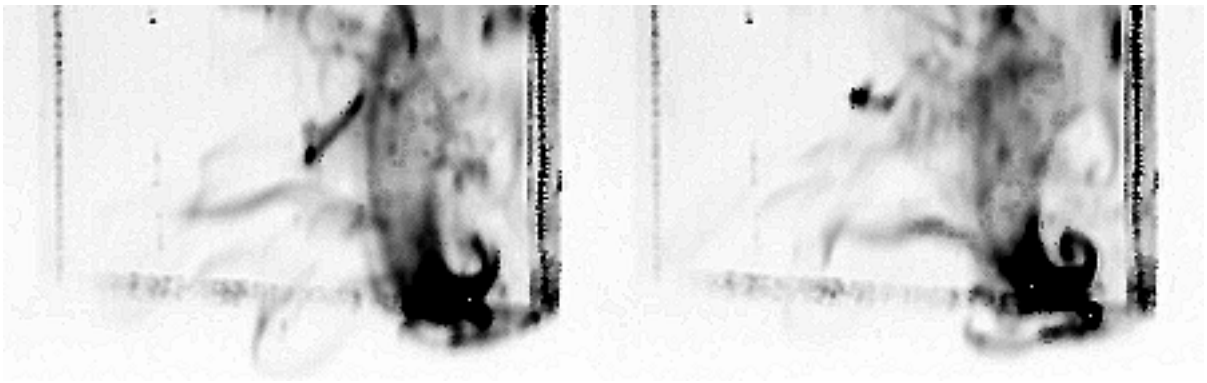

(a) ~ 0.9*c* of travel

(b) ~ 0.96*c* of travel

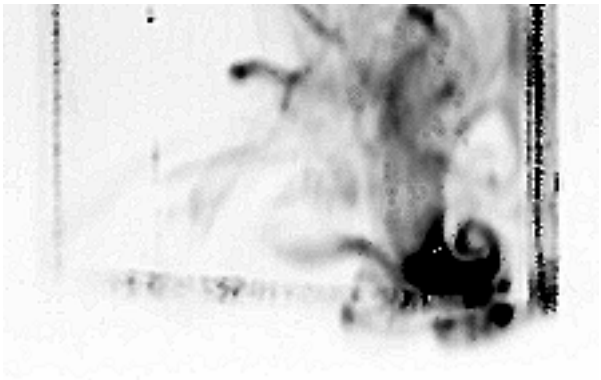

(c) ~ 1*c* of travel

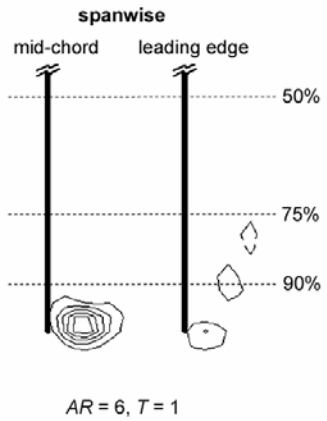

(d) spanwise DPIV, $T = 1$

Figure 4.5.6 (a)-(c) Bifurcation of tip vortex into helical corner vortex and a smaller, outboard tip vortex near the leading edge. *AR* = 6, *Re* = 3000. (d) Spanwise DPIV of same flow at *T* = 1.

time. This agrees with the global flow visualization snapshots given in Figure 4.5.3, which illustrate the spanwise flow within the LEVs directed away from the tip. It should be remarked that the same bending of the LEVs occurs for $AR = 2$. As with the $AR = 6$ case, the chordwise LEV core positions at each spanwise location predict the sign of the vorticity in the leading edge plane.

Lastly, the small positive vortex seen attached to the plate tip in the leading edge plane (see Figures 4.5.6d and 4.5.5a-c) must be explained. Initially, it seems that this vorticity may be due to the corner vortices described above. However, Figure 4.5.2 shows

that the 2 helical vortices in the corner are closer to the wake centerline than the leading edge itself. Also, according to Figures 4.5.2 and 4.5.5, the vorticity vectors of these corner vortices appear to be directed normal to the plate face and toward the center wake. Given this, it seems unlikely that the vorticity near the tip in the leading edge plane would be due to these vortices. Figure 4.5.6 shows that this vorticity may in fact be from the tip vortex bifurcating into a vortex line that ends up being the corner, helical vortex, and another vortex line parallel to the tip edge, which has the same rotational sense as the main tip vortex. The curled-up dye in the plate's corner in Figure 4.5.6b follows the rotational sense of the helical corner vortex that is there. Below and to the right of that dye, the remaining dye travels out along the tip edge toward the leading edge (see Figure 4.5.6c), and rotates with the same direction as the primary tip vortex at mid-chord. The motion and location of this dye along the tip edge entirely fits with the vorticity seen in the leading edge span at that location and time (see Figure 4.5.6d).

4.5.4 Connection between corner and global flow

A complete picture of the flow requires that the vortices in the plate's corners are reconciled with the global flow of the LEVs just described. A 3-D dye blob visualization of the LEV at one edge, as well as the corner vortices below it, was done using a laser cone for illumination, with the camera looking at the side of the plate (i.e., facing a spanwise plane parallel to the flow). Dye was deposited in the corner of the plate closest to the camera, as well as near the tip edge at mid-chord. The dye in the corner allowed the visualization of the 2 helical vortices that emanate from there, which were described in section 4.5.2. The dye at the tip near mid-chord was convected into the leading edge vortex of the edge closest to the camera.

Figure 4.5.7 provides 7 snapshots from this dye flow visualization. Image *a*, taken at about 1.1 chord lengths of travel, shows the two kinked vortices in the corner that are described by the vortex line model (see Figure 4.5.1d); the kinks are just starting to twist around themselves. Also, the lower portion of the LEV created by the leading edge closest to the camera can be seen, and it has an upward, spanwise velocity component. This LEV has been made visible by the dye blob originally placed near the tip at mid-chord, which was convected into the center wake by the LEV, then pulled out into the edge shear layer, and finally rolled-up into the vortex itself. Some of that same dye remains in the center wake, visible as a dark, horizontal band. This band travels upward at the spanwise velocity of the LEV, and feeds out into the leading edge shear layer (the outer shear layer of the LEV) from the center wake. Thus, this dye marks the rolled-up shear layer forming the outer boundary of the LEV, as well as the inner region of the vortex. Dye near the tip, seen below the corner, tags the tip-edge shear layer that rolls up into the tip vortex. Ripples in both the leading and tip edge shear layers (especially apparent in the later snapshots) are caused by the instabilities there, predicted by Koumoutsakos and Shiels (1996).

A short time later, after 1.2*c* of travel (see Figure 4.5.7b), the 2 kinks in the corner vortex have twisted around themselves to form the helical vortices described by the model and shown in Figure 4.5.1f. The LEV has grown larger, and the upward convection of the dye marking it reveals the upward spanwise flow within the vortex. Snapshots *c* and *d*, taken at about 1.3*c* and 1.5*c*, respectively, show that the 2 helical vortices at the corner have extended farther out, horizontally, into the wake. They have also moved closer to one another, and by snapshot *f* they have become a single entity, rotating in the direction of the upper of the two former helices. This is consistent with the visualization in Figure 4.5.4a,

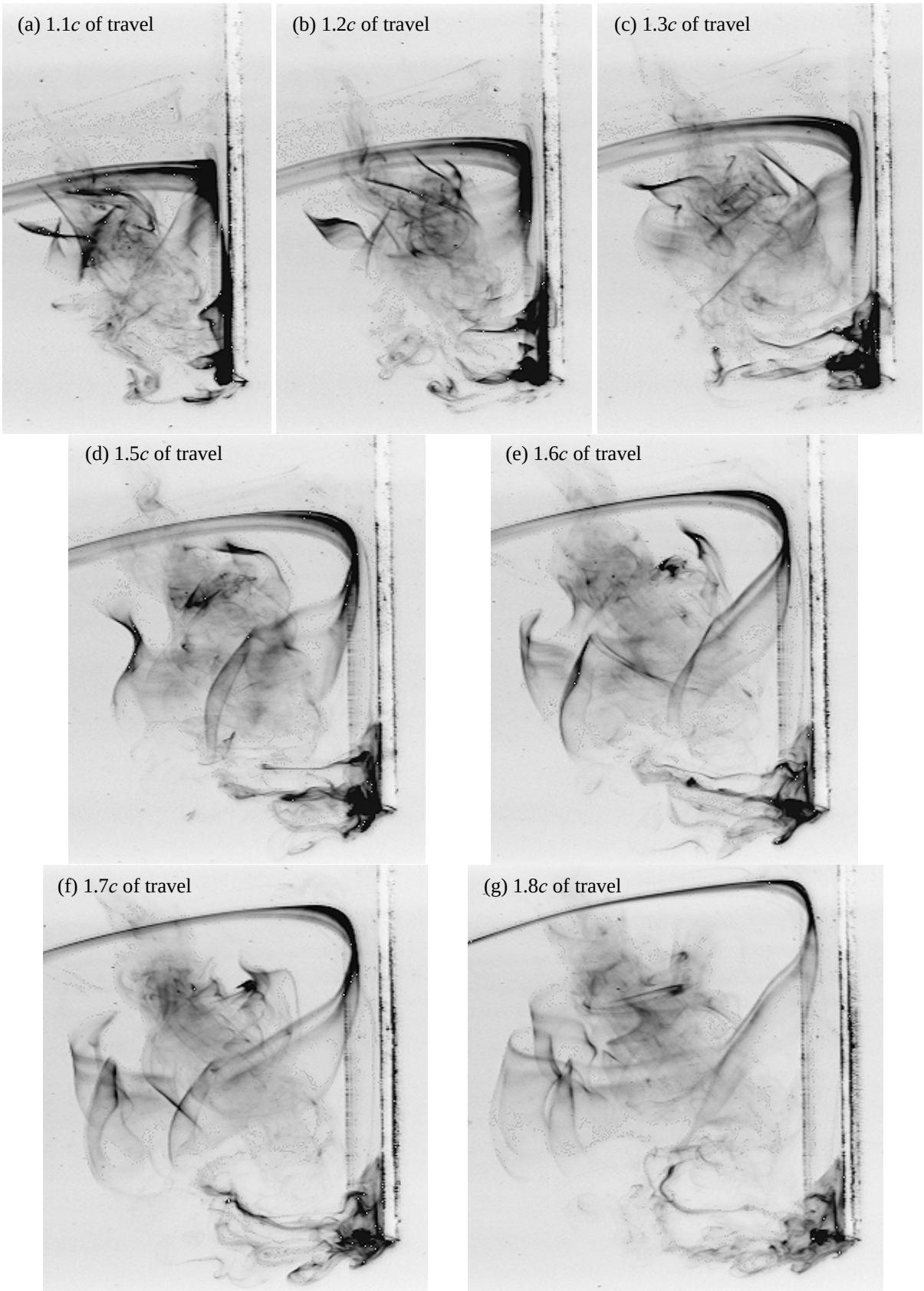

Figure 4.5.7 Dye blob vis., *AR* = 6, *Re* = 3000, reconciling corner vortices & the main LEV.

captured when the flow is more developed, which shows that the 2 helical vortices have merged. As expected, Figures 4.5.7c and *d* indicate that the LEV has grown larger and the dye has been convected farther upward as time progressed. The leading edge shear layer instability is also visible as vertically-oriented ripples in its ribbon-like structure, which rolls up into the LEV.

Figures 4.5.7f and *g* finally reveal how the corner vortex interacts with the main leading edge vortex. Especially visible in snapshot *g*, the corner vortex has been drawn into the LEV. However, it is not pulled straight through the LEV core. Instead, behaving as it should like a material line, it follows the rotating, helical velocity of the much stronger LEV, wrapping, so-to-speak, probably around an inner layer of the LEV between the LEVs outer shear layer and its core. This behavior is clearer in the video these images were taken from. The conclusion that the corner vortex is within the LEVs outer shear layer is based on an extrapolation of the visible part of the shear layer, above the corner, down to the level of the corner.

4.5.5 The decrease in LEV circulation near the tip

Kelvin's Theorem, $\frac{D\Gamma}{Dt} = 0$, for a baratropic, inviscid fluid subjected to only a potential body force, states that the circulation around a material loop does not change with time (Green, 1995). Since the circulation measured in the chordwise planes decreases with decreasing distance from the tip (see Figure 4.5.8), Kelvin's Theorem dictates that this "lost" circulation must go somewhere. Viscous dissipation cannot be solely responsible for this decrease in circulation, because there is not enough time for it to become significant. However, there are other plausible solutions to the problem. Given the vortex line model developed in section 4.5.2, it is possible that the vorticity of the LEVs near the tip is fed into

the corner vortices. Depending on how these vortices develop spatially, this might reduce the circulation of the LEVs near the tip, and increase that of the corner vortices. Another explanation for the drop in circulation is that interaction with the plate itself is responsible. Vorticity could be lost at the plate surface, or secondary vorticity generated near the plate surface, of opposite sign, might lower the total circulation measured at a single edge. Finally, since the flow is highly 3-D near the tip, the circulation measured in the 2-D DPIV sections may not reflect the actual circulation there.

4.5.6 Mid-chord vorticity features explained

A conspicuous feature common to both the AR = 2 and 6 cases is the rapid increase in vorticity in the mid-chord plane between T = 2 and 4. Section 4.4 showed that the vorticity from the tip vortex *appears* to quickly grow upward (i.e., away from the tip), become more complicated, and then undergo an "upward" pinch-off. This pinch-off event is important because it coincides with the unique, "inward" pinch-off of the LEVs at 50% span for AR = 2, and at 75% span for AR = 6. Either this swift increase in vorticity in the mid-chord plane (seen in the tiled vorticity plots of Figures 4.5.5 above) is a result of the tip vortex itself growing upward along the span, or it is due to vorticity generated somewhere else that is convected there. The alternative source of this vorticity can only be the leading edges, the corners, or both.

In order to test this hypothesis, a small drop of fluorescent dye was "painted" in each corner of the leeward face of the plate. If this dye was convected into the wake centerline at around 2 to 3 chord lengths, it would be likely that the vorticity production above the tip vortex in the mid-chord plane would be due to the vorticity generated in the corners or at the

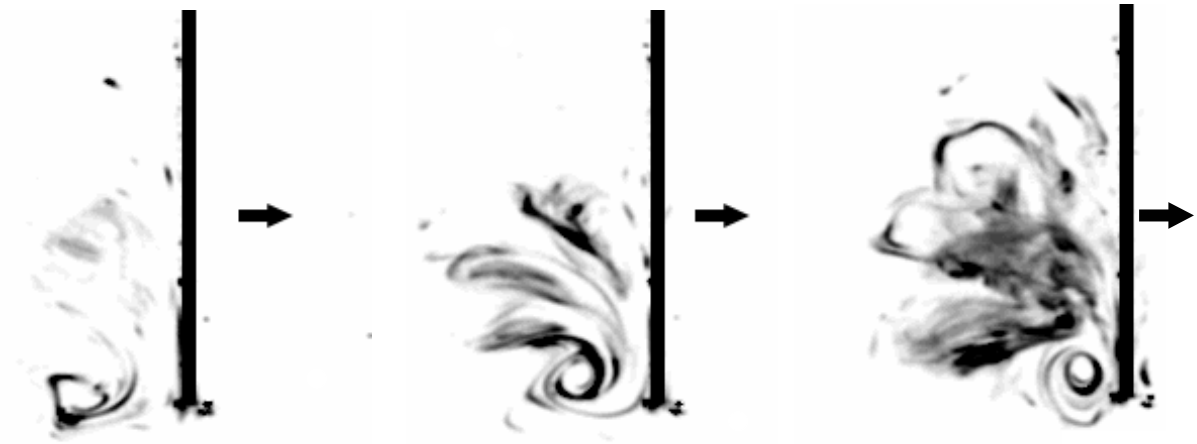

(a) t_{ref}, about 3*c* of travel (b) t_{ref} + 0.27 sec. (c) t_{ref} + 0.33 sec.

Figure 4.5.8 Mid-chord plane dye visualization, *Re* = 3000. Dye from the plate corners is convected into the mid-chord plane above the tip vortex.

leading edges. A spanwise laser sheet was placed at mid-chord, parallel to the flow like the DPIV laser sheet, to illuminate any dye in that location.

Figures 4.5.8a-c show three snapshots from this experiment, which was done at *Re* = 3000 with an *AR* of 6. The camera is facing the mid-chord laser sheet, so that it sees a side-view of the plate. For clarity, the plate has been artificially added to the image; it is moving to the right, and only its lower portion is visible. In Figure 4.5.8a, the plate has traveled about 3 chord lengths and, not surprisingly, some dye has been drawn into the tip vortex; there is little dye above the tip vortex at this time. The next snapshot, taken 0.27 seconds later and given in Figure 4.5.8b, shows a significant amount of dye in this mid-chord plane, which did not come from the tip vortex. It appears that the tip vortex aids the LEVs in convecting the dye into this plane, but the vortex itself does not enlarge and grow upward. After another 0.33 seconds (see Figure 4.5.8c), a substantial amount of dye from the corners has been pulled into this plane, and the area that dye occupies has grown larger and upward,

consistent with the DPIV. The tip vortex itself remains attached to the plate and coherent throughout this process.

This experiment demonstrates that, since dye from the corners is convected into the mid-chord plane by the LEVs (with the aid of the tip vortex), and the corners are a strong source of vorticity, it is likely that the accumulation of vorticity in the mid-chord plane is due to vorticity generated by the corners. The DPIV measurements show that the introduction of vorticity into this planar region, between the symmetrical LEVs, is then responsible for the interactions that produce the interesting phenomena in this spanwise plane and in the chordwise plane at 75% span (for AR =6, and 50% span for AR = 2).

4.5.7 Comparison of the flow structure with previous studies

The structure of the flow agrees well with the results of Champion and Coutanceau (1992), who studied the starting flow of AR = 2 to 5 circular cylinders with free, squared-off ends at Re = 1000 (see Chapter 1 for more details). They observed two helical LEVs (from 40 to 100% span) having spanwise flow away from the tip, consistent with the results of the present work. The duration of their experiments was T^* = 3.5, and the LEVs remained closely attached to the cylinder near its free end for the entire time. By T^* = 3.5, the LEVs from 80 to 60% span grew larger than those near the tip, increasing in size with increasing distance from the tip. The LEVs of the current study exhibited both of these behaviors. At the lower Reynolds number and shorter run-time of the cylinder experiments, however, no LEV pinch-off (such as that for the present work at AR = 6, 50% span) was observed. Also, due to the cylinder's lack of a sharp, thin tip edge, they reported only a very small tip vortex.

Champion and Coutanceau (1992) found that the LEVs from 0 to 40% span also had a helical structure, but with spanwise flow toward the tip. They observed a "collision"

between these opposing vorticity fluxes at 40% span and $T^* = 3.5$. Ellington et al. (1996) and Liu et al. (1998) reported a similar phenomenon in the LEV of a hawkmoth wing late in the downstroke. However, the opposite-sign spanwise flows in their inboard and outboard LEVs met at 75%, rather than 40% span. The results of the present work do not disagree with those of Champion and Coutanceau, in the sense that the lack of spanwise data for $AR = 6$ above 50% span does not confirm nor refute any spanwise flow (toward the tip) in the LEVs there. Champion and Coutanceau also report that the location of this meeting of opposite spanwise flows scaled linearly with AR. Although the spanwise DPIV of the present work for $AR = 2$ includes the flow over the full span, no significant spanwise flow toward the tip was observed. In fact, the current study shows that the flows for $AR = 6$ and 2 are similar in absolute terms spatially (they do not scale linearly), but that the $AR = 2$ flow progresses faster in time. Both of these results disagree with those of Champion and Coutanceau. However, the current $AR = 2$ data are for a plate with a clean free surface for its upper end condition, while the upper end condition of for the cylinder study was an end plate. This may at least account for the lack of spanwise flow (directed toward the tip) above 40% span for the $AR = 2$ plate.

The flat plate flow of the present work is similar to the hawkmoth studies of Ellington et al. (1996) and Liu et al. (1998), in that both cases exhibit LEVs that have significant spanwise flow, and thus helical structures. However, as mentioned above, the spanwise flow for the hawkmoth investigations is opposite that of the current flat plate experiments (at least from 50% span to the plate's tip), except for the tip-to-root flow that appears in the outboard hawkmoth LEV near the end of the downstroke. Ellington et al. (1996) hypothesized that the prolonged attachment of the LEV to the wing is due to the convection of vorticity out of the

LEV and toward the wing tip, via a strong root-to-tip spanwise flow. This, they postulated, would slow the increase in circulation of the LEV, compared to a 2-D case without spanwise flow, thus increasing the time required for the LEV to build up enough circulation to shed. The present work shows that the LEVs for $AR = 6$ remain attached to the plate outboard of 50% span for at least 8 chord lengths of travel, but with spanwise flow from tip to root that is *opposite* that implicated by Ellington et al. (1996) in keeping the LEVs attached. Based on the results of the current study, this author proposes that it is instead the low pressure created in the tip region by the induced 3-D flow from the tip vortices that is responsible for keeping the LEVs attached there, as well as for the high drag generated. The spanwise flow within the LEVs is a result of the flow induced by the tip, but not the mechanism responsible for the attachment of the LEVs there. Ellington et al. also observed a significant tip vortex, but they did not comment on any effect it may have on the LEV. Given the existence of this tip vortex, it is possible that its influence may be responsible for the behavior of the hawkmoth LEV. The discrepancy in spanwise flows between the investigation of Ellington et al. and the present work may simply be due to differences in kinematics. The hawkmoth wing has a sweeping shoulder motion that could create a pressure gradient from root to tip strong enough to generate a spanwise flow within the LEV in that direction.

The results of the present study are more consistent with the work of Birch and Dickinson (2001), who investigated the flow around a robotic flapping model of a fruitfly using DPIV and force measurements. They concluded that the tip vortex, along with flow from the previous stroke, creates a downward flow, or downwash, that reduces the effective angle of attack of the wing. This retards the build-up of circulation in the LEV, compared to a purely 2-D flow, thus keeping it attached longer. Since the angle of attack for the flat plate

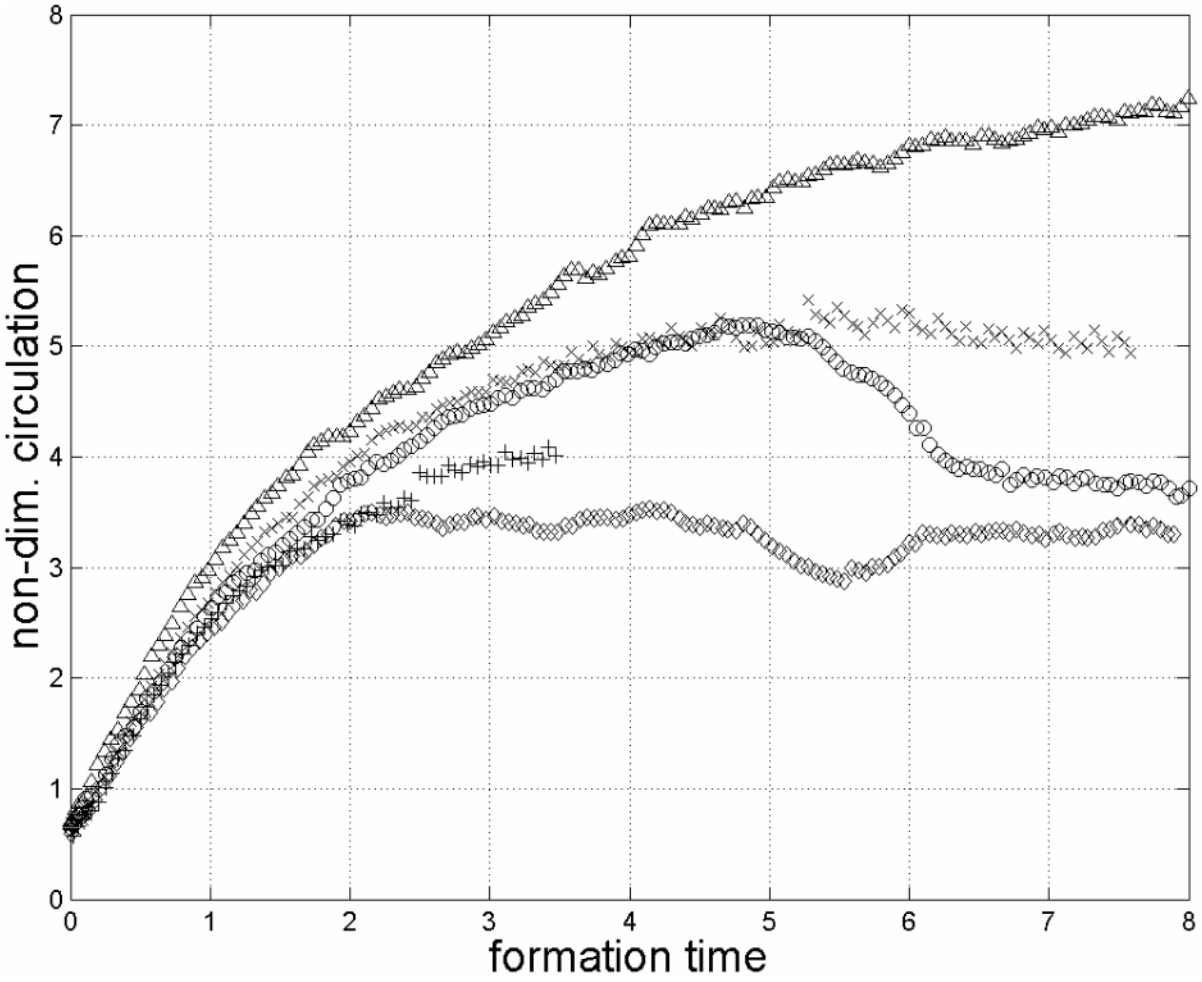

Figure 4.5.9 Circulation vs. formation time, *AR* = 6.
Triangles: total circ., 50% span; x's: LEV circulation, 50% span; circles: total circ., 75% span; crosses: LEV circulation, 75% span; diamonds: total circ., 90% span.

experiments of the present work was fixed at 90 degrees, no downwash can be defined, per se. In fact, due to this special-case α and the rectangular geometry of the plate, there are two equal but opposite corner vortices in addition to the tip vortex between them, generated at the tip edge. For this flow, the effect of the vortices at the tip can instead be discussed in terms of circulation and pressure.

As with the study by Birch and Dickinson (2001), the effect of the tip vortices in the current investigation was to decrease the circulation of the LEVs; in this case the LEVs became weaker with decreasing distance from the tip. Figure 4.5.9 gives the total and LEV

circulation for $AR = 6$, reproduced from section 4.3. The circulation and LEV formation numbers decrease from 50 to 90% span, and the vortices at 90% span remain attached to the plate for the full 8 chords of travel. Flow visualization and DPIV from this chapter showed that the induced 3-D flow from the tip is responsible for these trends in circulation. The significant influence of the tip vortex, especially at 90% span, is also reflected in the fact that the formation number of the tip vortex is the same as that for 90% span. In other words, when the tip vortex reaches its maximum circulation, its induced flow is strong enough to keep the LEVs at 90% span from gaining further circulation.

Although the effect of the tip vortex was to reduce the circulation of the LEVs for both the robotic fruitfly and the current flat plate experiments, the influence of this effect on the drag force was opposite for both studies. Upon suppressing the tip vortex with a wall adjacent to their model's wing tip, Birch and Dickinson (2001) measured an 8% increase in force on the wing. However, when a bottom wall was placed just below the plate tip for the present work, a drag minimum was measured in the place of the free end drag maximum, which was 46% higher at the peak. The most likely explanation for this dissimilarity is the substantial differences in Reynolds number and kinematics between the two cases.

The experiments of the present work were at a much higher Reynolds number (3000) than those of the fruitfly model ($Re = 160$), and the kinematics were much simpler. Birch and Dickinson (2001) found that, at their model's low *Re*, the LEV did not pinch-off when its circulation was increased (by 14%) with the addition of the tip vortex-suppressing end wall. Therefore, this stronger LEV that remained attached throughout the entire downstroke generated higher drag than the free end case; at a higher *Re*, the LEV would have been more likely to pinch-off. Additionally, the wing kinematics of their model, which consisted of

high yet varying angles of attack as well as sweeping shoulder motions, did not allow for the generation of a closed, low-drag leading and trailing edge vortex recirculating bubble, with or without tip vortex suppression. Section 4.2 of the current study shows that the lack of this bubble near the free end of the flat pate, due to the induced 3-D flow there, is partly responsible for the large difference in drag between the 2-D (grazing) and free end cases. Since the model fruitfly wing studied by Birch and Dickinson did not experience such a drastic change in flows when they diminished the effect of the tip vortex, the difference between that and their free end case was not as large as the one for the present work.

However, the absence of a recirculating LEV bubble for the current flat plate study is not the sole reason for the drag maximum measured for the free end case. There is substantial vorticity generated by the plate's tip and corners, which can be seen in the spanwise DPIV data (see Figure 4.5.5 above or section 4.4), that remains attached to the plate and grows stronger until the drag maximum around $T = 5$ (for $AR = 6$). This attached vorticity is a region of low pressure, which generates high drag. Additionally, the LEVs at 50% span, which are stronger than those closer to the tip, saturate around $T = 5$, thus contributing to the drag maximum before they pinch-off afterward. The reason why Birch and Dickinson (2001) did not measure a drag benefit due to influence of the tip is probably because of the differences in *Re* and kinematics discussed above. At such low Reynolds numbers, the strong pressure gradient near the tip, observed for the current study, is not as substantial. For the present case, it is the lower pressure near the tip that keeps the LEVs attached there and limits the growth of their circulation, compared to those away from the tip. This difference in circulation with distance from the tip creates a spanwise pressure gradient within the LEVs, which causes the spanwise flow within them from tip to root. Birch and

Dickinson measured very little spanwise flow within the LEV, which implies that the tip effect for the fruitlfly wing is very small. Finally, some dissimilarities in the results are very likely due to the fact that fruitfly wing kinematics have 3 degrees of freedom, while the simpler plate motion of the present work has only 1.

5 Summary and conclusions

5.1 Summary and conclusions

5.1.1 Objectives and methods

The primary objective of this work was to investigate the role of vortex formation in the drag force-generation of low *AR* flat plates at $\alpha = 90°$ starting from rest. This study was a first, fundamental step toward understanding the more complicated case of hovering flight, which relies primarily on drag for propulsion. The second goal of this investigation was to determine the effect of changing the *AR*, i.e., varying the relative importance of the plate's tip. By identifying how aspect ratio affects vortex generation and drag force, insight into *AR* selection in nature, as well as for micro air vehicle (MAV) design, can be gained.

Force measurements, DPIV of perpendicular sections, and 2-D and 3-D flow visualization were performed on flat plate models in a towing tank, at a moderate *Re* of 3000, to achieve these objectives. The drag of the two different *AR* plates (6 and 2) considered was measured with the bottom end (or tip) free, and a case where the tip of the $AR = 6$ plate "grazed" a bottom wall was also studied. These experiments demonstrated the effect of *AR* and tip vortex suppression, respectively, on the drag. The DPIV measurements were done in chordwise and spanwise planes to capture the velocity fields of the LEVs and the TV, respectively, both of which have been implicated by previous studies in the force generation of hovering flight (Ellington et al., 1996; Birch & Dickinson, 2001). Vorticity fields and circulation were calculated for each section to study the effect of the TV on the LEVs, and to establish the relationship between the vortex generation of the plate and the features of the drag force. Finally, since the flow is highly 3-D, flow visualization was used to characterize the overall vortex structure, study the interaction of the LEVs and the TV at the startup, and

account for features of the 2-D DPIV that were thought to be due to 3-D effects. After the formation time concept is described, the results of these experiments will be summarized, and conclusions based on the findings will be presented.

To compare results from experiments with different plate chord lengths and Reynolds numbers, whether within the present work or with other investigations, the formation time concept was used. Formation time is a dimensionless timescale, normalized in this case by the plate's chord length and mean velocity, and it is approximately equal to the number of chord lengths traveled. Its primary use is to connect the time required for a vortex to attain its maximum circulation, before pinch-off, with the kinematics that generated it. If this maximum circulation can be correlated with force phenomena, formation time can be used as a guide for wing kinematics. For example, if vortex saturation occurs after 5 chord lengths of travel, and correlates with a peak in the force, little will be gained by traveling farther, suggesting that the wing should then turn around and start another half-stroke.

5.1.2 Force measurements

Section 4.2 reported the data from the drag force measurements. The peak in the C_D during the initial acceleration of the plate was 1.8 times higher for $AR = 2$ than $AR = 6$. This was attributed to the inertia of the plate model, which was relatively higher for $AR = 2$ because of the definition of the drag coefficient, which accounts for the submerged plate area. At $T = 5$, for the $AR = 6$ free end case, a broad "hump" or maximum in the C_D was measured. For the $AR = 6$ grazing end case, a drag minimum was measured at the same formation time; the maximum was 46% higher than the minimum.

Lisoski (1993), who studied $AR = 6$ to 17 plates with the grazing end condition, also found drag minimums for each AR, albeit at a later time ($T^* = 8$) due to a much lower initial

acceleration. He observed that this grazing lower end condition, coupled with a clean free surface above, was the best for promoting a highly 2-D flow. Lisoski attributed the drag minimum to a closed recirculating bubble behind the plate, made up of the essentially 2-D LEVs. He hypothesized that the recirculating flow induces velocity, near the wake centerline, toward the rear face of the plate. This would raise the base pressure there, which would lower the drag. He postulated that the C_D minimum occurs when the LEVs reach their maximum strength, after which the recirculating bubble eventually breaks open, raising the C_D again. These results demonstrate that the effect of the tip or free end is to prevent the formation of this recirculating bubble over at least a portion of the span, which increases the drag. Additionally, since a drag maximum was observed for the free end case, it seemed that presence of the tip has more of an effect than simply suppressing the recirculating bubble, which the DPIV and flow visualization results later confirmed.

To gain insight as to why mixed end conditions (nominally 2-D at the root, 3-D at the tip) are beneficial, steady-state drag data for fully 2-D and 3-D end conditions were examined. A steady-state, infinite-AR normal flat plate has a C_D of 1.98, and for an $AR = 1$ normal flat plate (with all edges free), the steady-state C_D is 1.05. Separation and shear layer roll-up at all edges (as with a fully 3-D body), rather than just two for a 2-D body, creates a more contracted wake, and thus less drag. For the unsteady case, the present work shows that mixed end conditions produce more drag than nominally 2-D end conditions. The steady-state data suggest that an unsteady plate with two 3-D end conditions, i.e., a tip vortex at either end, would generate less drag than the mixed end condition case. In fact, for a rectangular solid oriented normal to the flow and having one free end (i.e., mixed end conditions), the steady-state C_D is about 1.5 for AR's between 1 and 4, while for the fully 3-D

case (a normal cube with all sides free), the C_D is a significantly lower 1.05; the 2-D case, namely, a rectangular solid of infinite *AR*, has a C_D of 2.2. The current study shows that the one tip vortex of the mixed end condition plate prohibits the low-drag, 2-D recirculating LEV bubble, induces highly 3-D, low pressure flow at the tip, and yet allows the LEVs away from the tip to grow strong and contribute to the drag. However, tip vortices at each end of the plate would reduce the strength of the LEVs over a greater portion of the span, thus diminishing their significant contribution to the drag force.

Since the free end effect presumably has less of an influence as *AR* increases, the issue of what magnitude *AR* is needed to obtain a significant benefit from the tip effect was explored. Lisoski (1993) also measured the drag on plates with a free lower end condition to determine if nominally 2-D flow was possible for this case. For an $AR = 17$ plate, he still measured a drag minimum. When the *AR* was reduced to 10, the drag minimum disappeared, although he observed no maximum. Therefore, given these results and those of the present work, it was concluded that a significant drag benefit due to the influence of the tip is only achieved when the *AR* is reduced below 10, with a 46% peak gain in the drag over the nominally 2-D case when the *AR* is set to 6. Based on these findings, it is recommended that a wing designed for hovering flight, which relies primarily on drag for propulsion, should have an *AR* of about 6 or less. The works cited in Chapter 1 indicate that, consistent with this recommendation, hovering animals in nature have *AR*'s between 2.75 and almost 6. Their single wings also have only one tip vortex, consistent with the above discussion on end conditions.

For $AR = 2$, the C_D was higher than that of $AR = 6$ even after the initial peak at the startup. This was attributed to the relatively greater influence of the plate tip at $AR = 2$,

which will be discussed in more detail in section 5.1.4. The drag for $AR = 2$ did not exhibit a single maximum like that of $AR = 6$. Instead, "wiggles" in the C_D were observed between $T = 3$ and 7, and were found to correspond with vorticity induced by the plate's tip impinging the free surface. Unfortunately, any features due to the formation and saturation of the LEVs or the TV were masked by these drag oscillations.

5.1.3 Chordwise flow sections: vorticity, circulation, and formation number

Chordwise (horizontal) sections of the flow velocity were captured quantitatively at 50, 75, and 90% span (measured from the free surface), for AR's = 6 and 2, in order to investigate the LEVs (see section 4.3). For both $AR = 6$ and 2, the total circulation generated at a single plate edge (the flow is symmetrical) decreased with decreasing distance from the plate tip. The $AR = 6$, 50% span case was the only one that exhibited LEV pinch-off. At 75% span for the same AR, the LEVs exhibited a near-pinch-off, but subsequently merged again with the shear layers that formed them. After this merging, the LEVs were drawn toward the center wake, where they subsequently pinched-off "inwardly" from the edge shear layers, then remained trapped in the plate's wake. The spanwise DPIV data showed, as expected, that this was a result of the highly 3-D flow induced by the plate tip. No pinch-off occurred at 90% span, only a saturation in the circulation, and the vortices there remained attached to the plate throughout the entire run. The formation number for the LEVs at 50% span was 4.5, for 75% span the formation number before the initial, near-pinch-off was 3, and the formation number at 90% span was 2. Therefore, the formation number, like the circulation, was found to decrease with diminishing distance from the tip. This shows that the effect of the tip is to limit the growth of the circulation of the LEVs closer to it, as compared to those farther away. Additionally, the reduction in formation number with

decreasing distance from the tip illustrates that the induced flow from the tip affects the LEVs closer to it more quickly.

The formation time $T = 5$, when the force peak for $AR = 6$ is observed, corresponded to certain features in the LEV circulation. First, it is at about that time that the LEVs at 50% span saturate. Second, there is a drop at $T = 5$ in the total circulation at 75% span, as well as a minimum in the circulation at 90% span. Decreases or increases in circulation based on 2-D DPIV, after the formation number but before viscous diffusion becomes significant, indicate substantially 3-D flow. The spanwise DPIV indeed revealed this to be the case around $T = 5$.

The $AR = 2$ flow exhibited no LEV pinch-off similar to that of $AR = 6$ at 50% span. However, LEV saturation did occur, and, like the $AR = 6$ case, the formation number decreased with decreasing distance from the plate tip. Upon comparison of the circulation and vorticity fields of $AR = 2$ and 6, the flows were found to have similar features spatially, but in the absolute sense. In other words, the flow at $AR = 6$, 90% span was very much like that of $AR = 2$, 75% span, and both spanwise locations are at almost the same absolute distance from the plate tip. However, temporally the $AR = 2$ flow developed more quickly after about $T = 3$. This implies that the effect of the tip increases with decreasing AR.

5.1.4 Spanwise and chordwise flow sections, and measured drag revisited

Section 4.4 presented the chordwise vorticity data discussed in the previous section along with the spanwise vorticity fields. These spanwise vorticity fields were calculated from DPIV data taken in a plane at mid-chord, parallel to the free stream, and another plane at one of the leading edges (since the flow is symmetrical). The full set of spanwise and chordwise vorticity fields were compared with the measured drag force, in order to correlate

any features between the two. Additionally, the circulation of the tip vortex itself, in the mid-chord plane, was calculated from the DPIV data, for comparison with the chordwise circulation.

It was found that the TV formation number is the same as that of the LEVs at 90% span, for both $AR = 6$ and 2. This indicates that the TV has a strong influence on the LEVs there, limiting their growth much more than those away from the tip (which have higher formation numbers and circulation).

Substantial vorticity, in addition to that of the TV, was measured in the mid-chord and leading edge planes for both *AR*'s. The vorticity in the mid-chord plane, which appears to "grow" out of the TV and up the span very quickly after $T = 2$, could not be explained based on the 2-D DPIV data alone. In the leading edge plane, more coherent vortices were observed, implying that the LEVs bend and impinge the leading edge plane as the plate travels. The 2-D and 3-D flow visualization presented in section 4.5, discussed next, was needed to explain and verify these phenomena.

The "inward" pinch-off of the LEVs of $AR = 6$, 75% span and $AR = 2$, 50% span, was observed to coincide with features of the mid-chord vorticity. At the same formation time that the "inward" LEV pinch-off occurs, the vorticity in the mid-chord plane that is above the TV pinches-off upwardly and away from the TV. This pinched-off vorticity is located at the spanwise location where the "inward" LEV pinch-off occurs. Thus, the "inward" pinch-off of the chordwise LEVs is due to substantial out-of-plane flow.

Consistent with to the flow in the chordwise planes, the vorticity in the mid-chord and leading edge planes of $AR = 6$ and 2 were very similar spatially, in the absolute sense. However, as with the chordwise flow, the spanwise vorticity of $AR = 2$ was temporally more

accelerated. This adds support to the above conclusion that the influence of the tip increases with decreasing *AR*, which was expected.

For *AR* = 6, the "hump" or maximum in the drag force at *T* = 5 corresponds to chordwise and spanwise flow phenomena. As discussed above, the LEVs at 50% span saturate around this formation time, and thus contribute to the drag force until they pinch-off at *T* = 6.67. Also by this formation time, the vorticity in the mid-chord plane has increased substantially, and it remains attached to the plate; the "upward" pinch-off just described starts to occur at this time. The drag maximum at *T* = 5 is therefore due to the low pressure created by the saturated LEVs at 50% span, in addition to the strong attached vorticity visible in the mid-chord plane. This attached vorticity is also a region of low pressure and thus high drag on the plate.

Finally, the fact that the drag coefficient for *AR* = 2 is consistently higher than that of *AR* = 6 was explained using the spanwise vorticity fields. As mentioned above, the attached vorticity observed in the mid-chord plane, due to flow induced from the plate tip, is a region of low pressure that creates high drag. This vorticity exists over a relatively larger portion of the span for *AR* = 2 versus *AR* = 6, thus the C_D for *AR* = 2 is larger.

5.1.5 The structure of the flow from dye visualization

Dye flow visualization was used to devise a vortex line model for the flow near the tip at the startup, and also to capture the global structure of the flow. Additionally, it allowed the local flow at the tip to be reconciled with the global flow. Finally, flow visualization proved invaluable in explaining the DPIV vorticity field data taken in the spanwise planes.

At the startup, the LEV and the TV are essentially 2-D, and they join together at the corner of the plate. A vortex line model, backed up by evidence from flow visualization, was

used to show that the induced flow from the LEV and the TV eventually cause this corner vortex to bend up, and fold at its ends. These folds at either end then kink and twist around themselves, forming two helical vortices that appear to "sprout" perpendicularly from the face of the plate in the corner.

Globally, there is a tip vortex that is especially strong at mid-chord, and the induced flow from it and the corner vortices causes the LEVs near the tip to remain closely attached. Away from the tip, the LEVs are larger, and grow farther out into the wake. Within the LEVs, there is an upward (i.e., away from the tip) spanwise flow, which gives them a helical or tornado-like structure. Since the LEVs farther (spanwise) from the tip are stronger (shown by the chordwise LEV circulation data), the pressure within them is lower than their counterparts near the tip. This creates a spanwise pressure gradient within the LEVs that is responsible for the spanwise flow seen in the visualizations. The 2 helical vortices in each corner of the plate "connect" with the global flow by simply being convected, as material lines, into the LEVs nearest them. They "wrap around" within the larger LEV helices, following the induced velocity there.

The larger-scale flow visualizations also showed that the LEVs bend so that they have significant vorticity vectors normal to leading the edge planes. By comparing the locations of the chordwise LEV vortex cores at different spanwise stations, the sign of any LEV vorticity that impinges the leading edge planes, between those chordwise sections, can be predicted.

Finally, the rapid increase in vorticity in the mid-chord plane, above the tip vortex, was found to be due to vorticity from the plate's corners been convected into the center wake by the LEVs.

5.1.6 Comparison with previous work (see section 4.5.7 for a more detailed discussion)

The results of the current work agreed very well with those of Champion and Coutanceau (1992), who performed similar experiments with low *AR* circular cylinders with one end free. However, the mechanism responsible for keeping the LEVs attached to the plate near the tip was not that hypothesized by Ellington et al. (1996), who studied the LEV of a flapping model of a hawkmoth. Ellington et al. attributed the prolonged attachment of the hawkmoth LEV to a strong root-to-tip spanwise flow within its core. They hypothesized that this spanwise flow convects vorticity out of the LEV and toward the tip, which slows the accumulation of circulation within the LEV and thus keeps it attached longer. The spanwise flow within the LEVs of the present study (from tip to root) was the opposite of that found by Ellington et al. Therefore, another mechanism must prevent the LEVs from pinching-off. Based on the results of the current work, this author proposes that it is instead the low pressure created at the tip by the induced 3-D flow from the tip vortices that keeps the LEVs attached there and limits their strength. This low pressure is also responsible for the high drag generated. The spanwise flow within the LEVs is a result of the flow induced by the tip, and not the mechanism actually responsible for the attachment of the LEVs near the tip. Since Ellington et al. also observed a significant tip vortex, it may be the cause for the behavior of the hawkmoth LEV. The discrepancy in spanwise flows between that investigation and the present work may simply be due to differences in kinematics. The hawkmoth wing has a sweeping shoulder motion that could create a pressure gradient from root to tip strong enough to generate a spanwise flow, within the LEV core, in that direction.

The findings of the current investigation are more consistent with that of Birch and Dickinson (2001), who studied the flow around a flapping model of a fruitfly wing.

Combining DPIV and force measurements, they found that the tip vortex, coupled with flow from the previous wing stroke, generates downwash that lowers the effective angle of attack of the wing. They hypothesized that this downwash slows the acquisition of circulation within the LEV, compared to the 2-D wing case, thus delaying its pinch-off. To test this idea, they placed a wall at the tip of their wing model in order to suppress the TV. This resulted in a 14% increase in the LEV circulation, which supports their hypothesis.

Circulation measurements from the present work also show that the effect of the induced flow from the tip is to decrease the circulation of the LEVs as they get closer to the tip. This is in agreement with the results of Birch and Dickinson (2001). However, when a wall was placed just below the plate's free end in order to suppress the tip vortex, the drag on the plate decreased substantially. Although this disagrees with the results of the similar experiment performed by Birch and Dickinson, this discrepancy is most likely due to the large differences in Reynolds number and kinematics between the two studies. Whereas the current flat plate experiments were done at a Reynolds number of 3000, with a 1 degree of freedom motion, the fruitfly model of Birch and Dickinson (2001) operated at $Re = 160$ with 3 degrees of freedom.

At this low *Re*, the LEV of the fruitfly model did not pinch-off when the TV was suppressed. Instead, it simply grew larger and generated more force on the wing. In this Reynolds number regime, the tip vortex appears to be a hindrance rather than an asset (Birch and Dickinson, 2001). However, for the higher *Re* flat plate, the induced 3-D flow from the tip generates substantial vorticity in the tip region (visible in the spanwise DPIV data in Chapter 4). This vorticity remains attached to the plate throughout the run and generates high drag, since it is a region of low pressure. Birch and Dickinson may not have found a

drag benefit due to the induced flow from the wing tip because the pressure gradient there was not as strong as that of the current work. It is the strong tip effect of the present flat plate study that restricts the circulation acquired by the LEVs near the tip, which leads to the spanwise flow within the LEVs. Birch and Dickinson measured only a very small spanwise flow within the fruitfly wing LEV, which supports the hypothesis of a weaker tip effect.

Lastly, it should be remarked that the differences in kinematics between the current flat plate investigation and the insect flight work of Birch and Dickinson certainly creates discrepancies in the two sets of results. For example, the effect of the tip vortex in the present flat plate study is to prohibit the generation of the low-drag, recirculating LEV bubble observed in nominally 2-D flat plate flow at very high angles of attack. Such a bubble is not observed over the fruitfly wing because of the constantly changing angle of attack and the wing's sweeping motion, which form non-symmetric vortices at the leading and trailing edges. This lack of a recirculating bubble for the fruitfly wing also explains why the difference in measured drag between the free end and end-wall cases was not as large as that for the similar experiments of the present work.

The results of the current study agree well with the data on hovering flight. As presented in section 5.1.2, the aspect ratios determined to give the greatest amount of drag force, about 6 or less, are consistent with the range of AR's found in actual hovering animals, which are between 2.75 and almost 6 (Ellington, 1984; Dhawan, 1988; Dickinson, 1999). Additionally, the maximum in the drag force, for $AR = 6$, occurred at about 5 chord lengths of travel, which is within the horizontal wing-stroke amplitude range of 3 to 5 chord lengths observed for insects (Weis-Fogh, 1973; Wang et al., 2004). The relationship between the drag force and plate aspect ratio was found to be a result of the vortex dynamics. Thus,

MAV wing kinematics and geometry should be designed so as to take advantage of vortex formation time, coupled with wing size and shape, for generating optimal drag force.

Despite the above discussion, one may still question the applicability of the results from the present work to the more complicated case of hovering flight. In order to address this issue, it is easiest to identify the flow features found for hovering kinematics that are not present during the simpler motion of the current flat plate study. First, since there is no shoulder-type movement about the plate root (as in the wing sweeping and two-degree of freedom translation about a ball-and-socket-type joint exhibited during hovering), there is no difference in plate velocity from root to tip. Therefore, the forced root-to-tip pressure gradient seen, for example, in the flow around a hawkmoth wing (Ellington et al., 1996) is not modeled by the present case. Second, since the angle of attack of the current flat plate does not change, there is no dominant LEV, and at $\alpha = 90°$, no downwash, as observed for a fruitfly wing (Birch & Dickinson, 2001), can be defined. There are, in fact, two opposite-sign LEVs of equal strength, two equal but opposite-sign corner vortices (due to the rectangular geometry), and a tip vortex between the vortices near the corners.

From the results of Ellington et al (1996), it appears that the effect of the forced root-to-tip pressure gradient, at Reynolds numbers on the order of 1000, is to induce spanwise flow within the LEV core from root-to-tip, which is opposite that of the current study. However, given the present results (which report a strong tip effect), and the fact that Ellington et al. observed a significant tip vortex, it is possible that the spanwise flow is not the mechanism responsible for the prolonged attachment of the LEV. Alternatively, since Ellington et al. did observe spanwise flow in the same direction of the present work, over the outboard region of the hawkmoth wing late in the downstroke, it may be that the current flat

plate case is most applicable to the outboard portion of a hovering wing. This is reasonable, since the root-to-tip pressure gradient is relatively minor if only that region is considered. Conversely, the tip effect for that portion of the wing is very strong. Limiting the applicability of the current flat plate case to only the outboard portion of the wing may, however, be dismissing the observed agreement in *AR* range (i.e., the range needed to achieve high drag) between the present results and those of hovering animals.

Changes in α are a necessity for the reciprocating motion of a hovering wing, and they allow for more control of the resultant wing force vector. However, although changing the α for the present work would alter the formation and interaction of the LEVs, the corner vortices, and the TV, the results of Birch and Dickinson (2001) suggest that it would not change the influence of the tip on the LEVs. It seems likely that the tip effect would still limit the accumulation of circulation within the LEVs, as reported for the current study and by Birch and Dickinson, prolonging their attachment to the plate.

Finally, the fact that the *AR*'s and stroke distance recommended by the present work for a flapping MAV agree with the data on hovering flight also provides justification for the applicability of this simple model.

5.2 Recommendations for future work

Given the connections between drag, *AR*, and vortex dynamics found with this simple geometry and motion, it seems worthwhile to continue this work by adding degrees of freedom. The eventual goal would be to understand the physics behind the more complex kinematics and wing shapes found in nature, in order to create a man-made MAV. Two more translational degrees of freedom could be added, to more closely match natural flapping, as well as rotation about a spanwise axis to allow time-varying angles of attack. Additionally,

the current study could be repeated at a different angle of attack, in order to investigate the effect of making the two corner vortices, as well as the two LEVs, non-symmetric. Different wing tip geometries could also be explored, such as rounded or pointed (triangular) shapes. This type of work has been and continues to be done in the fruitfly Reynolds number regime (see Birch and Dickinson, 2001, for example), so that future work should be focused on the higher *Re* range of the current study.

6 References

Batchelor, G. K. 1967. *An introduction to fluid dynamics* 1st ed. Cambridge. Cambridge University Press.

Birch, J., & Dickinson, M. H. 2001. Spanwise flow and the attachment of the leading-edge vortex on insect wings. *Nature* **412**, 729-33.

Blevins, R. D. 1984. *Applied fluid dynamics handbook*. New York: Van Nostrand Reinhold Company.

Champion, J.-L., and Coutanceau, M. 1992. Development of the near wake structure on a cantilevered circular cylinder with a free-end. In H. Eckelmann, J. M. R. Graham, P. Huerre, & P. A. Monkewitz (Eds.), *Bluff-body wakes, dynamics, and instabilities. IUTAM Symposium, Göttingen, Germany, Sept. 7-11.* pp. 43-46. New York: Springer-Verlag.

Chua, K., Lisoski, D., Leonard, A., & Roshko, A. 1990. A numerical and experimental investigation of separated flow past an oscillating flat plate. *ASME FED International Symposium on Nonsteady Fluid Dynamics, Book No. H00597* **92**, 455-464.

Daniel, T. L. 1984. Unsteady aspects of aquatic locomotion. *Amer. Zool.* **24**, 121-134.

Dennis, S. C. R., Qiang, W., Coutanceau, M., & Launay, J.-L. 1993. Viscous flow normal to a flat plate at moderate Reynolds numbers. *J. Fluid Mech.* **248**, 605-635.

Dhawan, S. 1991. *Bird flight.* Bangalore: Indian Academy of Sciences.

Dickinson, M. H., & Götz, K. G. 1993. Unsteady performance of model wings at low Reynolds number. *J. Exp. Biol.* **174**, 45-64.

Dickinson, M. H., Lehmann, F.-O., & Sane, S. P. 1999. Wing rotation and the aerodynamic

basis of insect flight. *Science* **284**, 1954-1960.

Dudley, R. 2000. *The biomechanics of insect flight: form, function, evolution.* Princeton: Princeton University Press.

Ellington, C. P. 1984. The aerodynamics of hovering insect flight. *Phil. Trans. R. Soc. Lond.* B **305**, 1-181.

Ellington, C. P., van den Berg, C., Willmott, A. P., & Thomas, A. L. R. 1996. Leading-edge vortices in insect flight. *Nature* **384**, 626-630.

Fage, A., & Johansen, F. C. 1927. On the flow of air behind an inclined flat plate of infinite span. *Roy. Soc. Proc., A* **116**, 170-197.

Gharib, M., Rambod, E., & Shariff, K. 1998. A universal time scale for vortex ring formation. *J. Fluid Mech.* **360**, 121-140.

Green, S. I. (Ed.). 1995. *Fluid vortices*. Boston: Kluwer Academic Publishers.

Jeon, D. 2000. *On cylinders undergoing one- and two-degree of freedom forced vibrations in a steady flow.* Ph.D. Thesis, California Institute of Technology.

Koumoutsakos, P., & Shiels, D. 1996. Simulations of the viscous flow normal to an impulsively started and uniformly accelerated flat plate. *J. Fluid Mech.* **328**, 177-227.

Lian, Q.-X., & Huang, Z. 1989. Starting flows and structures of the starting vortex behind bluff bodies with sharp edges. *Exps. Fluids* **8**, 95-103.

Lisoski, D. L. A. 1993. *Nominally 2-dimensional flow about a normal flat plate.* Ph.D. Thesis, California Institute of Technology.

Liu, H., Ellington, C. P., Kawachi, K., van den Berg, C., & Willmott, A. P. 1998. A

computational fluid dynamic study of hawkmoth hovering. *J. Exp. Biol.* **201**, 461-477.

Maxworthy, T. 1979. Experiments on the Weis-Fogh mechanism of lift generation by insects in hovering flight. *J. Fluid Mech.* **93**, 47-63.

McCormick, B. W. 1995. *Aerodynamics, aeronautics, and flight mechanics* 2nd ed. New York: John Wiley & Sons, Inc.

Pullin, D. I., & Perry, A. E. 1980. Some visualization experiments on the starting vortex. *J. Fluid Mech.* **97**, 239-255.

Ramamurti, R., & Sandberg, W. C. 2002. A three-dimensional computational study of the aerodynamic mechanisms of insect flight. *J. Exp. Biol.* **205**, 1507-1518.

Roshko, A. 1954. On the drag and shedding frequency of two-dimensional bluff bodies. *NACA Tech. Note* **3169**.

Roshko, A. 1955. On the wake and drag of bluff bodies. *J. Aero. Sci.* **22**, 124-132.

Sarpkaya, T., & Isaacson, M. 1981. *Mechanics of wave forces on offshore structures*. New York: Van Nostrand Reinhold Company.

Sarpkaya, T., & Kline, H. K. 1982. Impulsively-started flow about four types of bluff body. *J. Fluids Engr.* **104**, 207-213.

Slaouti, A., & Gerrard, J. H. 1981. An experimental investigation of the end effects on the wake of a circular cylinder towed through water at low Reynolds numbers. *J. Fluid Mech.* **112**, 297-314.

Wang, Z. J. 2000. 2D mechanism of hovering. *Phys. Rev. Lett.* **85**, 2216-2219.

Wang, Z. J., Birch, J. M., & Dickinson, M. H. 2004. Unsteady forces and flows in low Reynolds number hovering flight: two-dimensional computations vs. robotic wing

experiments. *J. Exp. Biol.* **207**, 449-460.

Weis-Fogh, T. 1973. Quick estimates of flight fitness in hovering animals, including novel mechanisms for lift production. *J. Exp. Biol.* **59**, 169-230.

Westerweel, J., Dabiri D., & Gharib, M. 1997. The effect of a discrete window offset on the accuracy of cross correlation analysis of digital PIV recordings. *Exp. In Fluids* **23**, 20-28.

Willert, C. E., & Gharib, M. 1991. Digital particle image velocimetry. *Exp. In Fluids* **10**, 181-193.

Williamson, C. H. K., & Roshko, A. 1988. Vortex formation in the wake of an oscillating cylinder. *J. of Fluids and Struct.* **2**, 355-381.

Appendix

A.1 PMAC motion control programs

A1.1 PMAC program for carbon fiber plate, standard velocity profile

```
;  Program for Thesis
;
;  Formation number study for flat plate at 90 degrees of attack.
;
;  Plate accelerates linearly over a distance of 1/4 chord length
;  to a constant velocity, and overall travels 15 chord lengths.
;
;  Chord length = 5cm
;
; 11/18/03
;*****************************************

A
CLOSE
DELETE GATHER
DELETE TRACE
OPEN PROG 1 CLEAR

FRAX(X)
INC

P1 = 5*15              ; Distance of travel during experiment (cm)
P2 = 6                 ; Desired max velocity during experiment (cm/s), gives Re = 3000
P3 = 0.4167*1000       ; TA
TS0
TA(P3)
F(P2)
X(-P1)


DWELL4000
LINEAR
ABS
TA1000
F(2)
X0

CLOSE
```

A1.2 PMAC program for carbon fiber plate, ramp velocity profile

```
;  Program for Thesis
;
;  Formation number study for flat plate at 90 degrees of attack.
;
;  Plate accelerates linearly over a distance of 2.5 chord lengths
;  to a constant velocity (then decelerates TRAPEZOID!), and overall travels 15 chord
lengths.
;
;  Chord length = 5cm
;
; 4/02/04
;*****************************************

A
CLOSE
DELETE GATHER
DELETE TRACE
OPEN PROG 1 CLEAR

FRAX(X)
INC

P1 = 5*15              ; Distance of travel during experiment (cm)
P2 = 6                 ; Desired max velocity during experiment (cm/s), gives Re = 3000
P3 = 4.1667*1000       ; TA
P4 = P3/4
TS(0)
TA(P3)
F(P2)
X(-P1)


DWELL4000
LINEAR
ABS
TA1000
F(2)
X0

CLOSE
```

A1.3 PMAC program for glass plate used for DPIV, standard velocity profile

```
;  Program for Thesis
;
;  Formation number study for flat plate at 90 degrees of attack.
;
;  Plate accelerates linearly over a distance of 1/4 chord length
;  to a constant velocity, and overall travels 13 chord lengths.
;
;  Chord length = 6.35cm (glass)
;
; 11/30/03
;*****************************************

A
CLOSE
DELETE GATHER
DELETE TRACE
OPEN PROG 1 CLEAR

FRAX(X)
INC

P1 = 6.35*13          ; Distance of travel during experiment (cm)
P2 = 4.724            ; Desired max velocity during experiment (cm/s), gives Re = 3000
P3 = 0.672*1000       ; TA
TS0
TA(P3)
F(P2)
X(-P1)


DWELL4000
LINEAR
ABS
TA1000
F(2)
X0

CLOSE
```

A1.4 PMAC program for glass plate used for flow vis., standard velocity profile

```
;  Program for Thesis
;
;  Formation number study for flat plate at high angles of attack.
;
;  Plate accelerates linearly over a distance of 1/4 chord length
;  to a constant velocity, and overall travels 11 chord lengths.
;
;  Chord length = 8.89cm
;
; 10/18/02
;*****************************************

A
CLOSE
DELETE GATHER
DELETE TRACE
OPEN PROG 1 CLEAR

FRAX(X)
INC

P1 = 8.89*11                ; Distance of travel during experiment (cm)
P2 = 1.125*2                ; Desired max velocity during experiment (cm/s), gives Re =
2000
P3 = (0.79/2*10)*1000/2     ; Time to complete linear acceleration to constant velocity (ms)

TS0
TA(P3)
F(P2)
X(-P1)


DWELL4000
LINEAR
ABS
TA1000
F(3)
X0

CLOSE
```

A.2 Force balance calibration

Example of calibration curve for N1 force transducer.